THREE-DIMENSIONAL ANALYSIS OF AIRFLOW AND TEMPERATURE IN A THYRISTOR VALVE HALL

BY

JEFFREY R. BERG

A Thesis
Presented to the Faculty of Graduate Studies
In Partial Fulfillment of the Requirements for the Degree of

MASTER OF SCIENCE

Department of Mechanical and Manufacturing Engineering
University of Manitoba
Winnipeg, Manitoba

THE UNIVERSITY OF MANITOBA

FACULTY OF GRADUATE STUDIES

*****

COPYRIGHT PERMISSION

A Thesis/Practicum submitted to the Faculty of Graduate Studies of The University of

Manitoba in partial fulfillment of the requirement of the degree

of

MASTER OF SCIENCE

ABSTRACT

A numerical analysis is performed for the three-dimensional, turbulent flow of air in a thyristor valve hall located at the Dorsey Converter Station, owned and operated by Manitoba Hydro. The goal of this analysis was to determine the configurations that result in increased air-side cooling effectiveness in the valve hall. Slight modifications are made to the actual valve hall geometry in order to decrease the computational effort. These modifications allow for the use of symmetry planes which decrease the size of the computational domain used while not significantly altering the fidelity of the model to the application. The governing equations are solved using the Computational Fluid Dynamics (CFD) code CFX-5. This computer code uses a finite volume method of solution and is based on a finite element approach for representing the geometry. The effects of inlet and outlet opening geometry, inlet air mass flow rate, and inlet air angle on the thermal performance for the air-side cooling of the thyristor valve hall geometry are examined.

Two different computational domains are used to model the valve hall geometry depending on the location of the inlet and outlet openings. When the inlet and the outlet openings are symmetrical with the tower centreline on two axes, one-quarter of one tower is modeled which is assumed to be representative of the entire valve hall. Converged steady-state results are obtained for a total of twenty-one unique cases using this computational domain by varying the inlet opening mass flow rate, aspect ratio, area, and location as well as the inlet air angle. The results of a base case using this computational domain are presented in detail first, followed by the results of a parametric study. When the inlet and the outlet openings are symmetrical with the tower centreline on one axis, one-half of one tower is modeled which is assumed to be representative of the entire valve hall. Converged steady state solutions are obtained for a total of two unique cases on this computational domain by varying the inlet opening area.

From the base case, it is determined that the current inlet air mass flow rate used in the valve hall is sufficient to effectively cool the towers; however, due to an uneven distribution of mass flow through the individual gaps of the tower, some gaps receive sufficient cooling air flow, while others are starved of air flow. The maximum temperatures on the block surfaces that are starved of air are much higher than those that receive sufficient air flow.

The results of the twenty-one cases studied when the inlet and outlet openings are symmetrical with the tower centreline on two axes show that modest improvements in cooling effectiveness can be made in the valve hall by varying the inlet opening aspect ratio, area, and location as well as the inlet air angle with the same inlet mass flow rate used in the base case. For the best performing case with the current mass flow rate, all four of the above parameters are varied. More dramatic improvements in cooling effectiveness can be made for this configuration when the inlet mass flow rate is doubled using the same size inlet opening as the base case. For these cases, dramatic improvements in cooling effectiveness are not achieved for every inlet air angle used. Instead, for the particular inlet size and location used, an optimal inlet air angle exists which optimizes cooling effectiveness in the valve hall.

The results of the cases studied with the inlet and outlet openings symmetrical with the tower centreline on one axis show that dramatic improvements in cooling effectiveness can be made by locating the inlet opening on one of the side walls and by varying the size and location of the inlet opening with the same equivalent mass flow rate as in the base case. These improvements, however, were not observed for all cases studied using this configuration.

.

ACKNOWLEDGEMENTS

I would like to express my deepest appreciation to my advisors Dr. Hassan Soliman and Dr. Scott Ormiston for their guidance with this thesis and throughout the Master of Science program. I would also like to recognize Dr Eric Bibeau and Dr. Ioan Ciric for their participation on the examining committee. I also appreciate the effort from Manitoba Hydro staff, in particular Mr. Harry Jhinger and Mr. Ed Didychuk for their support with this project. I am grateful to Manitoba Hydro and the Natural Sciences and Engineering Research Council of Canada for their financial support of this project. Lastly but certainly not least, I would also like to thank my wife, Michelle and my family, both by birth and by marriage for their unwavering support without which the completion of this thesis would have not been possible.

TABLE OF CONTENTS

LIST OF FIGURES

LIST OF TABLES

NOMENCLATURE

A	area [m^2]
b	heat generating block length used in Shuja *et al*. (2000, 2001) [m]
c	heat generating block length used in Shuja *et al*. (2000, 2001) [m]
C	wall roughness constant
C_p	specific heat capacity [J/kg·K]
$C_{\varepsilon 1}$	turbulence model constant for the ε equation
$C_{\varepsilon 2}$	turbulence model constant for the ε equation
C_μ	k-ε turbulence model constant
D	generic tier number
F_{cal}	calibration factor used with scalable wall functions
g	gravitational acceleration [m/s^2]
I	turbulence intensity
J	total number of blocks in a tower for Ramirez-Iraheta *et al*. (2006)
k	turbulence kinetic energy per unit mass [m^2/s^2]
K	total number of towers for Ramirez-Iraheta *et al*. (2006)
L_1	defines location of inlet opening [m]
L_2	defines length of inlet opening in y direction [m]
L_3	defines length of inlet opening in x direction [m]
L_4	defines location of inlet opening [m]
L_5	defines length of inlet opening in z direction [m]
L_6	defines length of inlet opening in x direction [m]
L_7	defines location of inlet opening [m]

L_8	defines length of inlet opening in *z* direction [m]
L_9	defines length of inlet opening in *x* direction [m]
L_{10}	defines location of outlet opening [m]
L_{11}	defines length of outlet opening in *y* direction [m]
L_{12}	defines length of outlet opening in *x* direction [m]
L_{13}	defines location of outlet opening [m]
L_{14}	defines length of outlet opening in *z* direction [m]
L_{15}	defines length of inlet opening in *x* direction [m]
$\dot{m}$	mass flow rate [kg/s]
n	normal distance to the wall
P	time averaged pressure [Pa]
P_{k1}	turbulence production due to viscous forces in the *x* direction [kg/m·s^3]
P_{k2}	turbulence production due to viscous forces in the *y* direction [kg/m·s^3]
P_{k3}	turbulence production due to viscous forces in the *z* direction [kg/m·s^3]
P^*	dynamic pressure [Pa]
q''	uniform heat flux generated by block surfaces [W/m^2]
$\dot{Q}$	flow rate [m^3/s]
R	viscosity ratio
R_A	Inlet opening aspect ratio
T	temperature [°C]
T_D	temperature difference defined in Section 5.3 [°C]
T_{max}	maximum temperature in the domain [°C]
u	time averaged velocity component in *x* direction [m/s]

u^*	velocity scale used with scalable wall functions
u_τ	friction velocity [m/s]
U_t	near wall tangential velocity [m/s]
v	time averaged velocity component in y direction [m/s]
V_{drop}	voltage drop in the valve hall [MV]
V_j	resultant jet velocity at the inlet opening [m/s]
$\dot{W}_{gen}$	generated power [MW]
w	time averaged velocitycomponent in z direction [m/s]
x	co-ordinate along width of domain [m]
y	co-ordinate along length of domain [m]
y^+	non-dimensional wall distance
$\tilde{y}^+$	fixed non-dimensional wall distance
Δy^+	non-dimensional distance from wall node to first interior node
z	co-ordinate along height of domain [m]

Greek Symbols

ε	turbulence dissipation rate [m^2s^3]
ε_s	surface emissivity
ρ	density [kg/m^3]
μ	dynamic viscosity [kg/m·s]
μ_t	eddy viscosity [kg/m·s]
λ	thermal conductivity [W/m·K]
θ	defines angle of orientation of inlet air

κ	von-Karman constant
σ_{ε}	turbulence model constant for the ε equation
σ_k	turbulence model constant for the k equation
τ_w	wall shear stress (N/m^2)
ω	turbulence frequency [1/s]
Γ_{k}	combined viscosity for the k equation
Γ_{ε}	combined viscosity for the ε equation

Subscripts

a	air
$c1$	Case 1
g	gap
i	inlet
o	outlet
$r1$	Region 1
$r1$	Region 2
w	water

Chapter 1

INTRODUCTION

The study of cooling air flow over heated structures is of considerable interest in industrial applications today. Some applications of relevance are the packaging of electronic devices, the design of power transformers, the design of DC/AC converter towers, and the design of systems to cool spent nuclear fuel. Due to the complexity of the flow in these applications, relatively few studies have been done on this topic. Most of the studies that have been attempted on this topic involve a simplified geometry and/or a simplified flow structure which limits their value in real world applications.

Ongoing research in computational methods has led to the development of increasingly accurate numerical methods for the prediction of fluid flow and heat transfer. These advances, combined with the emergence of increasingly faster computers, have made the study of air flow over heated structures more amenable for numerical analysis. The improved understanding of the underlying flow structure and temperature distribution gained from numerical analysis can be used to determine and analyze possible design modifications which could lead to more effective cooling. The results from these analyses can then be used to optimize cooling effectiveness.

The focus of the current study is on a geometry that is relevant to thyristor valve halls in DC/AC converter stations. Because thyristor valve halls differ greatly from application to application, a single valve hall at Manitoba Hydro’s Dorsey Converter Station will be analyzed in this study.

Dorsey Converter Station is located about 26 kilometers northwest of Winnipeg, Manitoba. Approximately 70% of the power generated in Manitoba is transmitted through Dorsey Converter Station. This power is generated by three power stations in northern Manitoba. The power generated by these stations is transmitted to Dorsey Converter Station from the North, by way of two high voltage direct current (HVDC) transmission lines: Bipole 1 and Bipole 2. The HVDC is then converted into alternating current (AC), which supplies Manitoba's southern power system, as well as the interconnecting power systems that link the province with Ontario, Saskatchewan, and the United States (Manitoba Hydro, 2002).

Each of the two bipoles consists of the same major components: the HVDC switchyard, converter buildings, valve halls, synchronous condensers, converter transformer area, and 230-kV switchyard. The converter buildings contain the valve halls, the control room, mechanical and electrical services, as well as the maintenance facilities. Each valve hall contains a number of electrical thyristor valves which turn on and off in a controlled sequence to convert HVDC to AC. The Bipole 1 building contains six valve halls and the Bipole 2 building contains four valve halls. This thesis will study one of the four valve halls in Bipole 2. This valve hall is called Valve Group 41 (VG41). The elevation view of VG41 is shown in Figure 1.1 and the plan view is shown in Figure 1.2. VG41 is 16.75 m x 15.6 m in the *x* and *y* directions respectively, as shown in Figure 1.2, and 13.35 m in the *z* direction, as shown in Figure 1.1.

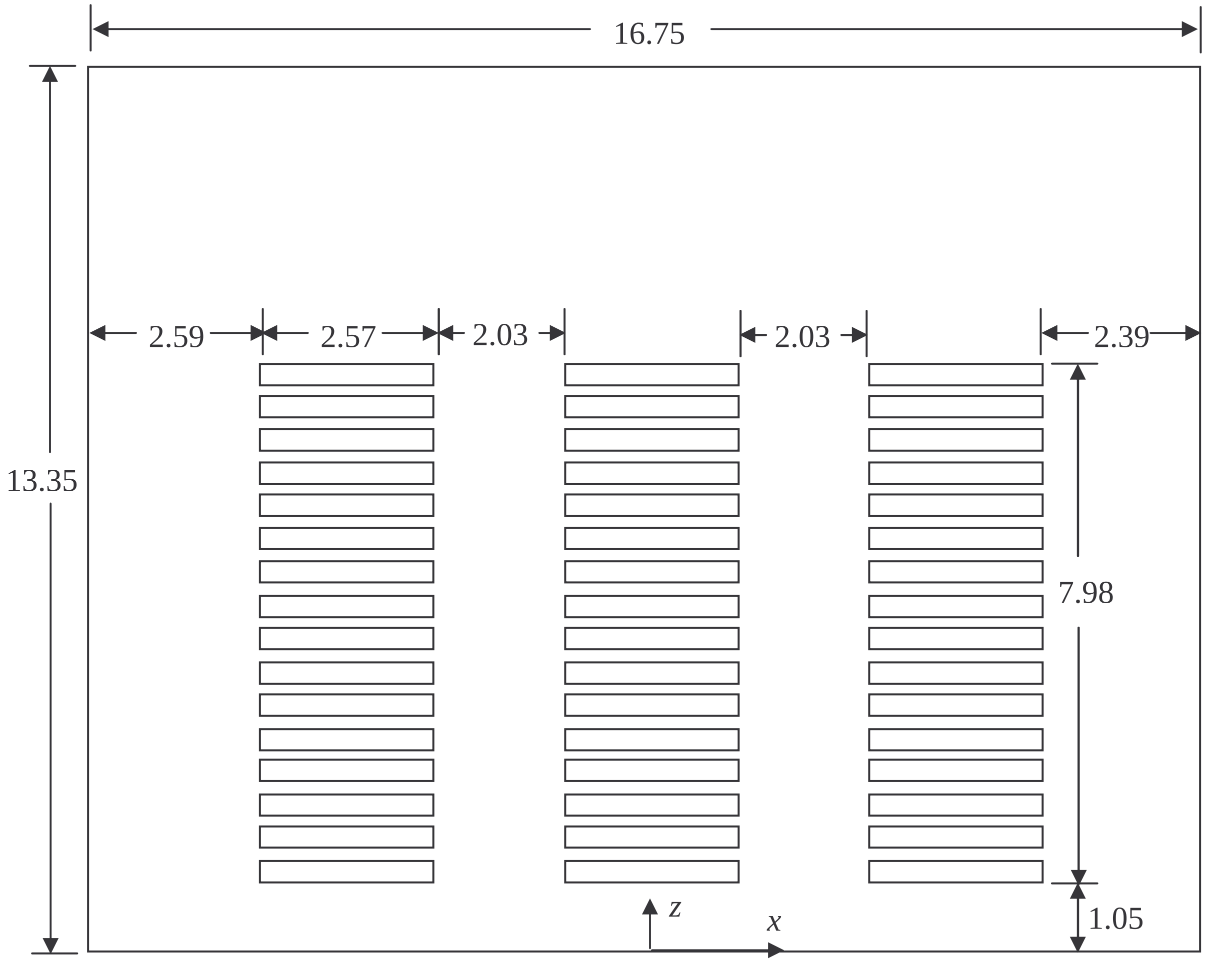

Figure 1.1: Elevation view of VG41 (dimensions in meters)

The converter valves are arranged in the form of three towers in each hall. The towers are 7.98 m in height and 2.57 m x 3.56 m in cross section. Each of the three towers is made up of 16 tiers, as shown in Figure 1.1. Each tier can further be subdivided into four thyristor modules and two reactor modules, as shown in Figures 1.3 and 1.4. A large quantity of heat is generated within the converter valves due to electrical losses in the conversion process. This heat is removed by a combination of cooling systems using water and air flows. The water-based cooling system removes approximately 95% of the heat generated by the thyristor valves and the remaining 5% is removed by an air-conditioning system that has a constant volumetric flow rate of 6.84 m^3/s. The cold air enters the room through six grills on the floor of the valve hall, as shown in Figure 1.2.

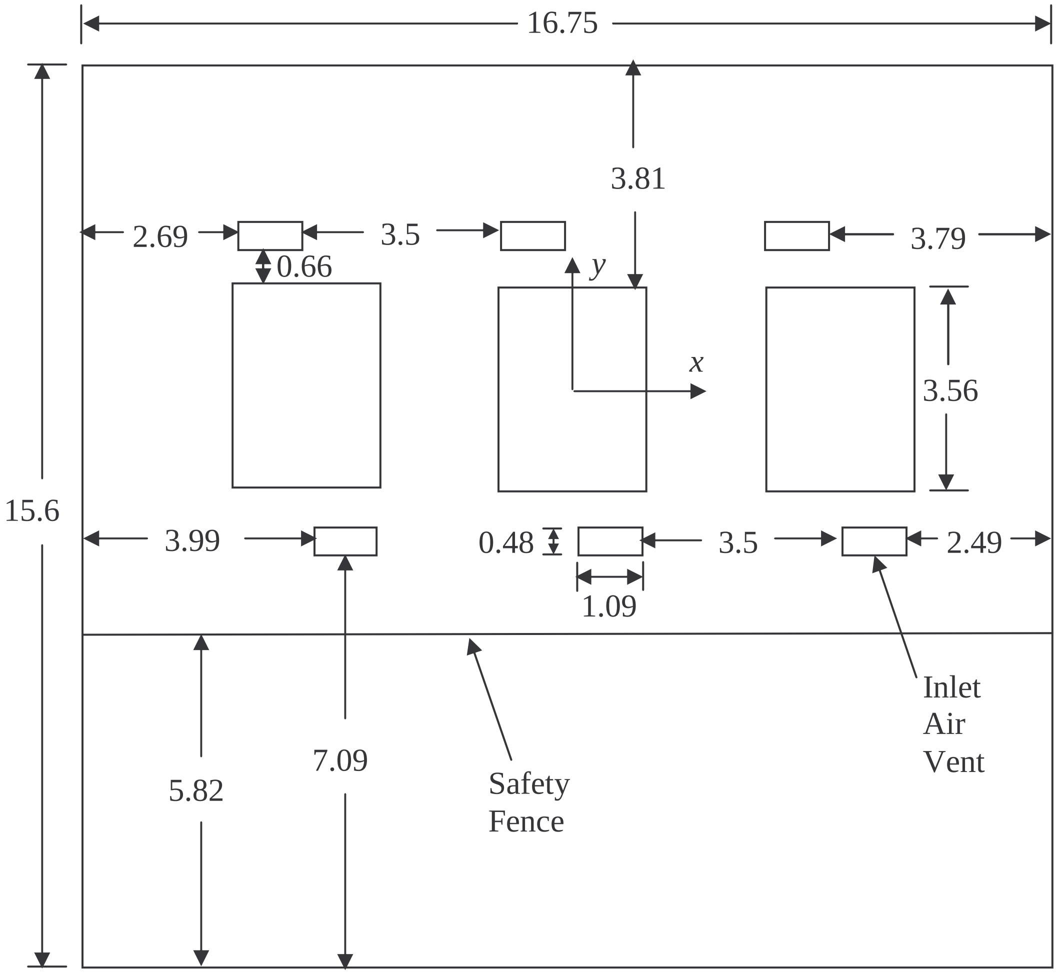

Figure 1.2: Plan view of VG41 (dimensions in meters)

These grills direct the air into the room at an angle of 60° from the horizontal towards the towers. The return air is drawn from the top of the hall. A 5 m high safety fence is located as in Figure 1.2. This fence is designed to keep people out of the high voltage area during operation. This fence is constructed with steel mesh and is largely permeable to air. The design requirements specify that the environmental temperature in the hall remain between 5°C and 40°C. Air temperatures, however, are only measured near the

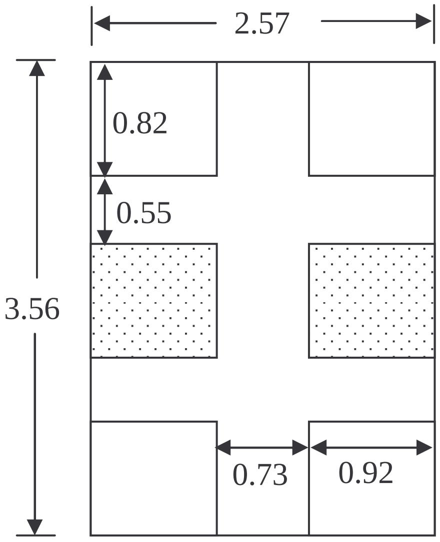

Figure 1.3: Top view of a single tier (dimensions in meters, reactor modules shaded)

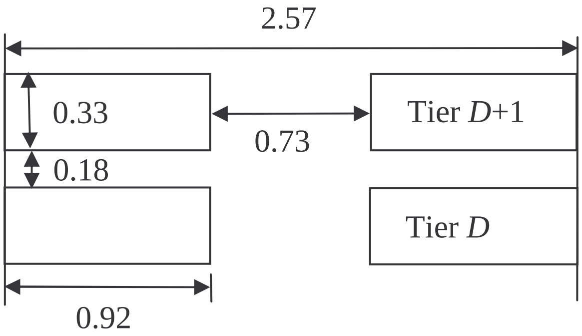

Figure 1.4: Elevation view of consecutive tiers (dimensions in meters)

inlet and the outlet vents and not between the tiers in the tower where the heat is generated and thus the highest temperatures are expected.

The optimum design of the air cooling system is one which minimizes the maximum air temperature in the room while at the same time has a flow rate that is as low as possible, thus minimizing energy use. Determining the optimum design requires an evaluation of the number, location, and size of the inlet and outlet openings in the room, as well as the airflow rate and the angle at which it is introduced into the room. The aim of this project is to study the effects of these parameters on the velocity and temperature distribution in the valve hall in order to help to determine the most effective air-based cooling system design.

Towards this goal, M.Sc. research was conducted at the University of Manitoba by Ramirez-Iraheta (2004). Ramirez-Iraheta adopted a two-dimensional laminar flow for simulating the air flow in a valve hall in order to gain an understanding of the velocity and temperature distribution for various inlet flow rates, locations of the towers in the flow domain, and locations of the inlet and outlet openings.

The goal of the present work is to advance the work of Ramirez-Iraheta by considering the more realistic situation of three-dimensional, turbulent flow in the valve hall and to make recommendations for improving the effectiveness of the air-side cooling in the valve hall. As the valve hall to be modeled is already in existence, the size of the room as well as the size, location, and orientation of the towers are assumed to be fixed quantities. The air conditioners for the room are also already in existence, therefore an ideal solution would be one in which the current air flow rate were maintained. The inlet flow rate, however, was varied in this study to determine if doubling the flow rate from the current configuration would result in lower temperatures in the valve hall. The other parameters that were varied during the course of the work are the size, location, and orientation of the inlet and outlet openings as well as the angle of injection of the inlet air.

Chapter 2

LITERATURE REVIEW

2.1 Overview

The purpose of this chapter is to review previous relevant numerical studies. Because no fundamental studies were available involving three-dimensional turbulent mixed convection in a domain with heated structures, two- and three-dimensional studies involving natural convection of heated structures and two-dimensional studies involving mixed convection of heated structures were considered. These studies are presented chronologically, subdivided into three categories: two-dimensional natural convection with heated structures, three-dimensional natural convection with heated structures, and two-dimensional mixed convection with heated structures. This literature review uses the term Rayleigh number with its conventional meaning in the heat transfer literature.

2.2 Two-Dimensional Natural Convection with Heated Structures

Shuja *et al*. (2001) numerically investigated the two-dimensional laminar natural convection of air in a square cavity with a single heat generating body. All outer walls in the domain were adiabatic. Conjugate heat transfer was considered with uniform volumetric heat generation in the body. Cooling air entered the room from a single inlet and exited the room from a single outlet. The domain considered is shown in Figure 2.1. In this study, the effect of the aspect ratio (c/b) of the heat generating body was considered with all other quantities fixed. The authors concluded that for the conditions studied, as the aspect ratio of the body was decreased, the temperature on the surface of the body became more uniform and the maximum temperature on the body surface decreased. The authors also concluded that irreversibility decreased as the aspect ratio was decreased.

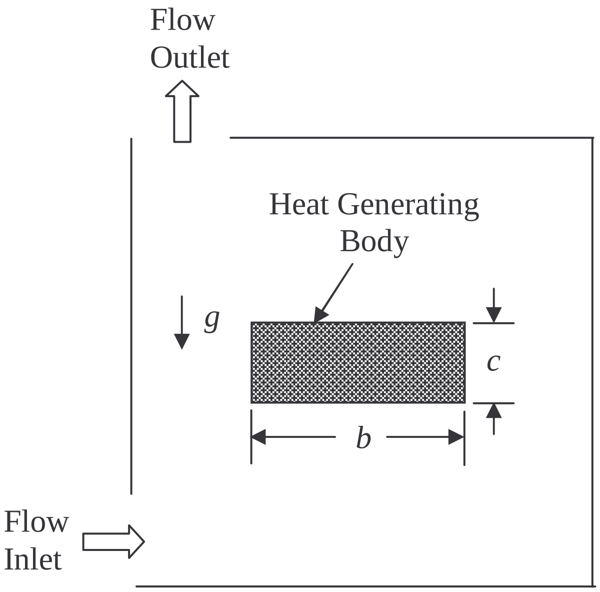

Figure 2.1: Domain for Shuja *et al*. (2000, 2001)

Merrikh and Lage (2005) numerically studied two-dimensional laminar natural convection in a square enclosure with disconnected conducting blocks. The vertical walls were held at constant temperatures with the higher temperature wall on the left side of the domain. The horizontal walls were adiabatic. The flow domain studied is shown in Figure 2.2. In this study the fluid properties, the size of the domain, and the total area of the blocks were held constant, while the number of blocks, the Rayleigh number, and the thermal conductivity of the blocks were varied. The authors found that when the number of blocks was low, the fluid had a tendency to flow predominantly between the enclosure wall and the first column of solid blocks. When the number of blocks was increased above a critical amount, the authors observed a transition with the flow beginning to penetrate into the interior channels of the domain. When the number of blocks was sufficient for this transition to occur, increasing the conductivity of the blocks caused the heat transfer rate across the cavity to increase. When the number of blocks was not sufficient for this transition to occur, however, increasing the conductivity of the blocks caused the heat transfer rate across the cavity to decrease. The authors also found that increasing the number of blocks caused the heat transfer rate across the cavity to decrease as did decreasing the Rayleigh number.

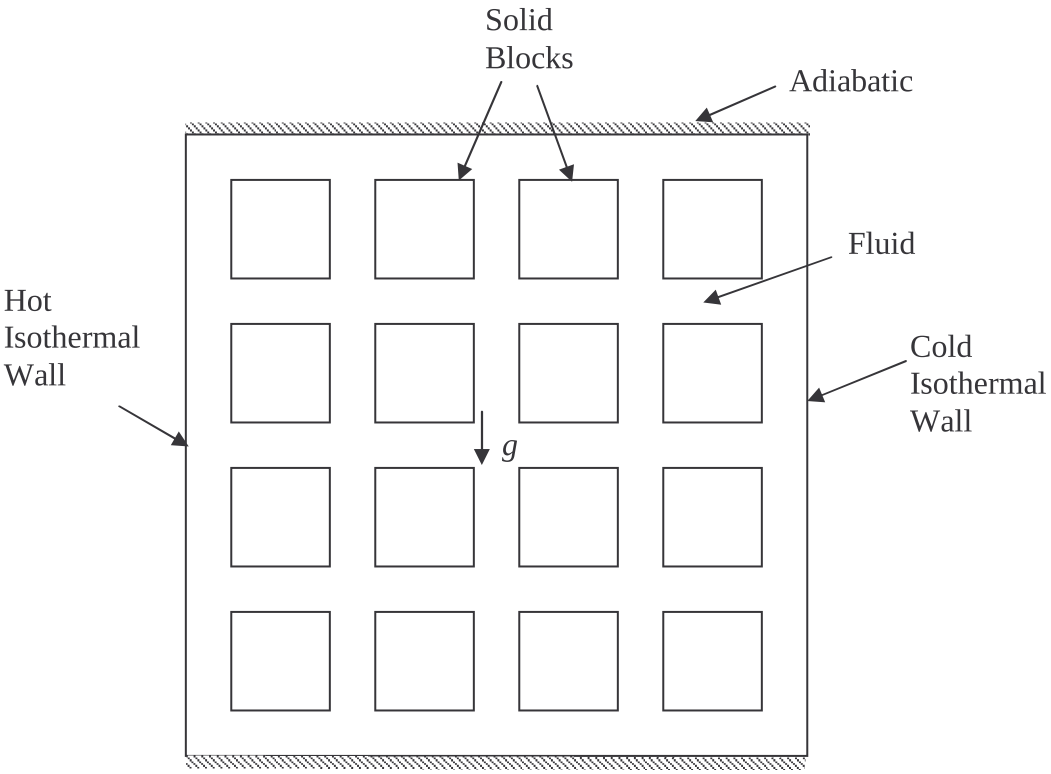

Figure 2.2: Domain for Merrikh and Lage (2005)

2.3 Three-Dimensional Natural Convection with Heated Structures

Afrid and Zebib (1991) numerically compared three-dimensional natural convection cooling of heated cubic aluminum blocks assuming either or turbulent and laminar flow under the same conditions. The k-ε model was used for turbulence effects. Laminar flow was induced by setting the turbulence model quantities to zero. Conjugate heat transfer was considered with uniform heat generation in the blocks. Air entered the room from the bottom wall of the domain and exited from the top wall in the domain. All variables were held constant in the laminar and turbulent simulations so that they could be compared with experimental results. The flow domain studied is shown in Figure 2.3. When turbulent conditions were assumed, the results showed much better agreement with the experimental results. The results also showed that turbulent natural convection cooling resulted in lower block temperatures than laminar natural convection cooling with all other quantities being equal. The authors also observed that the temperatures on the surfaces of and within the heated blocks were much higher than the bulk temperature of the air leaving the domain. The temperatures of the upper blocks were also generally higher than the temperature of the lower blocks.

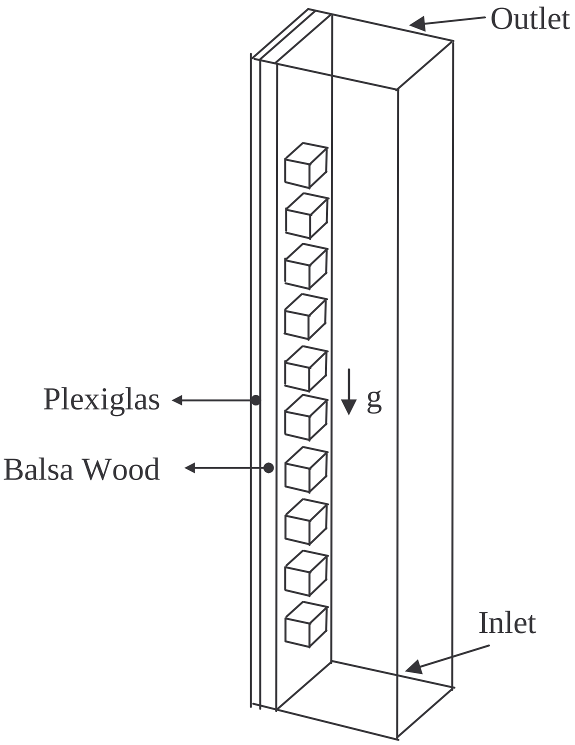

Figure 2.3: Domain for Afrid and Zebib (1991)

Moreno and Ramaswamy (1997) numerically studied laminar natural convection of air in both a two-dimensional and a three-dimensional cavity with two heated blocks to compare the results generated by both. A constant temperature wall boundary condition was placed on the surfaces of the blocks, and on the left, right, upper and lower surfaces of both geometries. The temperature of the blocks was specified as higher than the temperature of the outer walls. An isothermal wall boundary condition was placed on the front and back surfaces of the three-dimensional geometry. The geometry was fixed and the Rayleigh number was varied. The two domains are shown in Figure 2.4. The authors concluded that although the two-dimensional model can qualitatively predict the flow structure on the mid-plane for the three dimensional case, three-dimensional effects occur in the rest of the domain that cannot be predicted by the two-dimensional case. The magnitude of these effects increased as the Rayleigh number increased.

2.4 Two-Dimensional Mixed Convection with Heated Structures

Li and Chung (1994) numerically studied laminar two-dimensional mixed convection of air in a vertical rectangular channel with heated blocks to simulate the cooling of electronics packages. Conjugate heat transfer was considered with uniform heat generation in the blocks. The flow domain is shown in Figure 2.5. The authors fixed the size of the geometry and the thermal conductivity of the blocks. They investigated the effect of increasing the Rayleigh number with a fixed inlet mass flow rate for four flow conditions. The first condition was the case of buoyancy induced natural convection. The second condition was the case of buoyancy-assisted convection. This condition occurred when the inlet flow was in the same direction as the force of buoyancy. The third condition was buoyancy-opposed mixed convection with a net upward flow. This

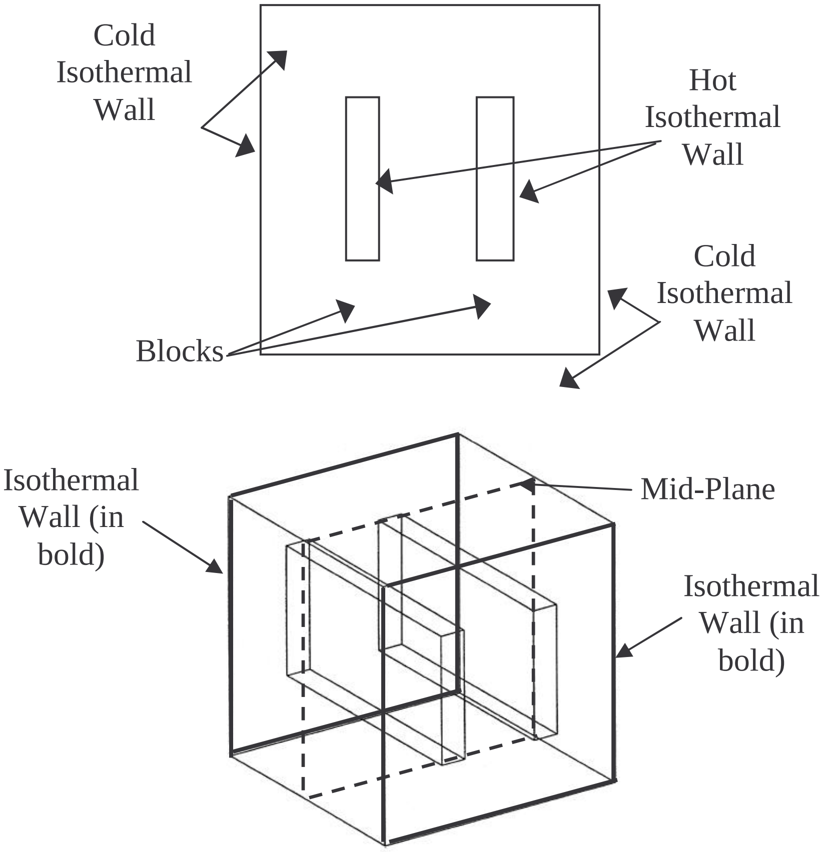

Figure 2.4: Two and three-dimensional domains for Moreno and Ramaswamy (1997)

condition occurred when a downward forced convective flow met with a stronger buoyancy induced flow, resulting in a net upward flow. The fourth flow condition was that of buoyancy-opposed mixed convection with net downward flow. This flow condition occurred when a downward forced convective flow was stronger than the buoyancy-induced flow, resulting in a net downward directed flow. The authors used an opening boundary condition on the top and bottom surfaces of the domain and varied the pressure on the inlet and outlet by trial and error until the desired inlet flow conditions and steady state results were achieved. The results show that for the cases of natural convection, buoyancy-assisted convection, and buoyancy-opposed mixed convection with net upward flow, increasing the Rayleigh number decreased the temperature of all the block surfaces. For the case of buoyancy-opposed mixed convection with net downward flow, increasing the Rayleigh Number caused the temperature of some block surfaces to become lower and others to become higher.

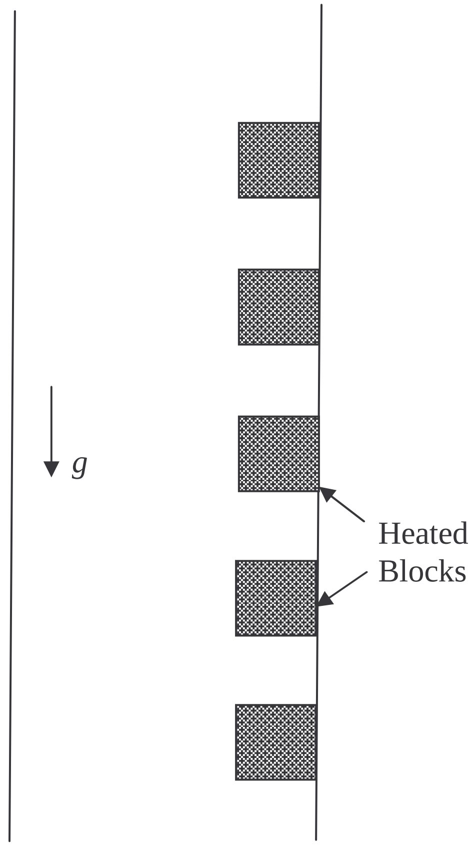

Figure 2.5: Domain for Li and Chung (1994)

Shuja *et al*. (2000) numerically studied two-dimensional mixed convection of air in a square cavity with a single heat generating body. All outer walls in the domain were adiabatic. Conjugate heat transfer was considered with uniform volumetric heat generation in the body. Cooling air entered the room from a single inlet and exited the room from a single outlet. The domain considered is shown in Figure 2.1. The authors studied the effects of cavity exit port locations on heat transfer and entropy generation for two body aspect ratios (*c/b*). They concluded that the location of the exit port can have a large effect on the surface temperature distribution and irreversibility in the cavity. Exit port locations near the left most part of the top wall resulted in the most uniform temperatures and the least amount of irreversibility while the opposite was true of exit port locations near the left most part of the bottom wall.

Ramirez-Iraheta *et al*. (2006) numerically investigated the two-dimensional laminar flow of air inside a cavity with a single inlet and a single outlet enclosing heat generating towers made up of rectangular blocks. The flow domain studied is shown in Figure 2.6. The effects of the number, position, and size of the towers, the inlet mass flow rate, and the location of the inlet and outlet openings on the velocity and temperature distributions within the domain were studied. The results showed that the position of the towers with respect to the inlet and outlet openings had a significant impact on the velocity and temperature in the domain. The tower locations that provided the lowest block temperatures were the ones that maximized the air flow between the blocks. The authors also found that the inlet mass flow rate had a significant effect on the velocity and temperature in the domain. Increased inlet velocities usually resulted in improved cooling; however, in some cases, lower inlet velocities resulted in more effective cooling.

Bellache *et al*. (2005) numerically studied two-dimensional turbulent ventilation patterns and thermal processes in ice rinks. The standard *k*-*ε* model was used to model the turbulence quantities. Air entered the room through a single inlet opening on the ceiling of the room and exited through a single opening, also on the ceiling. Heat transfer by

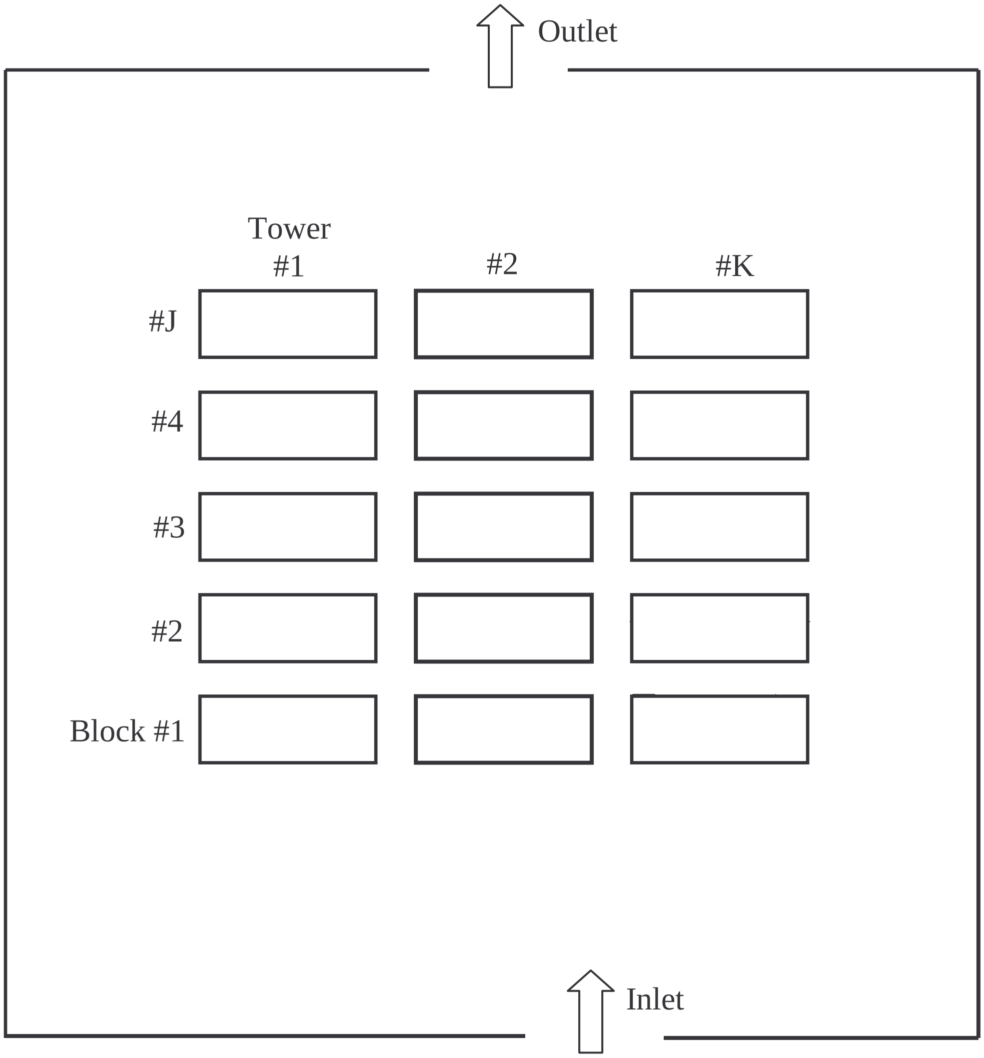

Figure 2.6: Domain for Ramirez-Iraheta *et al*. (2006)

means of conduction was modeled in the stands and within the ice surface. A uniform temperature boundary condition was applied on the length of the bottom wall directly below the ice surface. Radiation and convection were modeled for all inner surfaces within the domain. Convection was modeled for all the outside surfaces. Other than the location of the inlet and outlet openings, the size, location and boundary conditions were held constant. The numerical domain studied is shown in Figure 2.7. Four different inlet and outlet configurations were studied in this investigation in order to examine their effects on the spectator comfort level and heating requirements of the room. The generated numerical results were in good agreement with actual measured values and with previous simulations. It was determined that the location of the inlet and outlet ducts as well as the orientation of the inlet air can have a large effect on the heating load, the humidity, and the comfort of the spectators in the ice rink.

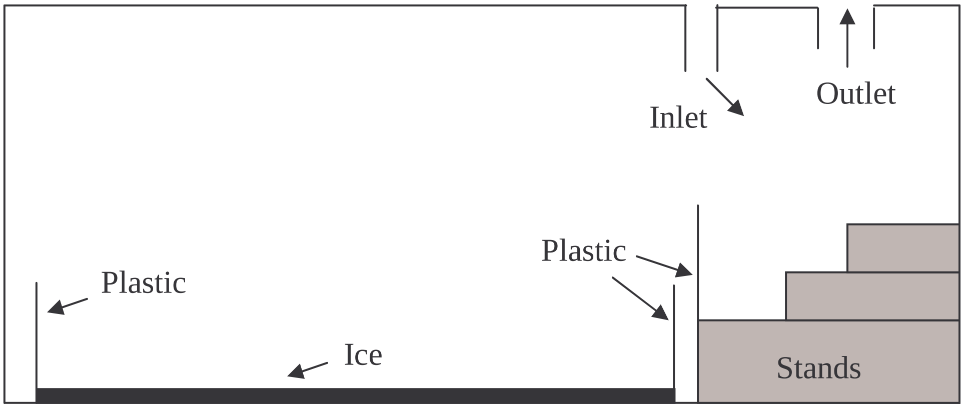

Figure 2.7: Domain for Bellache *et al*. (2005)

Bhoite *et al*. (2005) numerically studied two-dimensional laminar mixed convection of air in an enclosure with a series of heat generating blocks. Conjugate heat transfer in the blocks was modeled and a uniform heat rate was generated in the blocks. Air was introduced into the domain from the floor and exited from the ceiling of the room. All outer walls were considered to be adiabatic. The authors also made use of symmetry planes in order to decrease the computational effort. The numerical domain studied is shown in Figure 2.8. All quantities were fixed except the inlet mass flow rate and volumetric heat generation rate. The results showed good agreement when compared with experimental results. The authors found that at a fixed mass flow rate, increasing the heat generation rate had the effect of decreasing the ratio of the maximum domain temperature to the heat generation rate. This effect becomes much less pronounced with increasing mass flow rates. The authors also found that for a given heat generation rate; the maximum surface temperatures typically decreased with increasing mass flow rate. For very high heat generation rates, however, maximum surface temperatures initially increased followed by a decrease at higher mass flow rates.

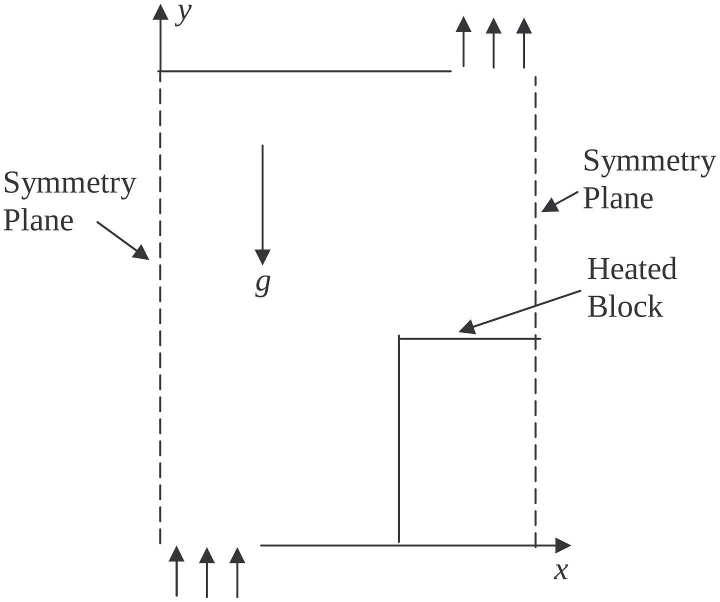

Figure 2.8: Domain for Bhoite *et al*. (2005)

2.5 Concluding Remarks

From the above investigations, it is clear that there is a significant interest in understanding the hydrodynamic and thermal characteristics of both natural and mixed convection involving heated structures. This literature review has presented some of the most recent and relevant fundamental literature in this field. To date, the vast majority of fundamental studies that have been conducted on this topic have been on two-dimensional geometries, with an assumed laminar air flow.

Very few fundamental three-dimensional studies have been conducted for the mixed convection of heated blocks. The reason for this is the very high computational effort associated with three-dimensional studies. Of the fundamental three-dimensional literature available, no studies have been conducted (to the author's knowledge) involving mixed convection. Also, none of the previous three-dimensional studies has made an attempt to improve cooling effectiveness. The geometry in real applications is typically three dimensional and air flow is turbulent in most cases. Results from two-dimensional laminar studies cannot be extended to three-dimensional turbulent cases.

This work will attempt to fill in the gap in the existing fundamental literature by studying three-dimensional mixed convection of air with heated structures in an existing room. Specifically, this thesis will study the effect of varying the size, location, orientation, and number of inlet and outlet openings, as well as the inlet mass flow rate and the angle of inlet flow on the cooling effectiveness in the room.

Chapter 3

MODEL DESCRIPTION

3.1 Domain

The valve hall geometry, as shown in Figures 1.1 and 1.2, is a very large domain with a complex arrangement of towers, inlets, and outlets. If modeled completely, a detailed simulation of this geometry, with currently available research computing resources would require enormous computation times. One strategy that can be used to reduce the required size of a solution domain is to take advantage of symmetry that exists in the application of interest. In the case of the valve hall, slight modifications can be made to introduce symmetry. These modifications allow a reduction in the computational domain size without significantly reducing the fidelity of the model to the key flow and heat transfer phenomena in the valve hall.

The modifications introduced to the VG41 geometry are:

Modification M1: Replace the walls on the left and right hand sides of Figures 1.1 and 1.2 by symmetry planes. This change implies modeling a large array of identical towers. Then, a single tower is considered representative of all the towers.

Modification M2: Remove the safety fence and move the wall outside the safety fence closer to the towers. This wall was placed at the same distance from the tower center line as the wall on the opposite side of the towers.

Modification M3: The floor cooling-air inlets were moved slightly to have their centers aligned with the centers of the towers.

Modification M4: The air outlets (which were distributed asymmetrically in the ceiling above the towers) were redistributed so that their size and location were the same as the inlet openings, except on the ceiling. The total area of the outlet openings matched the total area of the outlet openings for VG41.

Modification M5: In the towers themselves, the collection of four thyristor modules and two reactor modules in a typical tier was simplified into one block. This block geometry has the same overall dimensions as the set of modules. It also produces, through a constant heat flux on its surface, the same total rate of energy for dissipation to the air as the original set of modules.

Figure 3.1 shows an elevation view of the computational domain for the valve hall simulations. Modification M1 allowed the introduction of symmetry plane S2. Symmetry plane S1 was then introduced at the center line of each tower. The introduction of these two planes of symmetry reduces the computational domain size by a factor of six. The shaded region in Figure 3.1 shows the resulting computational domain. Figure 3.2 shows two plan views of the valve hall computational domain. In Figure 3.2a, the new locations of the inlet and outlet areas made by modifications M3 and M4, respectively, are shown with dotted lines. Figure 3.2a also shows the symmetry plane S3 introduced as a result of Modification M2 and the symmetric placement of the floor inlets. The shaded region in Figure 3.2a shows the resulting computational domain which will henceforth be referred to as Computational Domain 1 (CD1). In Figure 3.2b, the floor inlet areas are removed and replaced by inlets on the side wall. Symmetry plane S3 is not valid for this computational domain and the shaded region in Figure 3.2b shows the resulting

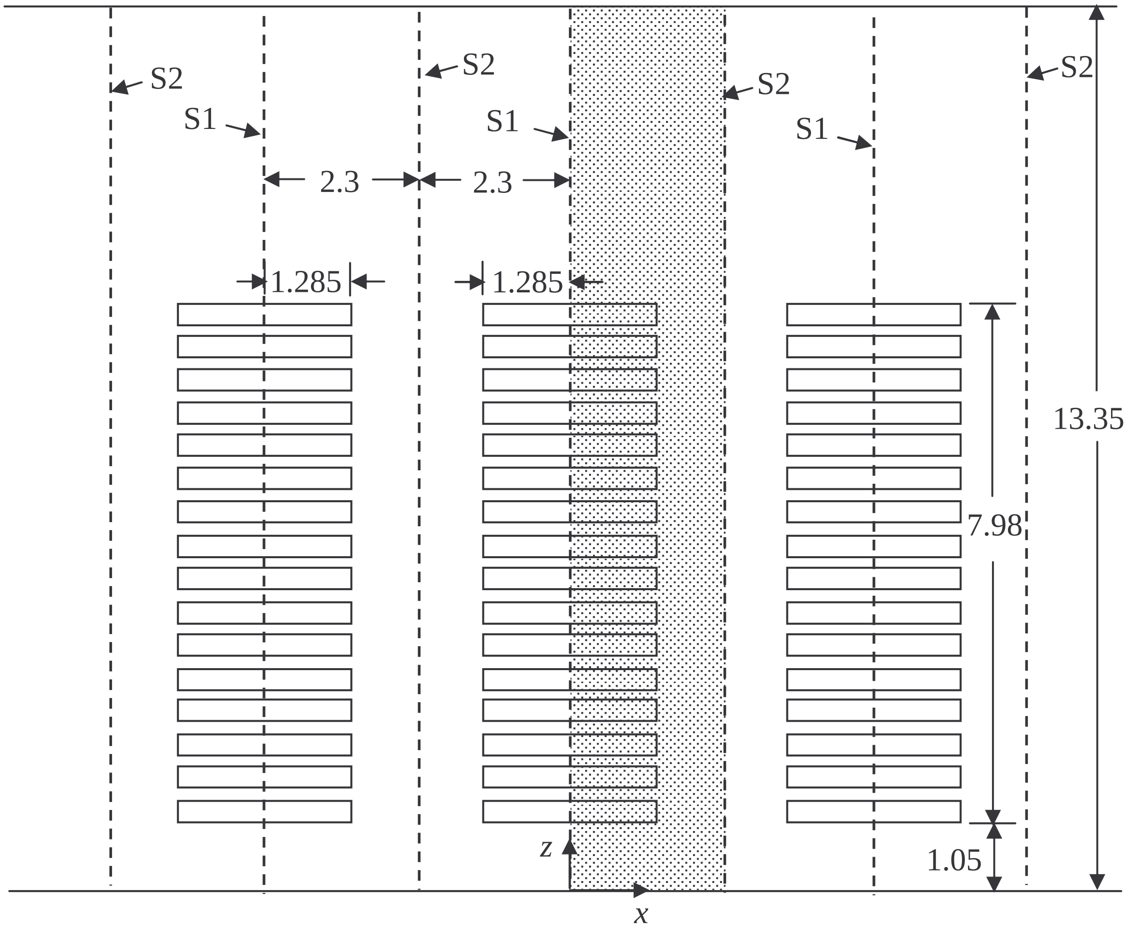

Figure 3.1: Elevation view of the valve-hall geometry used in the simulations with shaded area indicating area modeled (dimensions in meters)

computational domain which will henceforth be referred to as Computational Domain 2 (CD2).

The plan view of the tower is shown in Figures 3.2a and 3.2b. An elevation view of just the tower blocks is shown in Figure 3.3 with dimensions. Only the shaded area seen in Figure 3.3 is used with CD1. The entire area shown in Figure 3.3 is used with CD2.

Generic descriptions of CD1 are shown in Figures 3.4 (plan view) and 3.5 (elevation view). The size of the room and the size and location of the towers were fixed. One

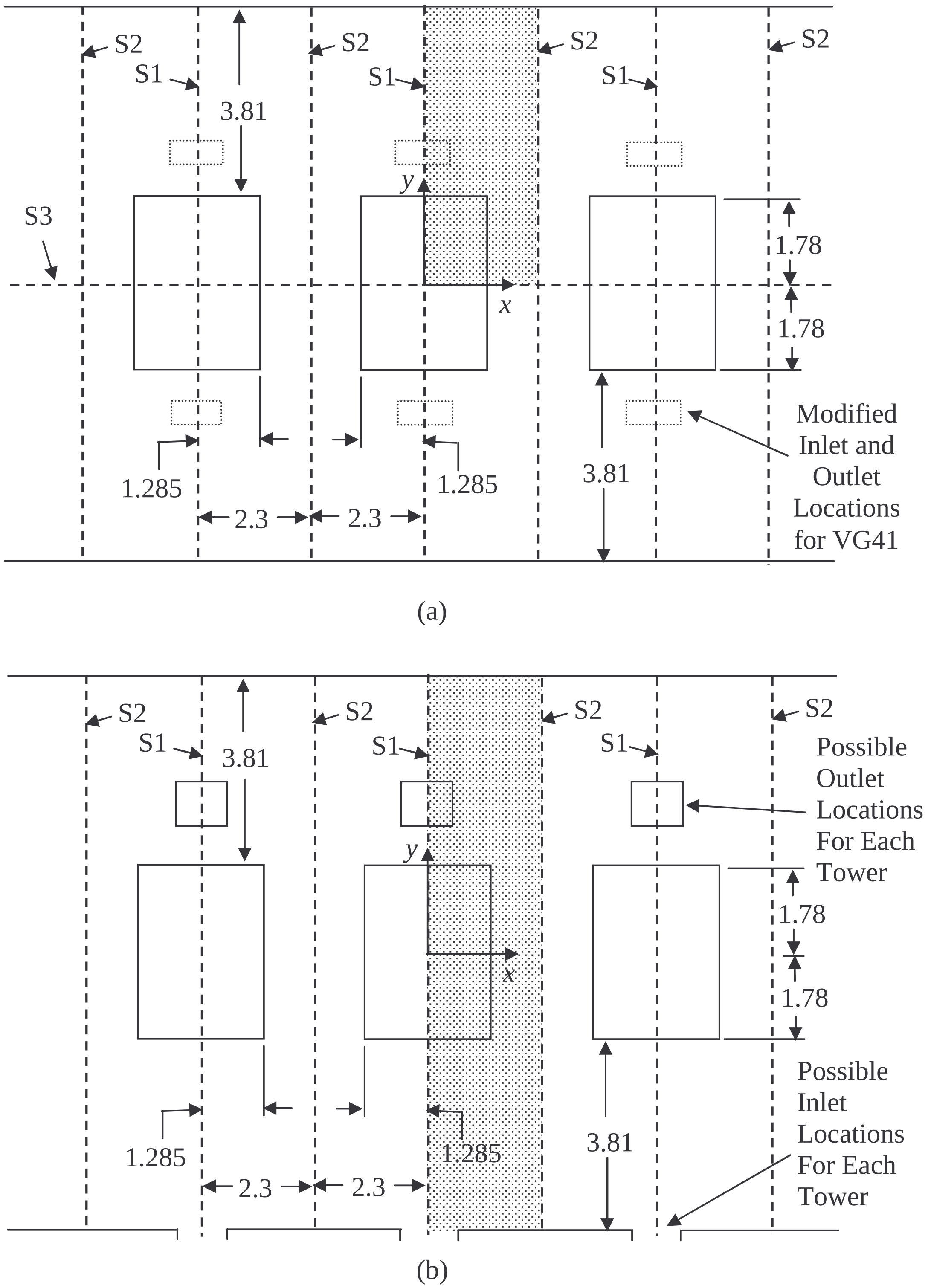

Figure 3.2: Plan view of the valve-hall geometry used in the simulations (a) CD1 (b) CD2 (shaded area indicates area modeled, dimensions in meters)

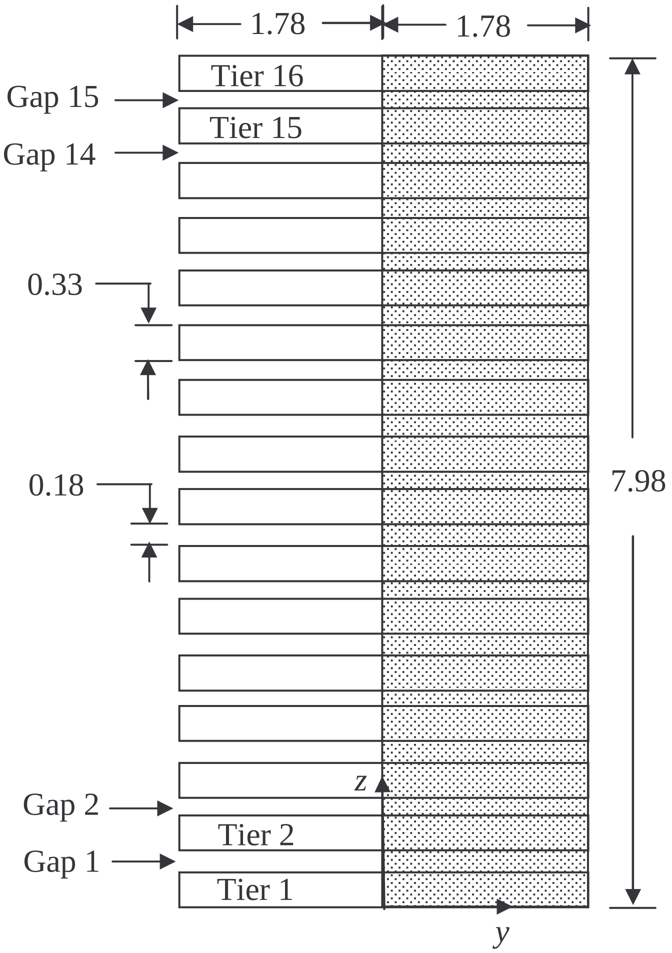

Figure 3.3: Elevation view showing details of tower geometry used in simulations (shaded area indicates area modeled for CD1, dimensions in meters)

outlet opening was used with this domain. Its size and location was also fixed. The lengths of all the fixed parameters are shown in Figures 3.4 and 3.5. One inlet opening was also modeled with CD1. This inlet opening could either be on the bottom wall or the side wall of the domain, but not on both. When the inlet opening was located on the bottom of the domain, its location was defined by length L_1 and its size was defined by lengths L_2 and L_3 in the y and x directions, respectively. When the inlet opening was located on the side-wall of the domain, its location was defined by length L_4 and its size was defined by lengths L_5 and L_6 in the z and x directions, respectively.

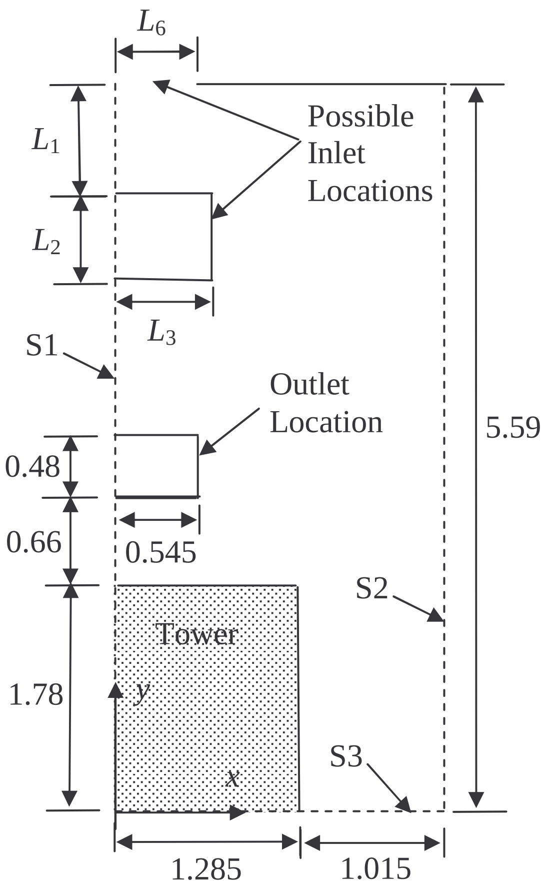

Figure 3.4: Plan view showing generic description of CD1 (dimensions in meters)

Generic descriptions of CD2 are shown in Figures 3.6 (plan view) and 3.7 (elevation view). The size of the room and the size and location of the towers were fixed. The lengths of all the fixed parameters are shown in Figures 3.6 and 3.7. One inlet opening was modeled with CD2. This inlet opening was located on the side wall of the domain at y = 5.59 m. The location of this opening was defined by length L_7 and its size was defined by lengths L_8 and L_9 in the z and x directions, respectively. One outlet opening was used with this domain. This outlet opening could either be on the top wall or the side

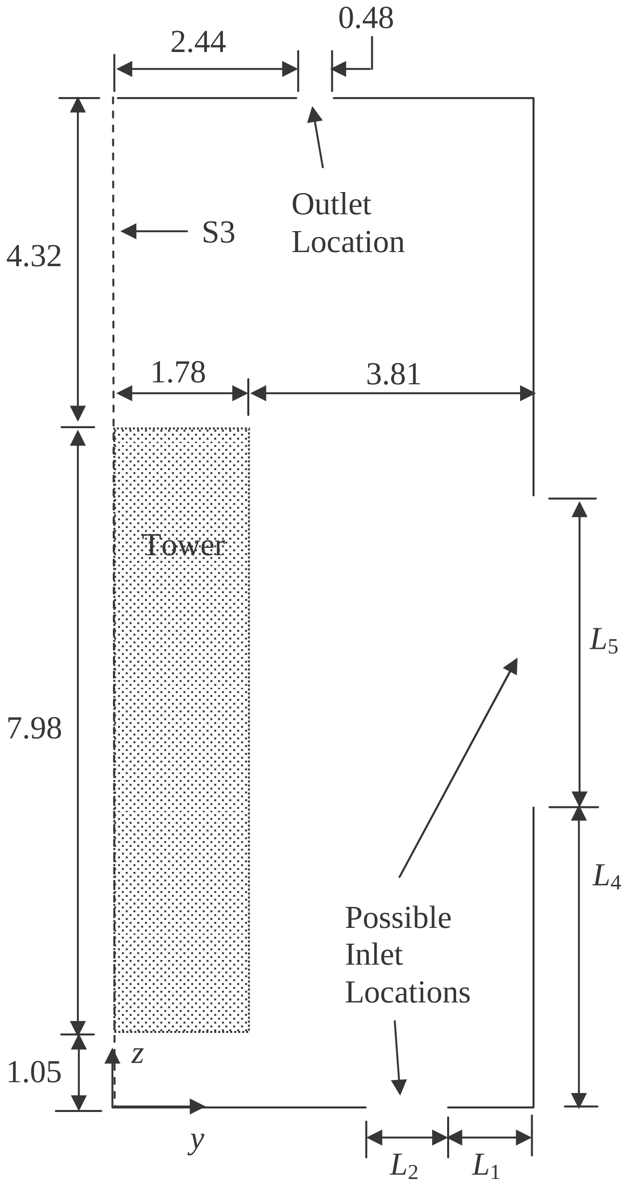

Figure 3.5: Elevation view showing generic description of CD1 (dimensions in meters)

wall ($y = -5.59$ m) of the domain but not on both. When the outlet opening was located on the top wall of the domain, its location was defined by length L_{10} and its size was defined by lengths L_{11} and L_{12} in the y and x directions, respectively. When the outlet opening was located on the side wall of the domain at $y = -5.59$ m, its location was

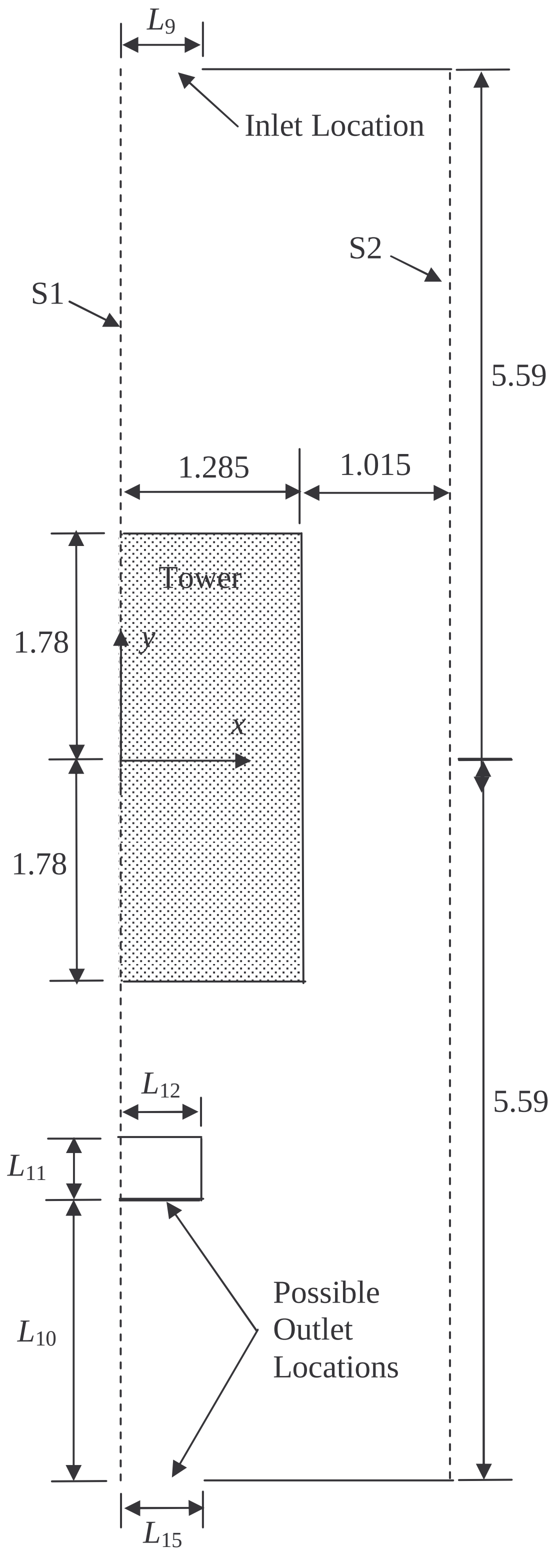

Figure 3.6: Plan view showing generic description of CD2 (dimensions in meters)

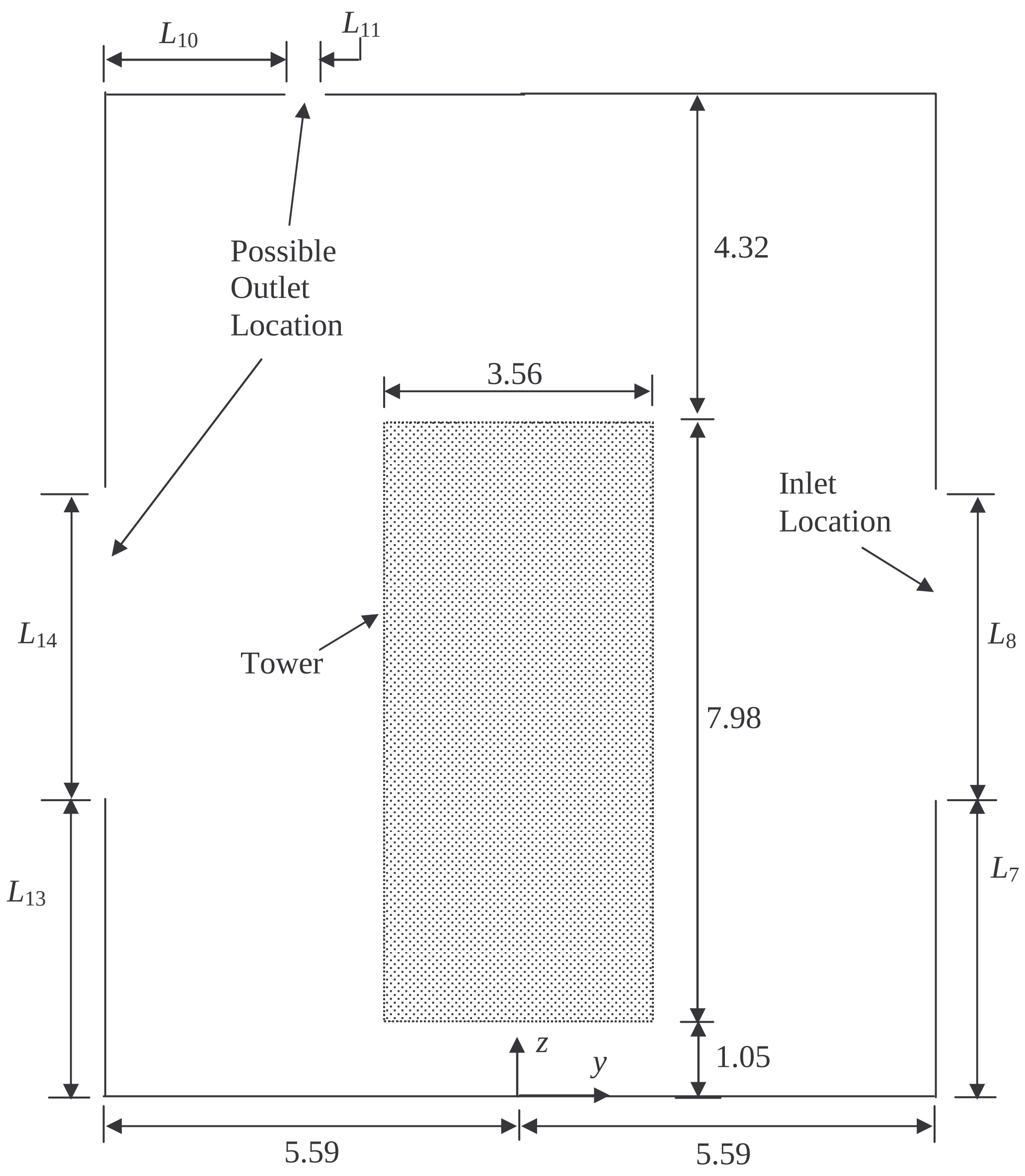

Figure 3.7: Elevation view showing generic description of CD2 (dimensions in meters)

defined by length L_{13} and its size was defined by lengths L_{14} and L_{15} in the z and x directions, respectively.

3.2 Assumptions

The following assumptions were made in the formulation of the governing equations of mass, momentum, and energy conservation.

- The air-flow was assumed to be turbulent.
- Steady-state conditions were assumed with respect to time.
- The air was assumed to be Newtonian.
- The properties of the air other than density were assumed to be constant.
- Viscous dissipation was assumed to be negligible.
- Radiation heat transfer was assumed to be negligible.
- The eddy-viscosity approximation was used to model the Reynolds stresses.
- A constant, uniform heat flux was assumed on the surfaces of the tower blocks.
- The outer walls in the domain were assumed to be adiabatic.

3.3 Governing Equations

Following the assumptions in Section 3.2, the governing equations of mass, momentum, and energy may be written in Cartesian coordinates as follows:

Mass Conservation Equation:

$$\frac{\partial u}{\partial x}+\frac{\partial v}{\partial y}+\frac{\partial w}{\partial z}=0 \tag{3.1}$$

Momentum Conservation Equations:

$$\rho\left[u\frac{\partial u}{\partial x}+v\frac{\partial u}{\partial y}+w\frac{\partial u}{\partial z}\right]=-\frac{\partial P}{\partial x}+(\mu+\mu_t)\left[\frac{\partial^2 u}{\partial x^2}+\frac{\partial^2 u}{\partial y^2}+\frac{\partial^2 u}{\partial z^2}\right] \tag{3.2}$$

$$\rho\left[u\frac{\partial v}{\partial x}+v\frac{\partial v}{\partial y}+w\frac{\partial v}{\partial z}\right]=-\frac{\partial P}{\partial y}+(\mu+\mu_t)\left[\frac{\partial^2 v}{\partial x^2}+\frac{\partial^2 v}{\partial y^2}+\frac{\partial^2 v}{\partial z^2}\right] \tag{3.3}$$

$$\rho\left[u\frac{\partial w}{\partial x}+v\frac{\partial w}{\partial y}+w\frac{\partial w}{\partial z}\right]=-\frac{\partial P}{\partial z}+(\mu+\mu_t)\left[\frac{\partial^2 w}{\partial x^2}+\frac{\partial^2 w}{\partial y^2}+\frac{\partial^2 w}{\partial z^2}\right]+\rho g \tag{3.4}$$

Energy Conservation Equation:

$$u\frac{\partial T}{\partial x}+v\frac{\partial T}{\partial y}+w\frac{\partial T}{\partial z}=\frac{\lambda}{\rho C_p}\left[\frac{\partial^2 T}{\partial x^2}+\frac{\partial^2 T}{\partial y^2}+\frac{\partial^2 T}{\partial z^2}\right] \tag{3.5}$$

where u, v, and w are the Cartesian time averaged velocity components with the commonly used over-bars omitted for convenience and P is the time averaged pressure with the over-bar also omitted for convenience.

Splitting the pressure into dynamic (P^*) and hydrostatic components:

$$P^* = P - \rho_i gz \tag{3.6}$$

the pressure gradients become:

$$\frac{\partial P}{\partial x}=\frac{\partial P^*}{\partial x} \tag{3.7}$$

$$\frac{\partial P}{\partial y}=\frac{\partial P^*}{\partial y} \tag{3.8}$$

$$\frac{\partial P}{\partial z}=\frac{\partial P^*}{\partial z}+\rho_i g \tag{3.9}$$

where ρ_i is the density of the air at the inlet

Substituting from Equations (3.8) to (3.10) into Equations (3.2) to (3.4), the resulting momentum conservation equations become:

$$\rho\left[u\frac{\partial u}{\partial x}+v\frac{\partial u}{\partial y}+w\frac{\partial u}{\partial z}\right]=-\frac{\partial P^*}{\partial x}+(\mu+\mu_t)\left[\frac{\partial^2 u}{\partial x^2}+\frac{\partial^2 u}{\partial y^2}+\frac{\partial^2 u}{\partial z^2}\right] \tag{3.10}$$

$$\rho\left[u\frac{\partial v}{\partial x}+v\frac{\partial v}{\partial y}+w\frac{\partial v}{\partial z}\right]=-\frac{\partial P^*}{\partial y}+(\mu+\mu_t)\left[\frac{\partial^2 v}{\partial x^2}+\frac{\partial^2 v}{\partial y^2}+\frac{\partial^2 v}{\partial z^2}\right] \tag{3.11}$$

$$\rho\left[u\frac{\partial w}{\partial x}+v\frac{\partial w}{\partial y}+w\frac{\partial w}{\partial z}\right]=-\frac{\partial P^*}{\partial z}+(\mu+\mu_t)\left[\frac{\partial^2 w}{\partial x^2}+\frac{\partial^2 w}{\partial y^2}+\frac{\partial^2 w}{\partial z^2}\right]+(\rho-\rho_i)g \tag{3.12}$$

3.4 Turbulence Closure

A turbulence model is required in order to calculate the eddy viscosity, μ_t. As no direct experimental studies have been conducted on this configuration, a simplified problem was used to aid in the selection of a turbulence model. Berg *et al*. (2006) simulated the flow of an isothermal jet issuing from a rectangular opening into an empty room, which was studied experimentally by Quinn (1992). The jet was turbulent with an inlet opening aspect ratio of 2:1, which is very similar to the aspect ratio of the current inlet opening in the valve hall (2.27:1). Two turbulence models were used in the study of Berg *et al*. (2006): the standard k-ω model of Wilcox (1988) and an extension of the standard k-ε model of Launder and Spalding (1974). The results generated using the k-ε model were in good agreement with the experimental results of Quinn, while the results generated using the k-ω model did not agree as well with the experimental results. Details of this simulation are given in Appendix A. Consequently, the k-ε model was chosen for this study under the assumption that the agreement will carry forward to this configuration.

3.4.1 The *k-ε* Model

The k-ε model assumes that μ_t is linked to the turbulent kinetic energy k, and the dissipation ε, using the relation:

$$\mu_t = C_\mu \rho \frac{k^2}{\varepsilon} \tag{3.13}$$

Where C_μ is a constant and the values of k and ε come from the turbulence kinetic energy equation and the dissipation rate equation as follows:

Turbulence Kinetic Energy Equation:

$$\rho\left[u\frac{\partial k}{\partial x}+v\frac{\partial k}{\partial y}+w\frac{\partial k}{\partial w}\right]=\frac{\partial}{\partial x}\left(\Gamma_k\frac{\partial k}{\partial x}\right)+\frac{\partial}{\partial y}\left(\Gamma_k\frac{\partial k}{\partial y}\right)+\frac{\partial}{\partial z}\left(\Gamma_k\frac{\partial k}{\partial z}\right)+ \\ P_{k1}+P_{k2}+P_{k3}-\rho\varepsilon \tag{3.14}$$

where $\Gamma_k=\left(\mu+\frac{\mu_t}{\sigma_k}\right)$

Dissipation Rate Equation:

$$\rho\left[u\frac{\partial \varepsilon}{\partial x}+v\frac{\partial \varepsilon}{\partial y}+w\frac{\partial \varepsilon}{\partial z}\right]=\frac{\partial}{\partial x}\left(\Gamma_\varepsilon\frac{\partial \varepsilon}{\partial x}\right)+\frac{\partial}{\partial y}\left(\Gamma_\varepsilon\frac{\partial k}{\partial y}\right)+\frac{\partial}{\partial z}\left(\Gamma_\varepsilon\frac{\partial \varepsilon}{\partial z}\right)+ \\ \left(1+\frac{\varepsilon}{k}C_{\varepsilon 1}\right)(P_{k1}+P_{k2}+P_{k3})-C_{\varepsilon 2}\rho\varepsilon \tag{3.15}$$

where $\Gamma_\varepsilon=\left(\mu+\frac{\mu_t}{\sigma_\varepsilon}\right)$

The turbulence production terms, P_{k1}, P_{k2}, and P_{k3} are modeled using:

$$P_{k1}=\mu_t\left(2\frac{\partial^2 u}{\partial x^2}+\frac{\partial^2 u}{\partial y^2}+\frac{\partial^2 u}{\partial z^2}+\frac{\partial u}{\partial y}\frac{\partial v}{\partial x}+\frac{\partial u}{\partial z}\frac{\partial w}{\partial x}\right) \tag{3.16}$$

$$P_{k2}=\mu_t\left(\frac{\partial^2 v}{\partial x^2}+2\frac{\partial^2 v}{\partial y^2}+\frac{\partial^2 v}{\partial z^2}+\frac{\partial v}{\partial x}\frac{\partial u}{\partial y}+\frac{\partial v}{\partial z}\frac{\partial w}{\partial y}\right) \tag{3.17}$$

$$P_{k3}=\mu_t\left(\frac{\partial^2 v}{\partial x^2}+\frac{\partial^2 v}{\partial y^2}+2\frac{\partial^2 v}{\partial z^2}+\frac{\partial w}{\partial y}\frac{\partial v}{\partial z}+\frac{\partial w}{\partial x}\frac{\partial u}{\partial z}\right) \tag{3.18}$$

The values for the k-ε constants used were $C_\mu = 0.09$, $C_{\varepsilon 1} = 1.45$, $C_{\varepsilon 2} = 1.9$, $\sigma_k = 1.0$, and $\sigma_\varepsilon = 1.3$.

3.5 Boundary Conditions

The boundary conditions for the numerical domain are as follows:

All outer walls are impermeable and no-slip:

$$u = v = w = 0 \tag{3.19}$$

All outer walls are adiabatic:

$$\frac{\partial T}{\partial z} = 0 \text{ on bottom and top walls of domain} \tag{3.20}$$

$$\frac{\partial T}{\partial y} = 0 \text{ on side walls of domain} \tag{3.21}$$

Block faces are impermeable and no-slip:

$$u = v = w = 0 \text{ on all block faces} \tag{3.22}$$

Uniform heat flux into the domain applied on all block faces:

$$\frac{\partial T}{\partial x} = -\frac{q''}{\lambda} \text{ on block faces at } x = 1.285 \text{ m where } q'' \text{ is a specified uniform heat flux} \tag{3.23}$$

$$\frac{\partial T}{\partial y} = -\frac{q''}{\lambda} \text{ on block faces at } y = 1.78 \text{ m} \tag{3.24}$$

$$\frac{\partial T}{\partial y} = \frac{q''}{\lambda} \text{ on block faces at } y = -1.78 \text{ m (for CD2 only)} \tag{3.25}$$

$$\frac{\partial T}{\partial z} = -\frac{q''}{\lambda} \text{ on top block faces} \tag{3.26}$$

$$\frac{\partial T}{\partial z} = \frac{q''}{\lambda} \text{ on bottom block faces} \tag{3.27}$$

No flow across symmetry planes:

$$u = 0 \text{ on S1 and S2} \tag{3.28}$$

$$v = 0 \text{ on S3 (for CD1 only)} \tag{3.29}$$

Temperature gradients normal to symmetry planes are set to zero:

$$\frac{\partial T}{\partial x} = 0 \text{ on S1 and S2} \tag{3.30}$$

$$\frac{\partial T}{\partial y} = 0 \text{ on S3 (for CD1 only)} \tag{3.31}$$

The outlet area is specified as an outlet with a specified average pressure:

$$\overline{P}^* = 0 \text{ over the outlet opening} \tag{3.32}$$

Uniform Cartesian inlet velocity (specified):

$$u = u_i,\ v = v_i,\ w = w_i \text{ at all inlets} \tag{3.33}$$

Uniform inlet air temperature (specified):

$$T = T_{i,a} \text{ at all inlets} \tag{3.34}$$

Uniform inlet turbulence intensity (specified):

$$I = I_i \text{ at all inlets} \tag{3.35}$$

The inlet turbulent kinetic energy is then calculated using:

$$k = k_i = \frac{3}{2} I_i{}^2 V_j{}^2 \tag{3.36}$$

where $V_j = \sqrt{(u_i{}^2 + v_i{}^2 + w_i{}^2)}$ is the resultant velocity of the jet at the inlet.

Uniform inlet eddy viscosity ratio (specified):

$$\frac{\mu_t}{\mu} = R_i \text{ at all inlets} \tag{3.37}$$

The inlet dissipation is then calculated using:

$$\varepsilon = \varepsilon_i = C_\mu \rho_i \frac{k_i^{\,2}}{\mu_t} \tag{3.38}$$

Scalable wall functions, (Grotjans and Menter, 1998) are used to determine the mean flow and turbulence transport equations in the region near the wall. The details of these wall functions are discussed in further depth in Appendix B.

3.6 **Parameters Studied**

The working fluid used in the study was air. Table 3.1 summarizes the parameters that were held constant for all simulations. The evaluations of the heat flux and the inlet turbulence parameters are discussed further in Chapter 5. Two total inlet mass flow rates $\dot{m}_i$ were used in this study. The first was the actual mass flow rate of air in the valve hall scaled for the portion of the valve hall modeled. This value was equal to 0.684 kg/s for CD1 and 1.368 kg/s for CD2 (because half of one tower is modeled opposed to one-quarter of one tower). The second inlet mass flow rate used was double the inlet mass flow rate in the current valve hall scaled for the portion of the valve hall modeled. This value was only used for CD1 and was equal to 1.368 kg/s. The location and size of the inlet opening were varied to study the effects on the velocity and temperature distribution. For CD1, this was achieved by varying the values of L_1 to L_3 (if the inlet opening was

Table 3.1: Parameters held constant for all simulations

$T_{i,a}$ (°C)	ρ_i (kg/m^3)	C_p (J/kg·K)	λ (W/m·K)	μ (kg/m·s)	q'' (W/m^2)	I_i	R_i
21.2	1.2	1004.4	0.0261	1.831 x10^{-5}	60.6	0.05	10

located on the bottom wall) or L_4 to L_6 (if the inlet opening was located on the side wall). For CD2, varying the location and size of the inlet opening was achieved by varying the values of L_7 to L_9. The component of the inlet velocity in the x direction u_i was always equal to 0 for all cases studied. When the inlet opening was located on the bottom wall of the domain, the inlet air angle θ was varied to study its effect on the velocity and temperature distribution in the valve-hall. The angle θ was defined as the angle (in degrees) that the inlet air flow makes with the horizontal in the y-z plane. This angle is less than 90º if the air is directed at the tower and greater the 90º if the air is directed away from the tower. The relationship between the angle θ and the components of the inlet velocity w_i and v_i can be explained with help from Figure 3.8. From Figure 3.8, at a given angle θ, the transformed inlet length $L_3^{'}$ becomes $L_3 \sin \theta$. The resultant jet velocity V_j at angle θ is then defined as in Figure 3.8. The velocity component w_i becomes $V_j \sin \theta$ or $\dot{m}_i / (\rho_i L_2 L_3)$. The velocity component v_i becomes $-V_j \cos \theta$ or $-w_i / \tan \theta$. When the inlet air openings were located on the side walls of the domain, the inlet air velocity was always directed normal to the inlet opening ($\theta = 90°$). In that case, the component of the inlet velocity in the z direction w_i was equal to 0 and the component of the inlet velocity in the y direction v_i was equal to $-\dot{m}_i / (\rho_i A_i)$ where A_i is the area of the inlet opening.

As previously mentioned, the location and size of the outlet opening was fixed for CD1. For CD2, however, the location and size of the outlet opening was varied study the effects on the velocity and temperature distribution. This was achieved by varying the values of L_{10} to L_{12} (if the outlet opening was located on the top wall) or L_{13} to L_{15} (if the outlet opening was located on the side wall).

A total of 23 different combinations of the varied parameters were studied in this work. These combinations are presented and discussed in Chapter 6.

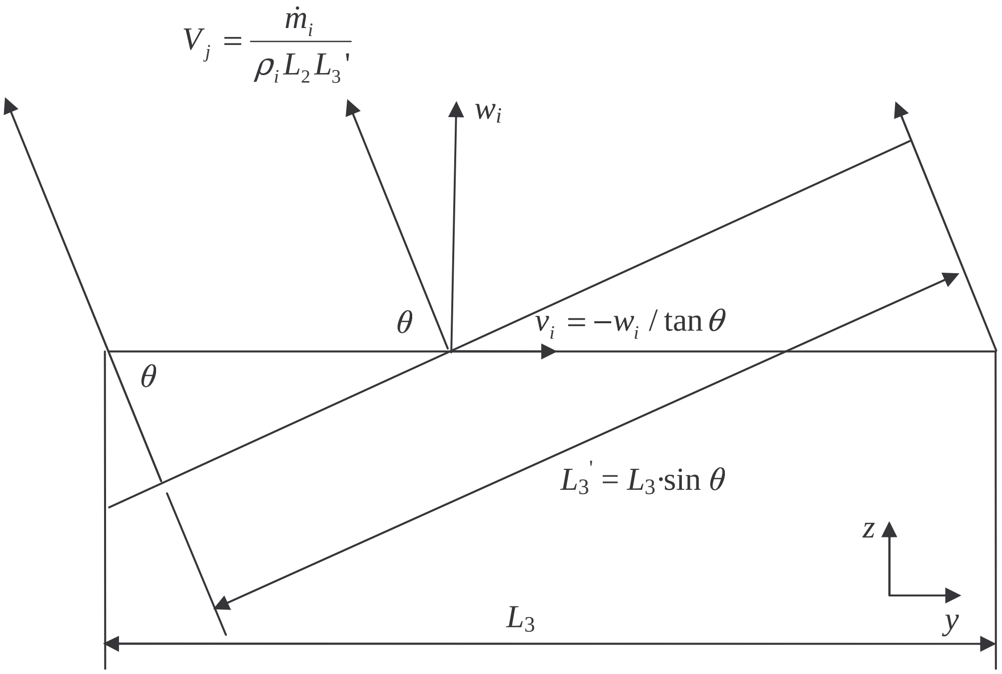

Figure 3.8: Determination of inlet velocity components at angle θ

Chapter 4

NUMERICAL SOLUTION METHOD

4.1 Introduction

This chapter will outline the numerical procedure used to obtain numerical solutions to the governing differential equations discussed in the previous chapter. The domain was first subdivided into many small control volumes by creating a computational grid. The computational grid consisted of hexahedral shaped control volumes. The governing equations were then integrated to produce linearized coupled algebraic equations for the velocity, pressure, energy, and turbulence model quantities. An iterative solution of these equations was then performed to obtain values for each of these quantities for each control volume in the domain.

4.2 Grid Generation

Grid generation software ICEM CFD 4.CFX, distributed by ANSYS Inc., was used to create the computational grids for the domain. The software has a geometry editing module which is capable of handling direct CAD geometry imports, geometry creation and editing, and boundary condition and region definition. The software also has a number of different meshing modules which can create shell, tetrahedral, prism, and hexahedral meshes.

Regardless of the configuration, the following basic steps are used to create the geometry for the mesh:

1. The entire geometry is first subdivided into two pieces in order to minimize the overall number of nodes used.

2. Points are created at the domain boundaries for the room, towers, and inlet and outlet openings by defining x, y, and z components of these points in space.

3. Curves are created between the endpoints in order to define the edges of the geometry.

4. Surfaces are created by interpolating between the quadrilateral regions defined by the curves.

5. The “repair” function is used to separate surfaces where more than one surface is defined in the same location.

6. Locations of the boundary conditions for the solver are established by defining as parts (and grouping, if desired) the applicable surfaces.

Once the geometry is defined, a mesh is created on the geometry. Because of the Cartesian nature of the geometry, the hexagonal meshing module (HEXA) was used for this project. HEXA is capable of creating structured and unstructured hexagonal meshes, as well as O-grids. In this case, structured hexagonal meshes were used. The first step in generating a mesh using HEXA is to define the block model. The block model is essentially a model of the geometry made up of hexagonal blocks. The blocks are used in HEXA to define the locations of the nodes to be used in the mesh. Initially, HEXA creates one block around the entire geometry. The user then subdivides this block in to a number of smaller blocks with the faces of the blocks corresponding to the surfaces of the geometry. Blocks which are not needed in the model are removed from the mesh. In this case all of the blocks corresponding to the interior surfaces of the tiers of the tower were removed from the mesh (they did not need to be modeled since a constant heat flux was to be applied on the outer surfaces of the tiers). Once all the blocks have been created, nodes can be placed on the edges of the blocks. A number of different grid spacing options are available, including uniform, geometric, and exponential grid spacing. In this case, as structured grids were used, only nodal spacings on dimensionally unique edges were specified with corresponding opposite edges inferred using the “copy to parallel” function. Once all the nodes are defined, the block faces are projected onto the geometry. This is done in order to impose the geometry onto the mesh. The final mesh is then saved in HEXA and then can be output in the specified format to be read by a CFD package. In this case, the grid was exported to a CFX-5 mesh file.

The geometries for this project were built in two regions which were later rejoined once the grid was completed. The reason for building the geometry in separate regions is that it allows more nodes to be placed in regions where the spatial derivatives of the governing equations are high (near the tower and air jets) and fewer nodes to be placed where there is very little change in the solution fields from node to node (away from the tower and air jets). In addition, depending on where the inlet and outlet openings were located in the domain, different divisions of the geometries were used. This was done because the need for nodal concentration in different areas depends highly on the orientation of the inlet and outlet openings. Non-uniform grid spacing was also employed for the meshes in this project in order to place more nodes in regions where the spatial derivatives of the governing equations are high and fewer nodes where there is very little change in the solution fields from node to node.

Mesh refinement was required in this project in the gaps between the blocks with an increased amount of nodes needed in order to obtain a converged solution. The distance between the wall and the first node was also decreased near some of the walls in order to achieve a y^+ value of less than 100 on all walls (recommended by CFX-5 for scalable wall functions). Sample grids for Geometry 1 and Geometry 2 showing the two grid regions are given in Appendix C.

4.3 **Overview of CFD Package**

The CFD package used in this work was CFX-5 (v5.7), distributed by ANSYS Inc. The CFX-5 package consists of pre-processing software (CFX-Pre), a CFD solver (CFX-Solver), and post-processing software (CFX-Post).

4.3.1 CFX-Pre

CFX-Pre is the pre-processing software for CFX-5. The grids that were generated using ICEM CFD 4.CFX were first imported into CFX-Pre. Fluid properties, boundary conditions, and solver parameters were then defined. Grid to Grid Interfaces were used to join the two meshes together that make up the entire flow domain. The Grid to Grid Interface (GGI) option in CFX-5 allows two grids with dissimilar nodal spacings to be joined together at faces with identical geometry. The initial guesses for all the flow variables at each node were specified. The expert mode was also used to specify solver parameters that are better suited to a hexahedral mesh as opposed to the default tetrahedral mesh. Domain parameters, solver control parameters, and expert parameters used are presented in Appendix D. Finally, the simulation was saved, and the solver definition file (DEF) was written. The DEF provides all the necessary information needed by the solver in order to begin solving the problem.

4.3.2 CFX-Solver

CFX-Solver is the CFD solver used in CFX-5. This solver uses a fully implicit, coupled, co-located, finite volume method of discretization (Patankar, 1980), but is based on the finite element method approach of representing the geometry. Mass conservation discretization is based on the work of Rhie and Chow (1983), Prakash and Patankar (1985), and Schneider and Raw (1987). The high-resolution scheme, based on the work of Barth and Jesperson (1989) was used for advection terms. Single precision was used in the computations, and the simulation was considered converged when the maximum dimensionless residual of all the discretised equations at any control volume was less than $1x10^{-5}$. The CFX-Solver graphical user interface (GUI) gives the user information regarding the simulations progress such as the root mean squared (RMS) and maximum residual of each of the discretised equations for each time step. It can also display the location of the maximum residual for each of the discretised equations.

4.3.3 CFX-Post

The CFX-Post GUI was used to view, analyze, and calculate relevant data from the converged numerical simulation. CFX-Post can be used to determine values for any variable defined in its library of properties at any point in the domain. New variables can also be defined based on the existing variables. Data can be extracted for points, areas (predefined boundary conditions and user defined areas), and volumes. CFX-Post will also interpolate the values of the variables if there is no data point at a requested location. CFX-post can also be used to create vector plots, contour plots, as well as 2-D and 3-D streamline plots. The plots generated by CFX-Post will be discussed further in Chapter 6.

Chapter 5

VALIDATION TESTS

5.1 Introduction

In order to ensure that the results obtained by the numerical model were sufficiently accurate, several validation tests were performed. An experiment was carried out in the actual valve hall with the same dimensions as in Figures 1.1 to 1.4. Data obtained from that experiment were used to determine how well the CFD code was able to predict the experimental measurements. Mesh independence tests were also completed for each of the two geometries used in the study.

5.2 Comparison with Experimental Results

5.2.1 Experimental Restrictions

Because of the high voltages associated with thyristor valve halls, safety was an important issue for Manitoba Hydro in conducting an experiment in the valve hall. Therefore, a number of safety-related restrictions were placed on the testing. First, people were not allowed to be within the area enclosed by the 5-m high safety fence (shown in Figure 1.2) while the valve hall was in operation. Second, people were not to be located above a height of 5 m from the floor while the hall was in operation. Third, no equipment could be installed in the region enclosed by the safety fence unless it was at a height of 12.28 m or above so that it could be grounded to a nearby I-beam[*]; even then, the equipment could not be electrically conductive or produce an electrical current. With

---

[*] Later, the restriction of 12.28m was relaxed to allow placement of infrared thermography targets (i.e. black tape) on the sides of the valve towers

these restrictions in place, the design of a suitable experiment to validate the numerical results proved to be quite challenging.

It was decided that it would be much easier to measure temperatures rather than the other parameters computed in the simulation. It was also decided that temperatures outside the safety fence and at a height of less than 5 m from the floor would be measured carefully using a handheld digital thermometer, while temperatures enclosed by the safety fence would be determined using infrared thermography.

.

5.2.2 Infrared Thermography

Infrared Thermography (IT) is the process of creating images that can show the temperature of a surface by measuring the thermal radiation that is received from the surface. That radiation is then converted into a temperature using the calibration equations that are programmed into the system. IT has been widely used in industry for many applications such as non-destructive testing and the maintenance of heated systems.

One major advantage of IT is that unlike thermocouples which are only able to measure discrete temperatures, IT is capable of providing an entire temperature field with a single thermal image. Another advantage is that it is a non-contact method. This can be very important when dealing with high voltage electrical equipment where it is essential not to disrupt electrical fields.

One major drawback of IT in this application is that it can only determine the temperature of objects that emit thermal radiation. Air is essentially transparent (it does not emit thermal radiation) and thus its temperature cannot be measured directly. It is desired in this experiment to measure both air and surface temperatures in the valve hall using IT.

One possible way of eliminating this problem is to measure the temperature of the air indirectly. That is, by placing an object in the airfield that would take on the temperature of the air without significantly altering the flow and then taking an image of that object.

5.2.3 Requirements of the Design

The design must have the following characteristics:

1) Non-Conductive

It was very important not to interrupt the electrical field around the thyristor towers. Any proposed solution, therefore, had to be constructed using an electrically non-conductive material.

2) Low Thermal Mass

Any object placed in an airfield will undergo a transient period, which is the period of time that it takes for the object to reach the same temperature as the airfield. For the experiment, it was desired for this time to be as short as possible. This can be achieved by using a material with a low thermal mass.

3) Non-Restrictive to Airflow

In order to achieve an accurate representation of an airfield, it was important that the majority of the airflow was not interrupted. Any solution, therefore, had to be as non-restrictive to airflow as possible.

4) Capable of Continuous Measurements

In order to compare experimental results with the CFD results, it is desirable to have as many measurements across the airfield as possible. A continuous temperature profile would be ideal, but this may not be possible due to Requirement 3.

5) Highly Emissive Material

In order to limit reflections from neighbouring objects, IT is most accurate when using a highly emissive material as a target.

6) Rigidly Fixed

In order to get accurate readings with the infrared camera, it was important that the materials be as stationary as possible when placed in airflow.

7) Strong

Once the test materials were set up in the valve hall, it was important that they be able to remain in place for a long period of time. The reason for this was that scheduled shutdowns of the valve hall only occur on a few occasions per year. If the test materials were to fail and electrical fields were in danger of being interrupted, an unscheduled shutdown would have to be imposed resulting in additional cost and lost revenue to Manitoba Hydro.

5.2.4 Selected Test Locations

Taking the above restrictions and requirements into account, three areas to conduct IT testing were determined. The locations of these areas are shown in Figures 5.1 and 5.2.

5.2.4.1 Area 1

Area 1 was located on the surface of the towers. The surface that was used for the experiment was the surface of the towers that can be viewed when standing on the outside of the safety fence, that is, the surface of the towers that can be seen in Figure 5.2.

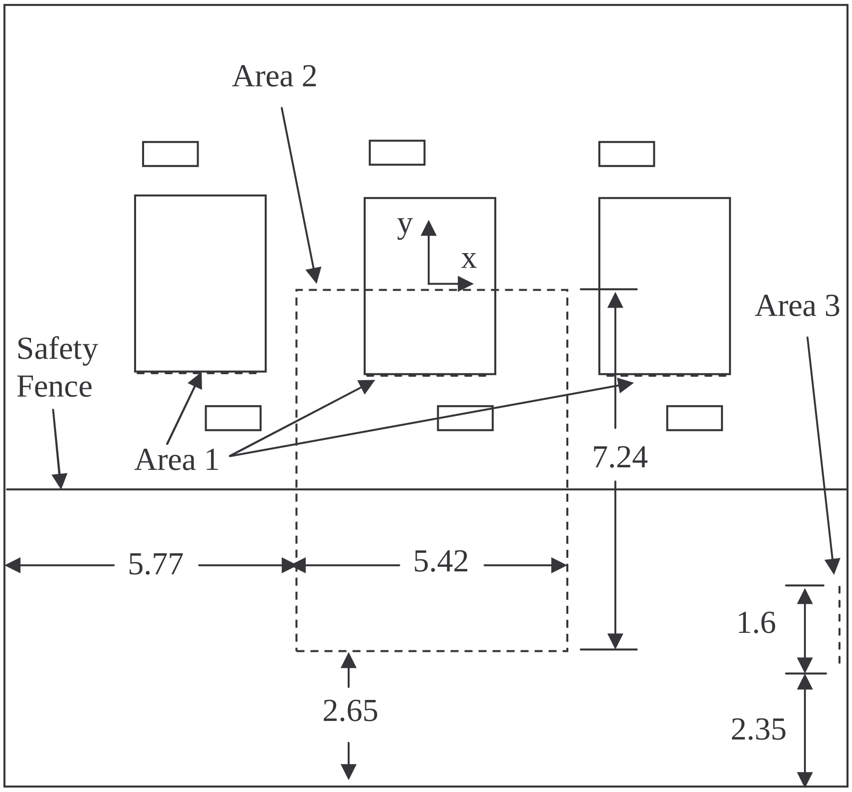

Figure 5.1: Plan view of valve hall showing the three areas for IT testing (all dimensions in meters)

In order to convert the radiation emitted by a surface into a temperature, the emissivity of the surface, ε_s is needed. The emissivity specifies how well a real surface radiates energy compared with an ideal blackbody. The emissivity can vary from 0 for an ideal non-emitting surface to 1 for a black body. For this experiment, 0.1 m x 0.1 m rectangular patches constructed with Scotch™ Super 88 electrical tape, ($\varepsilon_s = 0.98$) were attached to the surface of the towers in order to determine the temperature of the surface.

Once the experiment was conducted and the thermal photographs were analyzed, the actual surfaces of the towers were indistinguishable on a thermograph from the black tape patches attached to the surfaces of the towers. It was therefore concluded that the

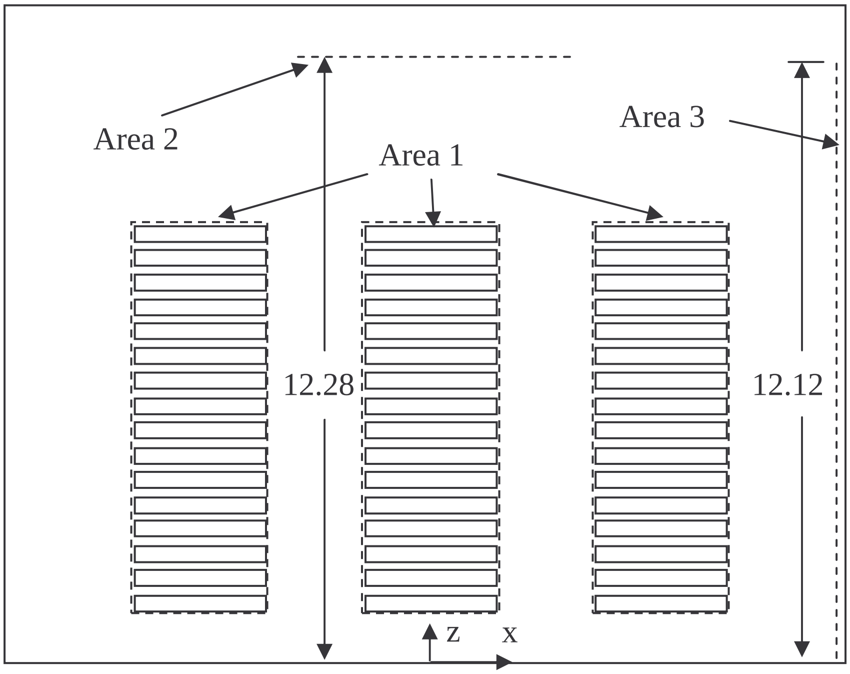

Figure 5.2: Side view of valve hall showing the three areas for IT testing (all dimensions in meters)

emissivity of the tower surface was identical to that of the black tape and therefore the temperature of the tower surface could be determined at any point on the surface.

5.2.4.2 Area 2

Area 2 was a horizontal plane located above the thyristor towers at a height of 12.28 m from the floor. Because this plane was located in an airfield away from the walls, the air temperature had to be measured indirectly using IT. Black tape patches of the same size and construction as in Area 1 were used to measure the air-temperature at uniform intervals on the plane. In order to place the black tape patches at regular intervals on the plane, they needed to be mounted to a surface. It was important that the surface be permeable so that the natural air flow pattern was not interrupted to a large degree. Fiberglass window screen was chosen to mount the black tape patches to. The screen had a permeability of 70%. In order to cover the entire area shown in Figure 5.1, three separate screens each 5.42 m x 2.36 m were used. These screens were stitched together and then attached to wood frames and fastened to I-beams near the ceiling of the room to create the entire 5.42 m x 7.24 m screen (Note: The 7.24 m length in the y-direction is 0.16 m larger than the length of the three screens put together. This is due to the width of the wood frames). Figure 5.3 shows the dimensions of one screen and the locations of the black tape patches.

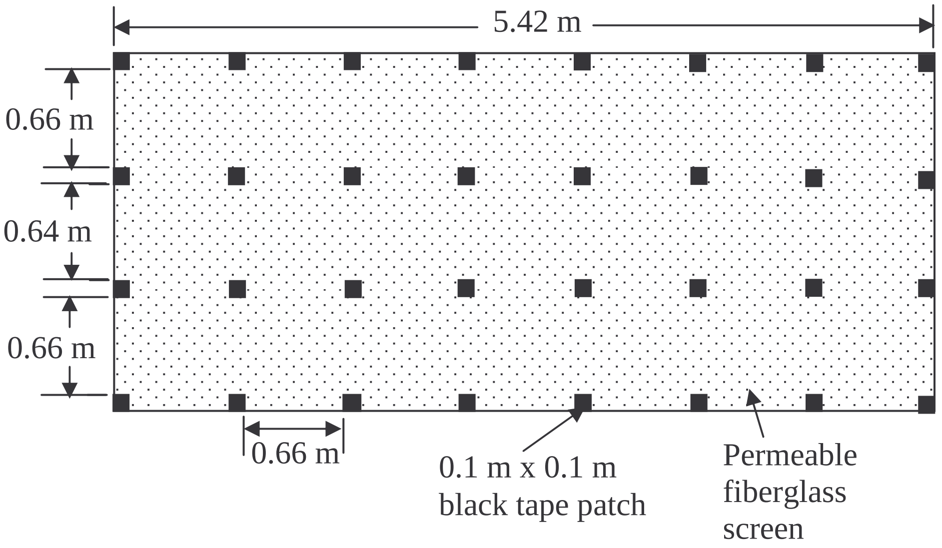

Figure 5.3: Single screen used in Area 2

5.2.4.3 Area 3

Area 3 was a vertical plane located 0.15 m away from the wall as shown in Figures 5.1 and 5.2. Once again, the region was located in an airfield and so the same method as in Area 2 was used to determine the temperatures. For this area, five screens each 1.60 m x 2.36 m were stitched together and then attached to wood frames and fastened to the wall to create the entire 1.60 m x 12.12 m screen (Note: The 12.12 m length in the z-direction is 0.32 m larger than the length of the five screens put together. This is due to the width of the wood frames). Figure 5.4 shows the dimensions of one screen and the locations of the black tape patches.

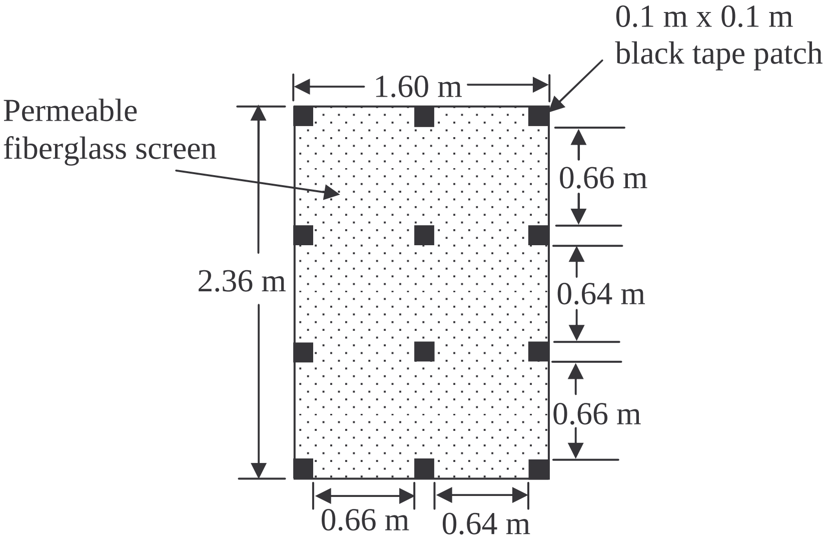

Figure 5.4: Single screen used in Area 3

5.2.5 Experimental Setup and Procedure

The necessary equipment to perform the experiment was installed by Manitoba Hydro personnel during a scheduled shutdown. After regular operation resumed, the equipment was allowed to come into thermal equilibrium with the room during a two-week period before the initial test was conducted. In total, two tests were carried out. The first test was done on February 22, 2005 and the second test was performed on April 14, 2005. The procedure for both tests was the same. The first step was recording the operating conditions in the valve hall related to the experiment (this step was later performed again at the end of the experiment and in both cases the data was the same before and after the experiment). The operating conditions for both experiments are shown in Table 5.1. It should be noted that $\dot{W}_{gen}$ and V_{drop} are the combined generated power and voltage drop for two valve halls connected in series. The generated power and voltage drop for VG41 should be approximately half this.

Table 5.1: Operating conditions for the two experiments

	Experiment 1	Experiment 2
$T_{i,w}$ (°C)	33.7	33
$T_{o,w}$ (°C)	50.1	48.4
$Q_{i,w}$ (m^3/s)	0.026	0.026
$T_{i,a}$ (°C)	21.2	27.4
$T_{o,a}$ (°C)	29.1	33.4
$\dot{Q}_{i,a}$ (m^3/s)	6.84	6.84
$\dot{W}_{gen}$ (MW)	885	833
V_{drop} (MV)	0.47	0.49
I (A)	1882	1700

The next step was recording air temperatures outside of the fenced in area. The temperatures were recorded with a Kestrel® 3000 Pocket Weather Meter supplied by Manitoba Hydro. This device has an accuracy of ± 1 °C. Temperatures were recorded at a height of $z = 1$ m and $z = 4$ m at regular intervals of x and y. It was found that at each height, all temperatures were within ± 0.5 °C of a certain value. Values for these temperatures in both experiments are shown in Table 5.2

Table 5.2: Air temperatures outside of the fenced-in area for the two experiments

	Experiment 1	Experiment 2
T (°C) $z = 1$ m	26.5 ± 0.5	30.0 ± 0.5
T (°C) $z = 4$ m	27.5 ± 0.5	31.1 ± 0.5

The third step of the experiment was to take infrared images in Areas 1, 2, and 3. The infrared camera used for the experiments was a Flir Systems Thermacam® PM 695 camera. This camera and its operator were supplied by Manitoba Hydro. This device has an accuracy of ± 2 °C. For the experiment, electrical lights were turned off to eliminate them as a possible radiation source. Operating parameters were entered into the camera so that the camera could convert radiation readings into temperature readings. Because the three areas were large in dimension and also to increase the resolution of each image, each of the three areas was photographed in parts. Each image location was carefully indexed so that the image could be easily identified later. When the experiment was completed, the data were analyzed using Thermacam Researcher™ 2.8 software. Temperatures at the centre of each black tape square along with the corresponding locations were recorded. Sample infrared thermographs for Areas 1, 2, and 3 are presented in Appendix E.

5.2.6 Comparison with Numerical Results

The numerical domain used to compare with the experimental results is shown in Figures 3.1 and 3.2a. CD1 was used to decrease computational effort. An inlet opening of the same size as in VG41 (for the same portion of the room) was used in the numerical model. The location of the inlet opening was the same as in VG41 except that the inlet opening was made to be symmetrical with S1 in order to maintain symmetry. Because the results of the first experiment showed higher air side heating rates, these results were used to compare with the numerical simulations. For the numerical model, the angle θ as defined in Section 3.6 was determined to be 60º during a previous inspection of the inlet flow during a shutdown of the valve towers. The inlet velocity normal to the vent was determined by dividing the overall inlet flow rate ($\dot{Q}_{i,a}$ = 6.84 m^3/s) by the total area of inlet openings (6 x 1.09 x 0.48 = 3.139 m^2) making w_i = 2.179 m/s. The inlet velocity in the y direction was then determined using $v_i = -w_i/\tan(60) = -1.258$ m/s. All the outer walls were assumed insulated. The average static pressure at the outlet was set to 0. The heat flux applied evenly to the tower walls ($q'' = 60.6$ W/m^2) was determined using the relation:

$$q'' = \rho_{i,a}\dot{Q}_{i,a}C_{p,a}(T_{o,a} - T_{i,a}) / A_{towers} \tag{5.1}$$

where A_{towers} is the total surface area of all the tower blocks in the valve hall. The properties of air used in Equation (5.1) were taken at 21.2°C.

Simulations on three meshes with different mesh sizes were carried out for the conditions of Experiment 1. Results of the mesh-independence tests indicated that the medium mesh was acceptable for predicting temperatures in the valve hall (see Section 5.3.1 for details). The medium mesh was thus chosen for comparisons with the results obtained from Experiment 1. Figure 5.5 shows temperatures on a line in Area 1 obtained in the experiment compared with those obtained numerically. The points used for the experimental results were taken about 0.64 m to the right (in the x direction) of the centre of Tower 2 and Tower 3 and at the centre of the height of each block (in the z direction). It should be noted that temperatures at these points on Tower 1 were not obtained during Experiment 1 because much of its field of view was blocked. Also temperatures were not obtained on blocks 8, 9, and 10 of Towers 2 and 3 due to an obstruction of view by the safety fence). It should also be noted that the temperatures obtained in the experiment were not located directly on the surface of the towers, but on a thin plastic cover a small distance away from the surface of the tower. Because of this, theoretical results were therefore taken at both 0.03 m and 0.06 m away from the surface of the tower (i.e., in the *y* direction) in order to match the conditions of the experiment. The theoretical results correctly predict the trend of the temperatures of the block faces becoming higher with increasing height; however, the theoretical results somewhat under-predict the temperatures near the bottom of the tower. There are a number of possibilities as to why this may have occurred. One possible explanation is that the actual temperature of the air issuing from the inlet opening into the room was higher than the inlet temperature used in the simulation. The inlet air temperature sensor in the valve hall is located upstream of the inlet opening in the duct work and also upstream of the duct heaters. The duct heaters are used to heat the inlet air in the first few hours after an extended shutdown. Because the experiment was conducted approximately two weeks after the end of a shutdown, the duct heaters should not have been in operation during this experiment. It is not, however, known for sure whether or not this was the case. Assuming that the duct heaters were not in operation during the experiment, there is a second possible explanation. In this study, only the air-side cooling was considered. In the actual valve hall, however, there is also a water cooling system which removes most of the heat produced by the towers. In Experiment 1, the average temperature of the cooling water exiting the blocks was 50.7°C, meaning that the temperature on the blocks on average was higher than this. The relatively high temperatures of the blocks may have also increased the temperature of the plastic cover which was not accounted for in the numerical simulations. This phenomenon was not investigated any further in this study; however, it would be advisable in future studies to measure the temperature of the inlet air directly as it enters the room in order to ensure that the correct value is used for the heat flux on the blocks.

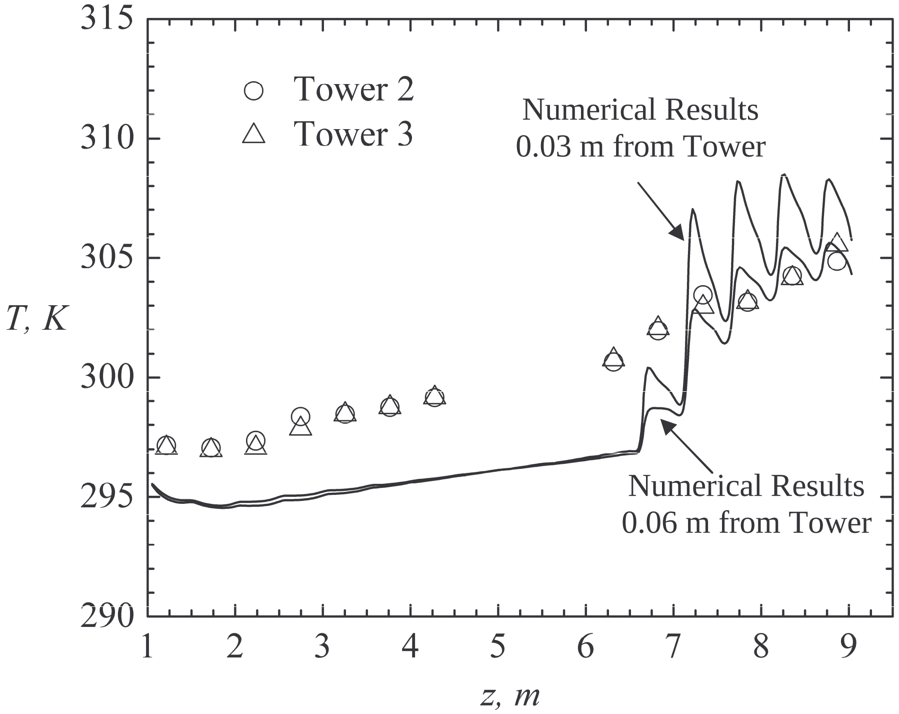

Figure 5.5: Comparison of experimental and numerical results on tower surface (Area 1)

Figure 5.6 shows temperatures on three lines in Area 2 obtained during Experiment 1 compared with numerical results. The first line corresponds to x = 0.37 m, the second line corresponds to x = 1.13 m, and the third line corresponds to x = 1.89 m. All three lines show good agreement with the experimental results with air temperature varying very little with y at this height.

Because of the use of symmetry planes S1 and S2, the walls at the minimum and maximum locations of x in Figure 1.2 are not modeled in the numerical simulations. As a result, the exact locations of the temperatures in Area 3 (0.15 m from the wall in the x direction) were not modeled in the numerical simulation. The location of Area 3, however, was far enough away from the inlet vents and the tower that it was expected that the air in this region was stagnant and thus the air temperature would only vary in the

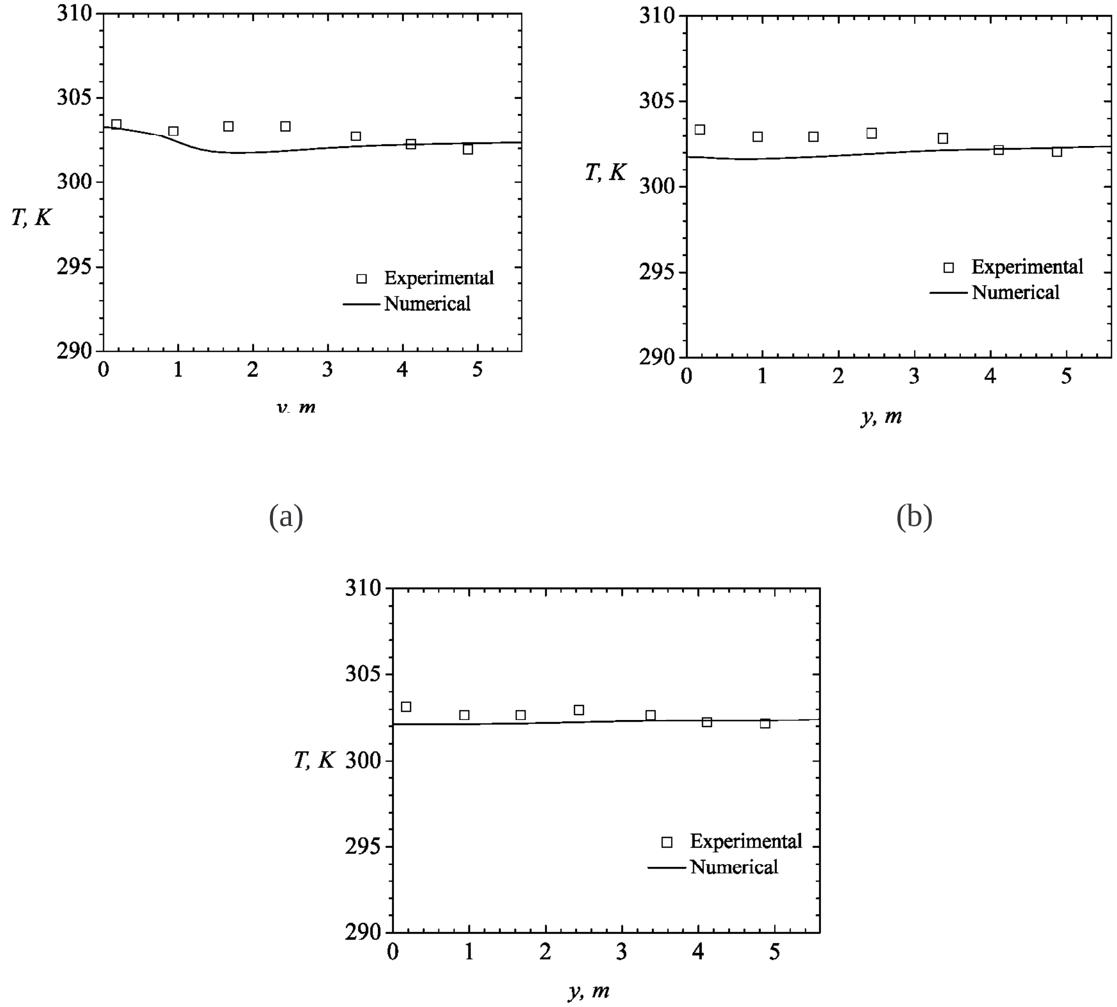

(a) (b)

(c)

Figure 5.6: Comparison of experimental and numerical results in Area 2: (a) x = 0.37 m, (b) x = 1.13 m, (c) x = 1.89 m

z direction due to the change in temperature between the inlet and the outlet vent. In the numerical simulation, there was a wall at the maximum location of y (y = 5.59 m). Similarly with the experiment, the location of this wall was such that the air in this region was expected to be stagnant and thus temperatures would only vary with z due to change in temperature between the inlet and outlet vents. Because of this similarity, it was decided to compare the temperatures in Area 3 in the experiment with the temperatures

0.15 m from the wall located at the maximum location of *y* in the numerical simulation. Because the temperature was only expected to vary in the z direction, lines for comparison were orientated in the vertical direction. The three lines used for comparison with the experiment were located at *y* =1.69 m (E1), *y* = 2.45 m (E2), and *y* = 3.19 m (E3). The three lines used for comparison for the numerical simulation were located at *x* = 0 m (N1), *x* = 1.15 m (N2), and *x* = 2.3 m (N3). Figure 5.7 shows the temperatures obtained in the experiment in Area 3 compared with the temperatures obtained numerically.

All the experimental points lie nearly on top of each other for the three lines measured. The three lines from the numerical results also lie nearly on top of each other. This shows evidence that the temperature does not vary in the *x* and *y* directions in this region, and instead varies only in the *z* direction due to buoyancy effects. While good agreement exists between the numerical and experimental results in the upper portion of the room, the experimental results show higher air temperatures in the lower portion of the room. If the duct heaters were in operation (as previously discussed) it would explain this discrepancy. Another possibility might be an exterior heat source through the floor of the room or an exterior heat sink through the ceiling of the room (or a combination of the two) contributing to the difference in temperatures. If there was a net heat gain through the floor of the room, it would result in a lower tower block heat flux than used in the numerical simulations (60.636 W/m^2). If there was a net heat loss through the ceiling of the room, it would result in a higher heat flux than used in the numerical simulations. Because the outside air temperature during the time of Experiment 1 was ≈ -15° C, most likely heat

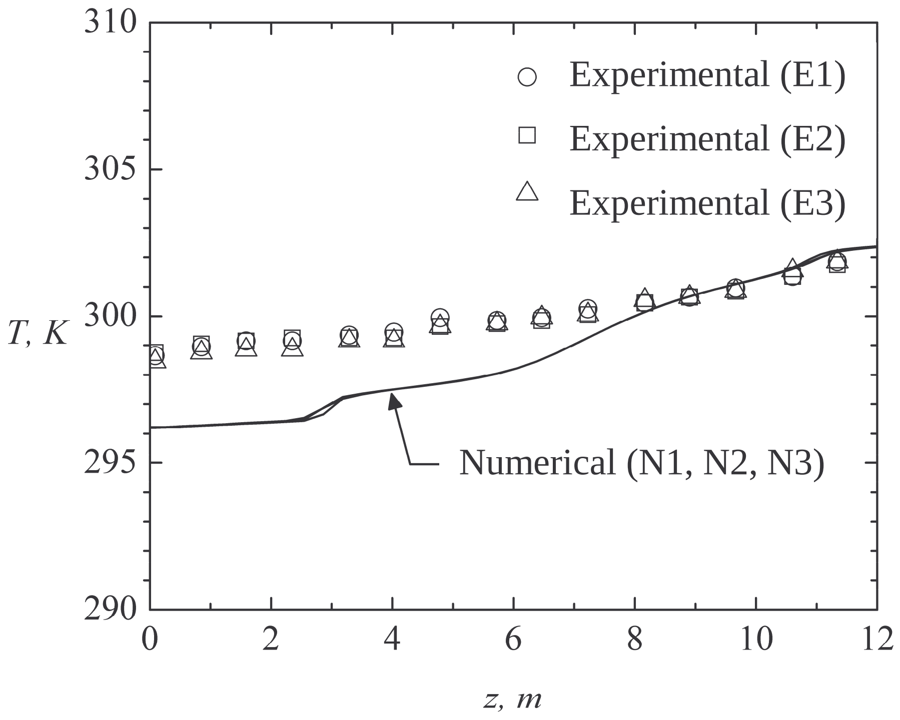

Figure 5.7: Comparison of experimental and numerical results in Area 3

was lost to through the metal ceiling of the room to the outside surroundings. This would mean that the towers produced more heat than specified in the simulations. Although this phenomenon was not investigated any further in this study, this maybe a topic for investigation in a future study on this topic.

5.3 Mesh-Independence Tests

The Computational Domain of interest is shown in Figures 3.1 and 3.2a for CD1 and Figures 3.1 and 3.2b for CD2. The objective of this section is to determine a grid structure that provides acceptable numerical accuracy. For the purpose of the mesh-independence tests, two cases were used. One of these cases corresponded to CD1, and the other corresponded to CD2.

Two methods were used to judge mesh independence of the results; the relative maximum temperature in the domain ($T_{max} - T_{i,a}$) and the relative temperature $T_D = (T - T_{i,a})$ along six different lines in the domain for CD1 and seven lines for CD2. The locations of the lines used are summarized in Table 5.3.

Table 5.3: Locations of the lines used for mesh independence

	CD1			CD2		
Line	x (m)	y (m)	z (m)	x (m)	y (m)	z (m)
F1	0	0 - 5.59	8.52	0	−5.59 - 5.59	8.52
F2	0	0 - 5.59	8.7	0	−5.59 - 5.59	8.7
F3	0 - 2.3	0	8.52	0 - 2.3	0	8.52
F4	0 - 2.3	0	8.7	0 - 2.3	0	8.7
F5	1.15	0 - 5.59	11.19	1.15	−5.59 - 5.59	11.19
F6	1.285	1.78	0 - 13.35	1.285	1.78	0 - 13.35
F7	N.A.	N.A.	N.A.	1.285	−1.78	0 - 13.35

5.3.1 Computational Domain 1

The mesh-independence tests for CD1 were conducted using coarse, medium, and fine meshes of 868,005, 1,141,442, and 1,475,794 nodes, respectively. These are increases of 32% and 70% in the number of nodes compared with the coarsest mesh. These meshes were dictated by computational resource constraints. The boundary conditions used for the mesh-independence test for CD1 correspond to Case 1 discussed in Section 6.3. The y^+ values were examined to ensure that they were less than 100 for all walls. Table 5.4 shows the values of T_{max} and ($T_{max} - \mathrm{T}_{i,a}$) for the three meshes. The percent difference for the value of ($T_{max} - \mathrm{T}_{i,a}$) between the coarse and the medium grids and between the medium and the fine grids are 1.74% and 1.01%, respectively.

Table 5.4: Values of T_{max} and $(T_{max} - T_{i,a})$ for the three meshes used for CD1

Grid	T_{max}, °C	$(T_{max} - T_{i,a})$, °C
Coarse	94.08	72.88
Medium	95.37	74.17
Fine	94.63	73.43

Figures 5.8 to 5.13 show T_D on lines F1 to F6, respectively for CD1. Table 5.5 shows the maximum and root mean squared (RMS) percentage errors for T_D between the three successive meshes on lines F1 to F6. Because the medium and the fine grids overlap on all the lines and because the percentage errors between the medium and fine grids were small, the medium mesh is considered adequate for CD1. Plots of the medium mesh for CD1 are presented in Appendix B.

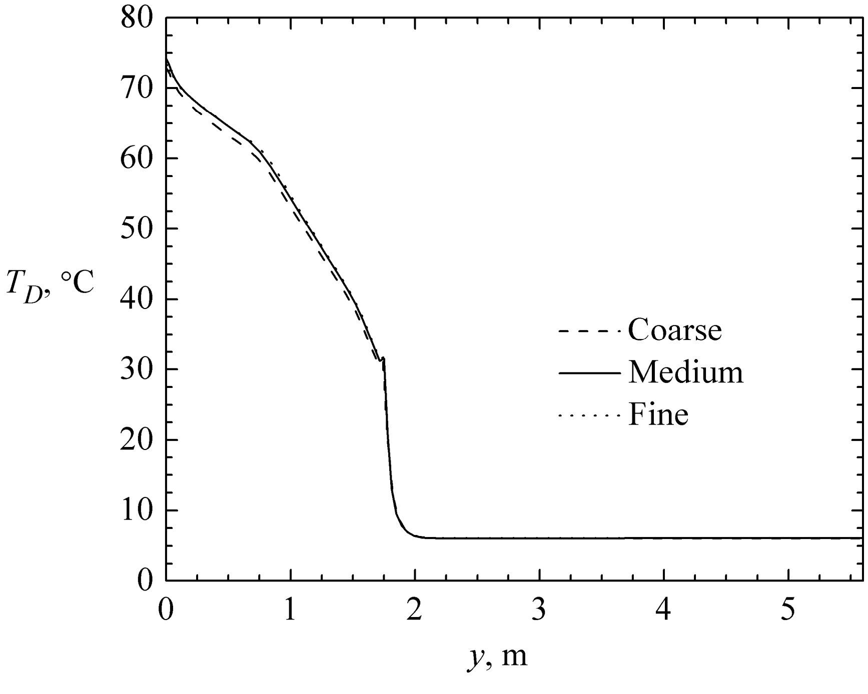

Figure 5.8: Relative temperature T_D on Line F1 for the coarse, medium, and fine grids for CD1

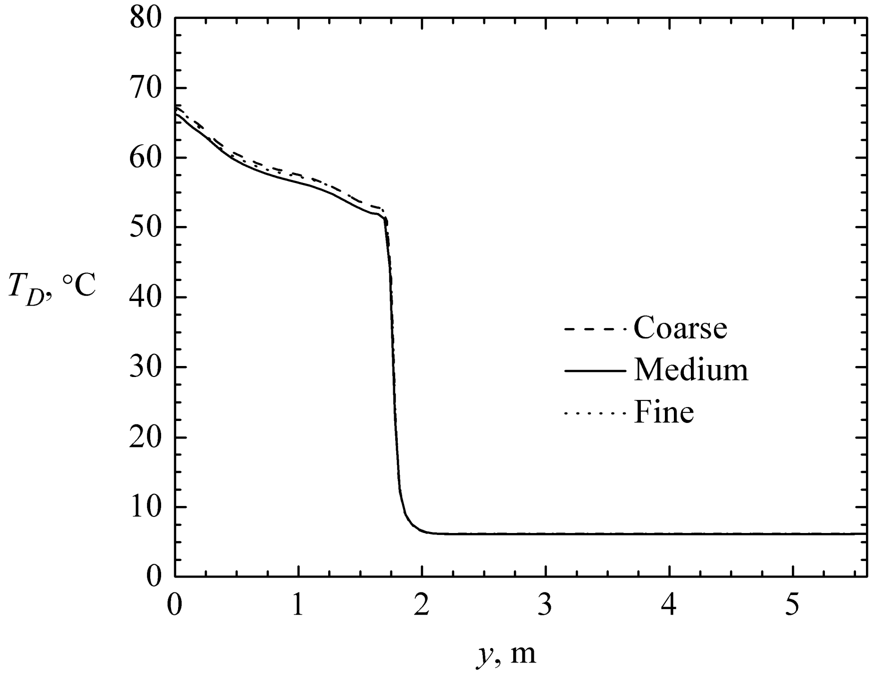

Figure 5.9: Relative temperature T_D on Line F2 for the coarse, medium, and fine grids for CD1

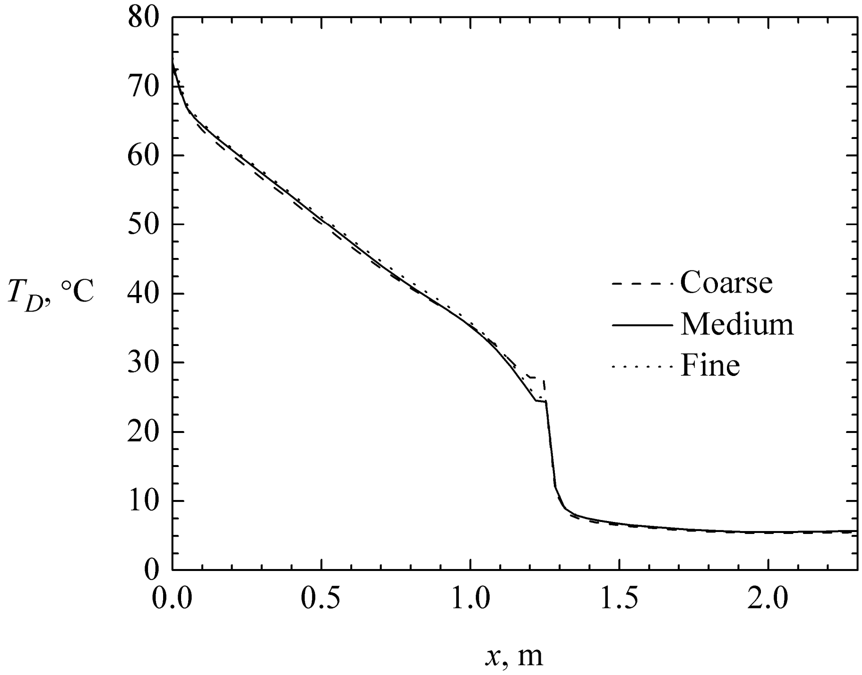

Figure 5.10: Relative temperature T_D on Line F3 for the coarse, medium, and fine grids for CD1

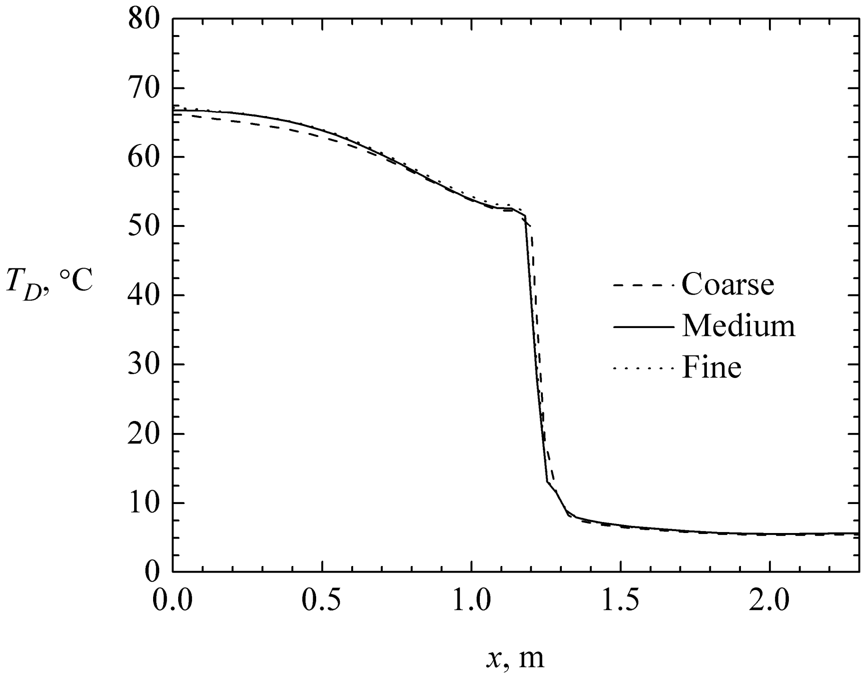

Figure 5.11: Relative temperature T_D on Line F4 for the coarse, medium, and fine grids for CD1

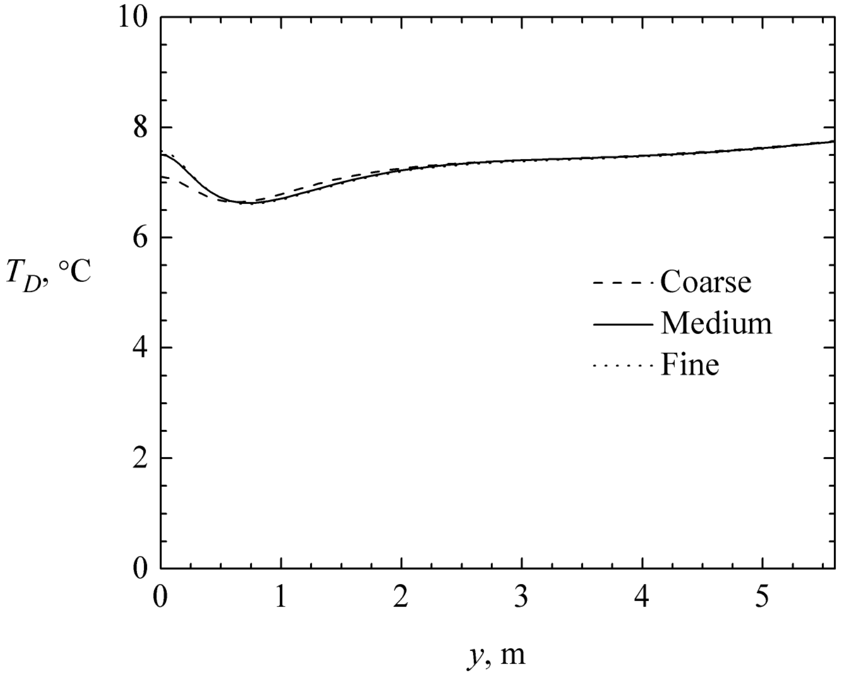

Figure 5.12: Relative temperature T_D on Line F5 for the coarse, medium, and fine grids for CD1

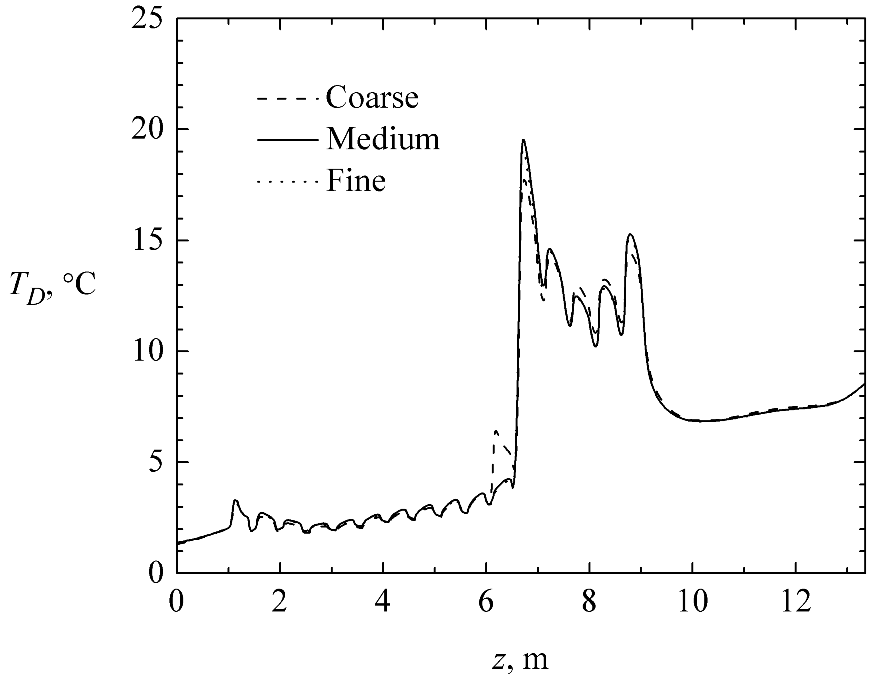

Figure 5.13: Relative temperature T_D on Line F6 for the coarse, medium, and fine grids for CD1

Table 5.5: Percentage deviations for T_D on F1 to F6 between successive grids for CD1

	Max. % error coarse-medium	RMS % error coarse-medium	Max. % error medium-fine	RMS % error medium-fine
F1	8.22	1.83	1.01	0.40
F2	7.87	1.88	1.16	0.42
F3	10.83	2.99	2.38	1.11
F4	3.58	2.16	1.43	0.64
F5	6.18	1.88	0.85	0.33
F6	76.10	10.29	3.33	1.22

5.3.2 Computational Domain 2

The mesh-independence tests for CD2 were conducted using coarse, medium, and fine meshes of 1,723,484, 2,148,130, and 2,512,420 nodes, respectively. These are increases of 25% and 46% in the number of nodes compared with the coarsest mesh. These meshes were dictated by computational resource constraints. The boundary conditions used for the mesh-independence test for CD2 correspond to Case 22 discussed in Section

6.8.1. The y^+ values were examined to ensure that they were less than 100 for all walls. Table 5.6 shows the values of T_{max} and $(T_{max} - T_{i,a})$ for the three meshes. The percent difference for the value of $(T_{max} - T_{i,a})$ between the coarse and the medium grids and between the medium and the fine grids were 7.48% and 2.24%, respectively.

Table 5.6: Values of T_{max} and $(T_{max} - T_{i,a})$ for the three meshes used for CD2

Grid	T_{max}, °C	$(T_{max} - T_{i,a})$, °C
Coarse	59.64	38.44
Medium	62.75	41.55
Fine	61.84	40.64

Figures 5.14 to 5.20 show T_D on lines F1 to F7 respectively for CD2. Table 5.7 shows the maximum and root mean squared (RMS) percentage errors for T_D between the three successive meshes on lines F1 to F7. Because the overall pattern of flow is very similar between the medium and fine grids, and because the percentage RMS errors between the medium and fine grids were small, the medium mesh is considered adequate for CD2. Plots of the medium mesh for CD2 are presented in Appendix B.

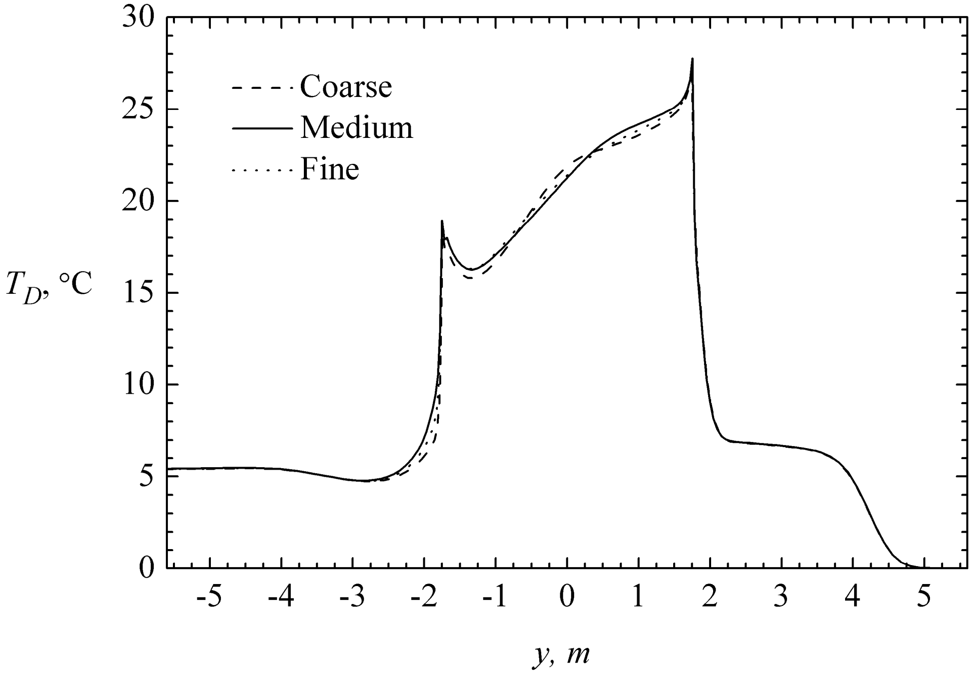

Figure 5.14: Relative temperature T_D on Line F1 for the coarse, medium, and fine grids for CD2

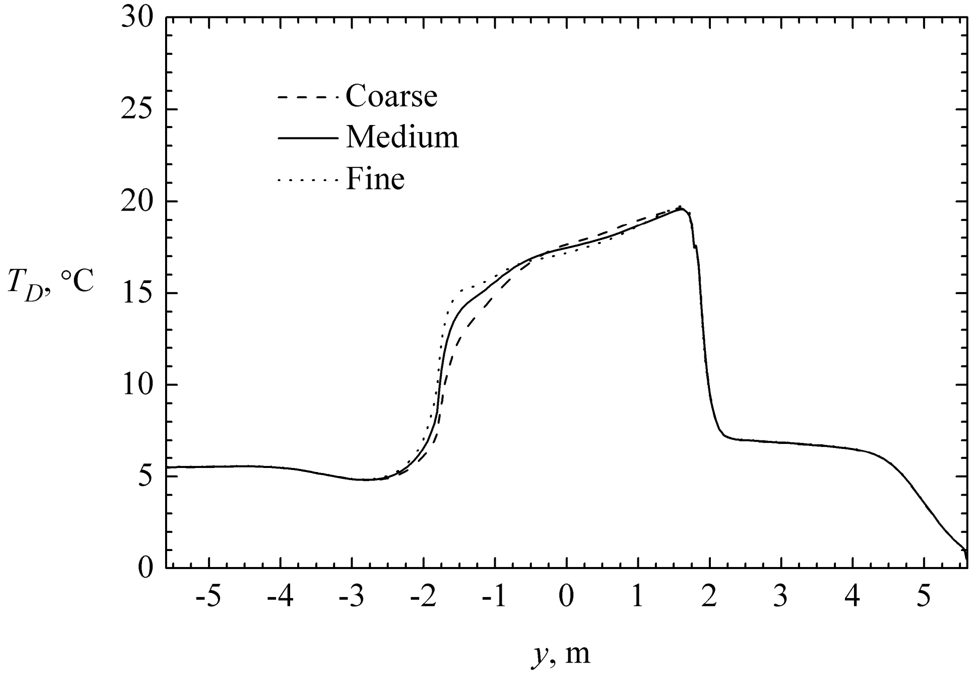

Figure 5.15: Relative temperature T_D on Line F2 for the coarse, medium, and fine grids for CD2

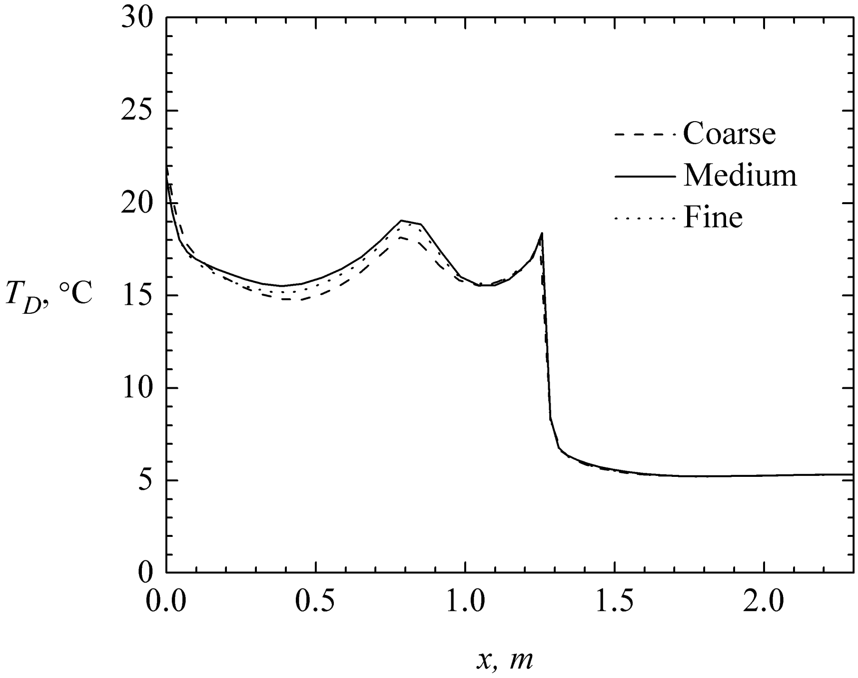

Figure 5.16: Relative temperature T_D on Line F3 for the coarse, medium, and fine grids for CD2

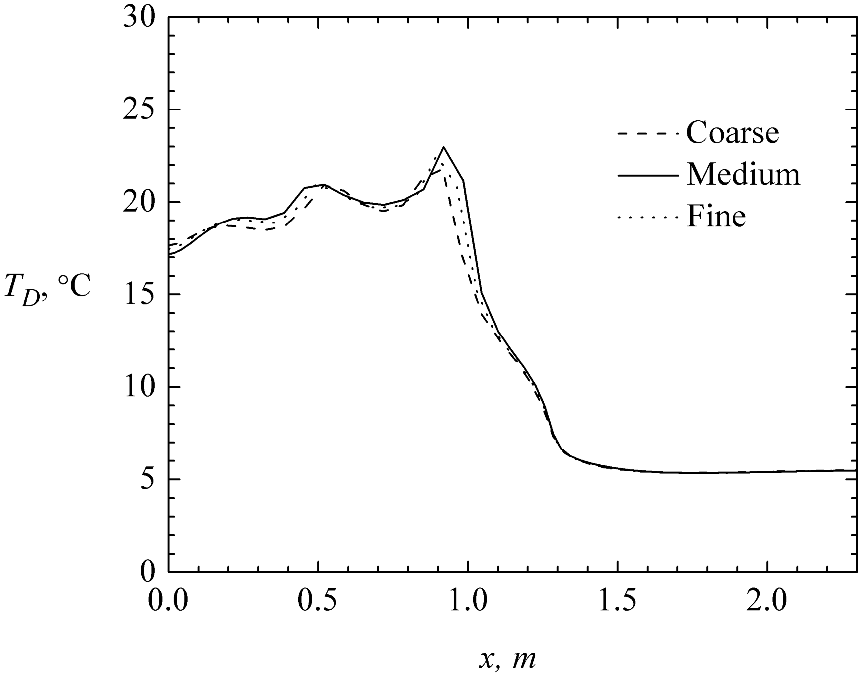

Figure 5.17: Relative temperature T_D on Line F4 for the coarse, medium, and fine grids for CD2

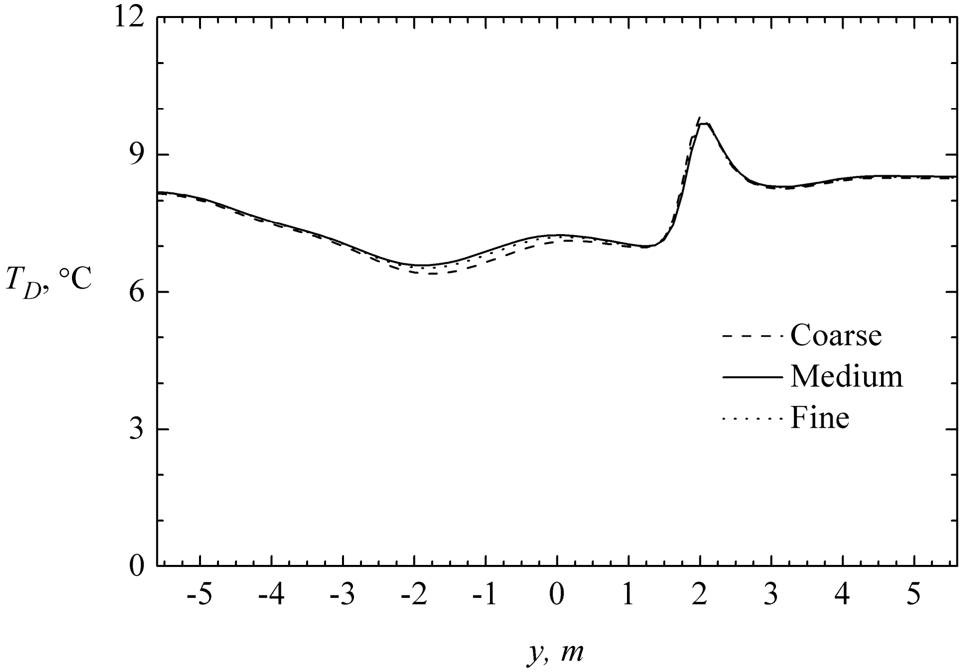

Figure 5.18: Relative temperature T_D on Line F5 for the coarse, medium, and fine grids for CD2

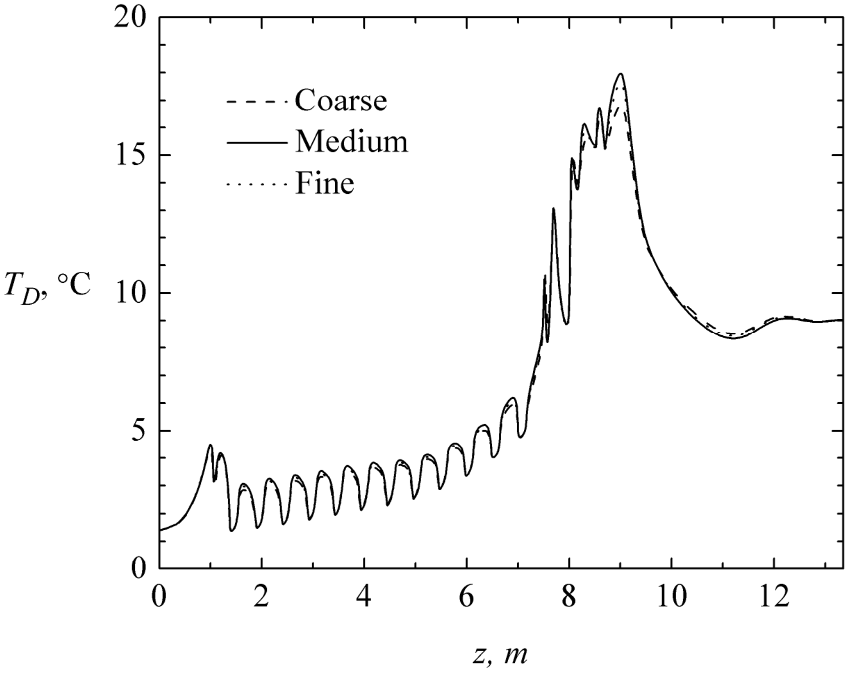

Figure 5.19: Relative temperature T_D on Line F6 for the coarse, medium, and fine grids for CD2

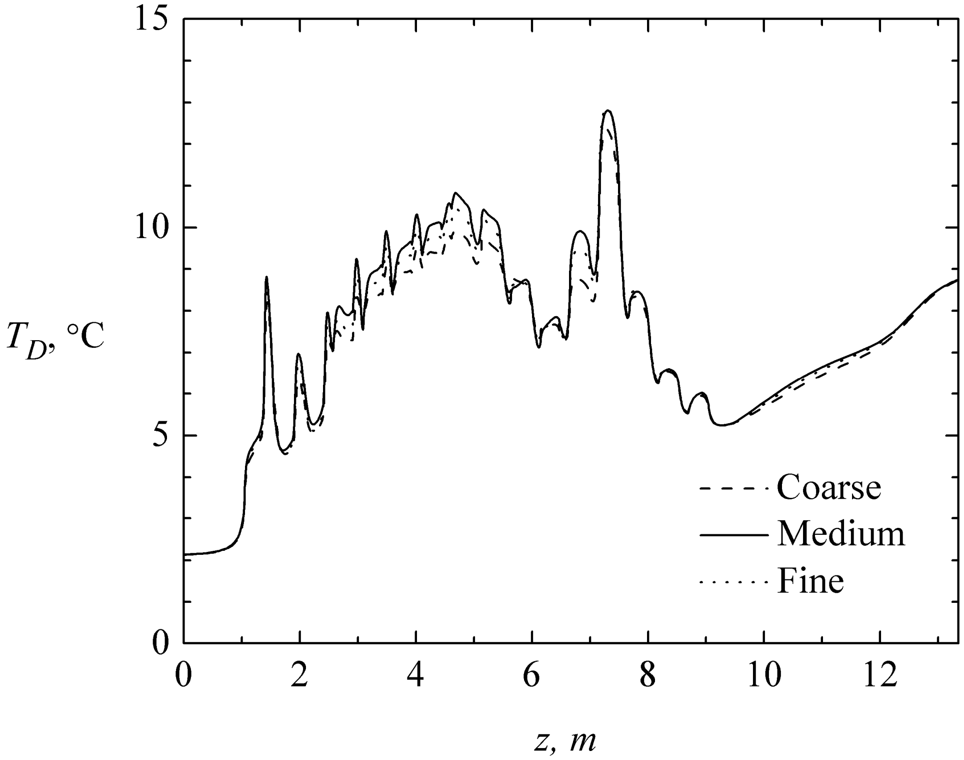

Figure 5.20: Relative temperature T_D on Line F7 for the coarse, medium, and fine grids for CD2

5.4 Effects of Inlet Turbulence Parameters

The effect on the results of varying the inlet turbulence parameters was examined. This effect was studied using CD1 with the medium grid and the same boundary conditions as in the mesh-independence test for CD1. First, the turbulence intensity at the inlet, I_i was varied from the default 0.05 to 0.025 and then to 0.1, while the viscosity ratio, R_i was held at the default of 10. Then, R_i was varied from the default 10 to 5 and then to 20 while the value of I_i was held constant at the default 0.05. This resulted in five different combinations of inlet turbulence parameters. For all cases investigated, the highest deviation in the maximum relative temperature ($T_{max} - T_{i,a}$) was less than 0.4%. It was therefore concluded that the inlet turbulence conditions do not have a large effect on the results. The default values of I_i = 0.05 and R_i = 10 were therefore used for all cases studied.

Table 5.7: Percentage deviations for T_D on F1 to F7 between successive grids for CD2

	Max. % error coarse-medium	RMS % error coarse-medium	Max. % error medium-fine	RMS % error medium-fine
F1	14.29	2.72	13.36	2.53
F2	16.55	4.05	12.72	3.29
F3	3.79	1.70	2.58	1.15
F4	11.61	2.04	3.36	1.26
F5	1.30	0.65	0.61	0.23
F6	9.81	2.18	3.61	1.30
F7	7.82	3.11	5.09	2.11

Chapter 6

RESULTS AND DISCUSSION

6.1 Introduction

In this chapter, detailed results are presented for the prediction of flow and heat transfer in Computational Domains 1 and 2 that were defined in Chapter 3. The effects of inlet and outlet opening geometry, inlet air mass flow rate, inlet air angle, and inlet and outlet opening orientation on the thermal performance for the air-side cooling of the thyristor valve hall geometry are discussed. For each computational domain, the particular dimensions and planes for plotting the results will be defined first. For CD1, a base case will be presented and discussed in detail, followed by the results of a parametric study.

6.2 Computational Domain 1

6.2.1 Parameters and Planes for Computational Domain 1

A total of 21 cases are presented for CD1. The particular parameters for each of these cases are summarized in Tables 6.1 to 6.3. For Cases 1 to 18 (Table 6.1), the inlet opening was located on the bottom wall of the domain and a uniform inlet angle was used for the entire opening. In these 18 cases, four parameters were varied: (1) the angle θ of the inlet flow, (2) the aspect ratio (L_2/L_3) of the inlet, (3) the area of the inlet ($L_2 \text{ x } L_3$) and (4) the mass flow rate $\dot{m}_i$ of the inlet. For Cases 19 and 20 (Table 6.2), the inlet opening was also located on the bottom wall of the domain; however this inlet opening was divided into two regions (1 and 2) each with approximately half the total inlet area. The inlet angle and the mass flow rate were different for each region. For Case 21 (Table 6.3), the inlet opening was located on the side wall of the domain.

Table 6.1: Summary of parameters used in Cases 1-18 (CD1)

Case	L_1 (m)	L_2 (m)	L_3 (m)	θ (deg)	$\dot{m}_i$ (kg/s)
1	2.67	0.48	0.545	60	0.684
2				75	
3				80	
4				82.5	
5				90	
6				60	1.368
7				70	
8				75	
9				80	
10				90	
11	2.67	0.48	0.2725	75	0.684
12	2.43	0.97	0.27	80	0.684
13	2.42	1.02	0.2		
14	2.42	1.02	0.14		
15	2.86	0.14	1.02		
16	2.67	0.235	0.545	75	0.684
17				80	
18				81	

Table 6.2: Summary of parameters used in Cases 19-20 (CD1)

Case	L_1 (m)	L_2 (m)	L_3 (m)	θ_{r1} (deg)	θ_{r2} (deg)	$\dot{m}_{i,r1}$ (kg/s)	$\dot{m}_{i,r2}$ (kg/s)
19	2.67	0.48	0.545	81	60	0.513	0.171
20	2.67	0.48	0.545	81	60	0.547	0.137

In addition to symmetry planes S1 and S3, four additional planes (P1 to P4) were selected for plotting purposes with CD1. The location of these planes is described graphically in Figure 6.1 and summarized in Table 6.4.

Table 6.3: Summary of parameters used in Case 21 (CD1)

Case	L_4 (m)	L_5 (m)	L_6 (m)	θ (deg)	$\dot{m}_i$ (kg/s)
21	1.38	8.3	0.069	90	0.684

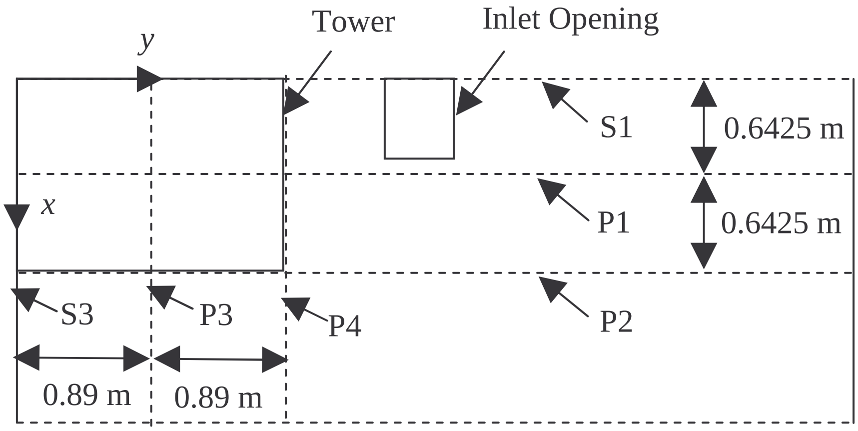

Figure 6.1: Locations of P1 to P4 for CD1

Table 6.4: Definition of planes used to describe CD1

Plane	x (m)	y (m)	z (m)
P1	0.6425	0 - 5.59	0 - 13.35
P2	1.285	0 - 5.59	0 - 13.35
P3	0 - 2.3	0.89	0 - 13.35
P4	0 - 2.3	1.78	0 - 13.35

6.3 Computational Domain 1 Base Case Results

The purpose of Case 1 is to examine a case with parameters as close as possible to the current conditions in VG41 under the constraints discussed in Section 3.1. This case allows examination of the predicted phenomena in the existing valve hall. It also serves as a datum for studying the effects of changing the geometry and flow parameters. In this base case, the size of the inlet openings, the inlet air angle, and the inlet mass flow rate were all the same as typically measured values in VG41. With the inlet parameters summarized in Table 6.1, the inlet velocity component in the z direction, w, is 2.179 m/s and the spanwise inlet velocity component, v, is -1.258 m/s. The resultant jet velocity V_j based on the transformed inlet length L_3' (as discussed in Section 3.6) is 2.516 m/s. A plan view of the computational domain is shown in Figure 6.2 with inlet and outlet openings marked.

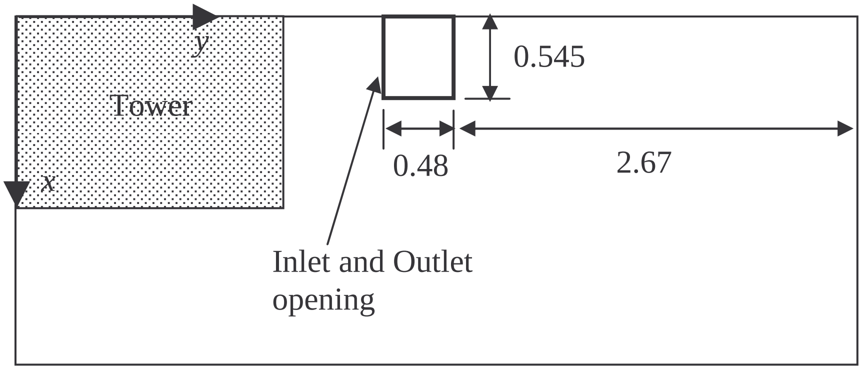

Figure 6.2: Plan view of computational domain showing locations of inlet and outlet openings for Case 1 (dimensions in meters)

Three-dimensional streamline plots are used to show the overall flow structure for Case 1. In steady-state flow, a streamline is the path that a particle of zero mass would take through a fluid domain driven by a vector field. Streamlines start at a given node and can be directed both forward and backward along the path tangent to the velocity field. Three-dimensional streamline plots are generated by seeding a number of massless particles on a given plane and creating a unique streamline for each of these particles. The number of particles seeded on a given plane, and thus the total number of streamlines in the plot, can be controlled by using a reduction factor in the computational code. If this reduction factor is increased, more nodal points are skipped and the number of streamlines decreases.

Figure 6.3a and 6.3b show a three-dimensional velocity streamline plot for Case 1 plotted over the entire domain from two views. In this plot, particles are seeded at the inlet opening and lines are created following the path of these particles through the domain to the outlet. Particles seeded on the half of the inlet opening closest to the tower in the *y* direction were seeded in blue, and particles seeded on the half of the inlet opening farthest from the tower in the *y* direction were seeded in red. This enables the path of flow originating from either half of the inlet opening to be differentiated.

A number of distinguishable flow features can be observed in Figure 6.3:

1. Many of the streamlines beginning from the half of the inlet opening closest to the tower (blue streamlines), actually pass under the tower. This flow changes direction as it reaches the boundaries of S3 and the floor. Eventually all of these streamlines flow around the domain where they either pass through the gaps in the tower entering on plane P2 or plane P4 or they are re-entrained by the jet. Figure 6.4 shows a streamline plot where only two streamlines are seeded on the half of the inlet opening closest to the tower. Streamline A passes directly through Gap 1 in the tower, while Streamline B passes under the tower, is re-entrained by the jet and passes under the tower again before it finally flows around the domain and is re-entrained by the jet.

2. Most of the streamlines beginning from the inlet pass eventually through the blocks of the tower. This flow will be discussed in later in detail as it is of the most importance.

3. Some of the flow (less than 3% of the inlet mass flow rate) issuing from the inlet opening passes along the entire vertical surface of the towers near P4 and exits the domain without actually passing through any of the blocks. This can be seen in Figure 6.3b.

4. The flow structure above the towers is complicated with all of the air eventually escaping through the outlet.

Figures 6.5a and 6.5b show close up views of a streamline plot created by seeding the opening of the first three gaps at P4 with particles of zero mass and following their paths both backwards and forwards in the velocity fields. The seeding plane used is shown in semi-transparent red. The flow entering the gap on plane P4 either originates directly from the inlet opening or enters the gap after passing under the tiers as discussed earlier. All of the flow passing through P4 is directed into the gaps. Because the flow cannot pass through the symmetry planes, it must exit through the other side of the gap on P2 as shown in Figure 6.5. Most of the streamlines descend after exiting Gap 1. This downward flow occurs because the flow exiting Gap 1 has a lower temperature than the surrounding air. The flow exiting Gaps 2 and 3 rises due to the fact that it is at a higher temperature than the surrounding air. The streamlines exiting Gap 3 rise in a more pronounced fashion due to the warmer relative temperature of the flow.

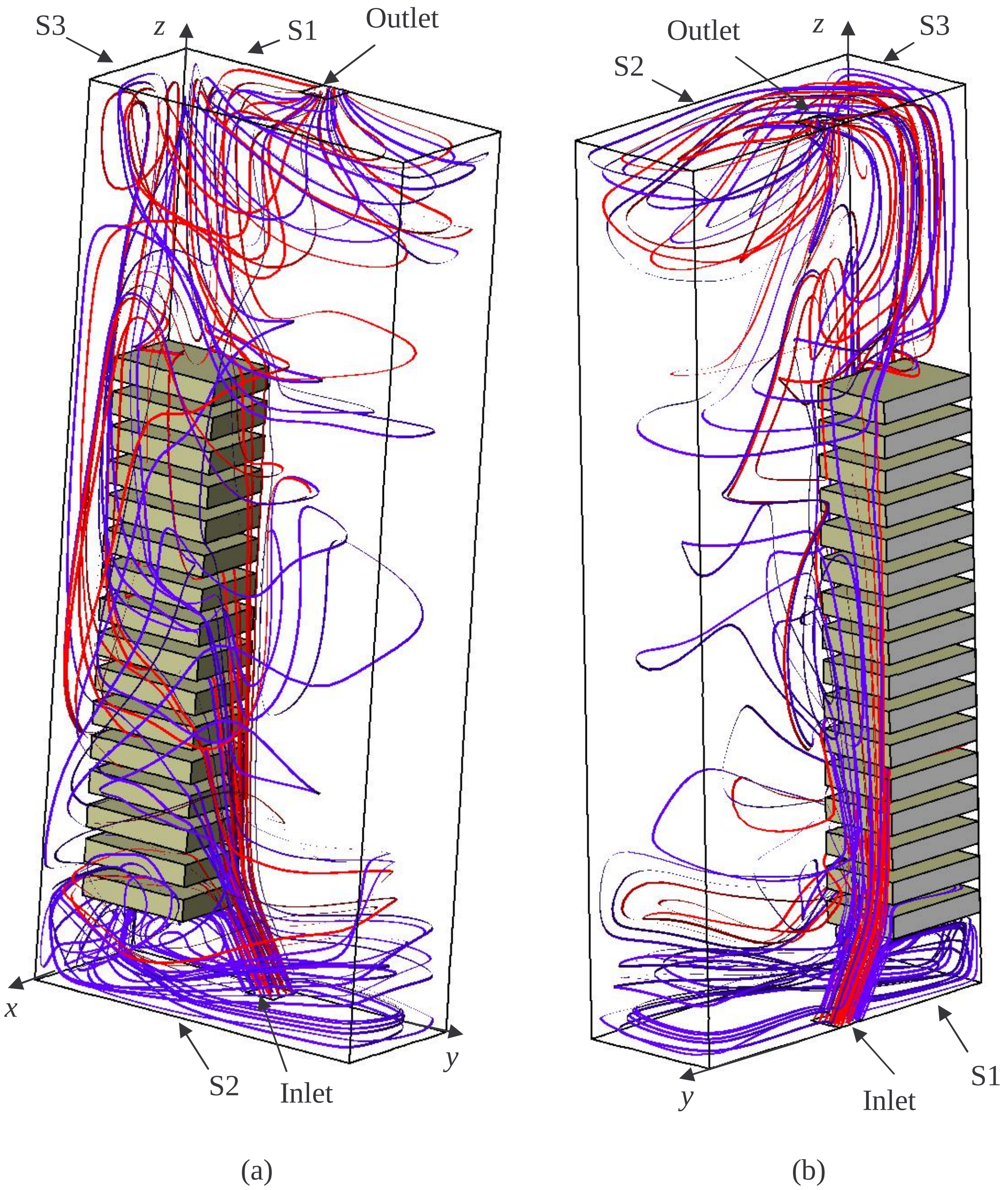

Figure 6.3: Three-dimensional streamline plots showing overall flow structure for Case 1 (a) View 1 (b) View 2

Figure 6.6 shows a close up view of a streamline plot created by seeding the opening of Gap 3 at P2. The seeding plane used is shown in semi-transparent red. This plot shows the streamlines that entered the gap on P4 now exiting through P2. In addition, Figure

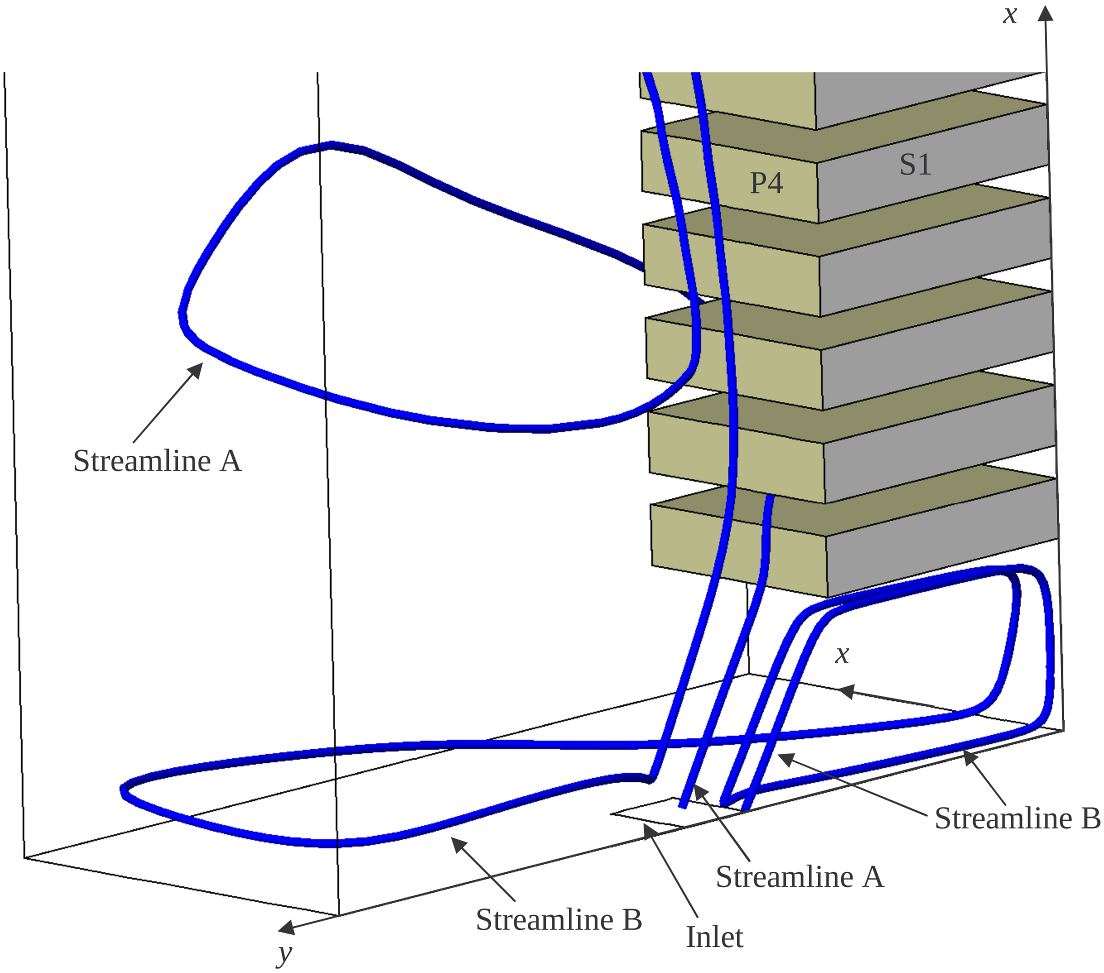

Figure 6.4: Two streamlines seeded at the inlet opening

6.6 shows flow that has passed under the tower entering the gap on P2. This flow also exits the gap through the same plane. The flow pattern described for Gaps 1 to 3 continues for all gaps until Gap 9.

Figure 6.7 shows the streamlines created from particles seeded on the edge of Gap 14 at P4. The seeding plane used is shown in semi-transparent red. In this plot, all of the streamlines that were seeded on P4 enter the gap slightly and then exit the gap on the

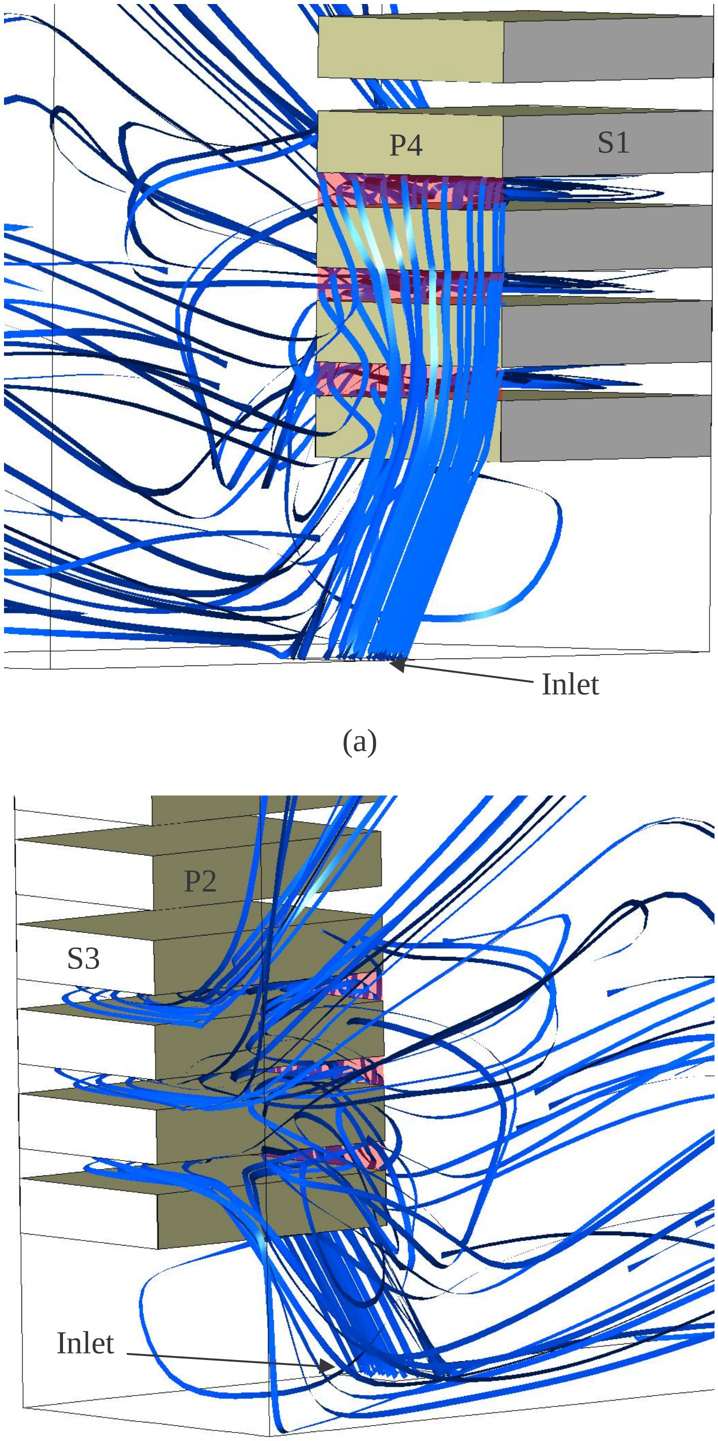

(a)

(b)

Figure 6.5: Streamline plot showing flow passing through seeding plane at P4 on Gaps 1 to 3 (a) View 1 (b) View 2 (seeding plane shown in red)

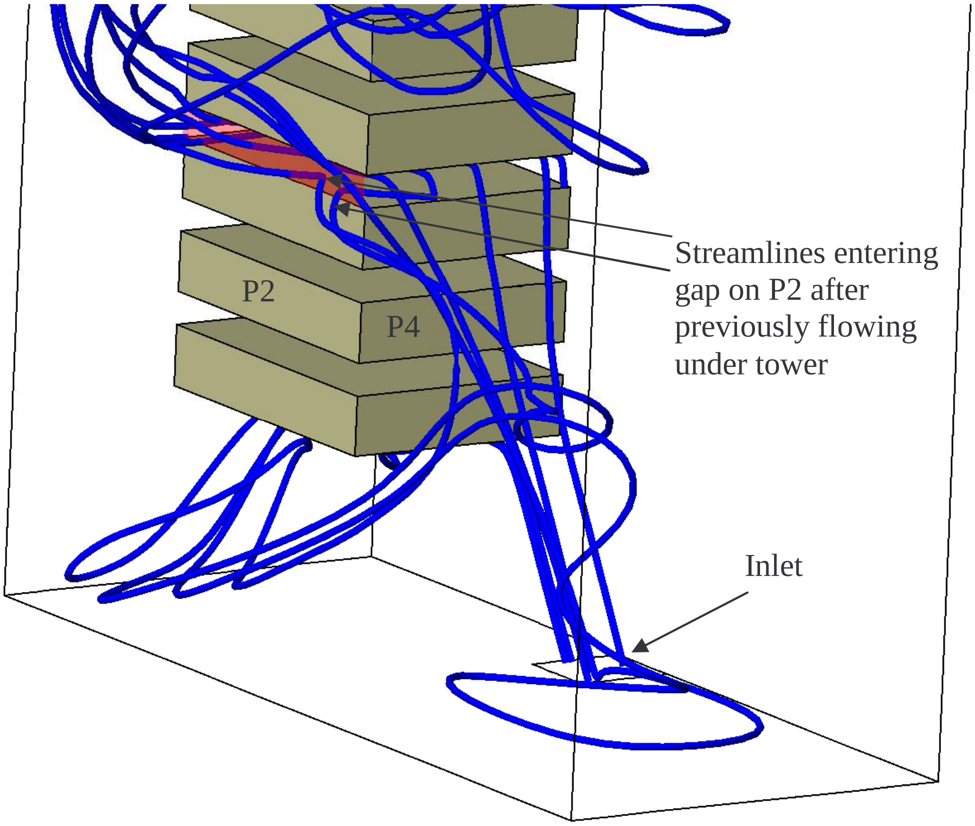

Figure 6.6: Streamline plot showing flow passing through seeding plane at P2 on Gap 3 (seeding plane shown in red)

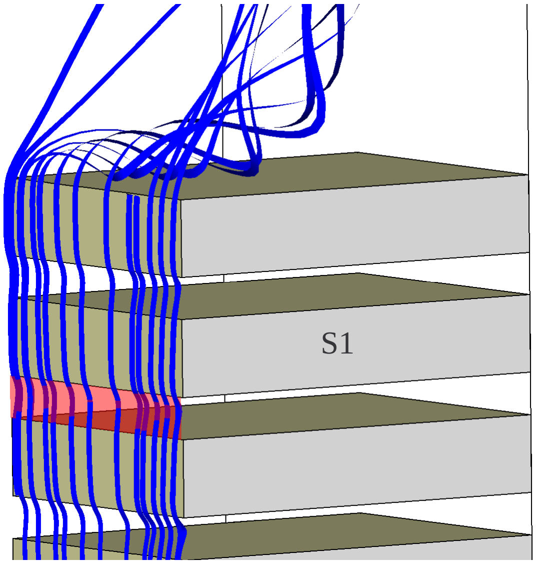

Figure 6.7: Streamline plot showing flow passing through seeding plane at P4 on Gap 14 (seeding plane shown in red)

same plane. Figure 6.8 shows the streamlines created from particles seeded on the edge of Gap 14 at P2. The seeding plane used is shown in semi-transparent red. Similarly with Figure 6.7, all of the streamlines that were seeded on P2 enter the gap slightly, and then exit through the same plane. The same flow pattern that exists in Gap 14 also applies to Gaps 11 to 15. If a very small reduction factor is used when viewing the streamlines, it is sometimes possible to see flow entering the gap on on either P2 or P4 near the junction of the two planes and exiting through the other plane also near the junction. Any net mass flow rate through Gaps 11 to 15 is caused by this phenomenon.

Figure 6.9 shows the streamlines created from particles seeded on the edge of Gap 10 at P4. From Figure 6.9, one can see that all of the flow passing through the seeding plane is directed into the gap. Similarly with Gaps 1-9, this flow exits through the other side of

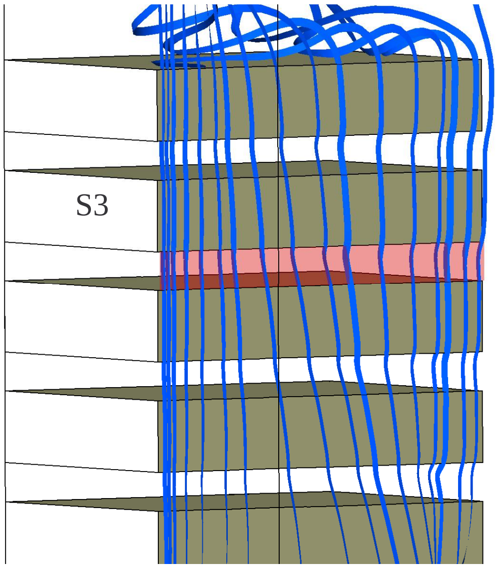

Figure 6.8: Streamline plot showing flow passing through seeding plane at P2 on Gap 14 (seeding plane shown in red)

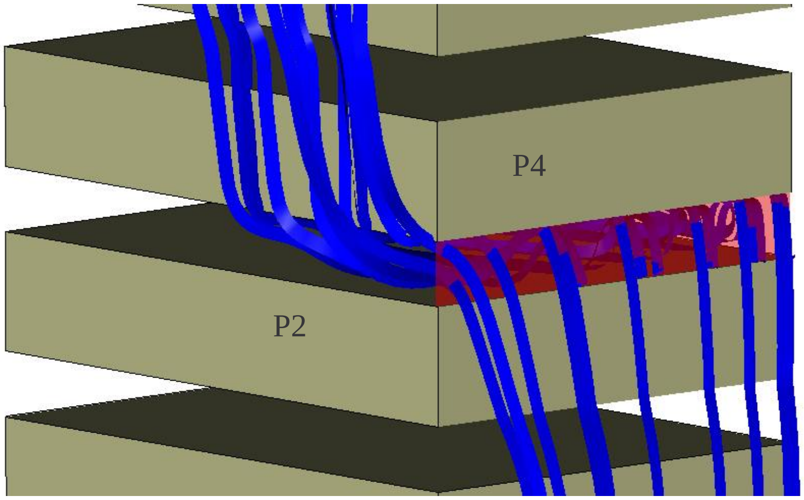

Figure 6.9: Streamline plot showing flow passing through seeding plane at P4 on Gap 10 (seeding plane shown in red)

the gap on plane P2. Figure 6.10 shows the streamlines created from particles seeded on the edge of Gap 10 at plane P2. This plot shows the streamlines that entered the gap on plane P4 now exiting through P2. In addition, Figure 6.10 shows flow that has already exited lower gaps on the same plane now entering this gap. This flow penetrates into the gap and then exits through the same entering plane (as was the case in Gaps 11 to 15). The flow structure in Gap 10 appears to have features similar to those seen in both Gaps 1 to 9 and Gaps 11 to 15.

Figure 6.11a shows *v*-velocity contours for Gap 3 on plane P4. A negative velocity indicates flow into the gaps. This plot shows that almost all of the flow is directed into the gap on this plane, with the highest normal velocities occurring near S1. There is also a region near the opposite edge of the gap with a higher normal velocity than in the

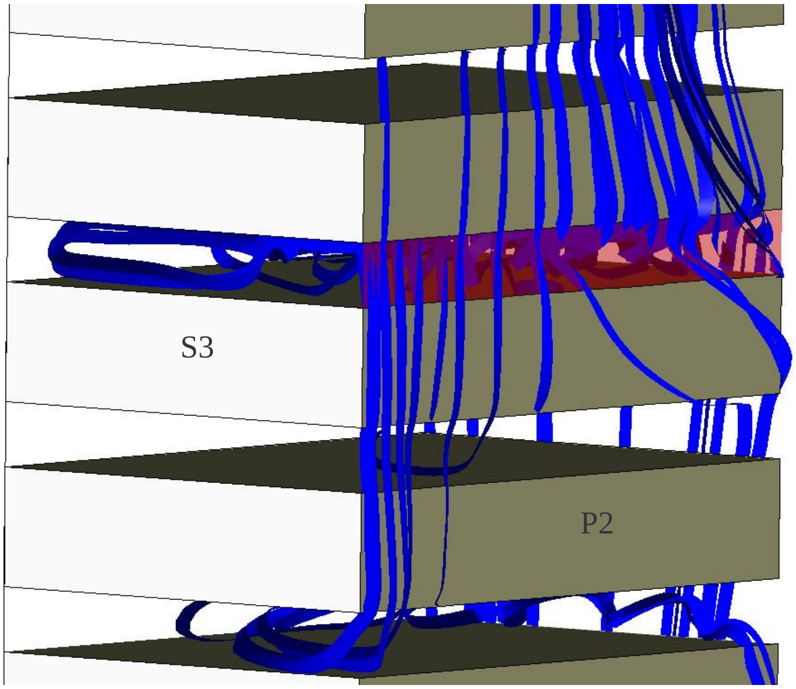

Figure 6.10: Streamline plot showing flow passing through seeding plane at P2 on Gap 10 (seeding plane shown in red)

surrounding area. This local minimum represents flow that has passed under the tower or exited from of the lower gaps on plane P2, swirled horizontally around the domain and then passes though the gap on plane P4 as discussed earlier. A similar flow pattern exists on P4 for all of Gaps 1 to 9 with the magnitude of the velocities on the plane decreasing with increasing gap number. Figure 6.11b shows *u*-velocity contours for Gap 3 on plane P2. A negative velocity indicates flow into the gap. The majority of the flow on this plane is directed out of the gap with the highest velocities occurring near S3. On the opposite side of the plane there is a region where the flow is directed into the plane. As shown in Figure 6.6, this represents flow that has passed under the tower or exited from one of the lower gaps on P2, and now passes though Gap 3 on P2. Above this latter region there is a region where a relatively high velocity is directed out of the gap. This

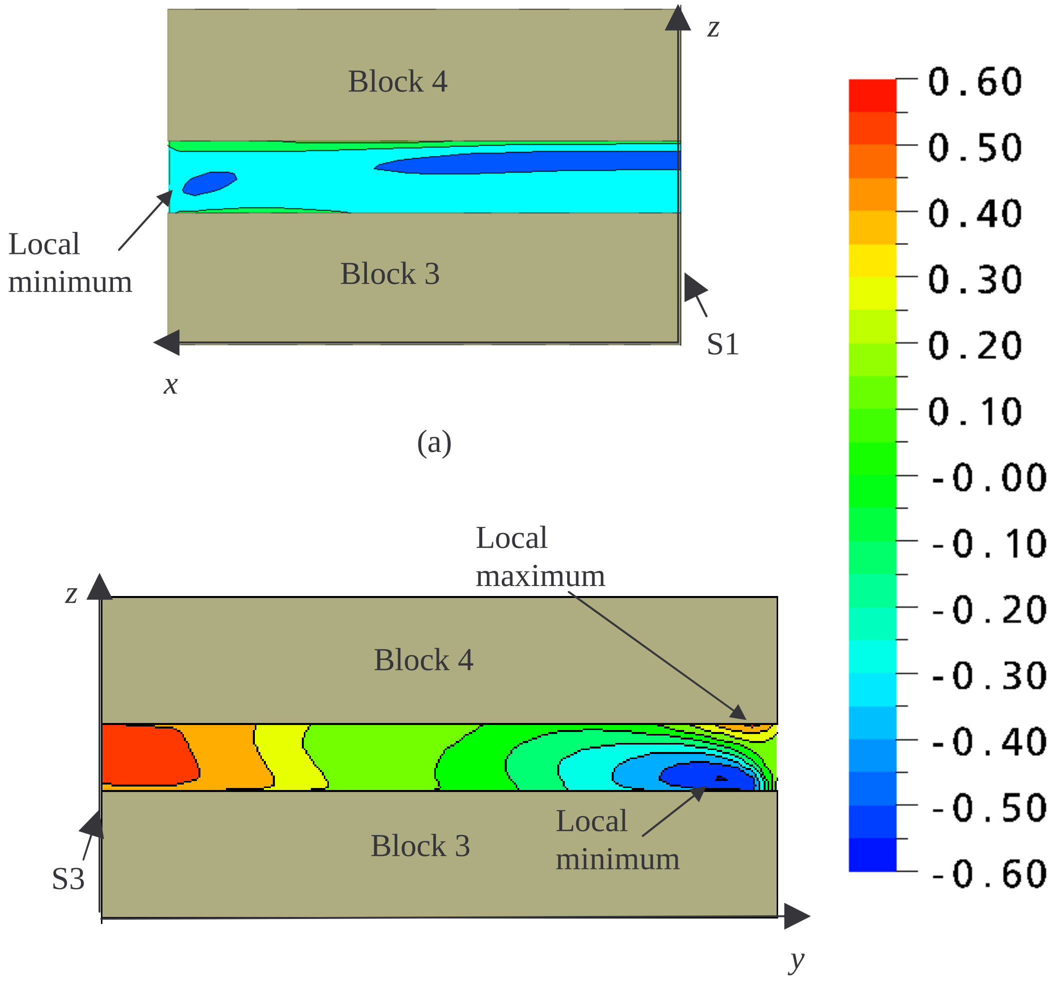

(a)

(b)

Figure 6.11: Normal velocity components at entrance planes for Gap 3 (a) *v*-velocity on P4 (b) *u*-velocity on P2 (velocities in m/s)

small region represents the flow that entered Gap 3 on P4 after passing below the towers and is now exiting the gap. A similar flow pattern exists on P2 for all of Gaps 1 to 9 with the magnitude of the velocities on the plane decreasing with increasing gap number.

Figure 6.12a shows *v*-velocity contours for Gap 14 on plane P4. Figure 6.12b shows *u*-velocity contours for Gap 14 on plane P2. A negative velocity indicates flow into the gaps. The trend observed on both planes is that flow enters the gap near the bottom of the

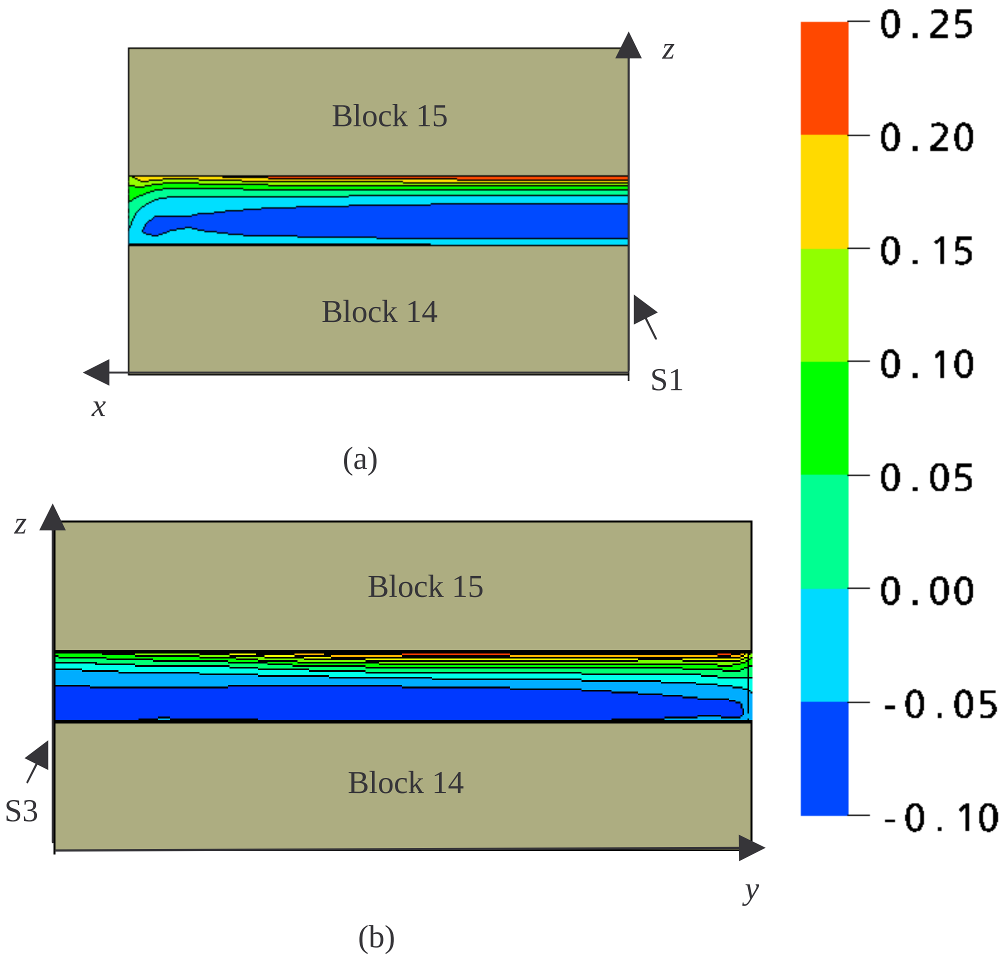

Figure 6.12: Normal velocity components at entrance planes for Gap 14 (a) *v*-velocity on P4 (b) *u*-velocity on P2 (velocities in m/s)

plane and flow exits the gap near the top of the plane. This is in agreement with what was observed regarding the velocity streamlines for the same gap (Figures 6.7 and 6.8). The same trend was observed in all of Gaps 11-15.

Figure 6.13a shows *v*-velocity contours for Gap 10 on plane P4. Again, a negative velocity indicates flow into the gaps. Air is flowing into the gap over most of the area. There is a small area where the flow exits the gap on this plane, but the magnitude of the velocity in that region is very small. Figure 6.13b shows *u*-velocity contours for Gap 10 on plane P2. There is an area on this plane near S3 where the flow is directed almost completely into the gaps. Half way along the gap in the *y* direction, the flow enters near the bottom of the gap and exits near the top of the gap. At the right edge of the gap, particularly near the top edge, the flow is predominantly exiting the gap. This is in agreement with what was observed regarding the velocity streamlines for the same gap (Figures 6.9 and 6.10).

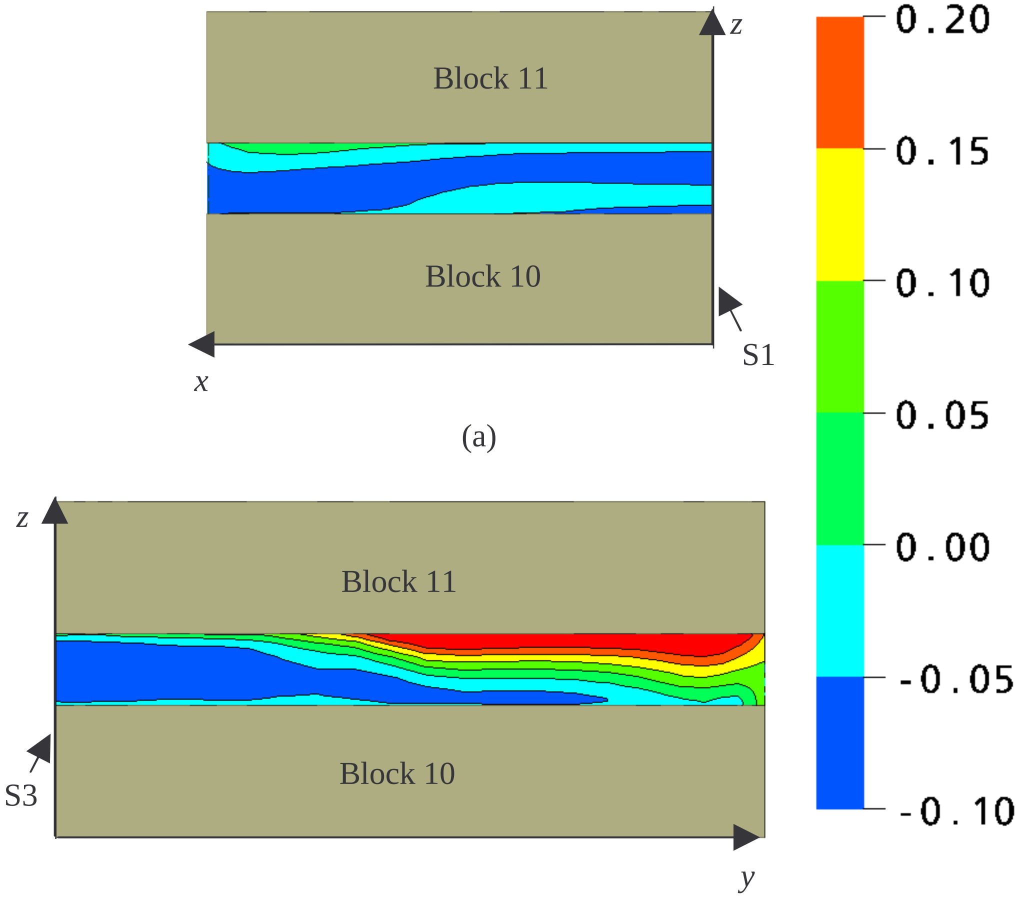

(a)

(b)

Figure 6.13: Normal velocity components at entrance planes for Gap 10 (a) *v*-velocity on P4 (b) *u*-velocity on P2 (velocities in m/s)

Figure 6.14 shows temperature contours on both P4 and P2 for Gap 3. The plot on P4 shows that almost all of the air on this plane is below 25°C. This is not surprising as the majority of the flow entering on this plane is coming directly from the inlet opening at 21.2°C. Approximately half of the fluid on P2 is below 25°C while most of the other half being between 25°C and 30°C. The temperatures on this plane increase as S3 is approached. This is due to the fact that flow exiting the plane near S3 has a longer length to travel between the blocks and thus undergoes more heating. The same trend was observed in Gaps 1 to 9 with the temperatures gradually increasing with increasing gap numbers.

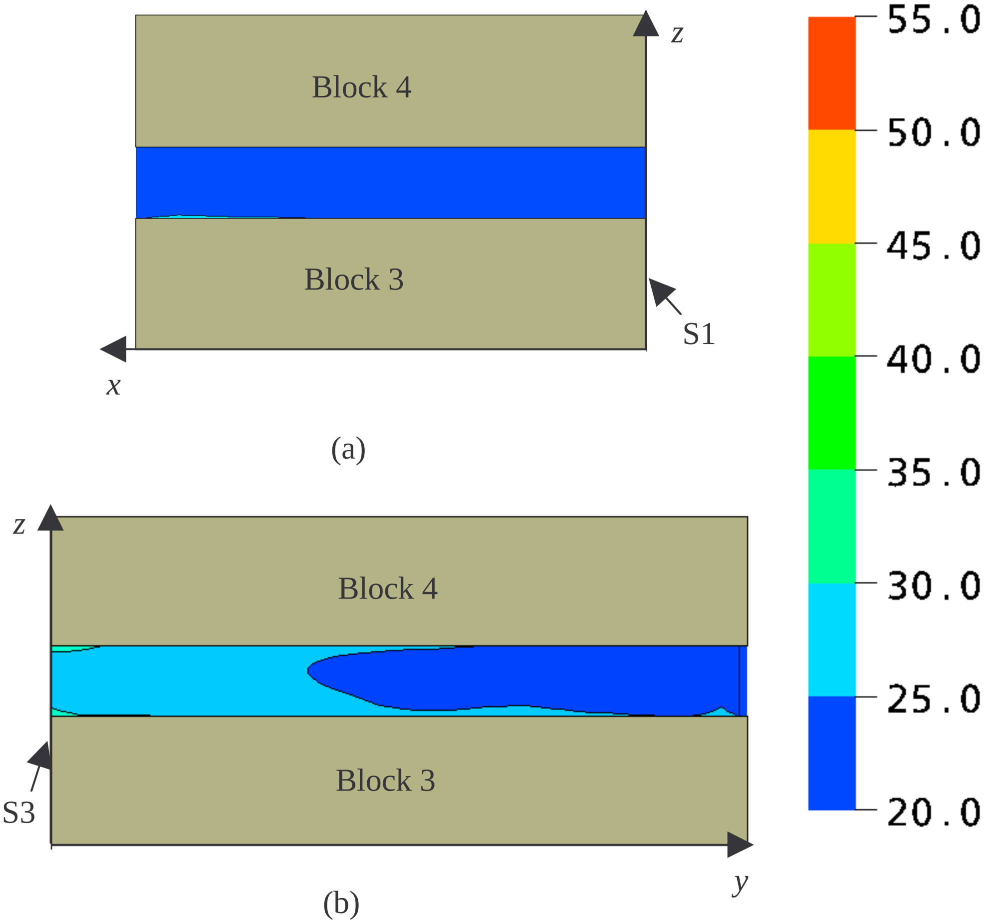

Figure 6.14: Temperature contours at entrance planes for Gap 3 (a) plane P4 (b) plane P2 (Temperatures in °C)

Figure 6.15 shows temperature contours on both P4 and P2 for Gap 14. These plots show that the temperature of the fluid in this gap is higher than for the lower gaps. In addition, the higher temperature at the top of the gap is consistent with flow entering a gap, being heated, and exiting the gap on the same plane, as seen in Figures 6.7 and 6.8. The temperature pattern on both entrance planes was very similar for Gaps 11-15.

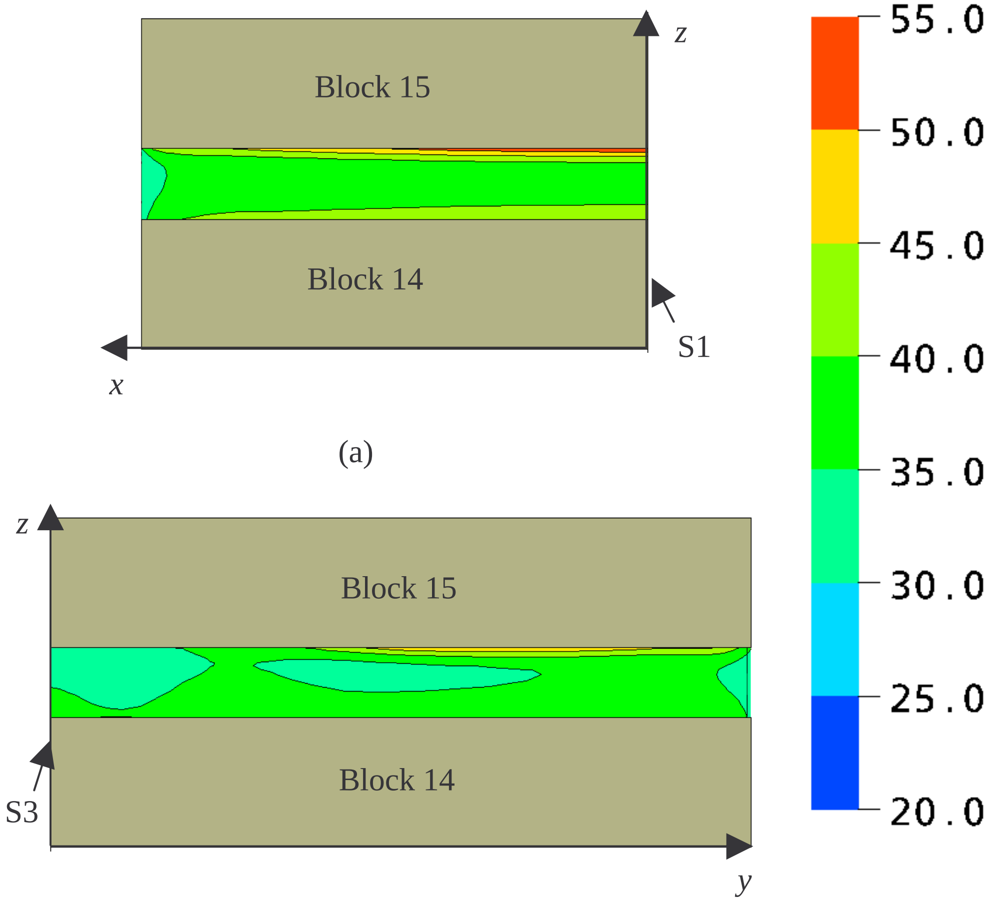

(a)

(b)

Figure 6.15: Temperature contours at entrance planes for Gap 14 (a) plane P4 (b) plane P2 (Temperatures in °C)

Figure 6.16 shows temperature contours on both P4 and P2 for Gap 10. The temperatures are relatively low for the plot on P4 because the majority of the flow on this plane is coming directly from the inlet. On P2, there are regions of low temperature due to flow entering the gap slightly and then exiting the gap on the same plane without a great deal of heating. The highest temperatures on this plane are near the top of the gap. This region of higher temperature is caused by air exiting the gap that had entered and penetrated the gap on either P2 or P4. This air followed a very complex path in order to exit the gap and thus is heated more than the surrounding air.

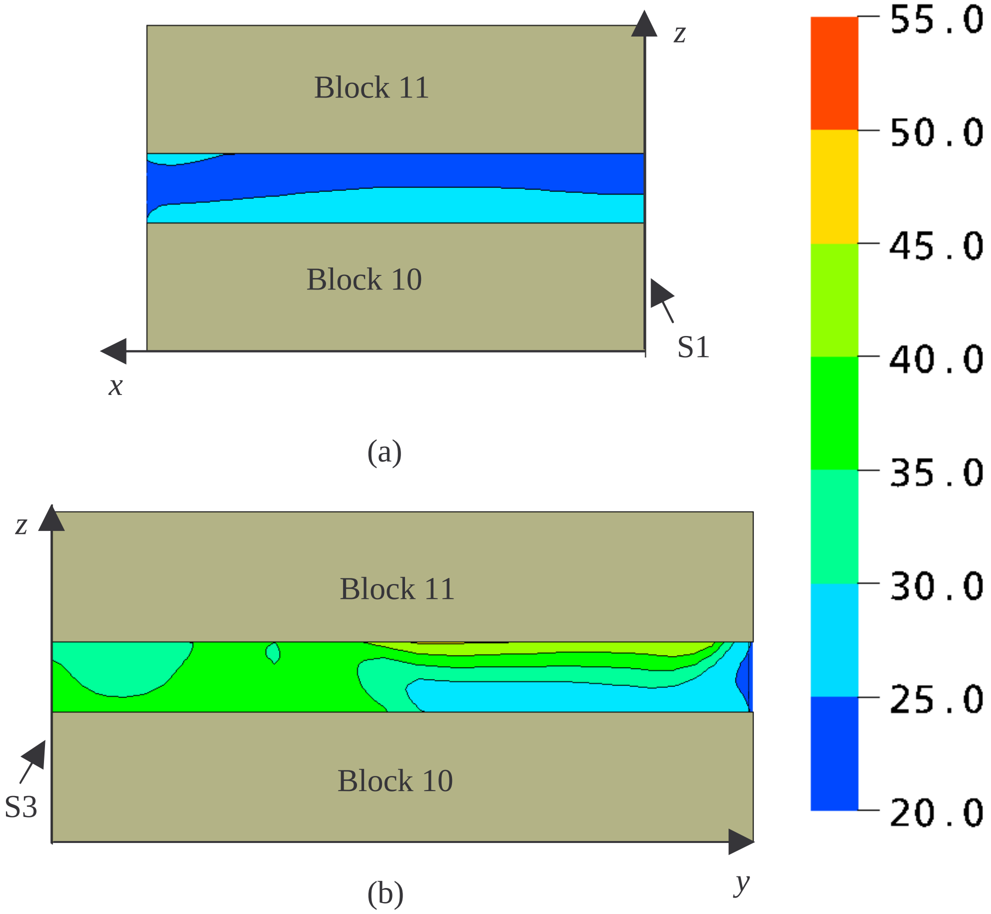

(a)

(b)

Figure 6.16: Temperature contours at entrance planes for Gap 10 (a) plane P4 (b) plane P2 (Temperatures in °C)

Figure 6.17 shows full-domain temperature contours on S1, S3, P1, P2, P3, and P4. These plots show that the temperature of the air away from the towers does not vary by a large amount. The temperature difference between the air entering the domain and the air exiting the domain is only 7.9°C. The temperature of the air away from the towers increases gradually between the inlet and the outlet, this temperature difference is by stratification due to buoyancy. As discussed earlier, the temperature of the air directly above the towers is higher than that of the surrounding air. This is air that has been heated by the tower and is rising due to its relatively higher temperature.

The contours on P2 and P4 include the vertical surface temperatures of the blocks. It is observed that the temperature of the vertical surfaces of the blocks increases with height. The temperature of the vertical surfaces of the blocks on P4 is also lower than the temperature of the vertical surfaces of the blocks on P2. This is due to the fact that the inlet air is coming into direct contact with the vertical surfaces of the tower on P4, as shown in Figure 6.3.

Figure 6.18, shows three-dimensional iso-volume plots of temperature from two views. In these plots, control volumes in the domain with a temperature of 50°C or above are colored according to the temperature scale on the right side of the plots. Temperatures below 50°C are not colored. As there were no temperatures above 50°C anywhere in the domain except in the gaps, only the tower is shown in these plots. No temperature in Gaps 1 to 9 exceeded 50°C. In Gap 10, temperatures above 50°C were observed only in a small area within the gap. The temperatures in Gaps 11 to15 exceeded 50°C for almost the entire area within the gaps with the highest temperatures occurring near the corner at the junction of the two symmetry planes. From Figure 6.17 and 6.18 it is also evident

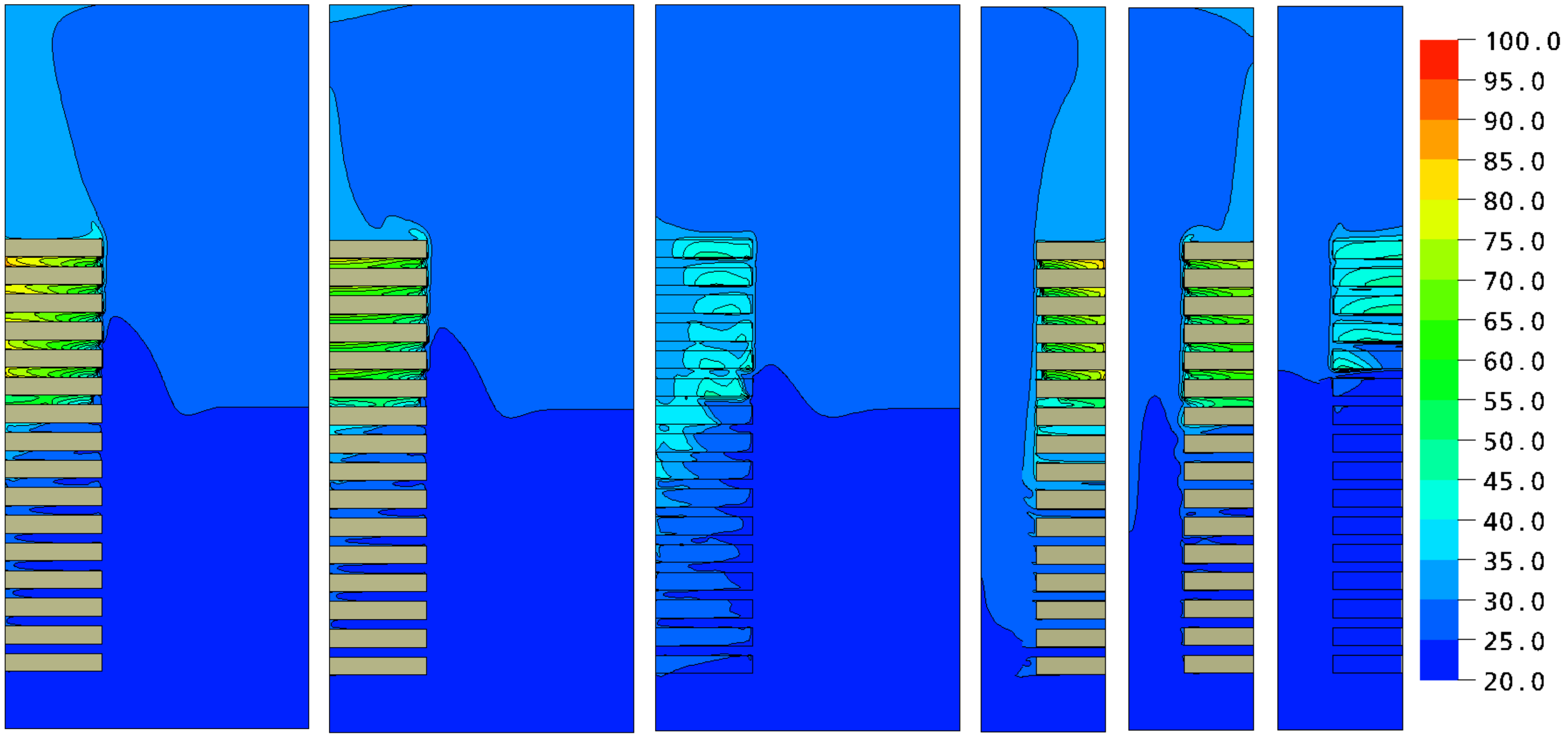

(S1) (P1) (P2) (S3) (P3) (P4)

Figure 6.17: Temperature contours for Case 1 on indicated planes (Temperatures in °C)

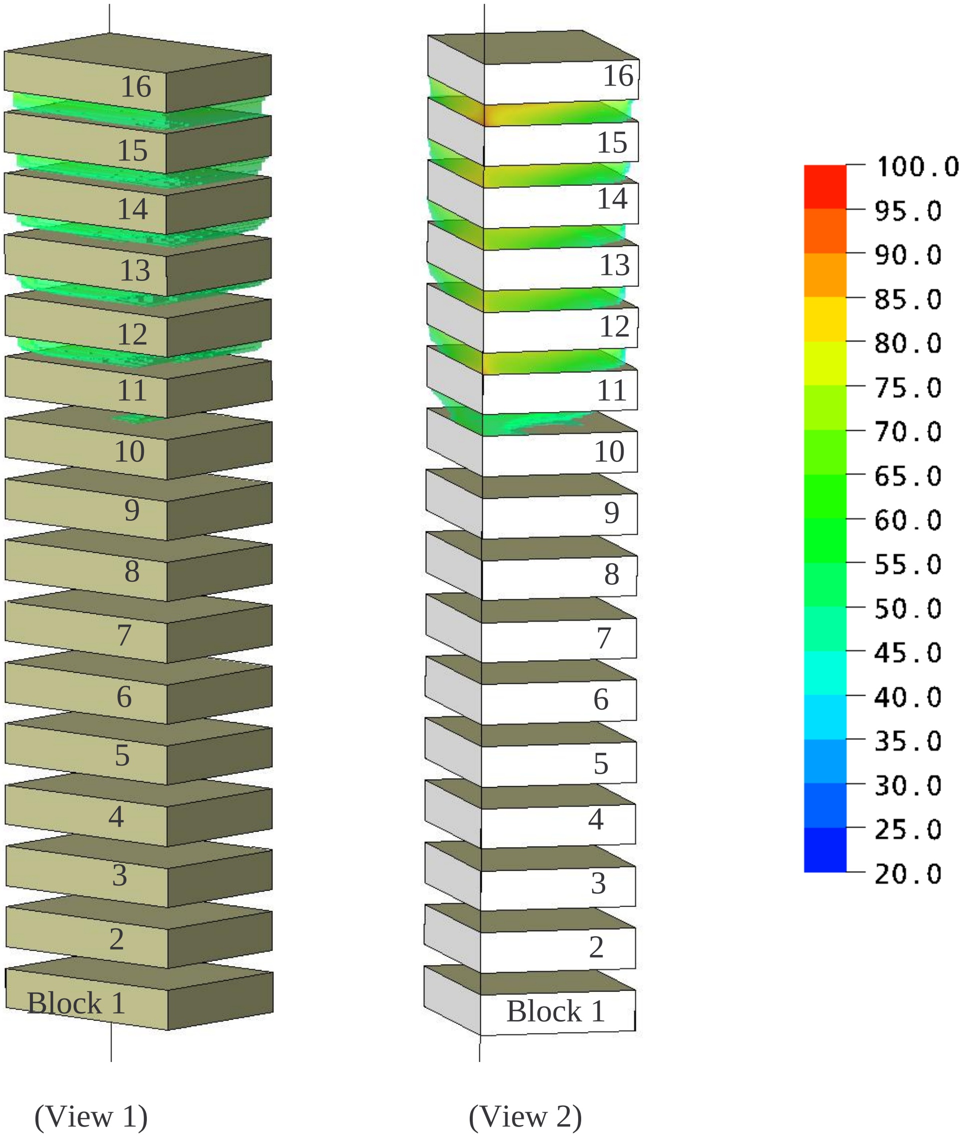

Figure 6.18: Iso-volume plot of all domain temperatures exceeding 50ºC for Case 1

that the highest temperatures in the domain appear to be located within Gap 15. The maximum temperature in the domain for Case 1 occurred on the lower horizontal surface of Gap 15 at the junctions of symmetry planes S1 and S3 and had a value of 95.37°C.

Figure 6.19 shows the temperature distribution on the lower horizontal surface of Gap 15. In other words, the top (and sides) of Block 14. It is evident that the temperature on the horizontal surface of the block increases as the *x*-*y* origin is approached. The same trend also occurred on all the horizontal block surfaces in Gaps 11 to 15. There are two explanations for this pattern. First, the *x*-*y* origin is the furthest point between the blocks from the gap opening and thus it is the least accessible to cooling air. The second explanation is that the *x*-*y* origin is at the junction of symmetry planes S1 and S3 with a stagnation point occurring because flow cannot pass through either of these planes.

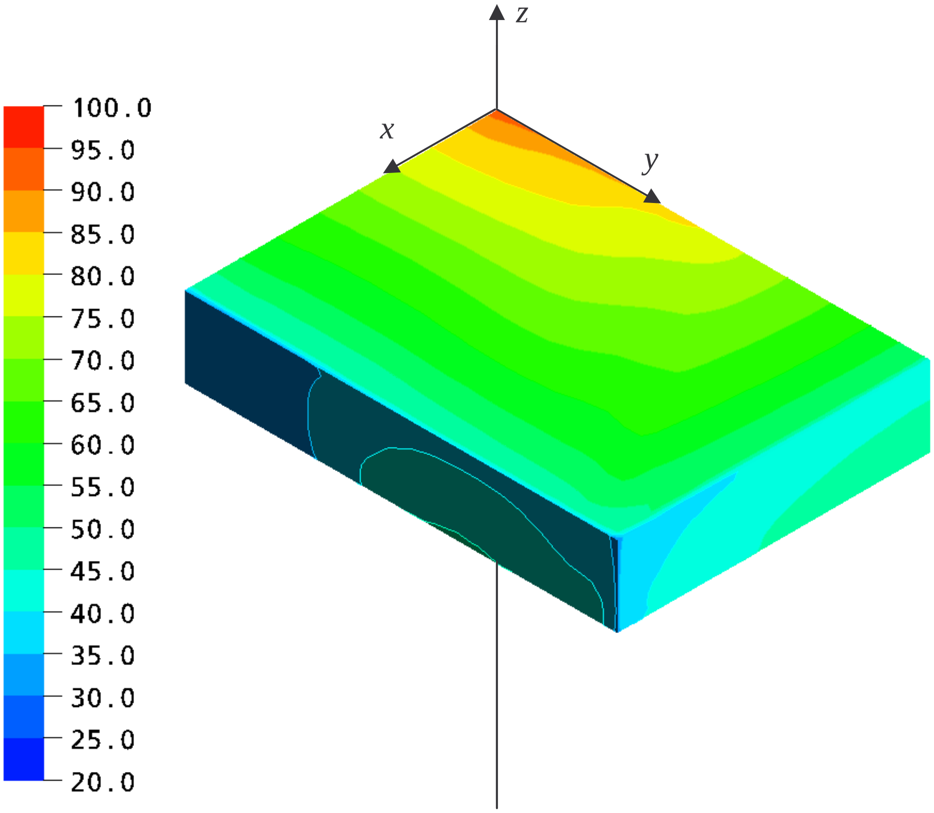

Figure 6.19: Temperature distribution on the lower horizontal surface of Gap 15 (Temperatures in °C)

Figure 6.20 shows the temperature distribution on the lower horizontal surface of Gap 9. The temperature of the block surface is highest near the *x* axis. The maximum temperature on this surface occurs at the intersection of planes S3 and P2. This distribution results because the majority of the air in this gap enters through P4 and exits through P2. Thus, the air that reaches the intersection of planes S3 and P2 is the air that has traveled the furthest distance from P4 and thus has absorbed more energy. This pattern of temperature distribution occurred on all the horizontal surfaces of the blocks in Gaps 1 to 9, with temperatures gradually increasing with gap number.

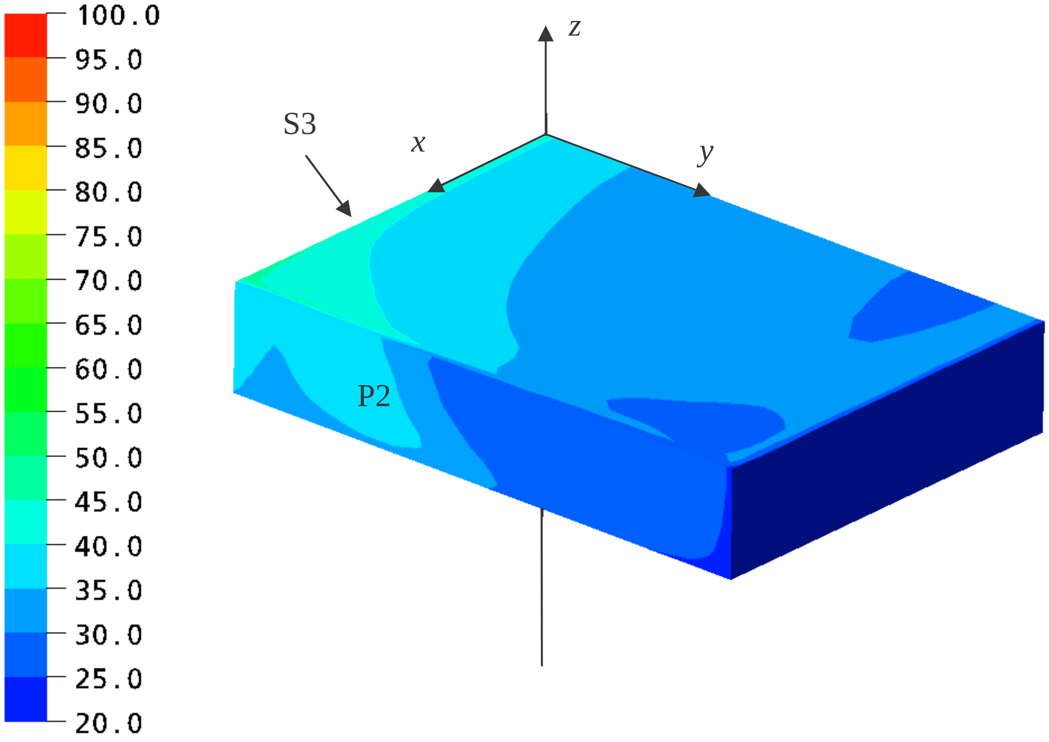

Figure 6.20: Temperature distribution on the lower horizontal surface of Gap 9 (Temperatures in °C)

Figures 6.21 and 6.22 show the temperature distribution on the upper and lower horizontal surfaces of Gap 10, respectively. In this gap, the lowest block surface temperatures occur near the entrance to the gap on P4. This is a result of cool air entering the gap on this plane. Relatively low temperatures also exist near the corner of the block at the junction of P4 and S3 as a result of air entering the gap on P2 after passing through lower gaps as observed in Figure 6.10. Temperatures on the upper surface of the gap are noticeably warmer than on the lower surface because as the flow follows the complex path between the blocks observed in Figures 6.9 and 6.10, its temperature increases and thus it rises before finally exiting the gap.

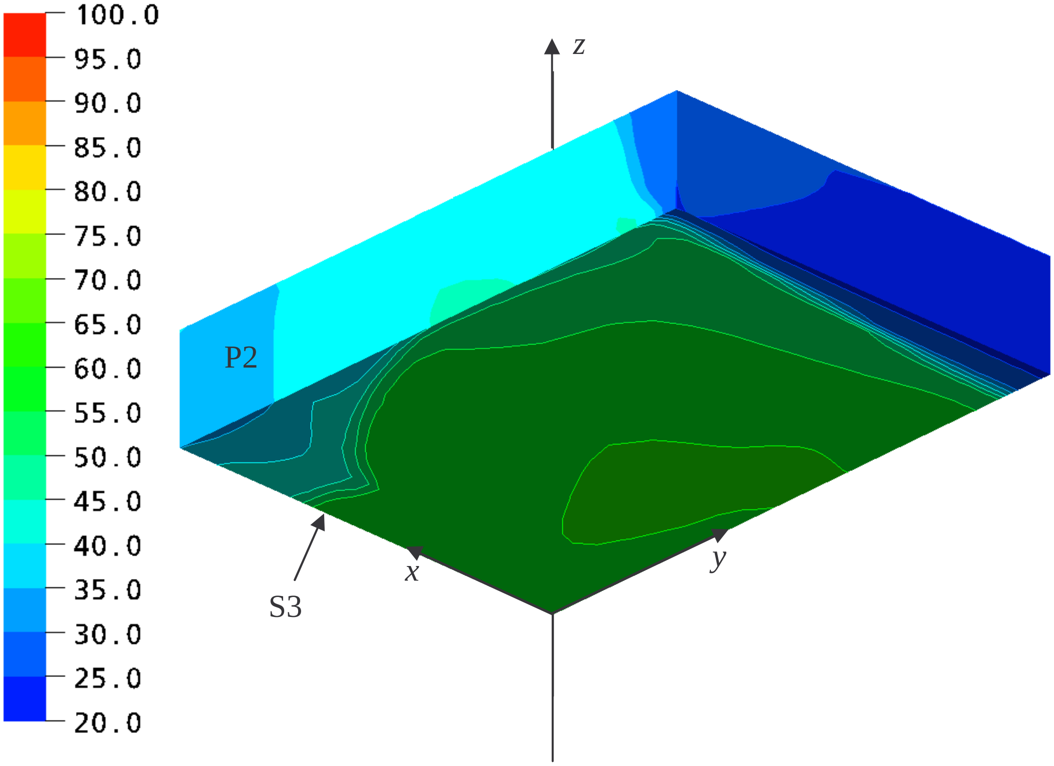

Figure 6.21 Temperature distribution on upper horizontal surface of Gap 10 (Temperatures in °C)

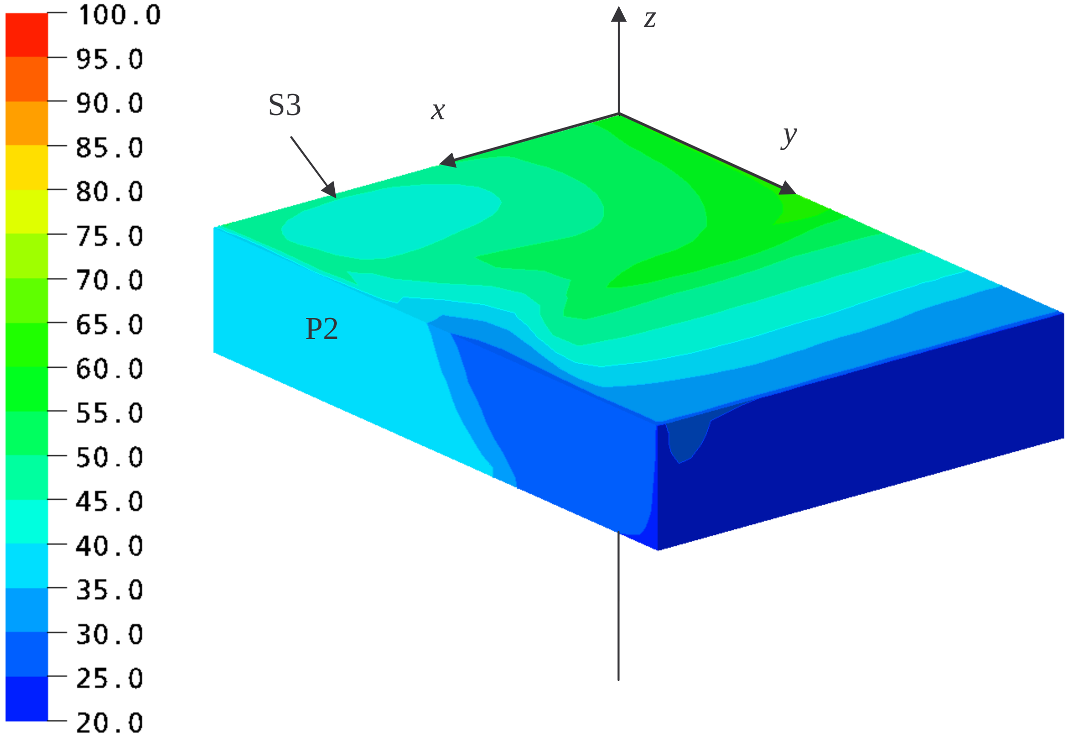

Figure 6.22: Temperature contours on lower horizontal surface of Gap 10 (Temperatures in °C)

Because of symmetry on planes S1 and S3, the net mass flow rate of air entering a particular gap on plane P4 must also be equal to the net mass flow rate exiting the same gap on plane P2. Because of interpolation used in the post-processing software, the calculated net mass flow rate through plane P2 was often not exactly equal to the calculated net mass flow rate through plane P4. The maximum deviation in any gap was always less than 0.12% of the inlet mass flow rate. Because of this deviation, the magnitude of the average of the two was taken to represent the net mass flow rate for the gap. Table 6.5 shows the average of the net mass flow rates for each gap, $\left|\dot{m}_g\right|$ in Case 1. It should be noted that this method for determining the mass flow rate does not show the direction of the flow and could also possibly be misleading in the case of a significant

Table 6.5: Mass flow rates and maximum gap temperatures for Case 1

Gap Number	$\lvert\dot{m}_g\rvert$ (kg/s)	$\frac{\lvert\dot{m}_g\rvert}{\dot{m}_i}\times 100$	$T_{max,g}$ (°C)
1	0.1765	25.81	27.57
2	0.1138	16.64	31.68
3	0.0812	11.87	33.38
4	0.0671	9.81	33.2
5	0.0577	8.44	33.78
6	0.0481	7.03	37.55
7	0.0401	5.86	40.44
8	0.0334	4.88	44.58
9	0.0265	3.87	49.53
10	0.0123	1.80	65.78
11	0.0004	0.06	89.44
12	0.0049	0.71	84.4
13	0.0040	0.59	81.52
14	0.0016	0.24	86.33
15	0.0000	0.00	95.37
Total	0.6676	97.61	

mass flow rate entering a gap on a plane and exiting the gap on the same plane. In that case, the overall mass flow rate for that gap could be much lower than the total mass flow rate entering and exiting the gap. The phenomenon of mass entering a gap on one plane and exiting on the same plane generally only occurred when the mass flow rate entering a gap on P4 was low and thus the maximum temperature in that gap was relatively high. Table 6.5 also shows the net mass flow rate through each gap as a percentage of the total inlet mass flow rate, as well as the maximum temperature in each gap, $T_{max,g}$.

A combined total of 72.57% of the inlet mass flow rate passes through Gaps 1 to 5. The maximum temperature in any of these Gaps is 33.78°C occurring in Gap 5. An amount equal to 25.81% of the inlet mass flow rate flows through Gap 1. Only 8.44% of the inlet mass flow rate flows through Gap 5. Even though the mass flow rate through Gap 1 was more than three times that of through Gap 5, the maximum gap temperature only varied by 6.21°C for these two gaps. Clearly, more flow than needed passed through Gap 1. A combined total of 23.44% of the inlet mass flow rate passes through gaps 6 to 10. The maximum temperature in these gaps is 65.78°C occurring in Gap 10. In Gaps 11 to 15 a combined total of only 1.6% of the inlet mass flow rate flows through these gaps. As a result, the maximum temperature in each of these gaps was greater than 81.5°C. These results indicate that the maximum temperature in a gap depends highly on the mass flow rate in that gap.

Only 3.88% of the inlet mass flow rate passes through Gap 9, and yet the maximum temperature is less than 50°C. If a scheme could be devised in which this mass flow rate passed through each of the fifteen gaps, the tower could be effectively cooled with as little as 58% of the total inlet mass flow rate used in Case 1. It is evident from these observations that the higher than desired maximum temperatures in some of the gaps are not a result of the total inlet mass flow rate being too low, but are a result of deficiencies in the local mass flow rates through the gaps containing the high maximum temperatures.

6.4 Presentation Method for Remaining Cases

The previous section discussed (in detail) the flow and temperature pattern in the valve hall for the base case (Case 1). It was desired to devise a concise method for presenting and comparing the remaining cases. Several options for achieving this goal were evaluated. It was decided that the most suitable method of presenting the remaining cases was in terms of the net mass flow rates and the maximum temperatures in each of the gaps between the tiers of the tower. In addition, streamline plots showing the overall flow structure for all the cases studied are shown in Appendix F.

6.5 Effect of the Inlet Air Angle

Of the twenty-one total cases for CD1, thirteen cases were devised to examine the effect of varying the inlet air angle on the velocity and temperature distribution in the valve hall. These cases are placed into three subcategories. Cases 1 to 5 study the effect of varying the inlet air angle when the inlet vent size, location, and mass flow rate are the same as in Case 1. Cases 6 to 10 study the effect of varying the inlet air angle when the inlet vent size and location are the same as in Case 1, but the inlet mass flow rate is double that of Case 1. Cases 16 to 18 study the effect of varying the inlet air angle with an inlet opening approximately half the size of that in Case 1 and with the same mass flow rate as in Case 1. Table 6.6 summarizes the thirteen cases divided into these three subcategories. Columns 2 to 4 of this table describe the size and location of the inlet opening in the domain. Column 5 is the inlet mass flow ratio, $\dot{m}_i / \dot{m}_{i,c1}$ where $\dot{m}_{i,c1}$ is the mass flow rate for Case 1. Column 6 is the inlet air angle. Column 7 is the inlet area ratio A_i/A_{c1} where A_i is the area of the inlet opening ($A_i = L_2 \text{ x } L_3$) and $A_{i,c1}$ is the area of the inlet opening in Case 1. Column 8 is the resultant velocity ratio, $(V_j / V_{j,c1})$ where V_j is the resultant inlet velocity as defined in Figure 3.8 and $V_{j,c1}$ is the resultant inlet velocity of the jet in Case 1. Column 9 is the maximum temperature in the domain. Column 10 lists the gap number that the maximum temperature is located in.

Table 6.6: Summary of cases used to study the effect of inlet air angle

Case	L_1 (m)	L_2 (m)	L_3 (m)	$\left(\frac{\dot{m}_i}{\dot{m}_{i,c1}}\right)^*$	θ (deg)	$\left(\frac{A_i}{A_{i,c1}}\right)^*$	$\left(\frac{V_j}{V_{j,c1}}\right)^*$	$T_{max,g}$ (ºC)	Gap
1	2.67	0.48	0.545	1	60	1	1	95.37	15
2					75		0.897	89.73	15
3					80		0.879	86.21	12
4					82.5		0.873	93.23	13
5					90		0.866	95.84	11
6	2.67	0.48	0.545	2	60	1	2	92.22	15
7					70		1.843	46.10	15
8					75		1.793	43.68	15
9					80		1.759	73.99	1
10					90		1.732	95.04	14
16	2.67	0.235	0.545	1	75	0.49	1.831	99.05	15
17					80		1.796	82.15	2
18					81		1.791	78.10	3

$^*\dot{m}_{i,c1}$ = 0.684 kg/s $A_{i,c1}$ = 0.2616 m^2 $V_{j,c1}$ = 2.516 m/s

6.5.1 Cases 1 to 5

The goal of Cases 1 to 5 was to determine if there was an angle which dramatically improved cooling effectiveness compared with Case 1 while maintaining the same inlet mass flow rate and inlet opening size and location. Figure 6.23 shows the net percentage of inlet mass flow rate through each gap as well as the corresponding maximum temperature in each gap for Cases 1 to 5. For Case 1, the maximum mass flow rate occurs in Gap 1 and is substantially higher than in all other gaps.. The mass flow rate decreases in each successive gap all the way to Gap 10. After gap 10, there is very little mass flow in the remaining gaps, and the temperature is highest in these gaps.

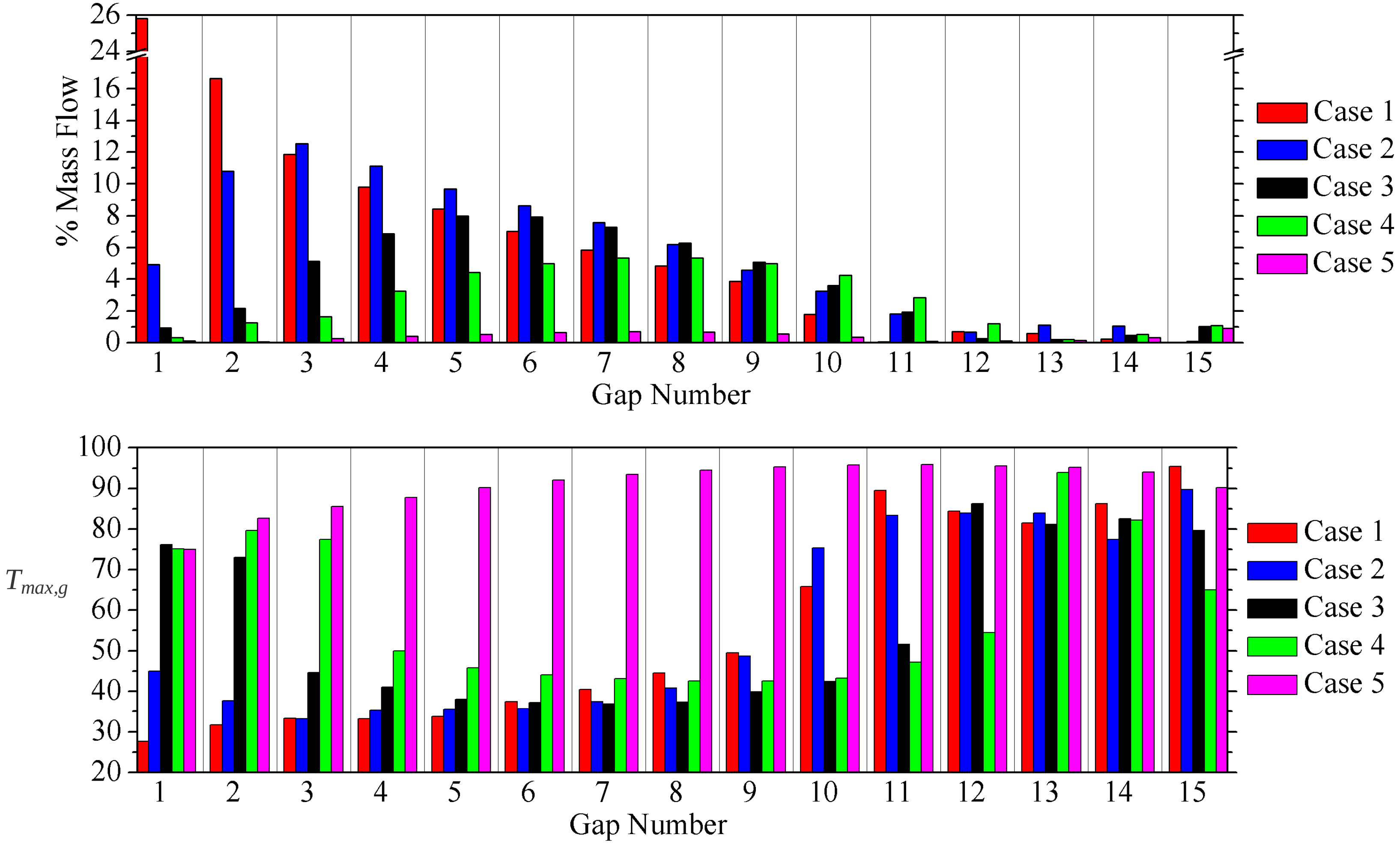

Figure 6.23: Percentage of inlet mass flow rate and maximum temperatures in each gap for Cases 1 to 5

For cases 2, 3, and 4 the mass flow rate in each gap increases as the gap number increases until it reaches a maximum, and then begins to decrease with increasing gap number. The maximum temperature in each gap shows the reverse trend, with the maximum temperature decreasing as the gap number increases until it reaches a minimum and then it begins to increase. The gap with the highest percentage of inlet mass flow rate has the lowest maximum temperature for these three cases. This suggests a trend with the maximum temperature in a gap decreasing as the mass flow rate passing through that gap increases. It also suggests that a uniform distribution of mass flow in all gaps should yield the overall lowest maximum domain temperature.

For Case 5, from Figure 6.23 it can be seen that, the percent net mass flow rate through each gap is less than 1%. This is to be expected as the inlet air for this case is orientated directly upwards. Most of the heat is removed from the blocks by a mechanism of free convection, which is not a very effective cooling mode. As a result, the temperature of the blocks and surrounding air increases considerably, relative to the other cases. In this case, most of the inlet air flows into the outlet after circulating around the room without flowing through the gaps between the blocks. For Cases 1 to 5, the maximum temperature in the domain occurs in gaps 11 to 15. Although the location of minimum mass flow and maximum temperature differed for the five cases, all five cases contained at least one temperature above 86ºC in this region. Because all of these cases were deficient in this region and because a large range of angles was used, it is highly unlikely that another angle would produce a dramatically improved cooling effect for all fifteen gaps compared with the cases studied. Of the five cases studied, the lowest maximum gap temperature occurred for Case 3. The maximum gap temperature for this case was 86.21ºC, which is a 9.16°C reduction compared with Case 1.

6.5.2 Cases 6 to 10

Cases 6 to 10 explored the effect of varying the inlet air angle with double the inlet mass flow rate while maintaining the same inlet opening size and location as in Case 1. The goal of Cases 6 to10 was to determine if there was an angle which dramatically improved cooling effectiveness compared with Case 1 when the mass flow rate was doubled. Figure 6.2 shows a plan view of the computational domain showing the locations of the inlet opening for Cases 6 to 10. Figure 6.24 shows the net percentage of inlet mass flow rate through each gap as well as the corresponding maximum temperature in each gap for Cases 6 to 10.

For Case 6, the maximum mass flow rate through any gap occurs in Gap 1. The mass flow rate decreases in each successive gap higher in the tower. As the mass flow rate decreases, the maximum temperature in the gaps increases. Maximum gap temperatures of less than 60ºC were achieved in all but one gap, Gap 15. In Gap 15, the maximum temperature was 92.22ºC. Comparing this with Case 1, in which all independent variables were identical except the inlet mass flow rate, this is a reduction of only 3.14ºC in the maximum domain temperature. The reason for the lack of improvement is that even though the overall mass flow rate was doubled compared with Case 1, the overall mass flow rate passing through Gap 15 was only equal to 0.52% of the total inlet mass flow rate for Case 6 or 1.04% of the total inlet mass flow rate of Case 1. In a trend that is similar to that found in Cases 2, 3, and 4, the individual gap mass flow rate in Cases 7, 8,

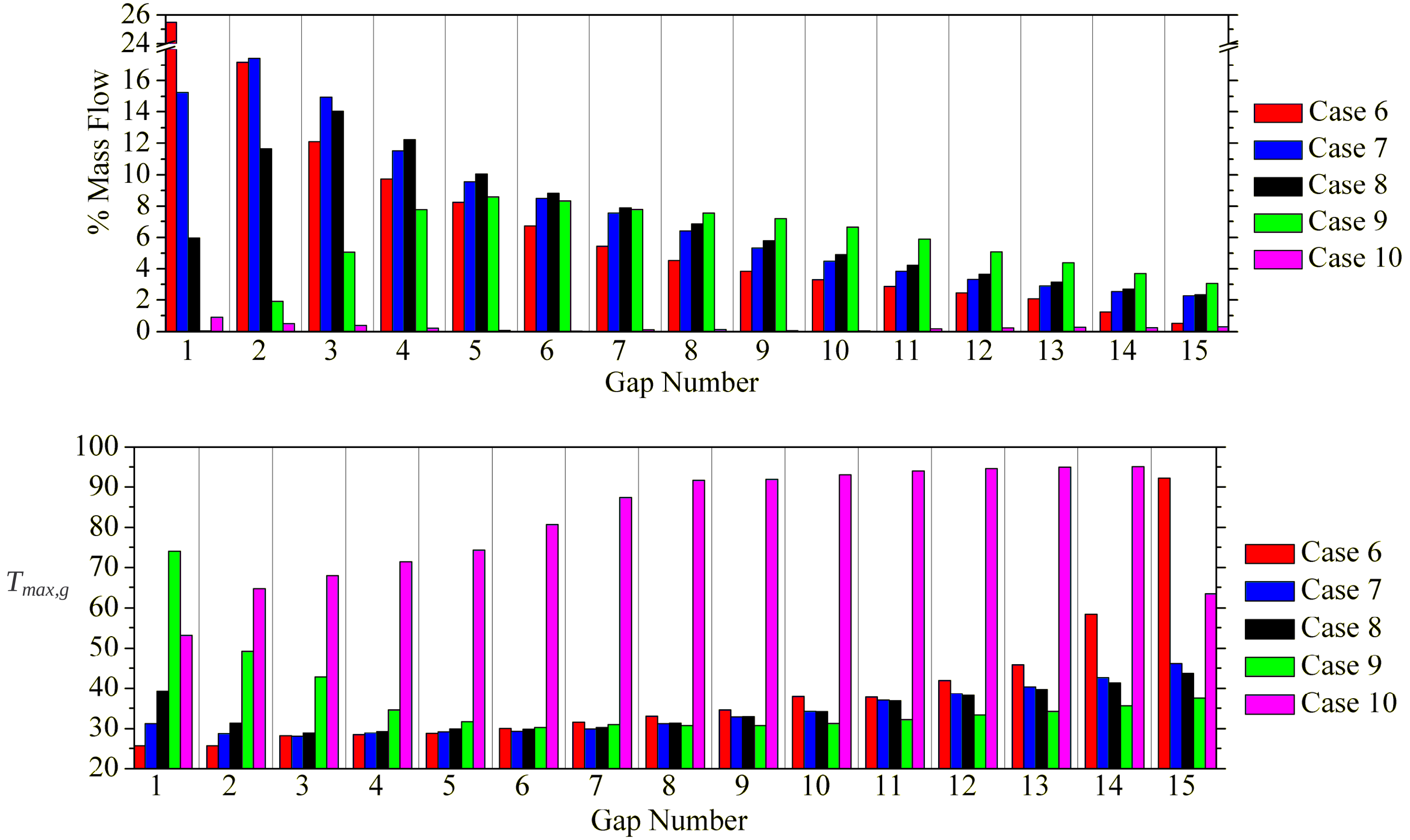

Figure 6.24: Percentage of inlet mass flow rate and maximum temperatures in each gap for Cases 6 to 10

and 9 increases as the gap number increases until it reaches a maximum, after which it decreases with increasing gap number. As seen earlier, the maximum temperature in each gap shows the reverse trend, with the maximum temperature in each gap decreasing as the gap number increases until it reaches a minimum, after which it increases. Although the gap with the highest mass flow rate does not always correspond to the same gap with the lowest maximum temperature for Cases 6 to 9, the gaps with the highermass flow rates are the gaps with relatively lower maximum temperatures.

For Case 7, the maximum temperature in the domain is 46.10ºC. This temperature occurred in Gap 15. This is a reduction of 49.27ºC compared with the maximum temperature in Case 1. The reason for this improvement is a higher mass flow rate through all the gaps. In this case, the mass flow rate through Gap 15 (the gap with the highest maximum temperature) is equal to 2.29% of the total inlet mass flow rate for Case 6 or 4.58% of the total inlet mass flow rate of Case 1.

For Case 8, the maximum temperature in the domain is 43.68ºC. Once again, this temperature occurs in Gap 15. This is a reduction of 51.69ºC compared with the maximum temperature in Case 1. The reason for this improvement is a higher mass flow rate through all the gaps. In this case, the mass flow rate through Gap 15 (the gap with the highest maximum temperature) is equal to 2.36% of the total inlet mass flow rate for Case 6 or 4.72% of the total inlet mass flow rate of Case 1. A comparison can also be made between Case 8 and Case 2 as the inlet air angle was the same and the only independent variable that varied between these cases was the mass flow rate. For both of these cases, the maximum domain temperature was observed in Gap 15. The maximum temperature for Case 8, however, was 46.05ºC lower than in Case 2. This improvement is due to the higher mass flow rate in Gap 15 for Case 8.

For Case 9, maximum gap temperatures of less than 50ºC were achieved in gaps except Gap 1, where the maximum temperature was 73.99ºC. Comparing the maximum temperature with that of Case 3, in which all independent variables were identical except the inlet mass flow rate, this is a reduction of 12.22ºC in the maximum domain temperature. When the maximum temperature in Gap 1 for Case 9 and Case 3 are compared, however, there is only a 2.22º C reduction for Case 9. The reason for the lack of improvement is that even though the overall mass flow rate was doubled compared with Case 3, the overall mass flow rate passing through Gap 1 for Case 9 was only equal to 0.05% of the total inlet mass flow rate for Case 6 or 0.1% of the total inlet mass flow rate of Case 3, thus accounting for the high temperature in this gap.

For Case 10, the overall percent mass flow rate through each gap is less than 1% of the total inlet mass flow rate. This is to be expected as the inlet air for this case is orientated directly upwards. The maximum temperature observed in the domain for Case 10 was 95.04ºC in Gap 14. Compared with Case 5, in which all independent variables were equal except the mass flow rate, this is a reduction of 0.8ºC in the maximum domain temperature. The reason for the lack of improvement can be attributed to the low mass flow rates between the blocks.

The results of Case 6 to 10 show that it is possible to dramatically decrease the maximum temperatures in the valve hall by increasing the inlet mass flow rate of air and by varying the inlet air angle. Case 8 (θ = 75º, $\dot{m}_i \,/\, \dot{m}_{i,c1} = 2$) achieved a 51.69ºC reduction in the maximum domain temperature compared with Case 1 (θ = 60º, $\dot{m}_i / \dot{m}_{i,c1}$ = 1). Dramatic improvements, however, are not guaranteed by increasing the mass flow rate. Case 6 (θ = 60º, $\dot{m}_i / \dot{m}_{i,c1}$ = 2) achieved only a 3.15ºC reduction in maximum temperature when compared with Case 1.

6.5.3 Cases 16 to 18

Cases 16 to 18 explored the effect of varying the inlet air angle with an inlet opening approximately half the size of that in Case 1 while maintaining the same mass flow rate as Case 1. The goal of Cases 16 to 18 was to determine if there is an angle which dramatically increases the cooling effectiveness compared to Case 1 by increasing the velocity of the inlet air jet while maintaining the same mass flow rate as Case 1. Figure 6.25 shows a plan view of the computational domain showing the locations of the inlet and outlet openings for Cases 16, 17, and 18. Figure 6.26 shows the net percentage of inlet mass flow rate through each gap as well as the corresponding maximum temperature in each gap for Cases 16 to 18.

For Case 16 the net mass flow rate increases from Gap 1 to Gap 4 where it reaches a maximum, and then decreases thereafter. The minimum temperature in the domain does not occur in Gap 4, but in Gap 5. The difference between the maximum temperature in Gaps 4 and 5, however, was only approximately 1°C. After Gap 5, the maximum temperature in each successive gap increases with a maximum domain temperature of 99.05°C occurring in Gap 15. This was the maximum domain temperature observed in any case for CD1. Detailed examination of the flow into opening planes on Gap 15 showed that there was little penetration of the flow into the gap. This accounts for the

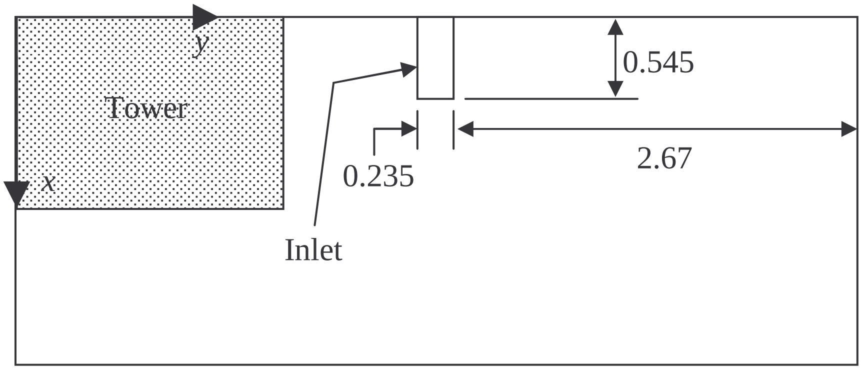

Figure 6.25: Plan view of computational domain showing the inlet for Cases 16, 17, and 18 (dimensions in meters)

the high maximum temperature observed in this case.

For Case 17, the net mass flow rate in the gaps up to Gap 6 where it reaches a maximum, and then decreases thereafter. The lowest maximum individual gap temperature does not occur in Gap 6, but in Gap 9. The difference between the maximum temperature in Gaps 6 and 9, however, was less than 2°C. After Gap 9, the maximum gap temperature increases with successive higher gaps. There was a sudden increase in maximum gap temperature from Gap 14 to Gap 15 (47.40°C to 79.25°C). This rise was caused by a large decrease in mass flow rate in Gap 15. For Case 17, the maximum domain temperature was 82.05°C in Gap 2. This is a reduction of 13.32°C compared with the maximum temperature in Case 1. The reason for this improvement is due to the increased mass flow rates through the highest gaps in the tower.

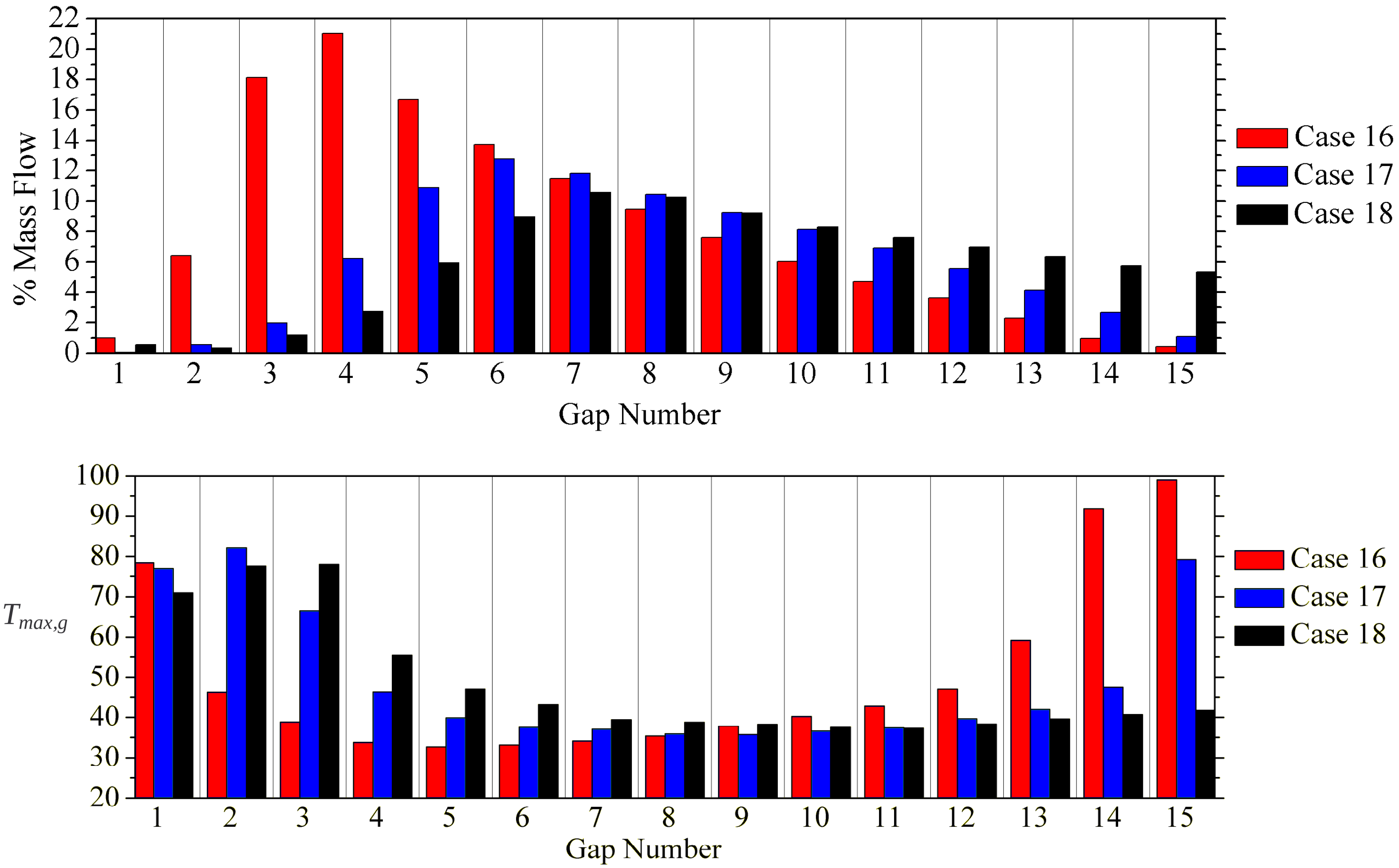

Figure 6.26: Percentage of inlet mass flow rate and maximum temperatures in each gap for Cases 16-18

For Case 18, the net mass flow rate in Gaps 1, 2, and 3 is very low. As a result, the maximum temperatures in these gaps are relatively high with the maximum domain temperature of 78.10°C occurring in Gap 3. After this gap, the net mass flow rate through each gap increases with higher gaps until Gap 7, after which it begins to decrease with each successive higher gap. Compared to Case 1, the maximum temperature for Case 18 is 17.27°C lower. The maximum domain temperature for this run was the lowest of all cases for Geometry 1. It is, however, interesting to note that although the only difference between Case 17 and Case 18 was a 1° difference in inlet air angle, the mass flow distribution and the maximum temperatures in the individual gaps are quite different. For example, the 1° difference in inlet air angle resulted in a 37.5°C reduction in maximum temperature in Gap 15 in Case 18 compared with Case 17. This improvement can be directly attributed to the increase in overall mass flow rate through Gap 15 for Case 18 (5.33%) compared with Case 17 (1.08%).

The results of Cases 16 to 18 show that it is possible to achieve increased cooling by varying the air inlet angle and by using an inlet opening approximately half the size of the inlet opening in Case 1 while maintaining the inlet mass flow rate. These improvements however, are not as dramatic as seen in Cases 6 to 10. Case 18 shows a 17.27°C reduction in maximum temperature compared with Case 1 compared with a 51.69ºC reduction for Case 8 compared with Case 1. Also, the maximum domain temperature for these cases appears to be much more sensitive to inlet air angle than Cases 6 to 10.

6.5.4 Summary of the Effect of the Inlet Air Angle

Cases 1 to 5 examined the effect of varying the inlet air angle θ while holding all other independent parameters the same as in the base case. In these cases varying θ had some effect on the maximum temperature in the domain. For the five cases, the lowest maximum temperature occurred in Case 3 ($\theta = 80°$), resulting in a 9.16°C reduction in the maximum domain temperature compared with Case 1. The sensitivity of results, however, was relatively low for these cases with a range in maximum domain temperature of only 9.63ºC from the best case (Case 3) to the worst (Case 5).

Cases 6 to 10 examined the effect of varying the inlet air angle θ with the same inlet location as the base case, but with double the mass flow rate. In these cases varying θ had a dramatic effect on the maximum temperature in the domain. The range in maximum domain temperature for these five cases was 51.36°C from the best case (Case 8) to the worst (Case 10). For these five cases, the lowest maximum temperature occurred in Case 8 ($\theta = 75°$) resulting in a 51.69°C reduction in the maximum domain temperature compared with Case 1.

Cases 16 to 18 examined the effect of varying the inlet air angle with an inlet opening approximately half the size of the base case while maintaining the same mass flow rate as the base case. In these cases, once again varying θ had an effect on the maximum temperature in the domain. For the three cases, the lowest maximum temperature occurred in Case 18 ($\theta = 81°$), resulting in a 17.27°C reduction in the maximum domain temperature compared with Case 1. The sensitivity of results for changes in θ for these three cases was higher for these three cases than it was in Cases 1 to 5. The 6° difference in inlet air angle between Case 16 and Case 18 resulted in a 20.95ºC change in maximum temperature between the two cases.

6.6 Effect of the Inlet Aspect Ratio

Of the 21 total cases studied for CD1, six cases were devised to explore the effect of varying the inlet aspect ratio on the velocity and temperature distribution in the valve hall. These six cases are subdivided into three groups of two cases each. In each of the three groups, the mass flow rate and the inlet air angle were identical. The area of the inlet opening and the inlet velocity were either very similar or identical in the three groups. The aspect ratio of the inlet opening was varied in each group of two cases to study its effect on the velocity and temperature distribution in the room. In order to compare the three groups of cases, the aspect ratio of the inlet opening must first be defined. Because of the use of symmetry plane S1, an actual inlet opening in the valve hall would have dimensions of L_2 x $2L_3$, as shown in Figure 6.27. The aspect ratio, R_A of the inlet openings is defined as:

$$R_A = \frac{L_2}{2L_3} \tag{6.1}$$

Table 6.7 summarizes the six cases subdivided into three groups.

6.6.1 Cases 16 and 11

Figure 6.28 shows the locations of the inlet opening for both Cases 16 and 11. Figure 6.29 shows the net percentage of inlet mass flow rate through each gap, as well as the corresponding maximum temperature in each gap for Cases 16 and 11.

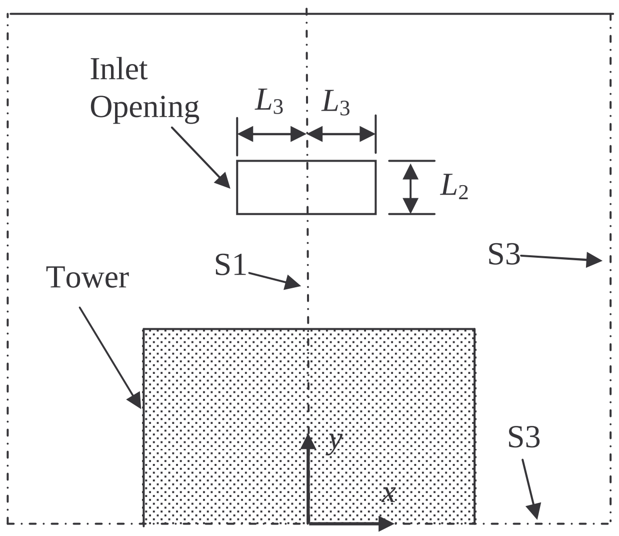

Figure 6.27: Lengths used in aspect ratio calculation

Table 6.7: Summary of cases used to study the effect of the aspect ratio

Case	L_1 (m)	L_2 (m)	L_3 (m)	R_A	$\left(\frac{\dot{m}_i}{\dot{m}_{i,c1}}\right)^*$	θ (deg)	$\left(\frac{A_i}{A_{i,c1}}\right)^*$	$\left(\frac{V_j}{V_{j,c1}}\right)^*$	$T_{max,g}$ (°C)	Gap
16	2.67	0.235	0.545	0.216	1	75	0.49	1.831	99.05	15
11		0.48	0.2725	0.881			0.5	1.793	96.93	15
3	2.67	0.48	0.545	0.44	1	80	1	0.879	86.21	12
12	2.43	0.97	0.27	1.796					82.73	12
15	2.86	0.14	1.02	0.069	1	80	0.546	1.611	93.23	15
14	2.42	1.02	0.14	3.643					80.25	15

* $\dot{m}_{i,c1} = 0.684$ kg/s $A_{i,c1} = 0.2616\ \text{m}^2$ $V_{j,c1} = 2.516$ m/s

In Gap 1, the maximum temperature for Case 16 was 29.48°C higher than for Case 11 (78.51°C vs. 49.03°C). This change in maximum temperature can be attributed to the higher overall mass flow rate through Gap 1 in Case 11. The increase in mass flow in Gap 1 for Case 11 occurs because the inlet opening in Case 11 has an edge located much

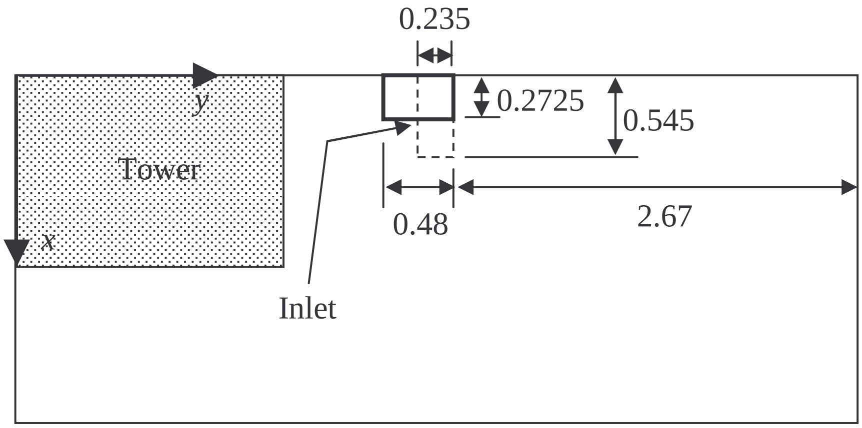

Figure 6.28: Plan view of computational domain showing the inlet opening for Case 16 (dashed line) and Case 11 (bold line) (dimensions in meters)

closer to the tower than in Case 16 as shown in Figure 6.28. In Gaps 2 to 11, the maximum temperature is less than 47°C for both cases. This is due to relatively high mass flow rates in these gaps for both cases. In Gaps 12 and 13, the maximum temperatures for Case 16 were considerably lower than for Case 11. The mass flow rates in Gaps 12 and 13 were much higher for Case 16 than for Case 11. The increased mass flow rates and decreased maximum temperatures in Gaps 12 and 13 for Case 16 are likely due to both the decreased aspect ratio and the increased distance of the inlet opening from the tower in Case 16. Because a lower amount of the inlet mass flow rate passes through Gaps 1 and 2 in Case 16, a higher mass flow is available in Gaps 12 and 13. The maximum temperatures in Gaps 14 and 15 were relatively high for both cases. The corresponding mass flow rates in these gaps were also very low in both cases. For Case 16, the maximum domain temperature was 99.05°C in Gap 15. For Case 11, the maximum temperature was 96.93°C, also in Gap 15.

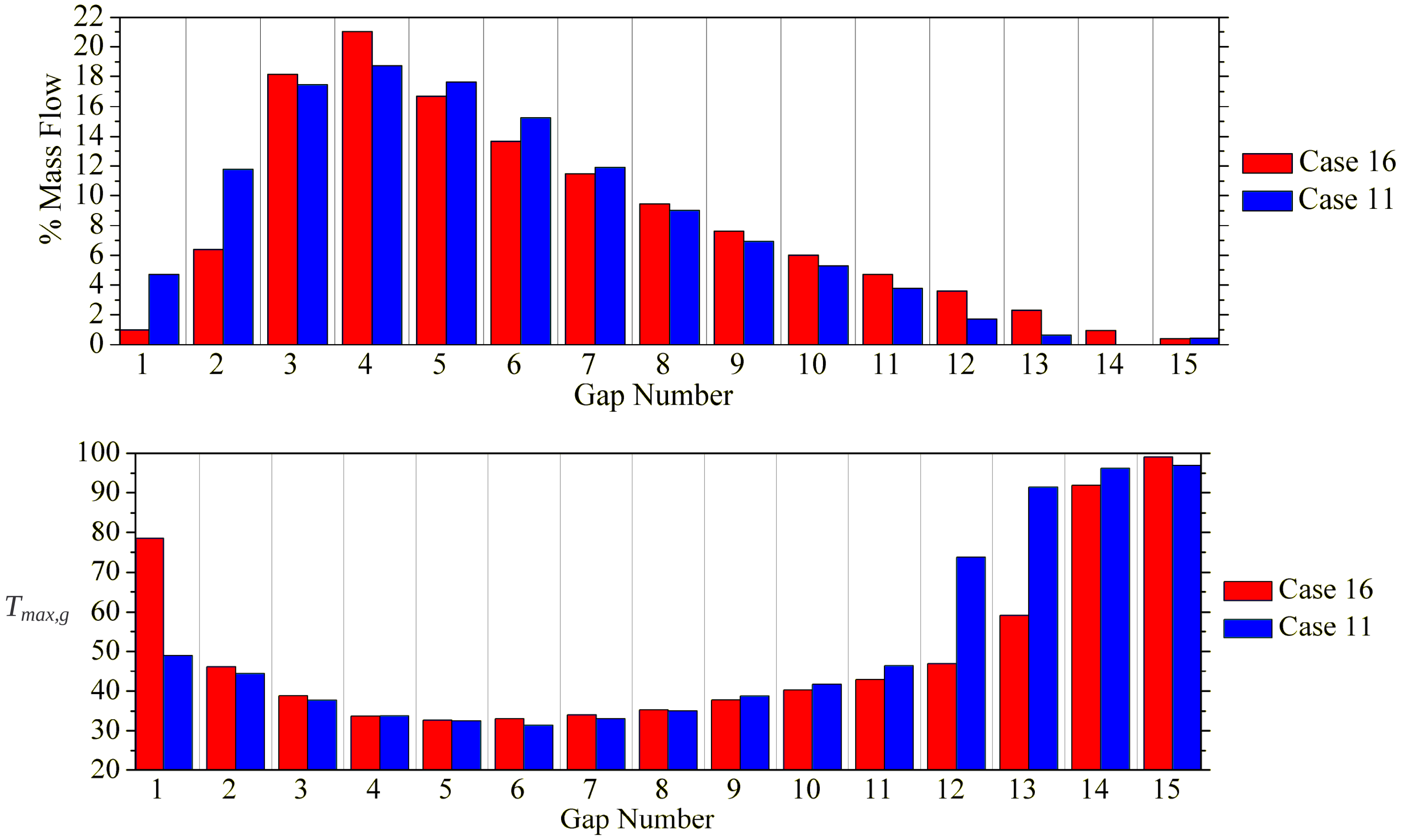

Figure 6.29: Percentage of inlet mass flow rate and maximum temperatures in each gap for Cases 16 and 11

A reduction of 2.12°C in maximum domain temperature was achieved by increasing the inlet opening aspect ratio in Case 11 versus Case 16. It should be noted that although a reduction in the maximum temperature was achieved in Case 11, this reduction was relatively small and the maximum temperatures for both these cases was higher than the maximum temperature in Case 1.

6.6.2 Cases 3 and 12

Figure 6.30 shows a plan view of the computational domain showing the locations of the inlet openings for both Cases 3 and 12. Figure 6.31 shows the net percentage of inlet mass flow rate through each gap as well as the corresponding maximum temperature in each gap for Cases 3 and 12.

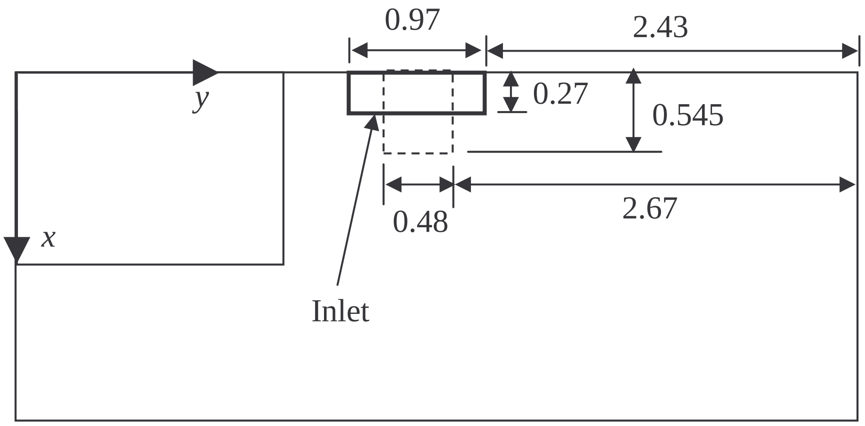

Figure 6.30: Plan view of computational domain showing the inlet opening locations for Case 3 (dashed line) and Case 12 (bold line) (dimensions in meters)

In Gaps 1 and 2, the maximum temperature for Case 12 was considerably lower than for Case 3. The change in maximum temperature can be attributed to the higher overall mass flow rate through Gaps 1 and 2 in Case 12. The increase in mass flow rate in these two gaps occurs because the inlet opening in Case 12 has an edge located much closer to the

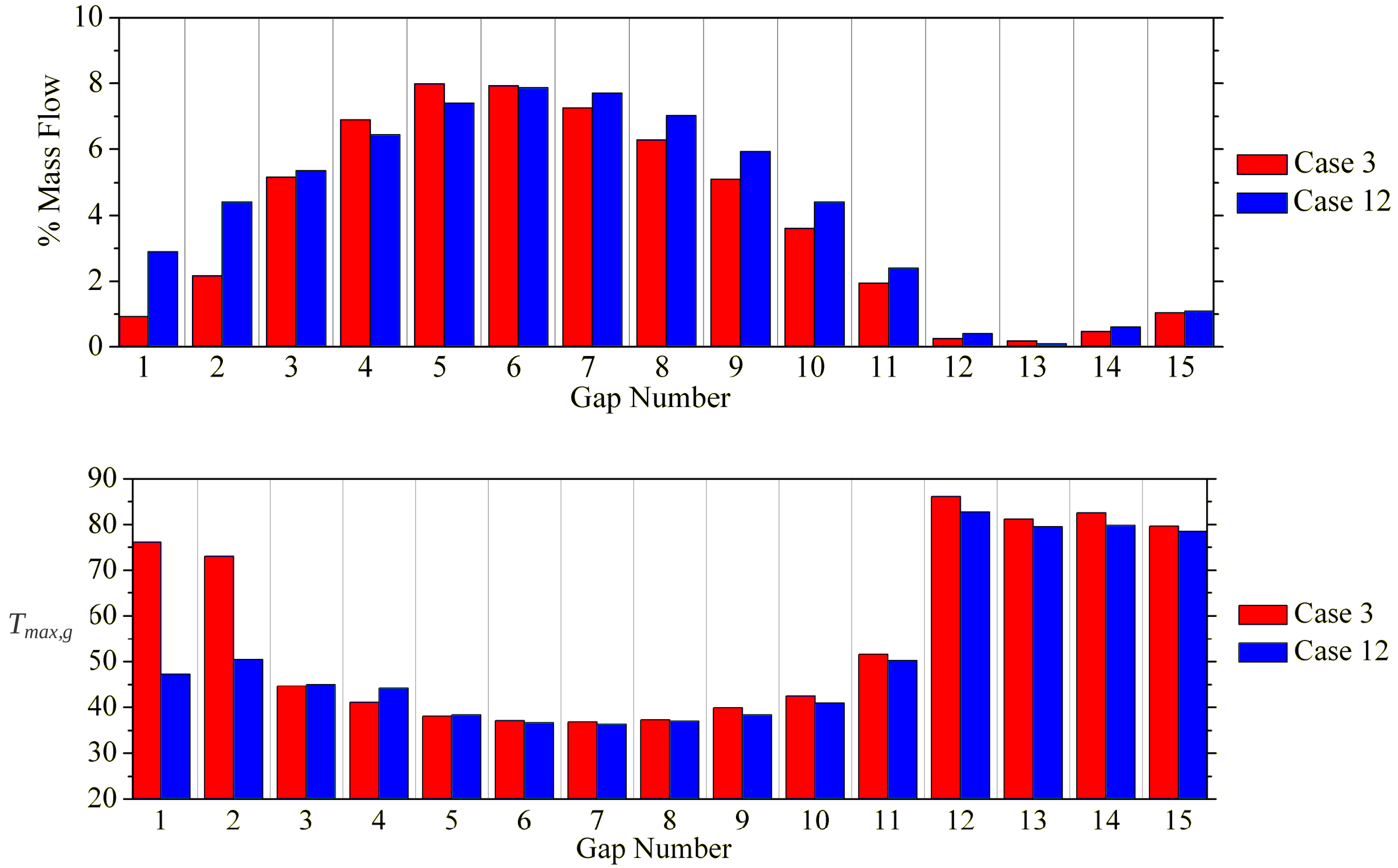

Figure 6.31: Percentage of inlet mass flow rate and maximum temperatures in each gap for Cases 3 and 12

tower than in Case 3 as shown in Figure 6.30. In Gaps 3 to 11, the maximum temperature is less than 52°C for both cases. This is due to relatively high mass flow rates in these gaps for both cases. In Gaps 12 to 15, the maximum temperatures are relatively high for both cases due to a low mass flow rate in these gaps. The maximum temperatures in these gaps are similar for both cases; however, the maximum temperatures in Gaps 12 to 15 are all lower for Case 12 than for Case 3. The decrease in maximum temperatures in Gaps 12 to 15 for Case 12 is likely due to the fact that the inlet opening for Case 12 extends farther in the positive y direction than in Case 3. This results in a greater percentage of the inlet mass flow rate passing through the uppermost blocks for Case 12.

The maximum domain temperature for Case 12 was 82.73°C in Gap 12. For Case 3, the maximum temperature was 86.21°C, also in Gap 12. Although the difference in maximum temperatures between the two cases was only 3.48°C, as in the previous set of cases, the lower maximum domain temperature occurred for the case with the higher aspect ratio.

6.6.3 Cases 15 and 14

Figure 6.32 shows a plan view of the computational domain showing the locations of the inlet opening for Cases 15 and 14. Figure 6.33 shows the net percentage of inlet mass flow rate through each gap as well as the corresponding maximum temperature in each gap for Cases 15 and 14.

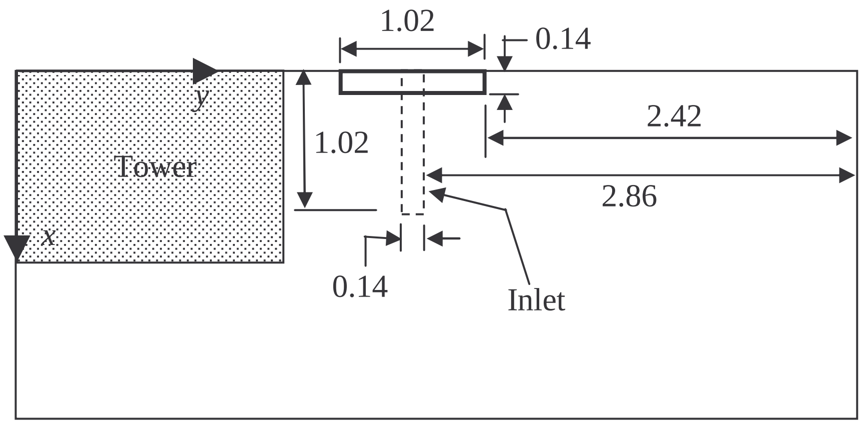

Figure 6.32: view of computational domain showing the inlet opening locations for Case 15 (dashed line) and Case 14 (bold line) (dimensions in meters)

The maximum temperature Gaps 1 and 2, for Case 14 was considerably lower than for Case 15. The difference in maximum temperature can be attributed to the higher overall mass flow rate through Gaps 1 and 2 in Case 14. The increase in mass flow rate in these two gaps occurs because the inlet opening in Case 14 has an edge located much closer to the tower than in Case 15 as shown in Figure 6.33. In Gaps 3 to 12, the maximum temperature is less than 49°C for both cases. This is due to relatively high mass flow rates in these gaps for both cases. In Gaps 13 to 15, the maximum temperatures are all lower for Case 14 than for Case 15. This is expected in Gap 13 as the mass flow rate through this gap is higher for Case 14. In Gaps 14 and 15, however, the individual gap mass flow rates are higher for Case 15. Upon detailed examination of the flow through these gaps, many of the streamlines entering Gaps 14 and 15 for Case 15 enter the gap through P4 near the junction of the two entering planes and exit through P2 also near this junction without penetrating very far into the gap. This flow contributes to the mass flow

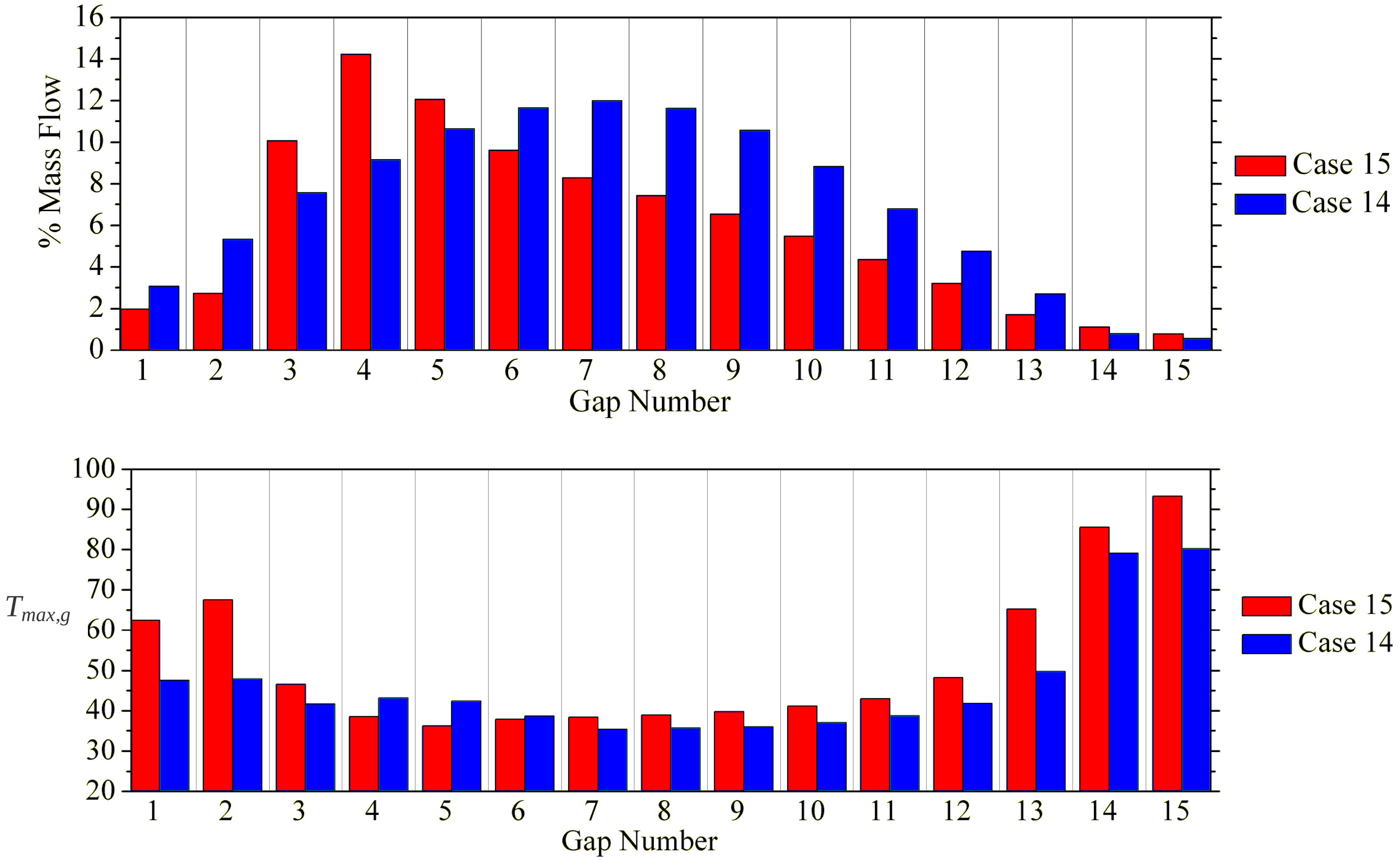

Figure 6.33: Percentage of inlet mass flow rate and maximum temperatures in each gap for Cases 15 and 14

rate without making a significant contribution to cooling the gap. For Case 14, even though the net mass flow rates through Gaps 14 and 15 are lower than for Case 15, the streamlines penetrate much further into the gap before exiting. As a result, these gaps are more effectively cooled in Case 14 than in Case 15.

The maximum domain temperature for Case 14 was 80.25°C occurring in Gap 15. For Case 15, the maximum temperature was 93.23°C, also occurring in Gap 15. As in the previous two sets of cases, increasing the aspect ratio of the inlet opening while holding the other variables constant had the effect of decreasing the maximum domain temperature. In this particular set of cases, the aspect ratio was increased by a higher amount than in the two previous cases resulting in the most dramatic drop in maximum temperature.

6.6.4 Summary of the Effect of the Inlet Aspect Ratio

The previous three groups of two cases each examined the effect of varying the inlet aspect ratio on the cooling effectiveness in the valve hall. In all three cases, increasing the aspect ratio, R_A, increased the cooling effectiveness in the valve hall with all other parameters equal.

6.7 Effect of Varying the Inlet Opening Velocity through Changes to the Inlet Opening Area with Constant Inlet Mass Flow Rate

Seven of the total twenty-one cases for CD1 were devised to explore the effect of varying the area of the inlet velocity through changes to the inlet opening area while maintaining a constant mass flow rate. The area of the inlet opening and the inlet velocity are grouped together because if one of these two variables is varied with a constant mass flow rate, the other variable is varied by the inverse amount. These seven cases are subdivided into three groups. Within each of the three groups, the inlet mass flow rate, orientation of the inlet opening and inlet air angle were held constant. Table 6.8 summarizes the seven cases divided into three subcategories.

6.7.1 Cases 2 and 11

The inlet opening for Case 2 is shown in Figure 6.2 and the inlet opening for Case 11 is shown in Figure 6.28. Figure 6.34 shows the net percentage of inlet mass flow rate through each gap as well as the corresponding maximum temperature in each gap for Cases 2 and 11.

The maximum temperature in Gaps 1 to 9 is below 50°C for both cases. This is due to the relatively high mass flow rate in these gaps in both cases. In Gaps 10 to 12, the maximum temperature is significantly higher for Case 2 than for Case 11. This is due to

Table 6.8: Summary of cases used to study the effect of varying inlet opening area/jet velocity with constant inlet mass flow rate

Case	L_1 (m)	L_2 (m)	L_3 (m)	$\left(\frac{\dot{m}_i}{\dot{m}_{i,c1}}\right)^*$	θ (deg)	$\left(\frac{A_i}{A_{i,c1}}\right)^*$	$\left(\frac{V_j}{V_{j,c1}}\right)^*$	$T_{max,g}$ (°C)	Gap
2	2.67	0.48	0.545	1	75°	1	0.897	89.73	15
11			0.2725			0.5	1.793	96.93	15

3	2.67	0.48	0.545	1	80°	1	0.879	86.21	12
17		0.235				0.49	1.796	82.15	2

12	2.43	0.97	0.27	1	80°	1	0.878	82.73	12
13	2.42	1.02	0.2			0.78	1.128	80.09	15
14	2.42	1.02	0.14			0.546	1.611	80.25	15

$^*\dot{m}_{i,c1}$ = 0.684 kg/s $A_{i,c1}$ = 0.2616 m^2 $V_{j,c1}$ = 2.516 m/s

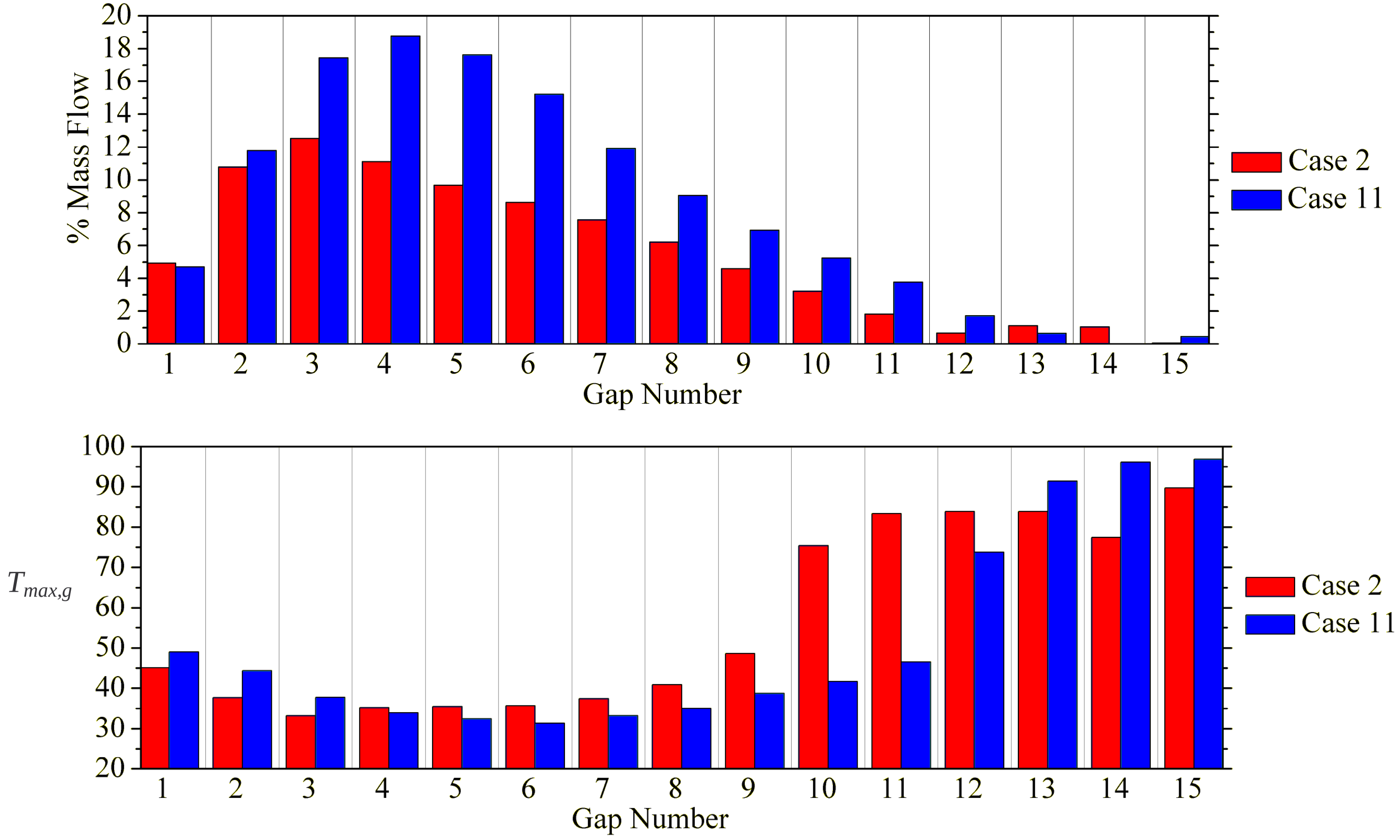

Figure 6.34: Percentage of inlet mass flow rate and maximum temperatures in each gap for Cases 2 and 11

the increased mass flow rate through these gaps in Case 11. The opposite trend, however, is true for Gaps 13 to 15 with the maximum temperatures in these gaps being significantly higher for Case 11 than Case 2. This is expected in Gap 13 and 14 as the individual gap mass flow rates are higher for Case 2. In Gap 15, however, the mass flow rate is higher for Case 11 (although both are less than 0.5% of the inlet mass flow rate). Upon detailed examination of the flow through this gap, some of the streamlines entering Gap 15 for Case 11 enter the gap through P4 near the junction of the two entering planes and exit through P2 also near this junction without penetrating very far into the gap. This flow contributes to the mass flow rate without making a significant contribution to cooling the gap. For Case 2, even though the net mass flow rate through Gap 15 is lower than for Case 11, the streamlines penetrate further into the gap before exiting. As a result, Gap 15 is more effectively cooled for Case 2 than for Case 11.

The maximum domain temperature for Case 2 is 89.73°C. The maximum domain temperature for Case 11 is 96.93°C. Both of these maximum temperatures occurred in Gap 15. For these two cases, increasing the inlet velocity by decreasing the inlet area had the effect of increasing the maximum domain temperature.

6.7.2 Cases 3 and 17

The inlet opening for Case 3 is shown in Figure 6.2 and the inlet opening for Case 17 is shown in Figure 6.27. Figure 6.35 shows the net percentage of inlet mass flow rate through each gap as well as the corresponding maximum temperature in each gap for Cases 3 and 17.

.

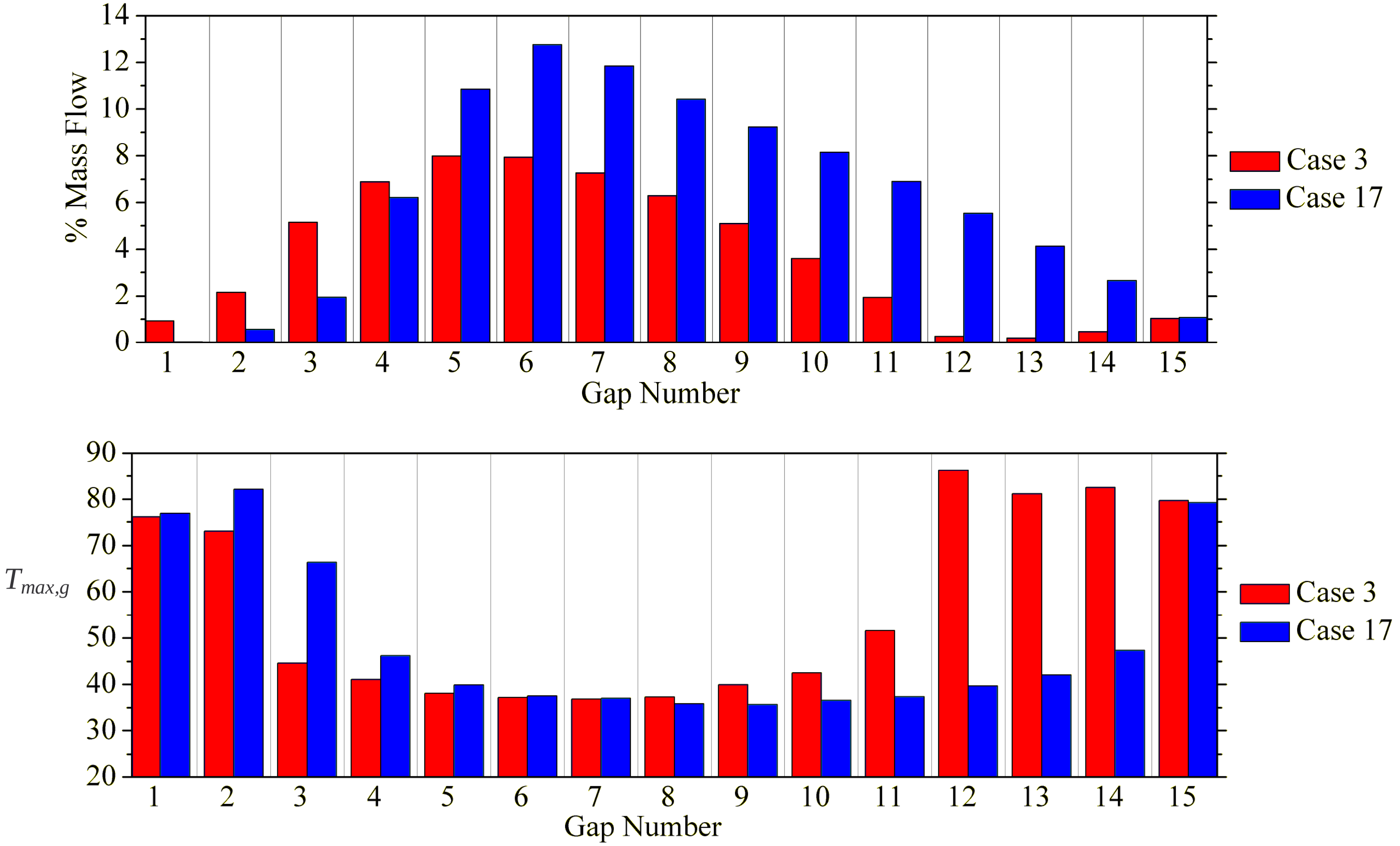

Figure 6.35: Percentage of inlet mass flow rate and maximum temperatures in each gap for Cases 3 and 17

The maximum temperatures in Gaps 1 to 3 are lower for Case 3 than for Case 17. This trend is due to the increased mass flow rate through these blocks in Case 3, most probably because the inlet opening for Case 3 has an edge much closer to the tower than does Case 17. The maximum temperatures in Gaps 4 to 11 are below 52°C for both cases. This behavior due to the relatively high mass flow rates through these gaps in both cases. The maximum temperature in Gaps 12 to 14 is considerably lower in Case 17 than in Case 3. The mass flow rates through these gaps are also much higher for Case 17 than for Case 3 as result of the edge of the inlet opening in Case 17 being located farther from the towers than in Case 3. This change in inlet edge location produces a higher percentage of the inlet mass flow rates being shifted to the upper gaps of the tower for Case 17. In Gap 15 the mass flow rate and maximum gap temperatures were almost identical for both cases.

The maximum domain temperature for Case 3 is 86.21°C in Gap 12. The maximum domain temperature for Case 17 is 82.15°C in Gap 2. For this group of cases, increasing the inlet velocity by decreasing the inlet area had the effect of decreasing the maximum domain temperature. This is the opposite effect that was observed in the previous group of cases. In Cases 2 and 11, decreasing the inlet area caused the flow to penetrate less into the upper gaps. In Cases 3 and 17, decreasing the inlet area caused flow to penetrate farther into the upper gaps. This example of the two opposite trends for the change in the same parameter further reinforces the complexity of the problem as these trends could not be predicted without the use of numerical simulation.

6.7.3 Cases 12 to 14

The inlet opening for Case 12 is shown in Figure 6.30. The inlet openings for Cases 13 and 14 are shown in Figure 6.36. Figure 6.37 shows the net percentage of inlet mass flow rate through each gap as well as the corresponding maximum temperature in each gap for Cases 12 to 14.

The maximum temperatures in Gaps 1 to 11 are below 51°C for all three cases. The relatively low maximum temperatures in these gaps are due to the relatively high mass flow rates through these gaps in all three cases. In Gaps 12 and 13, the maximum temperature in the gaps decreases as the inlet velocity increases. This decrease is due to increased mass flow rates in these gaps as the inlet velocity increases. In Gaps 14 and 15, the maximum temperatures are very similar for all three cases. The temperatures in these gaps are amongst the highest temperatures in the domain for all three cases. The explanation for the relatively high temperatures in these gaps is the low mass flow rate in these gaps for all three cases.

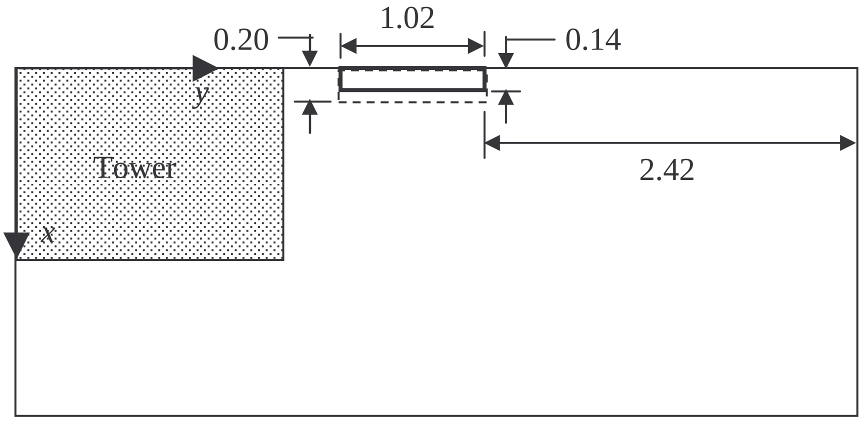

Figure 6.36: Inlet opening locations for Case 13 (bold line) and Case 14 (dashed line) (dimensions in meters)

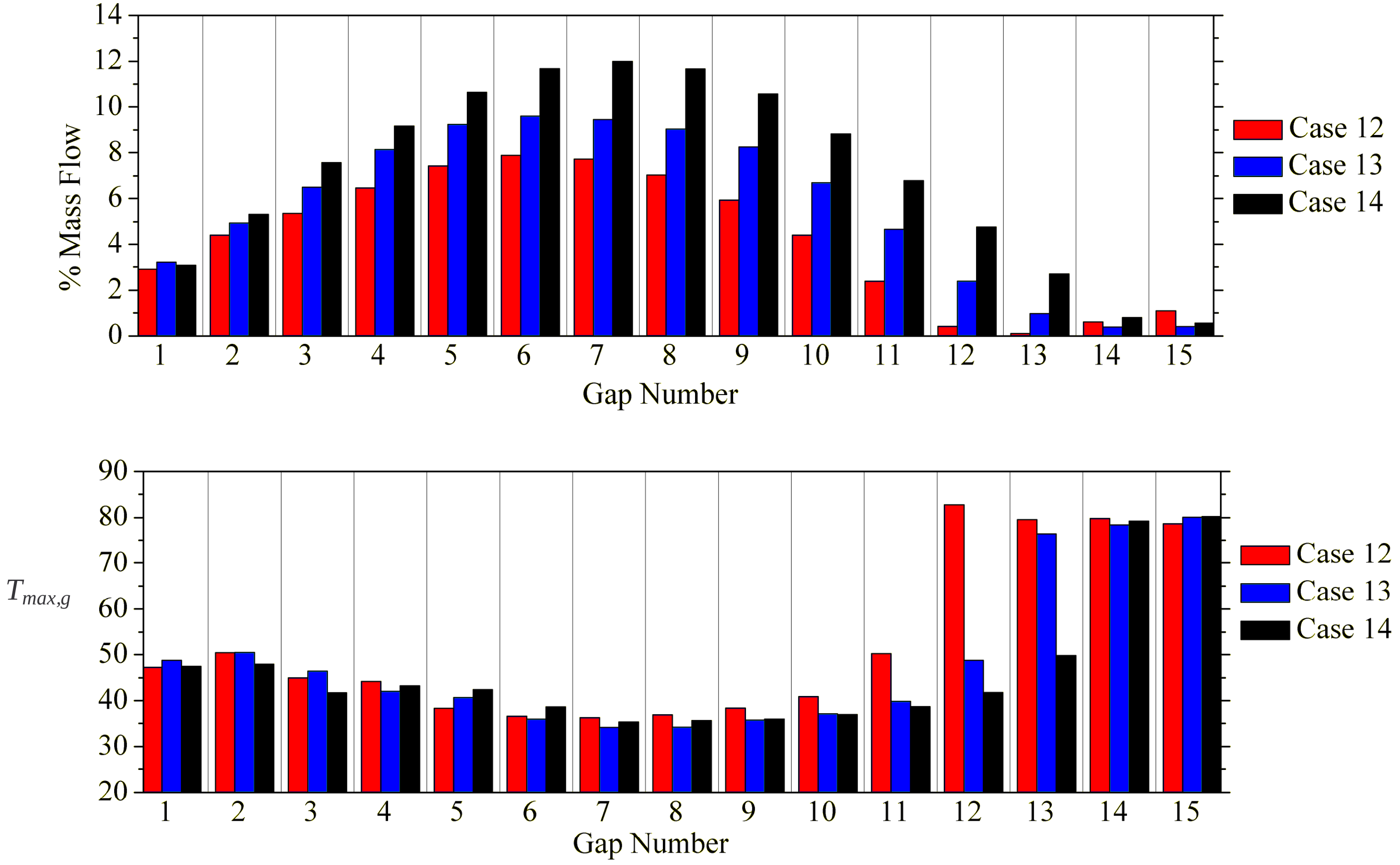

Figure 6.37: Mass flow rates and maximum temperatures in gaps for Cases 12 to 14

The maximum domain temperature for Case 12 is 82.73°C in Gap 12. The maximum domain temperature for Case 13 is 80.09°C in Gap 15. The maximum domain temperature for Case 14 is 80.25°C, also in Gap 15. In Cases 12 and 13, increasing the inlet velocity by decreasing the inlet area had the effect of decreasing the maximum domain temperature. In Cases 13 and 14, increasing the inlet velocity by decreasing the inlet area had the effect of increasing the maximum domain temperature. Once again, this reinforces the complexity of the flow.

6.7.4 Summary of Effect of Varying the Inlet Opening Velocity through Changes to the Inlet Opening Area with Constant Inlet Mass Flow Rate

In the previous three groups of cases, the inlet velocity was varied by changing the size of the inlet opening area while holding the mass flow rate fixed. In Cases 2 and 11, increasing the inlet velocity had the effect of increasing the maximum temperature in the domain because the flow did not penetrate as far into the upper gaps for Case 2. In Cases 3 to 17, increasing the inlet velocity had the effect of decreasing the maximum temperature in the domain because the flow penetrated deeper into the upper gaps for Case 17. In Cases 12 to 14, increasing the inlet velocity had the effect of decreasing the maximum temperature of the domain in one case and increasing the maximum temperature of the domain in another case. The results of these cases further reinforce the overall complexity of the flow and how trends can change as specific details of the problem are changed

6.8 Effect of Varying the Inlet Mass Flow Rate through Changes to the Inlet Opening Area with Constant Inlet Velocity

Four of the twenty-one cases for CD1 were devised to discuss the effect of varying the area of the inlet opening and mass flow rate while maintaining an approximately constant inlet velocity. The area of the inlet opening and the mass flow rate are grouped together because if one of these two variables is varied with a constant inlet velocity, the other variable is varied by the inverse amount. These four cases are subdivided into two groups of two cases each. In each of the two groups, the inlet air angle and orientation are fixed and the inlet velocity is approximately constant. The inlet opening area and the mass flow rate are varied to study their effects on the velocity and temperature distribution in the room. Table 6.9 summarizes the four cases divided into two subcategories.

6.8.1 Cases 8 and 16

The goal of studying Cases 8 and 16 is to determine if cooling effectiveness can be maintained in the valve hall when the inlet opening area and mass flow rate are decreased while the inlet velocity remains approximately constant. For both cases, the inlet air angle is 75° and the inlet velocity is approximately equal. The mass flow rate for Case 8 is double that of Case 16 and the area of the inlet openings is approximately double for Case 8 compared with Case 16. A plan view of the computational domain for Case 8 showing the location of the inlet opening is shown in Figure 6.2 and a plan view of the computational domain for Case 16 showing the location of the inlet opening is shown in Figure 6.25. Figure 6.38 shows the net percentage of inlet mass flow rate through each gap as well as the corresponding maximum temperature in each gap for Cases 8 and 16.

Table 6.9: Summary of cases used to describe effect of varying the inlet mass flow rate through changes to the inlet opening area with constant inlet velocity

Case	L_1 (m)	L_2 (m)	L_3 (m)	$\left(\frac{\dot{m}_i}{\dot{m}_{i,c1}}\right)^*$	θ (deg)	$\left(\frac{A_i}{A_{i,c1}}\right)^*$	$\left(\frac{V_j}{V_{j,c1}}\right)^*$	$T_{max,g}$ (°C)	Gap
8	2.67	0.48	0.545	2	75	1	1.793	43.68	15
16		0.235		1		0.49	1.831	99.05	15

Case	L_1 (m)	L_2 (m)	L_3 (m)	$\left(\frac{\dot{m}_i}{\dot{m}_{i,c1}}\right)^*$	θ (deg)	$\left(\frac{A_i}{A_{i,c1}}\right)^*$	$\left(\frac{V_j}{V_{j,c1}}\right)^*$	$T_{max,g}$ (°C)	Gap
9	2.67	0.48	0.545	2	80	1	1.759	73.99	1
17		0.235		1		0.49	1.796	82.15	2

$^*\dot{m}_{i,c1}$ = 0.684 kg/s $A_{i,c1}$ = 0.2616 m^2 $V_{j,c1}$ = 2.516 m/s

It should be noted that because the inlet mass flow rate for Case 8 was double that of Case 16, the percent mass flow rates through each gap in Figure 6.38 for Case 8 and Case 16 are relative to two different inlet mass flow rates.

The maximum temperature in each gap is higher in Case 16 compared with Case 8. This is not surprising, as the mass flow rate in Case 8 is double that of Case 16. The largest differences in the maximum gap temperatures between the two cases occur near the top and the bottom of the tower. In Gap 1, the maximum temperature for Case 8 was 39.30°C compared with 78.51°C for Case 16. The difference in maximum temperature can be attributed to the higher overall mass flow rate through Gap 1 in Case 8. The increase in mass flow in Gap 1 for Case 8 occurs because the inlet opening in Case 8 has an edge located much closer to the tower than in Case 16. The maximum temperatures in Gaps 14 and 15 were also considerably higher for Case 16 than for Case 8. Once again, this can be attributed to the higher overall mass flow rates through Gaps 14 and 15 in

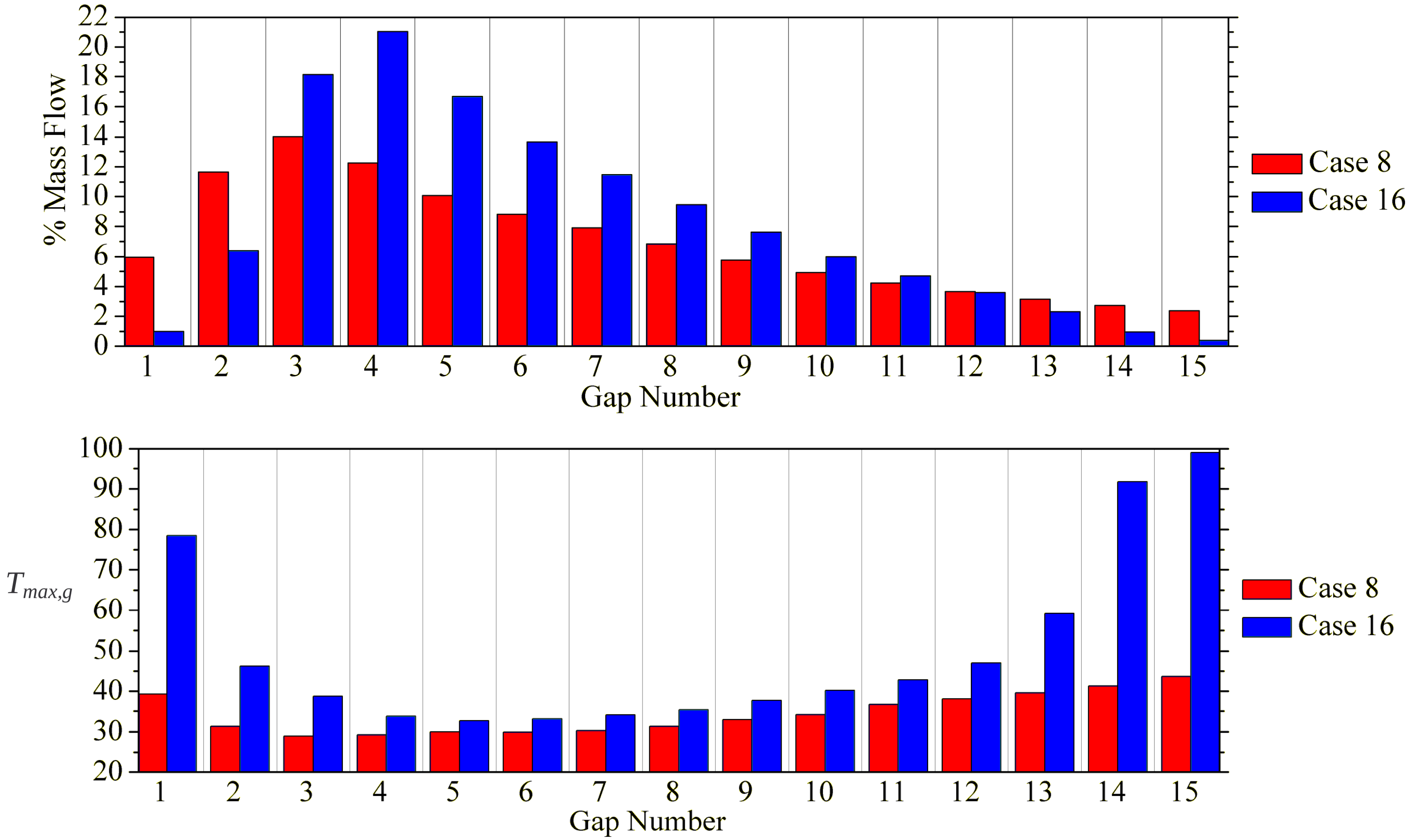

Figure 6.38: Percentage of inlet mass flow rate and corresponding maximum temperature in each gap for Cases 8 and 16

Case 8. The higher mass flow rates in Gaps 14 and 15 for Case 8 can be explained by the increased inlet mass flow rate. In Case 16, an amount approximately equal to 81% of the total inlet mass flow rate passes through Gaps 3 and 7 alone. As a result of this, less air is available in the higher gaps. In Case 8, an amount approximately equal to 53% of the total inlet mass flow rate passes through Gaps 3 and 7. Even though the total amount of air passing through Gaps 3-7 is greater in Case 8 than Case 16 because the total inlet mass flow rate was doubled there is still a greater amount of air available to pass through the higher gaps of the tower in Case 8, resulting in lower temperatures in these gaps.

The maximum domain temperature for Case 8 was 43.68°C compared with 99.05°C for Case 16. Both maximum temperatures occurred in Gap 15. Because the maximum temperature for Case 16 was more than 55°C higher than for Case 8, Cases 8 and 16 are evidence that cooling effectiveness is not necessarily maintained in the valve hall when the inlet opening area and mass flow rate are decreased while the inlet velocity remains approximately constant. It appears that the inlet mass flow rate and the inlet area are individually important variables in achieving effective cooling in the valve hall.

6.8.2 Cases 9 and 17

Similarly with the previous group of cases, the goal of studying of Cases 9 and 17 is also to determine if cooling effectiveness can be maintained in the valve hall when the inlet opening area and mass flow rate are decreased while the inlet velocity remains approximately constant. For both cases, the inlet air angle is 80° and the inlet velocity is approximately equal for the two cases. The mass flow rate for Case 9 is double that of Case 17 and the area of the inlet openings is approximately double for Case 9 compared with Case 17. A plan view of the computational domain for Case 9 showing the location of the inlet opening is shown in Figure 6.2 and a plan view of the computational domain for Case 17 showing the location of the inlet opening is shown in Figure 6.25. Figure 6.39 shows the net percentage of inlet mass flow rate through each gap as well as the corresponding maximum temperature in each gap for Cases 9 and 17 relative to their respective total inlet mass flow rates.

As in the previous group of cases, the maximum temperature in each gap is higher in Case 17 compared with Case 9. Once again, this is not surprising, as the mass flow rate in Case 9 is double that of Case 17. The difference, however, was not very large for many of the 15 gaps. In Gap 1, the maximum temperature in Case 9 is 73.99°C compared with 76.95°C for Case 17. The reason for the similarity between the two maximum temperatures is that almost none of the inlet mass flow rate passes through this gap in either case due to the high inlet air angle. In Gaps 2, 3, and 15, however, the difference in maximum temperature between the two cases is much higher with the largest difference being in Gap 15 where the maximum temperature is 37.43°C for Case 9 and 79.25°C for Case 17. As in the previous case, the lower maximum temperature observed in Case 9 is due to the fact that there is more air available near the top of the tower due to the increased inlet mass flow rate.

The maximum domain temperature for Case 9 is 73.99°C in Gap 1. The maximum temperature for Case 17 is 82.15°C in Gap 2. As in the previous case, the maximum domain temperature was higher for the case with half the inlet mass flow rate; in this case, however, the difference was only 8.16°C. This was due to the fact that Gap 1 was

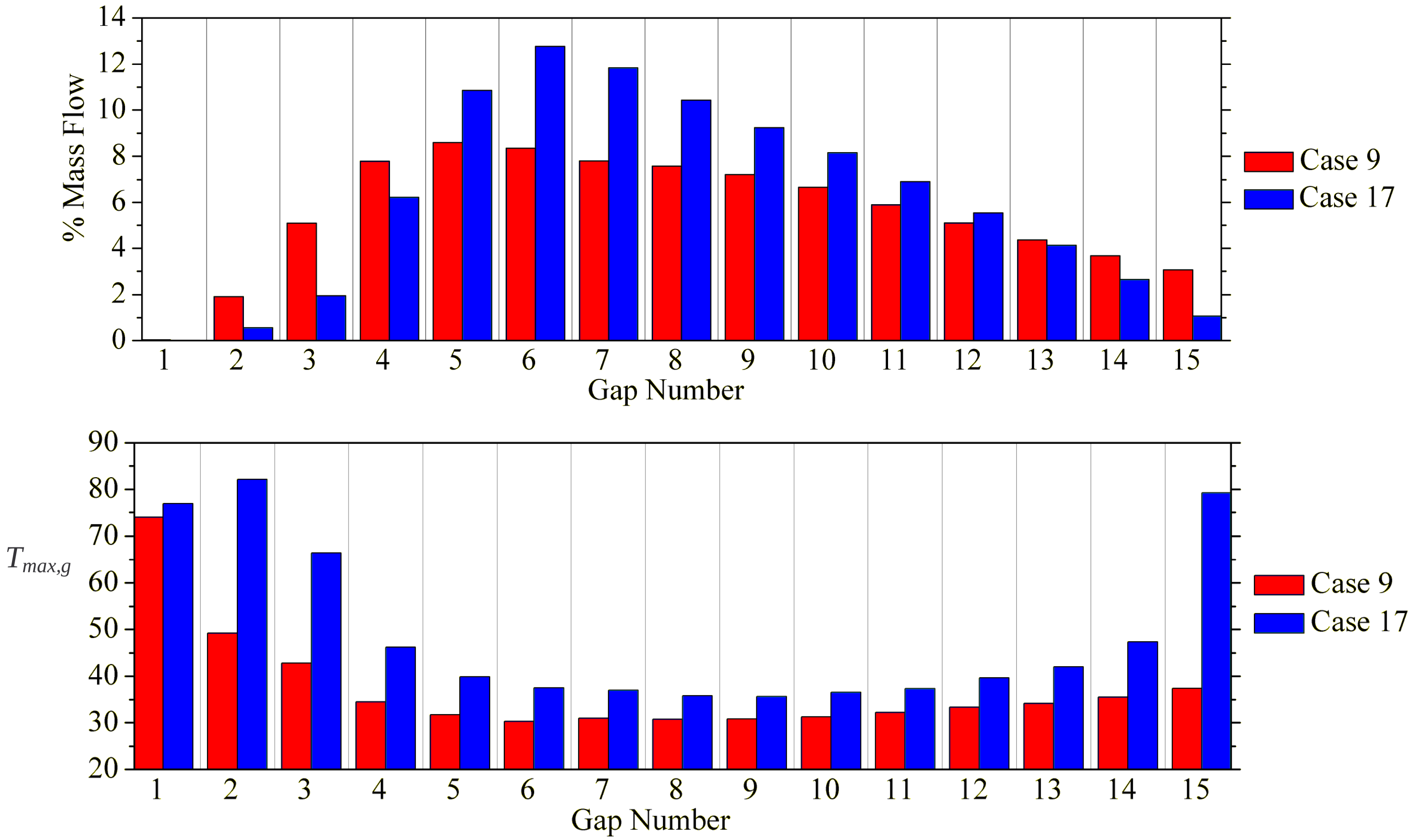

Figure 6.39: Percentage of inlet mass flow rate and corresponding maximum temperature in each gap for Cases 9 and 17

already deficient in mass flow for Case 9. When Gaps 2, 3, and 15 are used for comparison between these two cases, the maximum individual gap temperatures are much higher for Case 17 than for Case 9. Once again, these cases are evidence that cooling effectiveness cannot be maintained in the valve hall when the inlet opening area and mass flow rate are decreased while the inlet velocity remains approximately constant.

6.8.3 Summary of the Effect of Varying the Inlet Mass Flow Rate through Changes to the Inlet Opening Area with Constant Inlet Velocity

In the previous two groups of cases, the inlet mass flow rate was varied by varying the size of the inlet opening area with constant inlet velocity. In both groups of cases, decreasing the inlet velocity had the effect of increasing the maximum temperature in the domain. For Cases 8 and 16, the maximum domain temperature increased by more than 55°C when the inlet mass flow rate was cut in half. For Cases 9 and 17, the maximum domain temperature increased by only 8.16°C when the inlet mass flow rate was cut in half, however, the maximum individual gap temperatures increased by more than 20°C in three other gaps. The results of these cases show that cooling effectiveness is not maintained in the valve hall when the inlet mass flow rate is decreased by decreasing the inlet opening area while maintaining the same inlet velocity.

6.9 Effect of Using Multiple Inlet Angles

Cases 19 and 20 were devised to determine if dividing the inlet opening into two regions, each with a different inlet air angle and mass flow rate, could lead to improved cooling effectiveness in the valve hall. The area of each region was approximately half of the entire inlet opening area (a 1-cm space was used between the regions to avoid possible computational problems arising from specifying two velocities on the same node). A plan view showing the inlet opening is shown in Figure 6.40. An inlet air angle of 60° was used for Region 2 to aim the flow at the bottom portion of the tower. An inlet angle of 81° was used for Region 1 to aim the flow at the top portion of the tower. Although, the same total inlet mass flow rate was used for both cases, it was assumed that a higher percentage of the inlet air would be required in the inlet region furthest away from the towers in order to effectively cool the highest blocks in the tower. In Case 19, 75% of the inlet air was directed through Region 1 and the other 25% through Region 2. In Case 20, 80% of the inlet air was directed through Region 1 and the other 20% through Region 2. Table 6.10 summarizes the two cases. Figure 6.41 shows the net percentage of inlet mass flow rate through each gap as well as the corresponding maximum temperature in each gap for Cases 19 and 20.

In both cases, the maximum temperature in the lower gaps of the tower was higher than expected. It was expected that with an inlet angle of 60° for the inlet opening closest to the jets the maximum temperatures in the lower gaps would be relatively low. The reason for the high temperatures in these gaps was that almost all of the air issuing from the inlet opening closest to the jets was entrained by the jet issuing from Region 1 due to the differential mass flow rates used in the two regions. As a result, the mass flow rates in the lower gaps were much lower than expected. The maximum temperatures in the highest three gaps were also relatively high for both cases. This was due to a very low mass flow rate through these gaps in both cases.

The maximum temperature in Case 19 was 85.91°C, occurring in Gap 15. The maximum temperature in Case 20 was 85.75°C, occurring in Gap 13. Because of the high

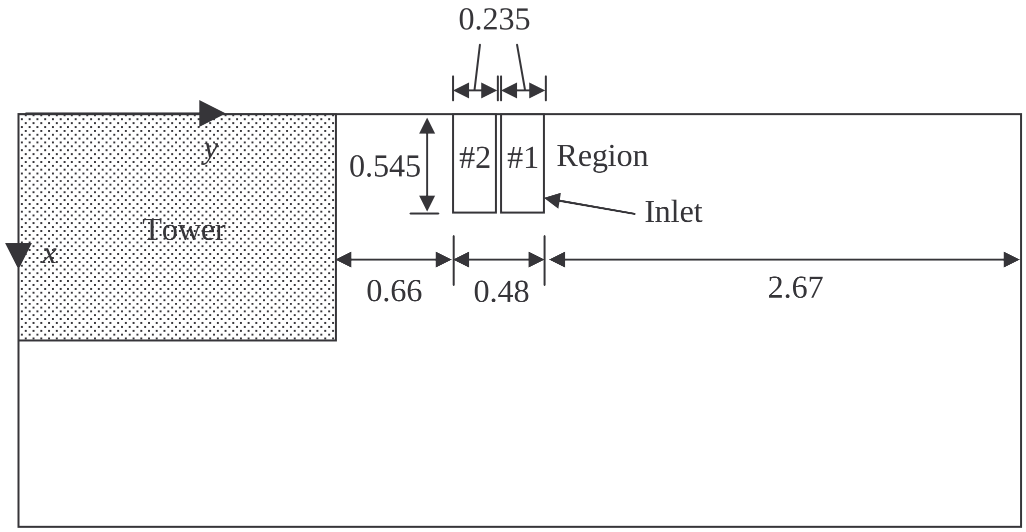

Figure 6.40: Plan view of the computational domain showing the inlet opening locations for Cases 19 and 20 (dimensions in meters)

Table 6.10: Summary of Cases 19 and 20

Case	L_1 (m)	L_2 (m)	L_3 (m)	θ_1 (deg)	θ_2 (deg)	$\left(\frac{\dot{m}_{i,r1}}{\dot{m}_{i,c1}}\right)^*$	$\left(\frac{\dot{m}_{i,r2}}{\dot{m}_{i,c1}}\right)^*$	$\left(\frac{V_{j,r1}}{V_{j,c1}}\right)^*$	$\left(\frac{V_{j,r2}}{V_{j,c1}}\right)^*$	T_{max} (°C)	Gap
19	2.67	0.48	0.545	81	60	0.75	0.25	1.343	0.511	85.91	15
20	2.67	0.48	0.545	81	60	0.8	0.2	1.433	0.409	85.75	13

$^*\dot{m}_{i,c1}$ = 0.684 kg/s $A_{i,c1}$ = 0.2616 m^2 $V_{j,c1}$ = 2.516 m/s

temperatures in both the upper and lower gaps of the tower for both cases, it is highly unlikely that any other combination of mass flow rates would be much more effective than the two cases studied assuming the same inlet air angles, the same inlet sizes and locations, and the same total mass flow rate. These two cases can also be compared with Case 18 as that case was the same as using an inlet opening with two regions with no mass flow through Region 2. Case 18 resulted in a lower maximum domain temperature

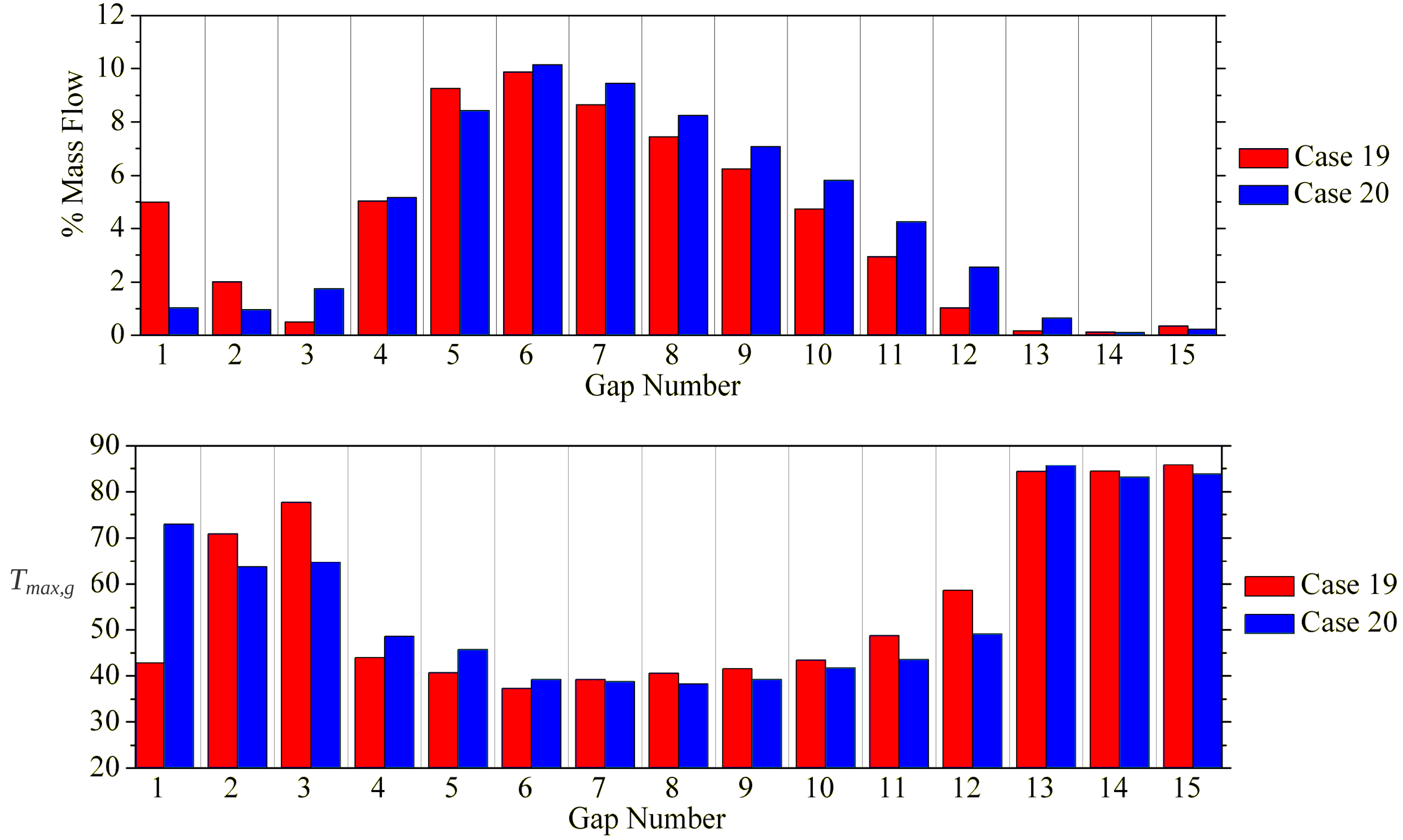

Figure 6.41: Percentage of inlet mass flow rate and corresponding maximum temperature in each gap for Cases 19 and 20

due to the higher mass flow rate through the highest gaps. The results of these two cases (19 and 20) indicate that it is more effective to direct all of the cooling air through the inlet region farthest away from the towers than to divide the cooling air between the two inlet regions.

6.10 Side Wall Inlet for Computational Domain 1

Case 21 was devised to determine if it was possible to achieve effective cooling by placing the inlet opening on the side wall of the domain under the constraint of CD1 (Symmetry in S3) using the same inlet mass flow rate as in Case 1. The inlet air for this case was directed normal to the inlet opening. Table 6.11 summarizes Case 21. Figure 6.42 shows a plan view of the domain and 6.43 shows an elevation view of the domain. Figure 6.44 shows the net percentage of inlet mass flow rate through each gap as well as the corresponding maximum temperature in each gap for Case 21. There were a number of instances in Cases 1 to 20, where the overall direction of flow through a gap or a number of gaps was in the opposite direction as the inlet air. That is, in these gaps a higher mass flow rate went into the gaps through plane P2 and out of the gaps through P4, instead of the reverse. The magnitude of the net mass flow rate in these cases, however, was small and therefore the direction of the flow was not discussed. For Case 21, however, the magnitude of the overall mass flow rate in the reverse direction was significant through a number of gaps. As a result, gaps in which the overall flow direction is in the opposite direction as the inlet air for Case 21 are marked with an asterisk in Figure 6.44.

Table 6.11: Summary of Case 21

Case	L_4 (m)	L_5 (m)	L_6 (m)	$\left(\frac{\dot{m}_i}{\dot{m}_{i,c1}}\right)^*$	$\left(\frac{A_i}{A_{i,c1}}\right)^*$	$\left(\frac{V_j}{V_{j,c1}}\right)^*$	$T_{max,g}$ (ºC)	Gap
21	1.38	8.3	0.069	1	2.19	0.397	85.44	13

$^*\dot{m}_{i,c1}$ = 0.684 kg/s $A_{i,c1}$ = 0.2616 m^2 $V_{j,c1}$ = 2.516 m/s

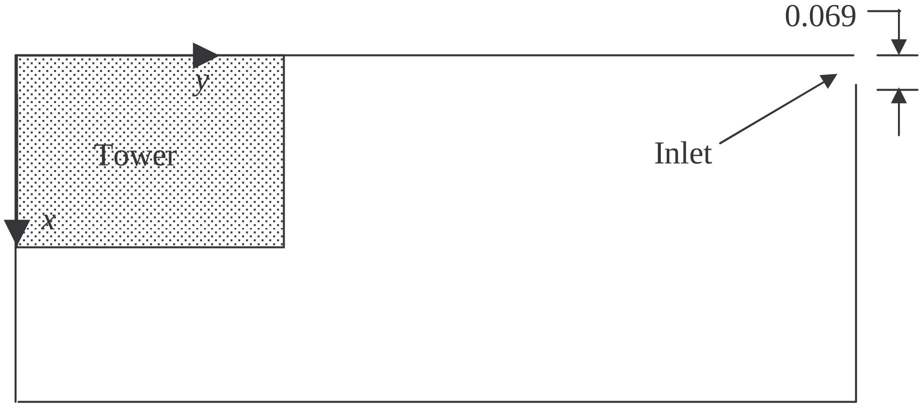

Figure 6.42: Plan view of the computational domain showing the inlet opening locations for Case 21 (dimensions in meters)

The velocity at the inlet opening into the domain is uniformly equal to 1 m/s. This air is at a temperature of 21.2°C. Air flow issuing from the top section of the inlet opening has a tendency to descend as it is progresses towards the towers due to the density difference between the surrounding air at this height and the cooling air. Flow exiting the inlet opening near the bottom of the inlet opening also has a tendency to descend, but the degree is much smaller as the temperature difference between the surrounding air at this level and the cooling air is much smaller at this height. As a result of the flow dropping, the highest overall mass flow rate and lowest maximum gap temperature occurred in Gap 1. The overall mass flow rate though each gap decreased with increasing gap number for Gaps 1 to 9. The net mass flow rate through these gaps was sufficient, however, so that

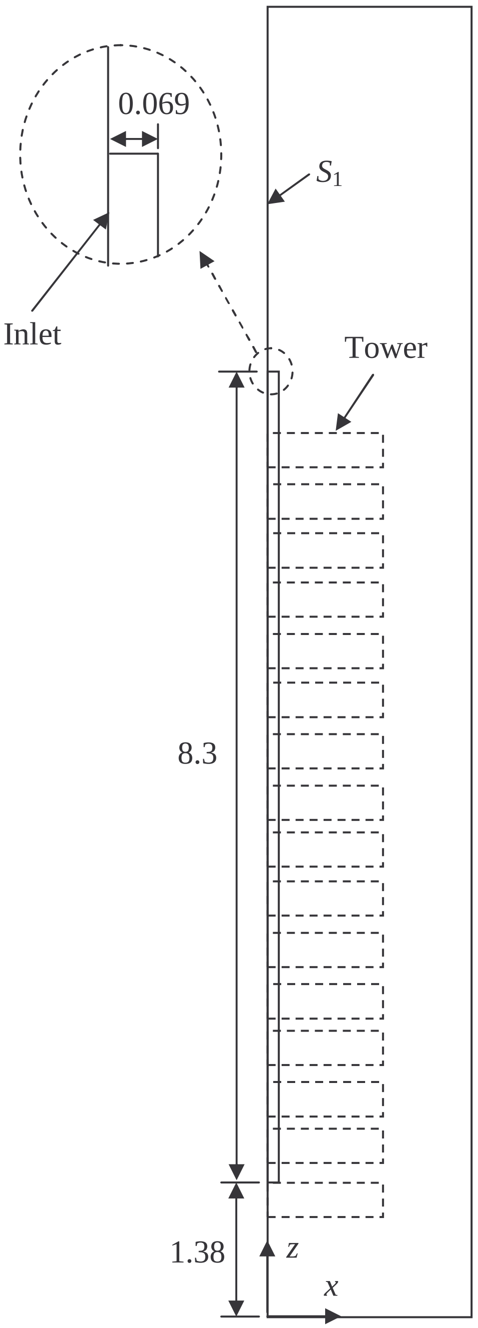

Figure 6.43: Elevation view of the computational domain showing inlet opening locations for Case 21 (dimensions in meters)

the maximum temperature in Gaps 1 to 9 was 55.65°C, occurring in Gap 7. In Gaps 10 to 15, however, there was a higher mass flow rate entering the gap through plane P2

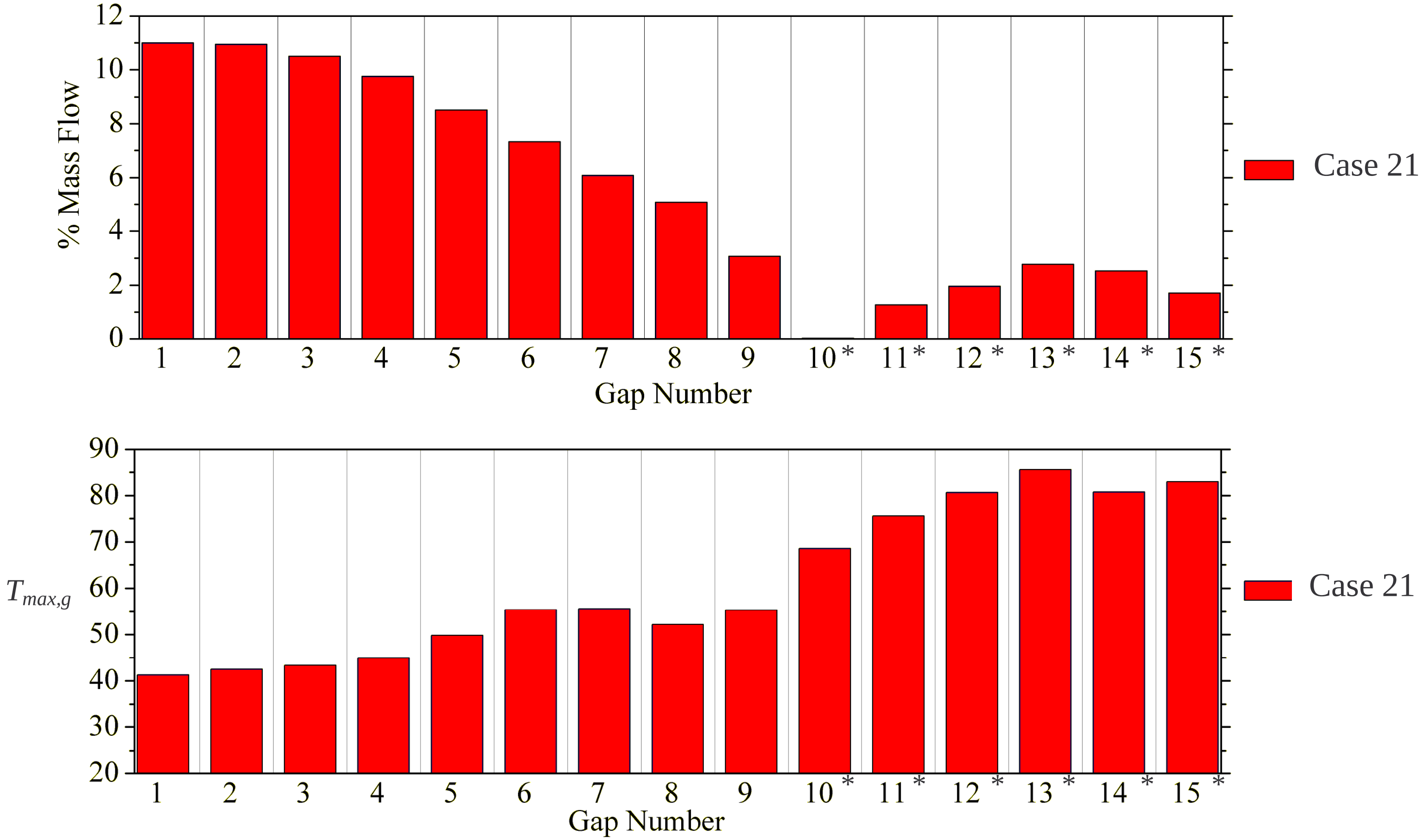

Figure 6.44: Percentage of inlet mass flow rate and corresponding maximum temperature in each gap for Case 21

and exiting the gap through P4. This is the reverse flow pattern of Gaps 1 to 9. In Case 1, the inlet air was directed in an upwards direction, and as a result, the inlet air not entering the gaps formed a plume of air rising towards the ceiling near P4. Another plume of air was formed near P2 as a result of the rising warm air exiting the gaps. As a result, hot air was effectively trapped in the gaps by the two rising plumes with little or none of the cooling air penetrating the gap. In this case (Case 21), however, there was no rising plume near P4 and more air was able to leave the gaps through this plane. Because the magnitude of the mass flow rate of this air was still relatively low, and because very little of the air entering Gaps 10-15 reaches the junction of the two symmetry planes S1 and S3, the maximum temperatures in Gaps 10-15 were relatively high for this case with the maximum domain temperature being 85.54°C in Gap 13. It is interesting to note that Gap 13 is not the gap where the lowest net mass flow rate occurs. The lowest individual gap net mass flow rate occurs in Gap 10 and is equal to 0.03% of the inlet mass flow rate. The maximum temperature in this gap (68.61°C), however, is noticeably lower than in Gap 13. Examination of the flow through this gap shows that some of the air issuing from the inlet opening enters Gap 10 on P4. An almost equal amount of flow exits the same gap on P4 thus effectively negating the net mass flow through the gap. This is an example of an occurrence where the net mass flow rate through a gap can be misleading. In Gap 13 all of the streamlines passing through P4 are exiting the gap.

Case 21 achieved a 9.83°C reduction in maximum domain temperature compared with Case 1. This was, however, higher than the maximum temperature in several of the cases studied for CD1 with the same mass flow rate and the inlet opening located on the floor.

6.11 Computational Domain 2

As mentioned in Chapter 3, CD2 makes use of two symmetry planes, S1 and S2, in order to decrease the computational effort. Symmetry plane S3 is not used in CD2. As a result, half of one tower is modeled, as shown in Figures 3.1 and 3.2b. Also, the inlet opening and the outlet opening are not symmetrical with S3 for CD2.

Obtaining a converged steady-state solution for CD2 proved to be much more difficult than for CD1. Because one-half of a tower is modeled instead of one-quarter, approximately double the number of nodes is required for CD2 than for CD1. In addition to this, convergence, in general, proved to be more difficult to achieve for CD2, with many simulations not reaching steady state conditions even after what should have been a sufficient number of timesteps. Instead, these solutions exhibited oscillations in the residuals of the governing equations from timestep to timestep. A possible explanation for the increased difficulty in obtaining convergence is that the flow is less restricted in CD2 compared with CD1. Flow within CD2 has double the area to travel in, and the gaps between the blocks themselves have three planes in which the flow can pass through instead of only two for CD1. This increased flow freedom creates more possible paths for the flow which may make achieving a steady state solution inherently more difficult. The oscillations in the residuals of the governing equations were the largest in the gaps with the lowest mass flow rates. When the effects of buoyancy were not modeled, the oscillations diminished, and achieving a steady-state solution was possible for all cases studied.. Although a total of twelve cases were attempted for CD2, a converged steady-state solution was achieved for only two cases with this geometry (with buoyancy effects modeled) because of the aforementioned difficulties. Although a converged solution was not obtained for the other cases of CD2, valuable insight can be still be obtained by looking at the flow patterns of the non-converged trial computations. A discussion of a sample of these computations is presented in Appendix G.

6.11.1 Dimensions and Planes for Computational Domain 2

In addition to S1, three additional planes were created for plotting purposes with CD1. The location of these planes is described graphically in Figure 6.45 and summarized in Table 6.12.

6.11.2 Cases 22 and 23

When compared with each other, the results for Cases 22 and 23 examine the effect of varying the inlet opening area and inlet velocity (under the constraints of Computational Domain 2) on the velocity and temperature distribution in the valve hall. When compared with the results of Computational Domain 1, Cases 22 and 23 examine the effect of locating the inlet opening on one of the side walls. In both of these cases, the outlet opening is identical and is located on the ceiling of the room on the opposite side of the *x* axis to the inlet opening.   The inlet mass flow rate is also identical for both cases and is equivalent to the mass flow used in Case 1[*]. Plan and elevation views of the computational domain for Cases 22 and 23 showing the location of the inlet openings are shown in Figures 6.46 and 6.47, respectively. Table 6.13 summarizes Cases 22 and 23.

For CD2, there are three planes in which flow can enter or exit through a gap. Because of this, the method that was used for CD1 for determining the average net mass flow rate through a gap cannot be used for CD2.

---

[*] The actual inlet mass flow rate used is double that of Case 1 to account for the fact that one-half of a tower is modeled instead of one quarter of a tower

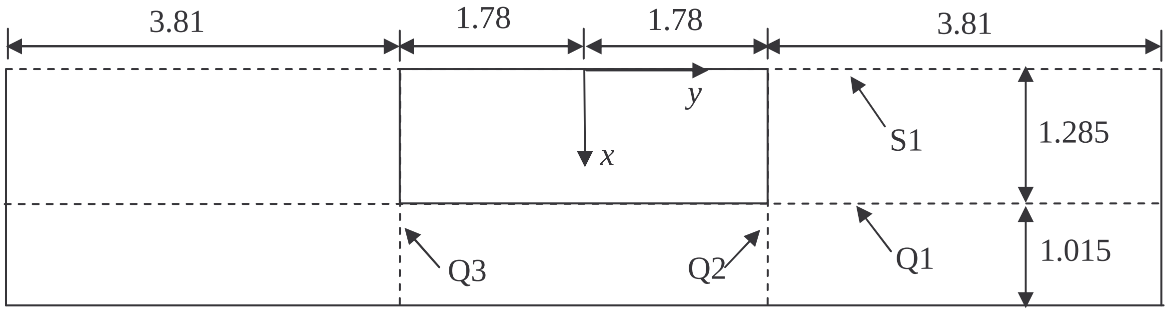

Figure 6.45: Locations of Q1 to Q3 for Computational Domain 2

Table 6.12: Definition of planes used to present the results for Computational Domain 2

Plane	x (m)	y (m)	z (m)
Q1	1.285	−5.59 - 5.59	0 - 13.35
Q2	0 - 2.3	1.78	0 - 13.35
Q3	0 - 2.3	−1.78	0 - 13.35

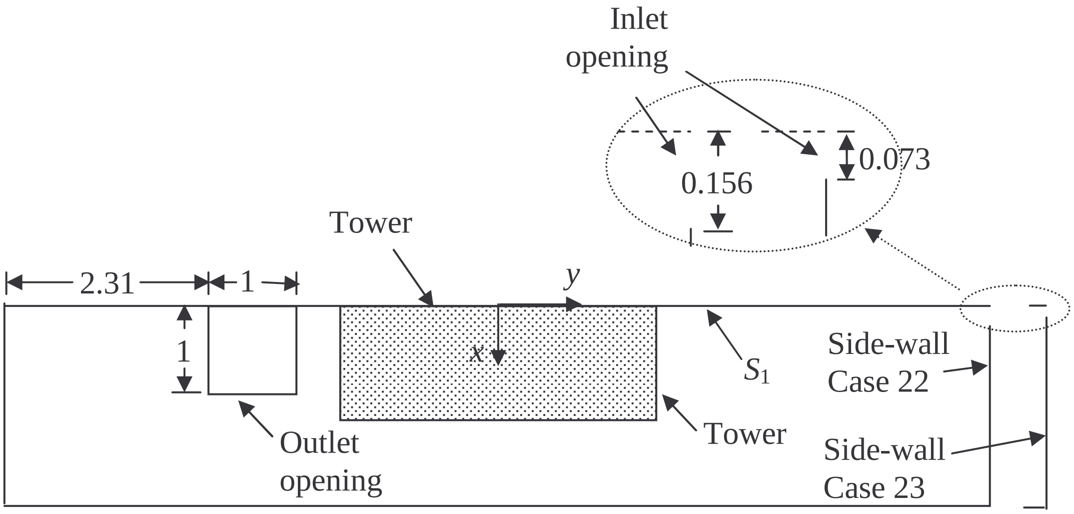

Figure 6.46: Plan view showing the inlet and outlet openings for Cases 22 and 23 (dimensions in meters)

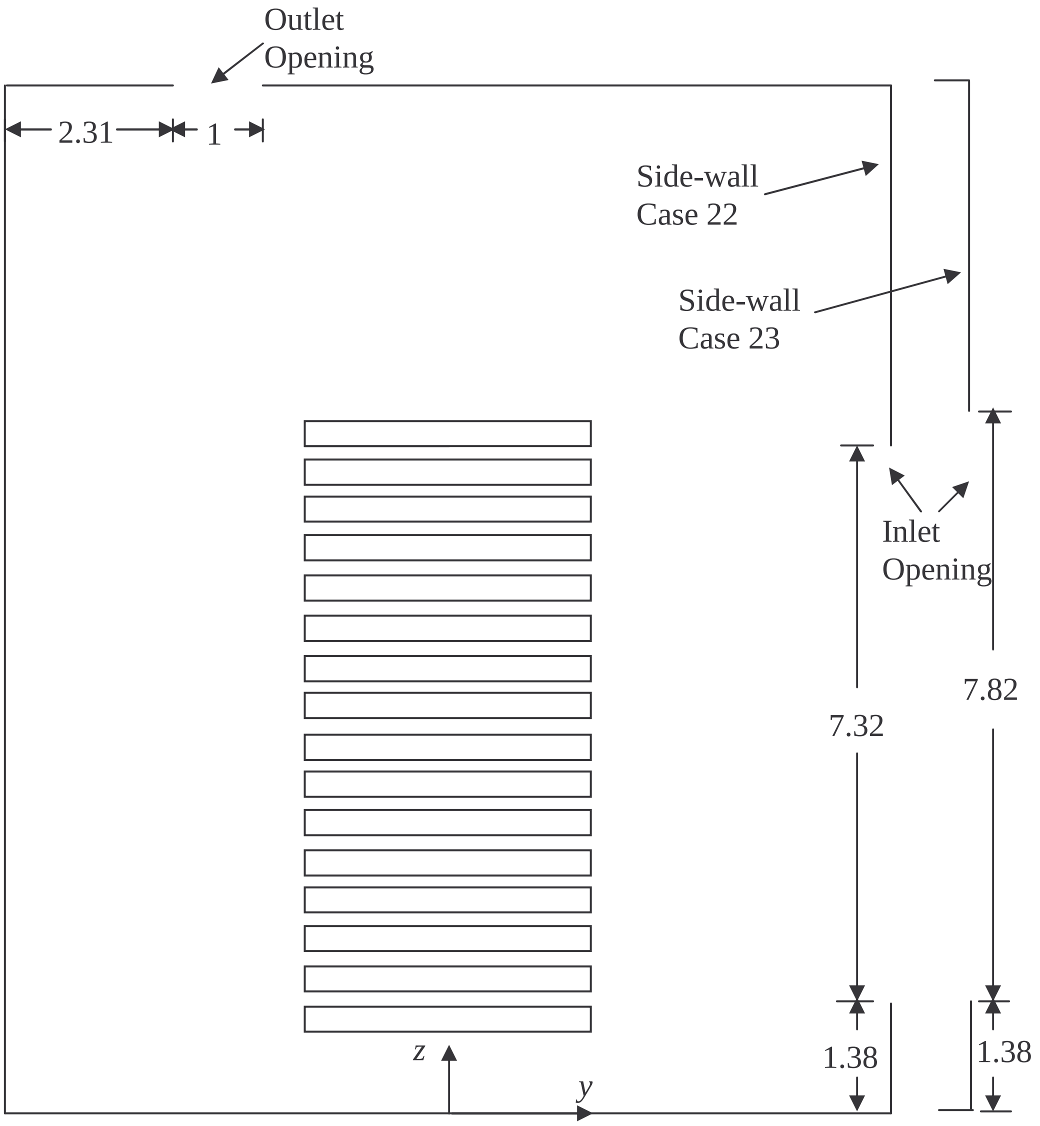

Figure 6.47: Elevation view showing the inlet and outlet openings for Cases 22 and 23 (dimensions in meters)

Table 6.13: Summary of Cases 22 and 23

Case	L_7 (m)	L_8 (m)	L_9 (m)	L_{10} (m)	L_{11} (m)	L_{12} (m)	$\left(\frac{\dot{m}_i}{2\dot{m}_{i,c1}}\right)^*$	θ (deg)	$\left(\frac{A_i}{2A_{i,c1}}\right)^*$	$\left(\frac{V_j}{V_{j,c1}}\right)^*$	$T_{max,g}$ (ºC)	Gap
22	1.38	7.32	0.156	2.31	1	1	1	90	2.183	0.397	62.75	12
23	1.38	7.82	0.073	2.31	1	1	1	90	1.091	0.795	50.11	15

* $\dot{m}_{i,c1}$ = 0.684 kg/s $A_{i,c1}$ = 0.2616 m^2 $V_{j,c1}$ = 2.516 m/s

Figure 6.48 shows the net mass flow rates entering and exiting each of the three planes on each gap for Case 22 and 23. For each case, the first column for each gap represents the mass flow entering or exiting the tower on Q1, the second column for each gap represents the mass flow entering or exiting the tower on Q2, and the third column for each gap represents the mass flow entering or exiting the tower on Q3. A net mass flow rate out of the gap on a given plane was given a positive sign convention, and a net mass flow into a gap on a given plane was given a negative sign convention. Since mass must be conserved in each gap, the net mass flow rates entering a gap must also be equal to the net mass flow rates exiting the same gap. Figure 6.48 also shows the corresponding maximum temperature in each gap.

In Case 22, flow issues from the inlet opening into the domain at 1 m/s and 21.2°C. As in Case 21, air flow issuing from the near the top of the inlet opening has a tendency to descend as it is progresses towards the tower due to the density difference between the surrounding air at this height and the cooling air. Flow from the bottom of the inlet opening also has a tendency to descend, but the degree is much smaller as the temperature difference between the surrounding air at this level and the cooling air is much smaller at this height. For Gaps 1 to 12, the net mass flow through the gaps on Q2 is into the gaps. In the first nine gaps, the net flow rate entering the gap on Q2 decreases with each successive gap. At the same time, more of the flow exits the gaps through Q1 with less flow passing through the entire gap to exit at Q3. In Gaps 9 to 12, the net flow rate through Q3 is actually into the gap and the flow rate into the gaps on Q2 increases slightly. The inlet air jet is below the level of Gap 13 by the time it reaches the tower.

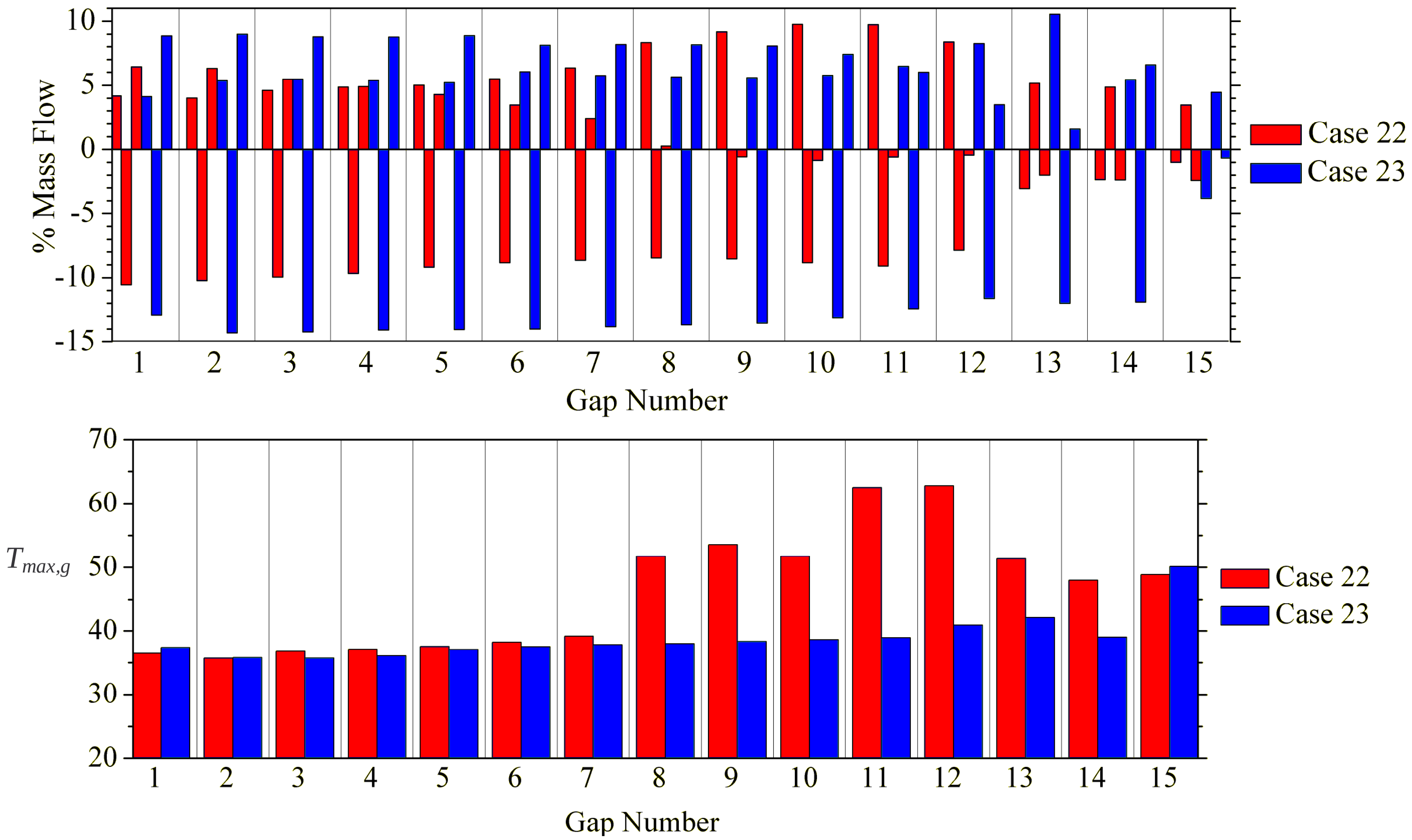

Figure 6.48: Percentage of inlet mass flow rate and corresponding maximum temperature in each gap for Cases 22 and 23

As a result, none of the air from the inlet opening passes directly through Gaps 13 to 15 without passing through other gaps first. Flow that has already passed through the tiers on either Q1 or Q3 enters Gaps 13 to 15 on these same planes and exits the gaps through Q2. This is the completely reversed flow pattern that occurs in Gaps 1 to 9. Despite the fact that none of the of the air passing though Gaps 13 to 15 was directly issued from the inlet opening, the maximum temperatures in these gaps is still relatively low, with the maximum temperature in Gaps 13 to 15 being 51.36°C. There are a number of factors that contribute to the reversal of flow in Gaps 13 to 15. First, flow that has already exited through the lower gaps of the tower through either Q1 or Q3 rises because it is warmer than the surrounding air. As a result, there is a large amount of air passing next to the openings of Gaps 13 to 15 on Q1 and Q3. This air is naturally drawn into the tower by natural convective forces because the temperature of this air is lower than the temperature of the air within the gap. At the entrance to the gaps on Q2 for Gaps 13 to 15, there is no rising plume of air because the inlet air descends as it approaches the tower. As a result, hot air is able to exit the gap on this plane. A current is created as a result of the air entering these gaps on Q1 and Q3 and exiting through Q2. Because cooling air passes though the entire length of the tier before exiting, no hot spots occur in these gaps.

In Case 21, the net flow pattern was also reversed for a number of gaps. The maximum temperatures in these gaps, however, were much higher for this case than for Case 22. The reason for this increase is that the net mass flow rate through these gaps was much smaller for Case 21 than for Case 22. Furthermore, for Case 21 when there is reversed flow, the air flow does not penetrate to the junction of the two symmetry planes (S1 and

S3) before exiting the gaps on P4 (as it does in Case 22) and as a result, the temperatures near the junction of S1 and S3 are considerably higher for Case 21 than for Case 22.

The maximum domain temperature for Case 22 is 62.75°C, occurring in Gap 12. The reason for the maximum temperature occurring in Gap 12 (and not in Gaps 13 to 15) is that the flow entering Q2 on this gap does not penetrate very far into the gap before exiting through Q1. In addition, very little flow enters Gap 12 on Q3. This creates a hot spot in this gap near Q3.

In Case 23, flow exits the inlet opening into the domain at 2 m/s and 21.2°C. This is double the velocity that was used in Case 22. The height of the inlet opening (L_8) was also increased compared with Case 22. The increases in the inlet velocity and the height of the inlet opening were made at the expense of the length of the inlet opening in the x direction (L_9) which was decreased in order to maintain the same mass flow rate as Case 22.

As a result of the increased inlet velocity and increased height of the inlet opening, flow directly issuing from the inlet opening enters more gaps for Case 23 than in Case 22. The net mass flow rate through the gap entrance on Q2 is into the gaps for Gaps 1 to 14. The net flow rate through the same gaps on Q3 is out of the gaps because some of the cooling air that enters these gaps on Q2 passes through the entire gap and exits on Q3. As a result, no hot spots occur in any of these gaps. The maximum temperature in Gaps 1 to 14 is 42.11°C, occurring in Gap 13.

The inlet air jet is below the level of Gap 15 by the time it reaches the tower in Case 23. As a result, none of the air from the inlet opening passes directly through Gap 15 without first passing through other gaps. For Gap 15, the flow pattern is reversed compared with the first fourteen gaps with a net mass flow entering the gaps on Q1 and Q3 and exiting the gaps on Q2. The explanation for the flow reversal in Gap 15 for Case 23 is the same as in Case 22. The maximum temperature in Gap 15 is 50.11°C. This is also the maximum temperature in the domain.

When compared with the results of the cases for CD1 that used the same equivalent mass flow rate, the results of Cases 22 and 23 demonstrate that it is possible to greatly improve cooling effectiveness in the valve hall by using a single inlet opening on one of the side walls of the domain instead of using inlet openings that are symmetrical with S3, as was done for CD1. The maximum domain temperature for Case 23 is 45.26°C lower than the maximum domain temperature for Case 1. When compared with Case 18 (the best performing case for CD1 with the same equivalent mass flow rate) the maximum temperature for Case 23 is still 27.99ºC lower.

When compared with each other, the results of Cases 22 and 23 demonstrate that varying the size of the inlet opening and inlet velocity with a constant mass flow rate can have a significant effect on the velocity and temperature distribution as well as the cooling effectiveness in the valve hall. When the non-converged trial computations for CD2 (Appendix G) are also included in the comparison, the results show that placing the inlet opening on one of the side walls with the same equivalent inlet mass flow rate as Case 1 does not guarantee cooling effectiveness in the valve hall as the two examples of non-converged solutions appear to perform worse than many of the Cases for CD1 with the same mass flow rate. More work needs to be done on the method of injection used in Cases 22 and 23 in order to achieve better understanding of the physics involved and to determine the operating conditions that produce better cooling effectiveness.

Chapter 7

SUMMARY, CONCLUSIONS, AND RECOMMENDATIONS

7.1 Summary

A numerical investigation was conducted in order to model the three-dimensional, turbulent flow of air in a thyristor valve hall. The effects of inlet and outlet opening geometry, inlet air mass flow rate, and inlet air angle on the thermal performance for the air-side cooling of the thyristor valve hall geometry were examined. Slight modifications were made to the actual valve hall geometry in order to decrease the computational effort. These modifications (shown in Figures 3.1, 3.2a, and 3.2b) allowed for the use of symmetry planes which decreased the size of the computational domain by either a factor of six or twelve (depending on the computational domain used) while not significantly altering the ability of the model to capture the physics of the flow and heat transfer phenomena. Two computational domains were used, depending on the location of the inlet and outlet openings. When the inlet and the outlet openings were symmetrical with the *x* axis, Computational Domain 1 was used (Figures 3.1 and 3.2a). When the inlet and the outlet openings were not symmetrical with the *x* axis, Computational Domain 2 was used (Figures 3.1 and 3.2b).

A base case was first simulated and the results were compared with experimental data taken in the valve hall. Reasonably good agreement with the experimental data was achieved. The results of this base case were also presented and discussed in detail. The results of this base case indicate that higher than desired maximum temperatures between some of the gaps occur due to deficiencies in the local mass flow rates through the gaps containing the high maximum temperatures. Converged steady-state solutions were also presented for a total of twenty-three unique cases on the two computational domains in terms of a parametric study.

7.2 Conclusions

The following conclusions were drawn from the results of the two computational domains:

1. Varying the inlet air angle with inlets on the bottom wall can have a large effect on the cooling effectiveness in the valve hall. For a given inlet opening size, location, and inlet mass flow rate, there appears to be an optimum inlet angle at which the maximum domain temperature is minimized. This angle is not the same for every inlet opening size and location. The angles in which the mass flow rates in all the gaps were most evenly distributed were the cases that performed the best for a given inlet opening size, location, and inlet mass flow rate.

2. Increasing the inlet mass flow rate improved the cooling effectiveness for all cases studied for inlets on the bottom wall. The degree to which the cooling effectiveness was improved, however, was not always the same for all cases. When comparing Case 2 to Case 8 for example, the maximum temperature in the domain was decreased by over 46°C by doubling the mass flow rate with all other parameters equal. When comparing Case 1 to Case 6, however, the maximum temperature in the domain decreased by less than 3°C by doubling the mass flow rate with all other parameters equal. In order to increase the cooling effectiveness in the room by increasing the inlet mass flow rate, it is important not only that the inlet mass flow increases, but also that the mass flow rates between the gaps also increases. In particular, the mass flow rate in the gap with the

highest temperature must increase in order to decrease the maximum temperature in the domain.

3. Increasing the inlet aspect ratio ($R_A = L_2 / 2L_3$) of the bottom wall inlet opening with all other parameters equal had the effect of increasing the cooling effectiveness in the valve hall for all cases studied. This increase in aspect ratio increased the dimension of the inlet opening perpendicular to the tower. As a result, the jet issuing from the inlet spread out over more gaps.

4. For bottom wall inlets, decreasing the area of the inlet opening/increasing the inlet velocity with a constant mass flow rate improved the cooling effectiveness in some cases, but also decreased the cooling effectiveness in others.

5. For bottom wall inlets, decreasing the mass flow rate by decreasing the area of the inlet opening, while maintaining the jet velocity did not preserve the cooling effectiveness in the valve hall that was observed when the mass flow rate was double that of Case 1. While the jet velocity was an important factor in the overall cooling effectiveness, the inlet mass flow rate appears to be a more important factor.

6. Dividing the bottom wall inlet opening into two regions each with different inlet air angles and mass flow rates did not improve cooling effectiveness for the two cases studied (Cases 19 and 20) . In fact, for these cases the results show that it is more effective to direct all of the inlet air through the region furthest away from the towers (as in Case 18) than to divide the inlet air between the two regions.

7. Locating the inlet opening on the side wall for Computational Domain 1 (Case 21) improved the cooling effectiveness in the valve hall when compared with Case 1. The maximum domain temperature in Case 21 was approximately 10°C lower than in Case 1. The maximum domain temperature in this case, however was higher than many of the cases for Computational Domain 1 with the same inlet mass flow rate in which the inlet was located on the floor.

8. The results of Computational Domain 2 show that it is possible to greatly improve the cooling effectiveness in the valve hall by using a single inlet opening on one of the side walls of the domain instead of using inlet openings that are symmetrical with S3. The maximum domain temperature for Case 23 is lower than the maximum domain temperature for Case 1 by more than 45 ºC. When compared with the best performing case for Computational Domain 1 with the same equivalent mass flow rate (Case 18), the maximum temperature for Case 23 is still approximately 28 ºC lower.

9. The results of Computational Domain 2 also show that varying the size of the inlet opening to increase inlet velocity with a constant mass flow rate can have a large effect on the velocity and temperature distribution as well as the cooling effectiveness in the valve hall. Placing the inlet opening on one of the side walls with the same equivalent inlet mass flow rate as in Case 1 does not guarantee improved cooling effectiveness in the valve hall.

7.3 Recommendations

Recommendations are proposed for immediate modifications to the air cooling system and for future work.

7.3.1 Possible Immediate Modifications to the Air Cooling System

Based on the conclusions above, three possible solutions to the problem of improving the air-side cooling effectiveness in the current valve hall are suggested. A detailed cost analysis would be required before implementation to determine the increased fixed and/or operating costs associated with each of the possible solutions compared with the possible benefits. The three possible solutions are as follows

1. Modify the size of the inlet air openings and the inlet air angle in the valve hall in order to match the conditions of Case 18. This modification would likely result in a moderate increase in cooling effectiveness in the valve hall without requiring larger air conditioning units. The inlet air fans, however, would likely have to be upgraded to account for the increase in static pressure due to the smaller inlet openings used in this case.

2. Modify the inlet air angle and double the inlet mass flow rate in the valve hall to match the conditions of Case 8. This modification would likely result in a large increase in cooling effectiveness in the valve hall but would require increased air handling capacity and would result in increased operating costs.

3. Modify the inlet location in the valve hall to match the conditions of Case 23. This modification will likely result in a large increase in cooling effectiveness in the valve hall without requiring larger air conditioning units but would require modification to the inlet air ducts to accommodate side wall located inlet ducts instead of bottom wall located ducts.

7.3.2 Study Areas of Further Work

Possible study areas for further work are as follows:

1. Continue studying the air-side cooling in the current valve hall. The increased understanding of the problem gained in this study combined with increased computational resources could be used to perform a more realistic simulation of the current valve hall configuration. In particular, if one full tower was modeled instead of the one-quarter or one-half tower modeled in this study, the inlet openings could be placed offset with the tower centerline as they are in the current valve hall. Also, instead of modeling the individual tiers of the tower as single rectangular blocks, the tiers could be modeled with holes to allow air to pass from gap to gap of the tower as in the actual valve hall.

2. Investigate further the air-side cooling for future possible thyristor valve hall designs. In such a study, one parameter that could be investigated is the location of the towers in the room. For example, if the tower was located closer to the inlet opening with the inlet openings defined as in Computational Domain 2, the problem of the flow descending as it approaches the tower could likely be avoided resulting in more even flow distribution through all the gaps in the tower thus increasing the cooling effectiveness in the valve hall. Another parameter that could be investigated is the height of the gaps between the blocks. If this height was increased the heat generated between the blocks would have a larger area in which to dissipate and cooling effectiveness would also likely increase.

REFERENCES

Afrid, M & Zehbib, A, 1991, Three-dimensional laminar and turbulent natural convection cooling of heated blocks, *Numerical Heat Transfer, Part A: Applications*, vol. 19, no. 4, pp. 405-424.

Barth, T.J. & Jesperson, D.C., 1989, The design and application of upwind schemes on unstructured meshes, *AIAA Paper 89-0366*.

Bellache, O, Ouzzane, M, & Galanis, N, 2005, Coupled conduction, convection, radiation heat transfer with simultaneous mass transfer in ice rinks, *Numerical Heat Transfer, Part A: Applications*, vol. 48, no. 3, pp. 219-238.

Berg, J.R., Ormiston, S.J., & Soliman, H.M., 2006, Prediction of the flow structure in a turbulent rectangular free jet', *International Communications in Heat and Mass Transfer*, Accepted February 2006.

Bhoite, M.T., Narasimham, G.S., & Krishna-Murthy, M.V. 2005, Mixed convection in a shallow enclosure with a series of heat generating components, *International Journal of Thermal Sciences*, vol. 44, no. 2, pp. 121-135.

Grotjans, H. and Menter F.R., 1998, Wall functions for general application CFD codes, *ECCOMAS 98 Proceedings of the Fourth European Computational Fluid Dynamics Conference*, pp.1112-1117.

Launder, B.E. & Spalding, D.B., 1974, The numerical computation of turbulent flows, *Computational Methods and Applied Mechanics Engineering*, vol. 3, pp. 269-289.

Li, H.F. & Chung, B.T., 1994, Mixed convection in a vertical channel with internally heated rectangular blocks, *American Society of Mechanical Engineers, Heat Transfer*, vol. 274, pp. 9-16.

Manitoba Hydro, 2002, Dorsey Converter Station, viewed 1 April 2006, http://www.hydro.mb.ca/our_facilities/cs_dorsey.pdf.

Merrikh, A.A. & Lage, J.L., 2005, Natural convection in an enclosure with disconnected and conducting solid blocks, *International Journal of Heat and Mass Transfer*, vol. 48, no. 7, pp. 1361-1372.

Moreno, R. & Ramaswamy, B., 1997, Numerical study of three-dimensional incompressible thermal flows in complex geometries, Part II: computational studies, *International Journal of Numerical Methods for Heat & Fluid Flow*, vol. 7, no. 5, pp. 497-524.

Patankar, S.V., 1980, Numerical Heat Transfer and Fluid Flow, Hemisphere Publishing Corporation, New York.

Prakash, C. & Patankar, S.V., 1985, A control volume-based finite-element method for solving the Navier-Stokes equations using equal-order velocity-pressure interpolations, *Numerical Heat Transfer*, vol. 8, pp. 259-280.

Quinn, W.R., 1992, Turbulent free jet flows issuing from sharp-edged rectangular slots: The influence of slot aspect ratio, *Experimental Thermal and Fluid Science*, vol. 5, pp. 203-215.

Ramirez-Iraheta, O.A., Soliman H.M., and Ormiston S.J., 2006, Effective Cooling of Heat Generating Stacks in a Cavity with Openings, *Heat and Mass Transfer*, vol. 42, pp. 398-410.

Rhie, C.M. & Chow, W.L., 1983, Numerical study of the turbulent flow past an airfoil with trailing edge separation, *AIAA Journal*, vol. 21, pp. 1525-1532.

Schneider, G.E. & Raw, M.J., 1987, Control volume finite-element method for heat transfer and fluid flow using colocated variables: I – Computational procedure; II – Application and validation, *Numerical Heat Transfer*, vol. 11, pp. 363-400.

Shuja, S.Z., Yilbas, B.S., & Igbal, M.O., 2000, Mixed convection in a square cavity due to heat generating rectangular body - Effect of cavity exit port locations, *International Journal of Numerical Methods for Heat & Fluid Flow*, vol. 10, no. 8, pp. 824-841.

Shuja, S.Z., Iqbal, M.O., and Yilbas, B.S., 2001, Natural Convection in a Square Cavity Due to a Protruding Body – Aspect Ratio Consideration, *Heat and Mass Transfer*, vol. 37, pp. 361-369.

Wilcox, D.C., 1988, Multiscale model for turbulent flows, *American Institute of Aeronautics and Astronautics Journal*, vol. 26, pp. 1311-1320.

Appendix A

TURBULENT FREE JET FLOW PREDICTIONS

Prediction of the flow structure in a turbulent rectangular free jet

J.R. Berg, S.J. Ormiston, H.M. Soliman*

Department of Mechanical and Manufacturing Engineering, University of Manitoba,
Winnipeg, Manitoba, Canada R3T 5V6

Abstract

A numerical analysis is conducted for turbulent flow of a rectangular free jet with an aspect ratio of 2:1. The computations were performed using two standard two-equation turbulence models (the k-ε and the k-ω models). Two inflow boundary conditions were evaluated with each model: a uniform inlet velocity profile and a profiled inlet velocity fitted to experimental data. The results show that the k-ε model with the profiled inlet velocity succeeded in predicting the main features of the flow, including the vena contracta and the saddle-shaped velocity profiles in the near-field region, and the rate of velocity decay in the far-field region.

Keywords: Rectangular free jet; Turbulence; Numerical simulation; k-ε model; k-ω model

1. Introduction

Turbulent rectangular jets can be found in a great deal of engineering applications. Some examples are in the propulsion of aircrafts, the dispersion of pollutants, and the cooling of electronic packages. While the flow characteristics of rectangular jets issuing from sharp-edged slots have been studied in a number of experimental investigations (e.g., [1–7]), very few numerical simulations have been conducted on these turbulent three-dimensional jets due to the high cost associated with these simulations. The experimental investigations have identified some unique flow features associated with rectangular jets issuing from sharp-edged slots. In the near-field region downstream from the slot, experiments have demonstrated the existence of a vena contracta effect resulting in an initial acceleration of the flow in the center of the jet. As well, off-center velocity peaks (saddle-backed velocity profiles) were noted along the major axis in the near-field region. Further downstream (in the far-field region), the stream-wise velocity decays at a rate that is dependent on the jet's aspect ratio. Most of the numerical simulations conducted so far have failed in predicting these flow features, particularly in the near-field region.

Miller et al. [8] simulated turbulent jets of circular and non-circular (elliptic, rectangular, and triangular) cross sections with identical equivalent diameters. When compared with the circular jet, the non-circular jets were found to provide more efficient mixing and therefore, an increase in spread and entrainment rates. These simulations were not compared with experimental results. Wilson and Demuren [9] performed a finite-difference numerical simulation on a three-dimensional rectangular jet with an aspect ratio of 2:1 using three different turbulence conditions at the jet inlet. They observed that the turbulence conditions at the jet inlet can have large effects on the flow structure downstream; however, no experimental validation was provided. Holdo and Simpson [10] examined a rectangular turbulent jet with an aspect ratio of 10:1 using large eddy simulation with four different boundary conditions at the jet inlet. When compared with the experimental results of Quinn et al. [3], the results of Holdo and Simpson show a good agreement in the far-field region, but they do not show the initial acceleration of the jet in the stream-wise direction within the first five equivalent diameters of the flow field.

The purpose of the present study is to explore the use of two-equation turbulence models in simulating the turbulent flow field in free jets issuing from sharp-edged rectangular slots. More specifically, can this approach of turbulence modeling succeed in predicting the main features of the flow, including the vena contracta and the saddle-shaped velocity profiles in the near-field region, and the rate of velocity decay in the far-field region?

2. Mathematical formulation

The geometry under consideration, together with the coordinate system is shown in Fig. 1. A turbulent free jet discharges from a rectangular vent of dimensions ($2L_{ya} \times 2L_{xa}$). Because of symmetry, only one quarter of the jet domain is modeled in this study. The planes $x = 0$ and $y = 0$ in Fig. 1 are symmetry planes, while the plane $z = 0$ is a solid wall except for the vent area. A computational domain was defined with dimensions L_x, L_y, and L_z in the lateral (x), span-wise (y), and stream-wise (z) directions, respectively. The jet exits through an open plane at $z = L_z$. Values of L_x, L_y, and L_z were selected such that they all exceeded 60 R_e, where R_e is the equivalent radius given by: $R_e = \sqrt{4L_{xa}L_{ya}/\pi}$.

2.1. Governing equations

The flow is considered to be three-dimensional, steady, isothermal, and turbulent. The fluid is incompressible and Newtonian, with constant density, ρ, and dynamic viscosity, μ. Under these conditions, only the time-averaged equations for the conservation of momentum and mass are required. These governing equations (also known as the Reynolds-averaged Navier-Stokes model) can be expressed in tensor form as:

Momentum:
$$\rho\left(u_j\frac{\partial u_i}{\partial x_j}\right)=-\frac{\partial P}{\partial x_i}+\frac{\partial}{\partial x_j}\left(\mu\frac{\partial u_i}{\partial x_j}-\rho\overline{u_i'u_j'}\right) \tag{1}$$

Continuity:
$$\frac{\partial u_i}{\partial x_i}=0 \tag{2}$$

Where, x_i are the Cartesian coordinate directions ($x_1 = x$, $x_2 = y$, $x_3 = z$), u_i are the Cartesian time averaged velocity components with the commonly used over-bars removed for convenience ($u_1 = u$, $u_2 = v$, $u_3 = w$), $\overline{u_i'u_j'}$ is the Reynolds stress tensor, and P is the pressure.

2.2. Turbulence models

Two eddy-viscosity turbulence models were used in this study. They are: the standard k-ε model developed by Launder and Spalding [11] and the standard k-ω model developed by Wilcox [12]. The eddy-viscosity models assume the following relationship for the Reynolds stresses in Eq. (1):

$$\rho\overline{u_i'u_j'}=-\mu_t\left(\frac{\partial u_i}{\partial x_j}+\frac{\partial u_j}{\partial x_i}\right)+\frac{2}{3}\rho\delta_{ij}k \tag{3}$$

where μ_t is the eddy viscosity, δ_{ij} is the Kronecker delta, and k is the turbulent kinetic energy per unit mass.

In the k-ε model, the eddy viscosity is computed using the relation:

$$\mu_t=C_\mu\rho\frac{k^2}{\varepsilon} \tag{4}$$

where C_μ is a constant and the values of k and the dissipation, ε, come from the solution of the following transport equations:

$$\rho u_i\frac{\partial k}{\partial x_i}=\frac{\partial}{\partial x_i}\left(\mu+\frac{\mu_t}{\sigma_k}\right)\frac{\partial k}{\partial x_i}+P_k-\rho\varepsilon \tag{5}$$

$$\rho u_i\frac{\partial \varepsilon}{\partial x_i}=\frac{\partial}{\partial x_i}\left(\mu+\frac{\mu_t}{\sigma_\varepsilon}\right)\frac{\partial \varepsilon}{\partial x_i}+P_k+\frac{\varepsilon}{k}(C_{\varepsilon 1}P_k-C_{\varepsilon 2}\rho\varepsilon) \tag{6}$$

and the turbulence production term, P_k, is modeled using:

$$P_k=\mu_t\frac{\partial u_i}{\partial x_j}\left(\frac{\partial u_i}{\partial x_j}+\frac{\partial u_j}{\partial x_i}\right) \tag{7}$$

The values for the k-ε equation constants used in this work are $C_\mu = 0.09$, $C_{\varepsilon 1} = 1.45$, $C_{\varepsilon 2} = 1.9$, $\sigma_k = 1.0$, and $\sigma_\varepsilon = 1.3$.

In the k-ω model the eddy viscosity is computed using:

$$\mu_t = \rho \frac{k}{\omega} \tag{8}$$

where the values of k and the turbulent frequency, ω, come from the solution of the following transport equations:

$$\rho u_i \frac{\partial k}{\partial x_i} = \frac{\partial}{\partial x_i}\left(\mu + \frac{\mu_t}{\sigma_k} \right)\frac{\partial k}{\partial x_i} + P_k - \beta' \rho k \omega \tag{9}$$

$$\rho u_i \frac{\partial \omega}{\partial x_i} = \frac{\partial}{\partial x_i}\left(\mu + \frac{\mu_t}{\sigma_\omega} \right)\frac{\partial \omega}{\partial x_i} + \alpha \frac{\omega}{k} P_k - \beta\ \rho\ \omega^2 \tag{10}$$

and P_k is the same as in the k-ε model. The values of the constants used in this model are: $\beta' = 0.09$, $\alpha = 5/9$, $\beta = 0.075$, $\sigma_k = 2$, and $\sigma_\omega = 2$.

Scalable wall functions were used in modeling the flow near the wall. This approach is an extension of the method of Launder and Spalding [11] in which the near wall tangential velocity is related to the wall shear stress by means of a logarithmic relation. The basic idea behind the scalable-wall-functions approach is to set a lower limit of 11.06 on the value of y^* used in the logarithmic formulation, where, $y^* = \rho\, u^* \Delta y / \mu$ and $u^* = C_\mu^{0.25} k^{0.5}$. If the calculated value of y^* at a mesh point was less than the set lower limit of 11.06, the value of y^* was adjusted to be equal to 11.06. This approach was found to be helpful in avoiding inconsistencies that may arise from mesh refinement. An upper limit of 100 is also advisable on the value of y^*, and in the present simulation, y^* never exceeded 35.

2.3. Boundary conditions

A symmetry boundary condition was applied on the boundary surface defined by $x = 0$, $0 \le y \le L_y$, and $0 \le z \le L_z$ and the boundary surface defined by $y = 0$, $0 \le x \le L_x$, and $0 \le z \le L_z$. An opening boundary condition with flow directed normal to the face was applied on the surface $x = L_x$, $0 \le y \le L_y$, and $0 \le z \le L_z$, the surface $y = L_y$, $0 \le x \le L_x$, and $0 \le z \le L_z$, and the surface $z = L_z$, $0 \le x \le L_x$, $0 \le y \le L_y$.

The inlet face defined by $z = 0$, $0 \le x \le L_x$, and $0 \le y \le L_y$ is composed of two regions: the inlet region at $0 \le x \le L_{xa}$, $0 \le y \le L_{ya}$ and the wall region defined by the remainder of the face. On the wall region, a stationary wall (no-slip) boundary condition was prescribed. On the inlet region, two different inlet boundary conditions were used: a uniform velocity profile with specified turbulence intensity or a prescribed velocity profile with specified turbulence intensity.

The turbulence intensity specified in both cases was I = 0.5% and k was computed from $k = 1.5 I^2 W^2$. For the k-ε model, ε was computed from $\varepsilon = (\rho C_\mu k^2) / (1000\ I\ \mu)$. For the k-ω model, ω was computed from $\omega = \varepsilon / k$.

3. Numerical solution

Four different simulating methods (SM) were used in the present study:

SM–1: The k-ε turbulence model was used with a uniform inlet-velocity profile,

SM–2: The k-ε turbulence model was used with an inlet velocity that was profiled to fit actual experimental measurements,

SM–3: The k-ω turbulence model was used with a uniform inlet velocity profile, and

SM–4: The k-ω turbulence model was used with an inlet velocity that was profiled to fit actual experimental measurements.

The numerical solution of the governing equations of motion with the above four simulating methods was obtained using the finite volume method of Patankar [13]. Cartesian velocity components were used on a structured, non-staggered grid. Mass conservation discretization was applied on the grid with pressure-velocity coupling based on the work of Rhie and Chow [14], Prakash and Patankar [15], and Schneider and Raw [16]. The high-resolution advection scheme based on the work of Barth and Jesperson [17] was used.

The coupled discretized mass and momentum equations and the turbulence model equations were solved iteratively using additive correction multi-grid acceleration. These computations were performed using a commercial CFD code (CFX–5, version 5.7). Solutions were considered converged when the maximum residual of all the discretized equations was less than 1×10^{-5}.

3.1. Computational mesh

Structured, non-staggered orthogonal grids were generated for the solution domain shown in Fig. 1. In the x-y plane, uniform spacing between nodes was used in the inlet region ($0 \le x \le L_{xa}$, $0 \le y \le L_{ya}$) in both the x and y directions. Beyond the inlet region, a geometrically expanding grid was used with an expansion factor of 1.15 in both the x and y directions. In the z direction, a geometrically expanding grid was used with an expansion factor of 1.1 and the spacing between the first two nodes was made approximately equal to the spacing between nodes in the inlet region of the x-y plane.

Mesh independence tests were performed using three computational grids with the following nodal distributions in the x, y, and z directions, respectively: $45 \times 55 \times 46$ (coarse), $60 \times 80 \times 56$ (medium), and $73 \times 105 \times 60$ (fine). The maximum differences in the centerline velocity (along the z axis) between the coarse and medium grids, and between the medium and fine grids, were

2.94 % and 0.97 %, respectively. Based on these results, the medium grid was selected for all computations in the present investigation.

4. Results and discussion

Numerical results were obtained for an air jet that had the same parameters as a jet that was tested experimentally by Quinn [1]. For the jet under consideration here, the inlet air vent has an aspect ratio of 2:1 with half-lengths of the inlet vent in the x and y directions given by: $L_{xa} = 1.42$ cm and $L_{ya} = 2.84$ cm. The size of the computational domain was selected as $L_x = L_y = L_z = 150$ cm, and since $R_e = 2.266$ cm for this jet, each dimension of the computational domain exceeded 66 R_e.

In obtaining the results corresponding to SM–1 and SM–3, a uniform velocity profile in the stream-wise direction, $w_{in} = 60$ m/s, was imposed at the inlet with both the lateral component of velocity, u_{in}, and the span-wise component of velocity, v_{in}, set equal to zero at this cross-section. For SM–2 and SM–4, prescribed velocity profiles were imposed at the inlet. These prescribed velocity profiles were generated from piecewise curve fits of the experimental data given for the inlet velocity in [1]. The stream-wise centerline velocity at the inlet was set at $w_{cl,in} = 60$ m/s, which matches the experimental value. Figure 2 shows the experimental data given in [1] for the inlet values of w and v, together with the curve fits developed in the present study to match these data. The parameter y_{hlf} used in the abscissa of Fig. 2 is the velocity half width of the jet; the value of y at which $w_{in} = 0.5\, w_{cl,in}$. It is worth mentioning that the cross-sectional average value of the stream-wise inlet velocity, $\overline{w}_{in}$, was found to be very close to the centerline value of $w_{cl,in} = 60$ m/s and that the inlet Reynolds number based on the equivalent diameter ($D_e = 2\, R_e = 4.532$ cm) and the average stream-wise inlet velocity ($\overline{w}_{in} = 60$ m/s) was about 2.08×10^5. In all four simulating methods, the turbulence intensity at the inlet was set at the measured value of $I = 0.5\%$.

Figure 3 shows the near-field stream-wise velocity decay along the jet centerline, as predicted by the four simulating methods used in the present study, along with the data reported by Quinn [1]. The experimental data show a vena contracta effect, which resulted in an initial acceleration of the flow. Figure 3 shows that this phenomenon was well predicted by SM–2, while SM–1 and SM–3 failed in predicting this phenomenon and SM–4 produced good predictions up to $z/D_e \cong 2$ but deviated from the data beyond this location. The results for the inverse stream-wise velocity decay along the jet centerline (including the far-field region) are shown in Fig. 4. These results are presented in terms of $w_{cl,\max}/w_{cl}$, where $w_{cl,\max}$ is the maximum stream-wise velocity along the centerline, which exists downstream of the jet's inlet plane. Figure 4 shows that SM–2 agrees remarkably well with the experimental data in the far-field region. While SM–1 failed to predict the vena contracta effect in the near-field region, as shown earlier, it appears to provide reasonable predictions of w_{cl} in the far-field region. On the other hand, the predictions from SM–3 and SM–4 are in significant deviation from the data. The trends seen in Figs. 3 and 4 suggest that the approach followed in SM–2 has the potential of producing results that are in close agreement with the data. In the following sections, the focus will be on SM–2 (only) and the objective is to assess the ability of this simulating method in predicting other characteristics of the flow.

Two parameters that are often used to characterize mixing in free jets are: the decay rate of the stream-wise velocity in the far-field, K_w, and the kinematic virtual origin of the stream-wise velocity in the far-field, C_w. Values of these parameters are normally obtained by fitting the far-field data, using linear regression, to the following equation:

$$w_{cl,\max} \big/ w_{cl} = K_w \left(z/D_e + C_w \right) \tag{11}$$

The values obtained based on the numerically-predicted velocity field are: $K_w = 0.193$ and $C_w = 3.70$, while the values reported by Quinn [1] based on the measured velocity field are: $K_w = 0.199$ and $C_w = 0.753$. The two values of K_w are in very close agreement, indicating that the mixing speed within the jet is very well predicted by SM–2. On the other hand, the two values of C_w deviate significantly; however, Quinn [1] pointed out that this parameter is very sensitive to the inlet velocity field and he noted that his values of C_w for jets of different aspect ratios did not vary in any systematic manner due to slight differences in the inlet velocity field from one jet to another.

The stream-wise velocity profiles in the central z-y and z-x planes at three downstream locations (z/D_e = 2, 5, and 10) are presented in Figs. 5 and 6, respectively. The parameters x_{hlf} and y_{hlf} used in abscissa of Figs 5 and 6 are the half-velocity widths (where w/w_{cl} reaches 0.5) in the central z-y and z-x planes, respectively. Good agreement can be seen between the w-profiles measured by Quinn [1] and the present numerical results based on SM–2. One of the interesting features about these profiles is the saddle shape that was noted by Quinn and others (e.g., [4–7]) at low z/D_e. This saddle shape is well predicted in the present computations at z/D_e = 2 in both Figs. 5 and 6.

The jet half-velocity width growth in the central z-y and z-x planes is shown in Figs 7 and 8, respectively. The growth rates, $dx_{hlf} \big/ dz$ and $dy_{hlf} \big/ dz$, predicted by SM–1 and SM–2 in the far-field region (z/D_e ≥ 10) can be seen to be fairly close to each other. In terms of deviation from their respective experimental values, the predicted dx_{hlf}/dz is about 27% higher than the measured value, while the predicted dy_{hlf}/dz is about 22% lower than the measured value. Keeping in mind the experimental uncertainty in the data, these deviations may be regarded as acceptable.

The lateral velocity profiles in the central *z-x* plane and the span-wise velocity profiles in the central *z-y* plane are shown in Figs. 9 and 10, respectively. Values of *u* are positive near the center of the jet, consistent with the spreading of the jet and the increase in x_{hlf} shown in Fig. 8. Away from the center, values of *u* become negative, indicating mass entrainment into the jet. At the boundary of the computational domain ($x/D_e = 33$), the value of *u* approaches zero. The *v*-profiles in Fig. 10 follow a similar behavior. No experimental values of *u* and *v* were reported in [1].

5. Concluding remarks

Two standard two-equation turbulence models along with two inlet velocity profile boundary conditions were used to simulate the flow of a three-dimensional turbulent free jet issuing from sharp-edged slots. The two inlet velocity profiles used in this study were a uniform profile and a profile fitted to actual experimental data from [1]. It was found that the simulating method SM–2, which was based on the *k-ε* model and the fitted inlet velocity profile, was the best in predicting the stream-wise velocity decay along the jet centerline (aspect ratio 2:1) in both the near-field and the far-field regions. The vena contracta observed experimentally was well predicted by SM–2.

Further results based on SM–2 were obtained for the stream-wise velocity profiles at various axial planes, the jet’s half-velocity width in both the lateral and span-wise directions, and the decay rate of the stream-wise velocity in the far-field. All these results were in good agreement with the experimental data. As well, the interesting flow feature of saddle-shape velocity profiles was predicted at small x/D_e (see Figs. 5 and 6). Profiles of *u* and *v* at various axial stations are also presented and they appear to be consistent in trend with the other results.

Nomenclature

C_w	kinematic virtual origin of *w*-velocity in the far-field region
C_μ	*k-ε* turbulence model constant
$C_{\varepsilon 1}$	*k-ε* turbulence model constant
$C_{\varepsilon 2}$	*k-ε* turbulence model constant

D_e	equivalent circular jet diameter, m
I	stream-wise turbulence intensity at the inlet plane
k	mean turbulence kinetic energy per unit mass, $m^2\ s^{-2}$
K_w	decay rate of *w*-velocity in the far-field region
L_x	length of the computational domain in the *x* direction, m
L_{xa}	half-length of the inlet vent in the *x* direction, m
L_y	length of the computational domain in the *y* direction, m
L_{ya}	half-length of the inlet vent in the *y* direction, m
L_z	length of the computational domain in the *z* direction, m
P	pressure, Pa
P_k	turbulence production due to viscous forces, $kg\ m^{-1}\ s^{-3}$
R_e	hydraulic radius, m
u	time averaged velocity component in the *x* direction, $m\ s^{-1}$
u_i'	velocity fluctuations in the x_i direction $m\ s^{-1}$
v	time averaged velocity component in the *y* direction, $m\ s^{-1}$
w	time averaged velocity component in the *z* direction, $m\ s^{-1}$
x	Cartesian coordinate along the lateral length of domain, m
x_{hlf}	half-velocity width in the *x* direction based on the *w*-velocity, m
y	Cartesian coordinate along the span-wise length of domain, m
y_{hlf}	half-velocity width in the *y* direction based on the *w*-velocity, m
z	Cartesian coordinate along the stream-wise length of domain, m

Greek Symbols

α	k-ω turbulence model constant
β	k-ω turbulence model constant
β'	k-ω turbulence model constant
δ_{ij}	Kronecker delta
ε	turbulence dissipation rate, $m^2\ s^{-3}$
μ	dynamic viscosity, $N\ s\ m^{-2}$
μ_t	eddy viscosity, $N\ s\ m^{-2}$
ρ	density, $kg\ m^{-3}$
σ_k	turbulence model constant for the *k* equation
σ_ε	k-ε turbulence model constant
σ_ω	k-ω turbulence model constant

ω	turbulence frequency, s^{-1}

Subscripts

cl	at the jet centerline
in	at inlet plane of jet
max	maximum value

Acknowledgement

The financial support provided by Manitoba Hydro and the Natural Sciences and Engineering Research Council of Canada is gratefully acknowledged.

References

[1] W.R. Quinn, Turbulent free jet flows issuing from sharp-edged rectangular slots: The influence of slot aspect ratio, Experimental Thermal and Fluid Science 5 (1992) 203-215.

[2] E.J. Gutmark, F.F. Grinstein, Flow control with noncircular jets, Annual Review of Fluid Mechanics 31 (1999) 239-272.

[3] W.R. Quinn, A. Pollard, G.F. Marsters, On “saddle-backed” velocity distributions in three-dimensional turbulent free jets, Proceedings of the AIAA 16th Fluid and Plasma Dynamics Conference, Danvers, MA, 1983, pp. 1677-1682.

[4] G.F. Marsters, Spanwise velocity distributions in jets from rectangular slots, AIAA Journal 19 (1981) 148-152.

[5] P.M. Sforza, W. Stasi, Heated three-dimensional turbulent jets, ASME Journal of Heat Transfer 101 (1979) 353-358.

[6] A.A. Sfeir, The velocity and temperature fields of rectangular jets, International Journal of Heat and Mass Transfer 19 (1976) 1289-1297.

[7] N. Trentacoste, P.M. Sforza, Further experimental results for three-dimensional free jets, AIAA Journal 5 (1967) 885-891.

[8] R.S. Miller, C.K. Madnia, P. Givi, Numerical simulation of non-circular jets, Computers and Fluids 24 (1995) 1-25.

[9] R.V. Wilson, A.O. Demuren, Numerical simulation of turbulent jets with rectangular cross-section, ASME FED-Vol. 238, 1996, pp. 121-127.

[10] A.E. Holdo, B.A.F. Simpson, Simulation of high-aspect-ratio jets, International Journal for Numerical Methods in Fluids 39 (2002) 343-359.

[11] B.E. Launder, D.B. Spalding, The numerical computation of turbulent flows, Computational Methods in Applied Mechanics and Engineering 3 (1974) 269-289.

[12] D.C. Wilcox, Multiscale model for turbulent flows, AIAA Journal 26 (1988) 1311-1320.

[13] S.V. Patankar, Numerical Heat Transfer and Fluid Flow, Hemisphere, New York, 1980.

[14] C.M. Rhie, W.L. Chow, Numerical study of the turbulent flow past an airfoil with trailing edge separation, AIAA Journal 21 (1983) 1525-1532.

[15] C. Prakash, S.V. Patankar, A control volume-based finite-element method for solving the Navier-Stokes equations using equal-order velocity-pressure interpolations, Numerical Heat Transfer 8 (1985) 259-280.

[16] G.E. Schneider, M.J. Raw, Control volume finite-element method for heat transfer and fluid flow using colocated variables: I – Computational procedure; II – Application and validation, Numerical Heat Transfer 11 (1987) 363-400.

[17] T.J. Barth, D.C. Jesperson, The design and application of upwind schemes on unstructured meshes, AIAA Paper 89-0366, 1989.

Figure Captions

Fig.	**Title**
1	Computational domain
2	Inlet velocity profiles
3	Stream-wise velocity decay along the jet centerline in the near-field region
4	Inverse stream-wise velocity decay along the jet centerline
5	Stream-wise velocity profiles in the central z-y plane
6	Stream-wise velocity profiles in the central z-x plane
7	Jet half-velocity width growth in the central z-y plane
8	Jet half-velocity width growth in the central z-x plane
9	Lateral velocity profiles in the central z-x plane
10	Span-wise velocity profiles in the central z-y plane

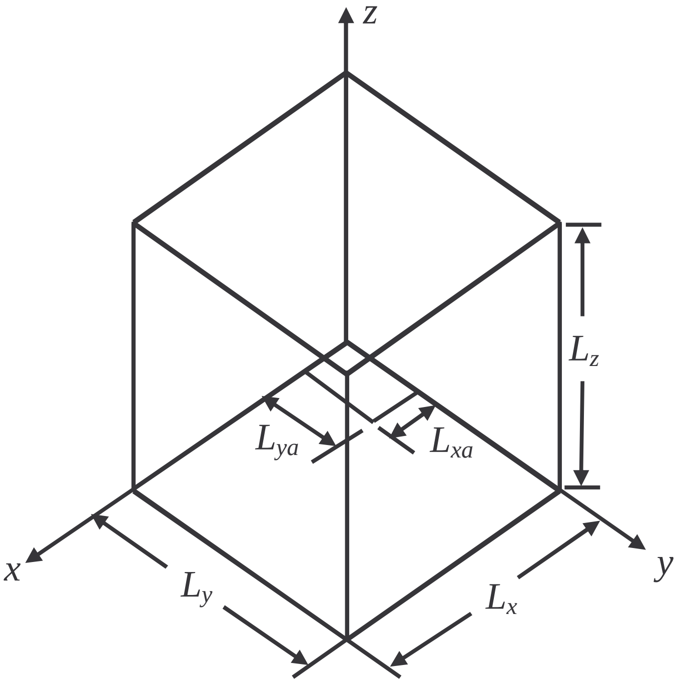

FIG. 1

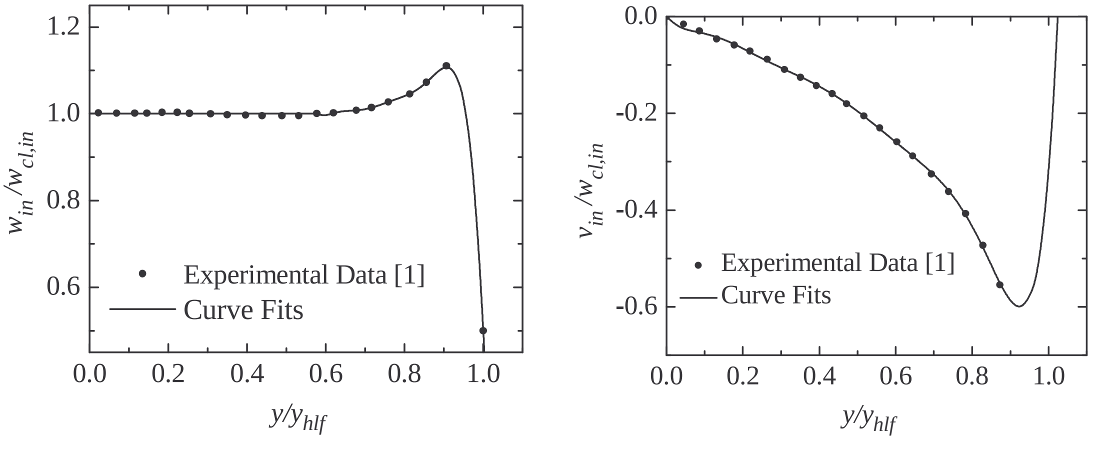

(a) Stream-wise velocity profile at $x = 0$ (b) Span-wise velocity profile at $x = 0$

Fig. 2

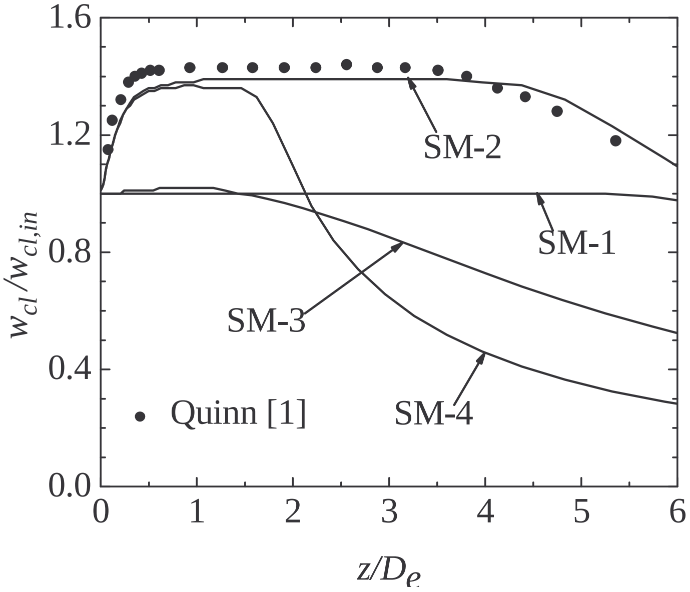
1.6
1.2
0.8
0.4
0.0
0
1
2
3
4
5
6
$w_{cl}/w_{cl,in}$
z/D_e
SM-1
SM-2
SM-3
SM-4
● Quinn [1]

Fig. 3

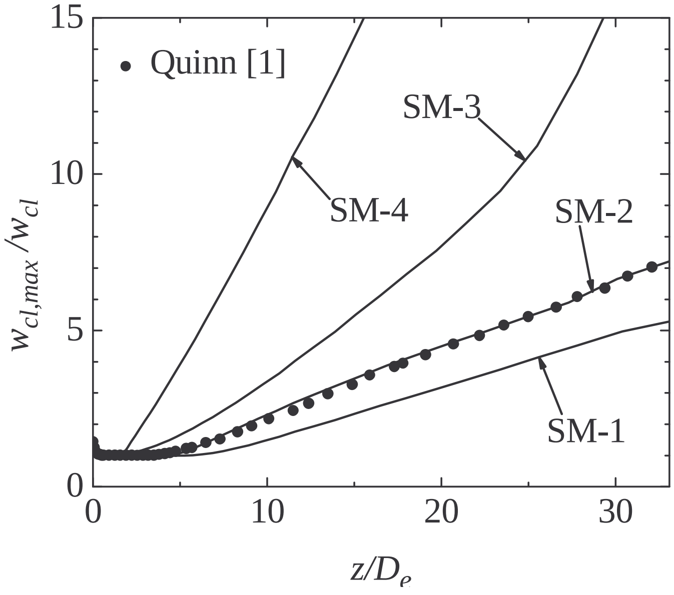
15
10
5
0
0
10
20
30
$w_{cl,max}/w_{cl}$
z/D_e
● Quinn [1]
SM-1
SM-2
SM-3
SM-4

Fig. 4

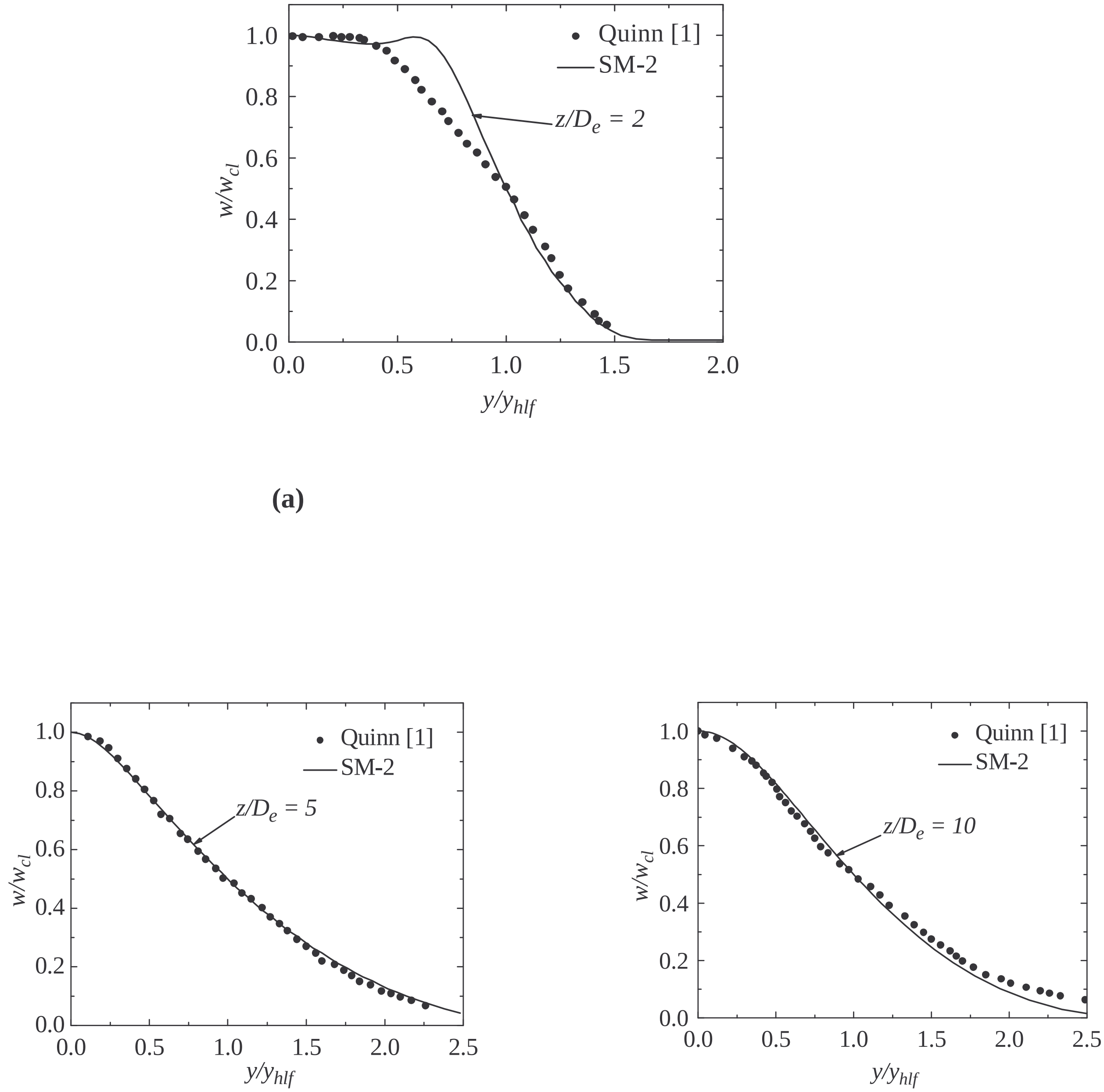
Quinn [1]
SM-2
z/De = 2
w/wcl
y/yhlf
1.0
0.8
0.6
0.4
0.2
0.0
0.0
0.5
1.0
1.5
2.0
Quinn [1]
SM-2
z/De = 5
w/wcl
y/yhlf
2.5
Quinn [1]
SM-2
z/De = 10
w/wcl
y/yhlf
2.5

(a)

(b)

(c)

Fig. 5

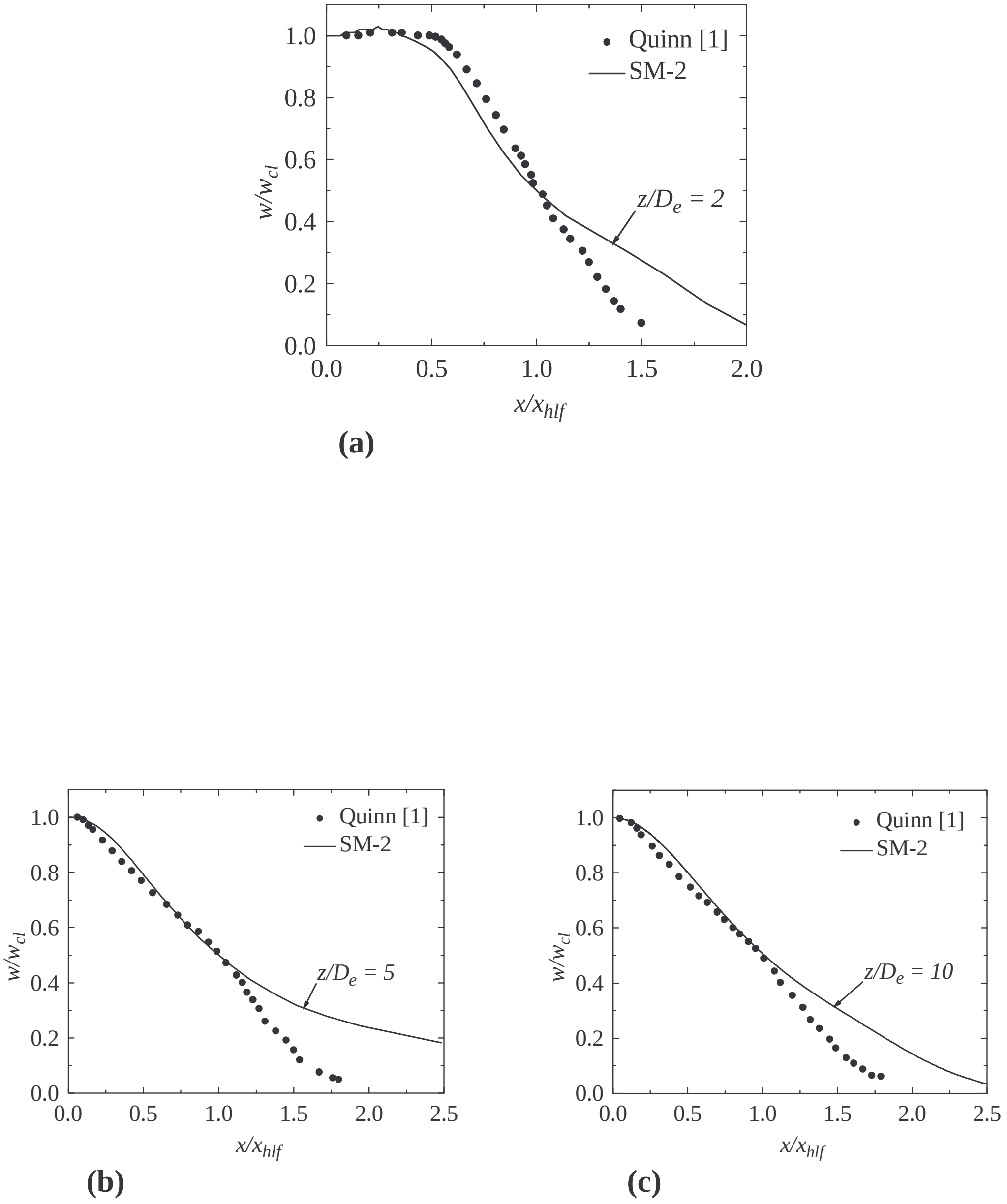

Quinn [1]
SM-2
$z/D_e = 2$
w/w_{cl}
x/x_{hlf}
1.0
0.8
0.6
0.4
0.2
0.0
0.0
0.5
1.0
1.5
2.0
(a)
Quinn [1]
SM-2
$z/D_e = 5$
w/w_{cl}
x/x_{hlf}
0.0
0.5
1.0
1.5
2.0
2.5
(b)
Quinn [1]
SM-2
$z/D_e = 10$
w/w_{cl}
x/x_{hlf}
0.0
0.5
1.0
1.5
2.0
2.5
(c)

Fig. 6

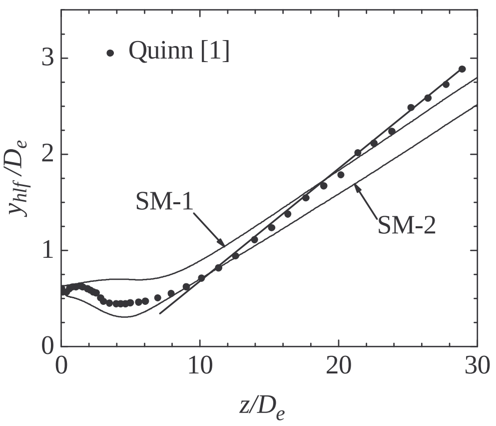

Fig. 7

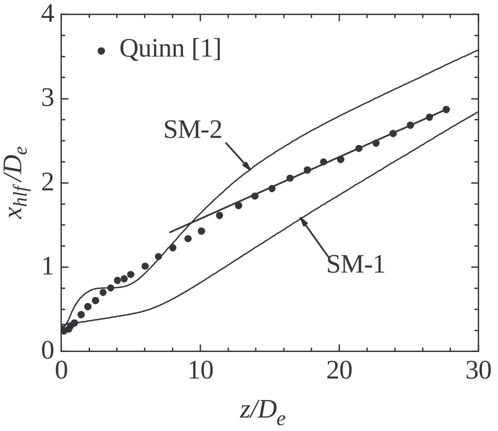

Fig. 8

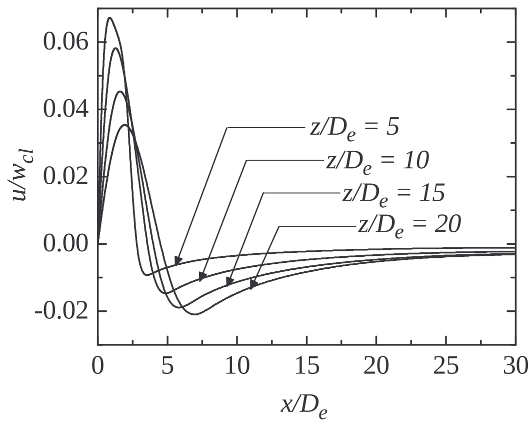

Fig. 9

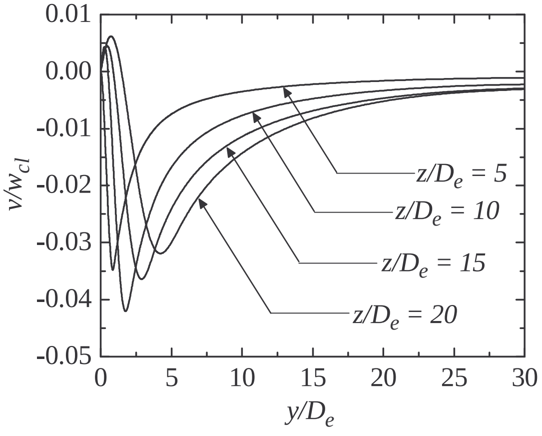

Fig. 10

Appendix B

SCALABLE WALL FUNCTIONS

B.1 Near-Wall Treatment

The wall function approach used in CFX-5 is an extension of the method of Launder and Spalding (1974). In the log-law region, the near wall tangential velocity U_t is related to the wall shear stress τ_w by means of a logarithmic relation. In the wall function approach, empirical formulas are applied which connect the wall condition with the dependent variables at the first near wall mesh node which is assumed to lie in the logarithmic region of the boundary layer.

The relation for the near wall velocity in the logarithmic region is given by:

$$U_t = u_\tau \frac{1}{\kappa} \log(y^+) + C \tag{B.1}$$

where

$$y^+ = \frac{(\rho u_\tau n)}{\mu} \tag{B.3}$$

$$u_\tau = \left(\frac{\tau_w}{\rho} \right)^{1/2} \tag{B.4}$$

where u_τ is the friction velocity [m/s] and y^+ is the non-dimensional wall distance, n is the normal distance to the wall, and ($\kappa = 0.41$) is the von-Karman constant. C is a constant depending on the wall roughness ($C = 5.2$ for a smooth wall).

Using the wall function approach, the near wall turbulence quantities k, ε, and μ_t in the logarithmic region are:

$$k = \frac{u_\tau^2}{\sqrt{C_\mu}} \tag{B.5}$$

$$\varepsilon = \frac{1}{\kappa}\frac{u_\tau^3}{n} \tag{B.6}$$

$$\mu_t = \rho \kappa u_\tau n \tag{B.7}$$

The fundamental principle of the scalable wall function approach used in CFX-5 (Grotjans and Menter, 1998), is to limit the y^+ value at the wall, $\tilde{y}^+$ used in the logarithmic formulation by a value of 11.06 using the intersection of the logarithmic and linear near wall profile. The value of $\tilde{y}^+$ is then determined using $\tilde{y}^+ = \max(y^+, 11.06)$. The computed $\tilde{y}^+$ value is not allowed to fall below this limit and therefore all mesh points are outside of the viscous sublayer. As a result, mesh inconsistencies associated with applying the k and ε equations in this region are avoided.

The flux boundary conditions applied at the wall for the scalable wall function approach used in CFX-5 are as follows:

$$\mu_t \frac{\partial U_t}{\partial n} = -\rho u_\tau \max\left(\left|u_\tau\right|, u^*\right) \tag{B.8}$$

$$\frac{\partial k}{\partial n} = 0 \tag{B.9}$$

$$\frac{\mu_t}{\sigma_\varepsilon}\frac{\partial \varepsilon}{\partial n} = -\frac{1}{\sigma_\varepsilon}\frac{(u^*)^5 \rho^2}{\tilde{y}^+ \mu} \times \left[\frac{2+e}{2+2e} + F_{cal}\,\frac{e}{2}\,\frac{\sigma_\varepsilon \sqrt{C_\mu}}{\kappa^2}\left(C_{\varepsilon 2} - C_{\varepsilon 1}\right)\right] \tag{B.10}$$

with:

$$e = \frac{\Delta y^+}{\tilde{y}^+} \tag{B.11}$$

and

$$u^* = C_\mu{}^{1/4} k^{1/2} \tag{B.12}$$

Here Δy^+ is the actual y^+ value from the wall to the first interior node, F_{cal} is a calibration function based on the coarseness of the mesh, and u^* is an alternative velocity scale used to prevent the flux from going to zero at separation points (as was a problem with standard wall functions).

The advantage of scalable wall functions as opposed to standard wall functions is that they can be applied on arbitrarily fine meshes and allow for consistent mesh refinement independent of Reynolds number. These features were the major shortcomings of the standard wall function approach.

Appendix C

SAMPLE COMPUTATIONAL MESHES

C.1 Grids for Computational Domain 1

Figure C.1 shows the full medium computational grid for Case 1. This grid consists of 1,141,442 nodes. The full grid is made up of two separate grids that are joined together on common faces. The outer grid, shown in Figure C.2, is made up of 250,010 nodes. The outer grids were identical for all cases studied in Computational Domain 1. The inner grid, shown in Figure C.3, is made up of 891,432 nodes. The inner grids were nearly identical for all cases studied in Computational Domain 1 with the only differences being as a result of the different sizes and locations of the inlet opening for the various cases studied. Figure C.4a and C.4b show a cross section of the mesh on S1 and S3, respectively with the interface between the two grids outlined.

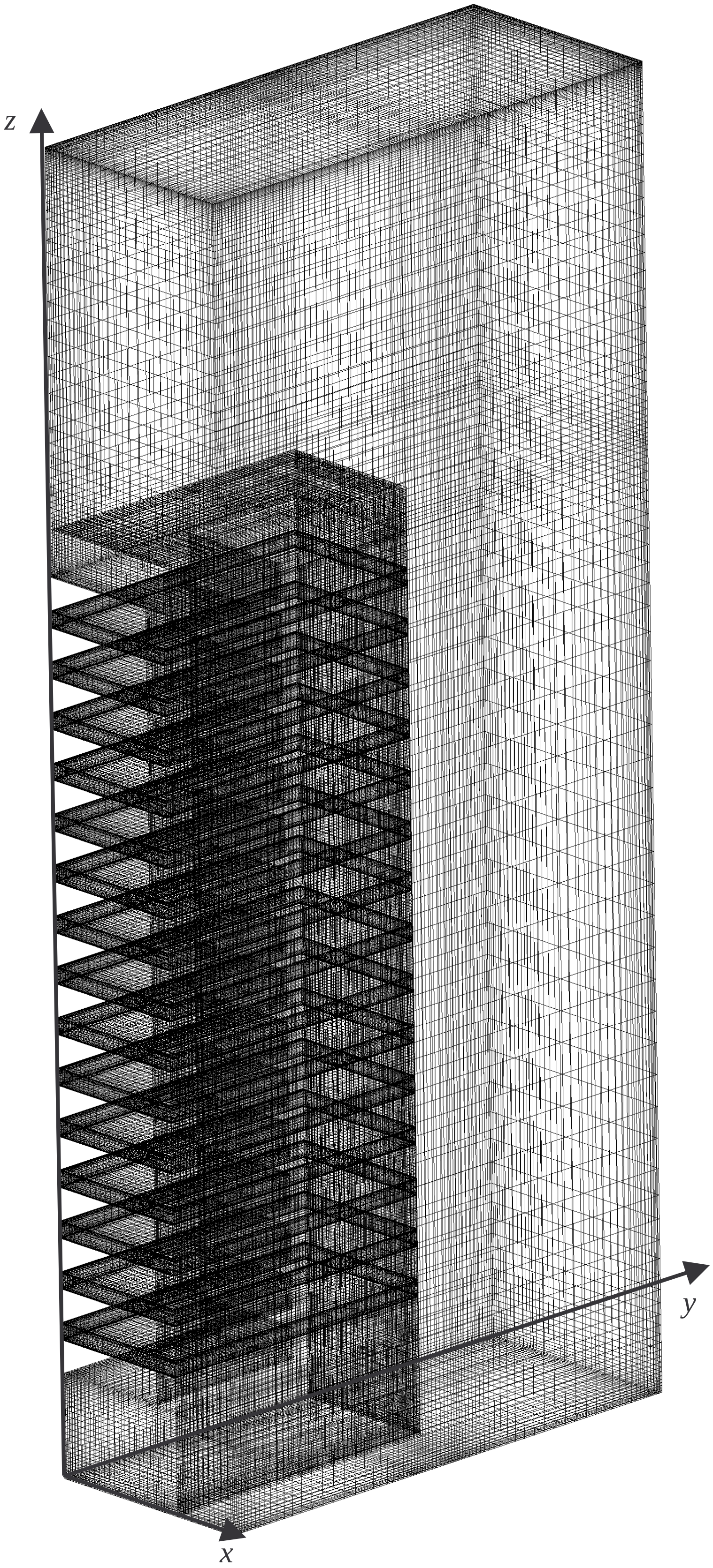

Figure C.1: Full computational grid for Case 1

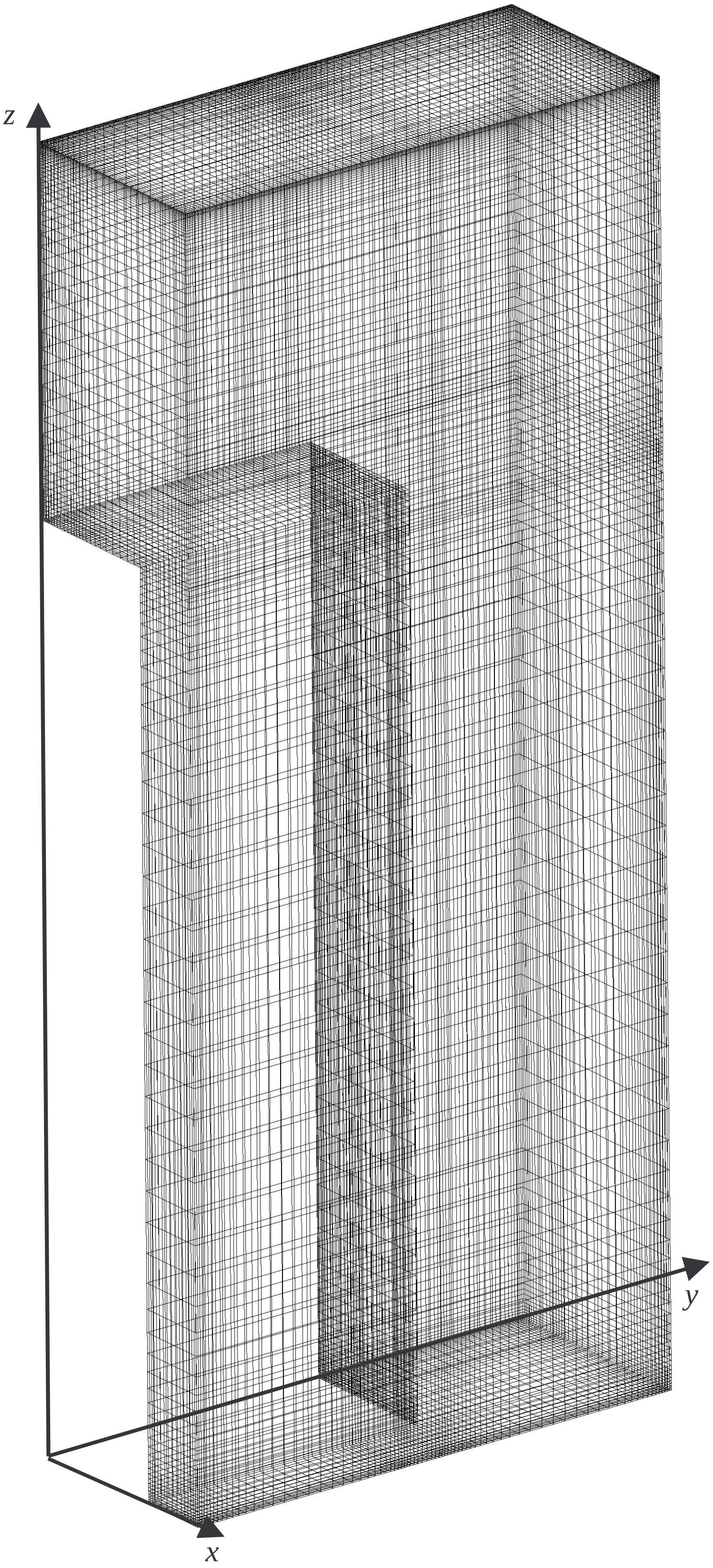

Figure C.2: Outer grid for Case 1

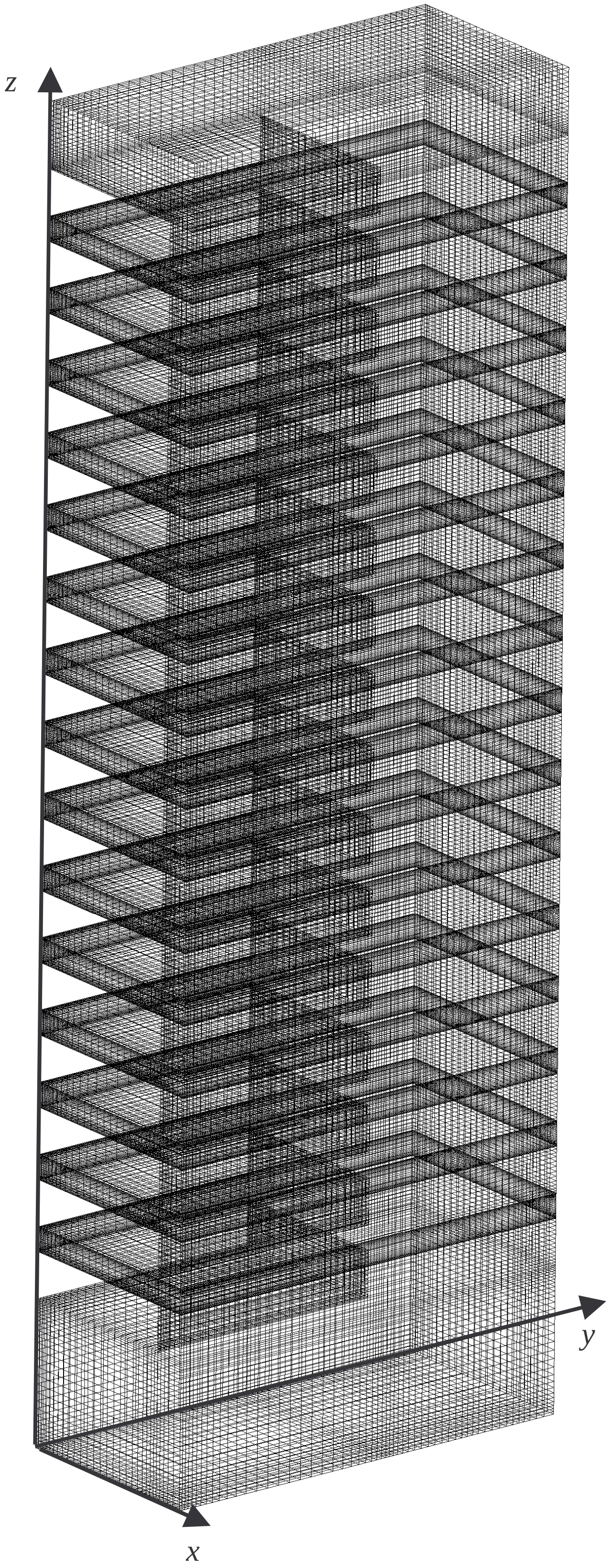

Figure C.3: Inner grid for Case 1

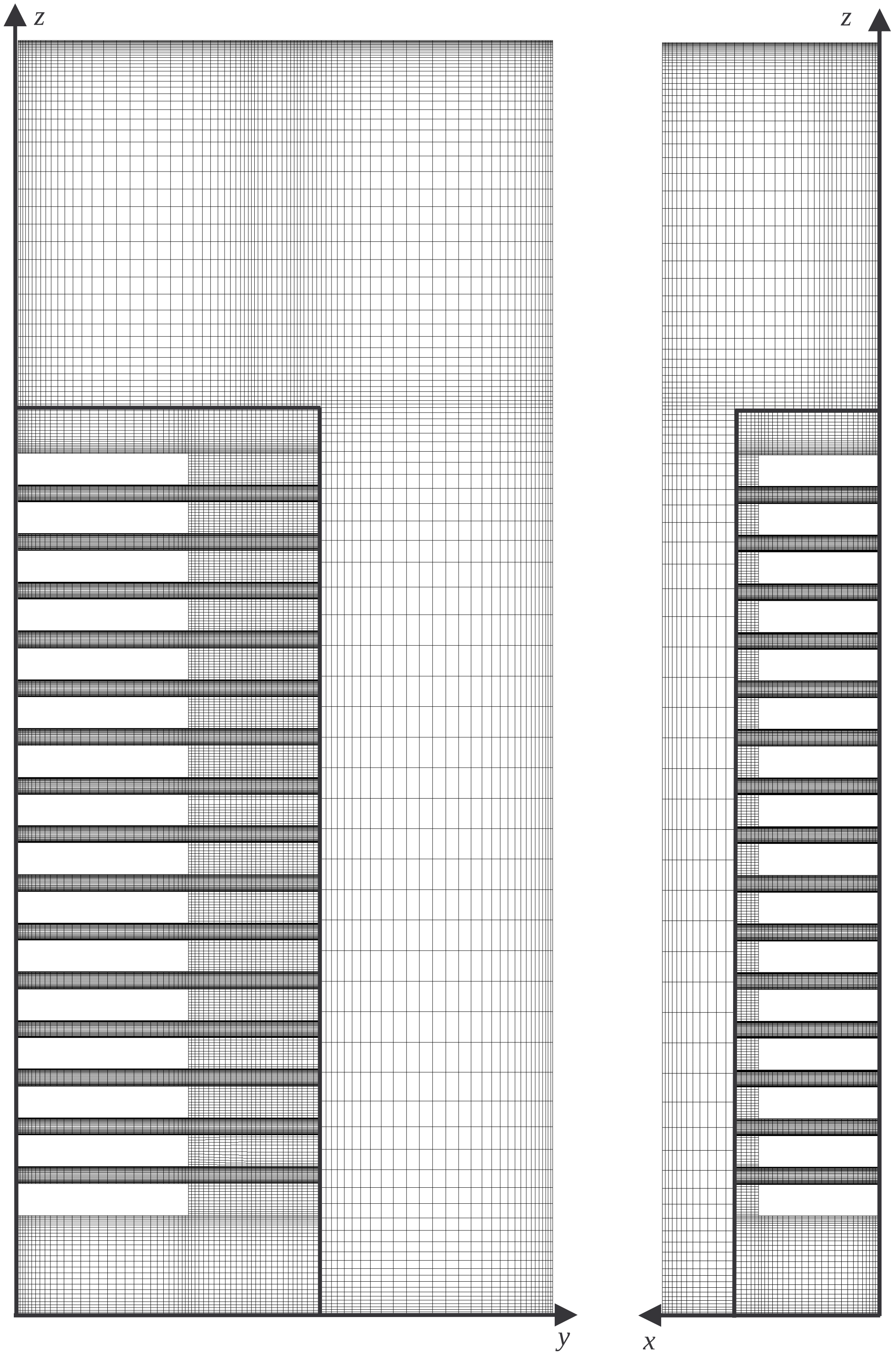

(a) (b)

Figure C.4: Cross section of mesh on (a) S1 and (b) S3 for Case1

C.2 Grids for Computational Domain 2

Figure C.5 shows the full medium computational grid for Case 22. This grid consists of 2,148,130 nodes. Again, the full grid is made up of two separate grids that are joined together on common faces. The outer grid, shown in Figure C.6, is made up of 577,514 nodes. The outer grids were nearly identical for both converged cases studied in Computational Domain 2 with the only differences being as a result of the different sizes and locations of the inlet and outlet opening for the cases studied. The inner grid, shown in Figure C.7, is made up of 1,570,616 nodes. The inner grids were identical for both converged cases studied in Computational Domain 2. Figure C.8 shows a cross section of the mesh on S1. The cross section of the mesh on S3 is the same as in Figure C.4b.

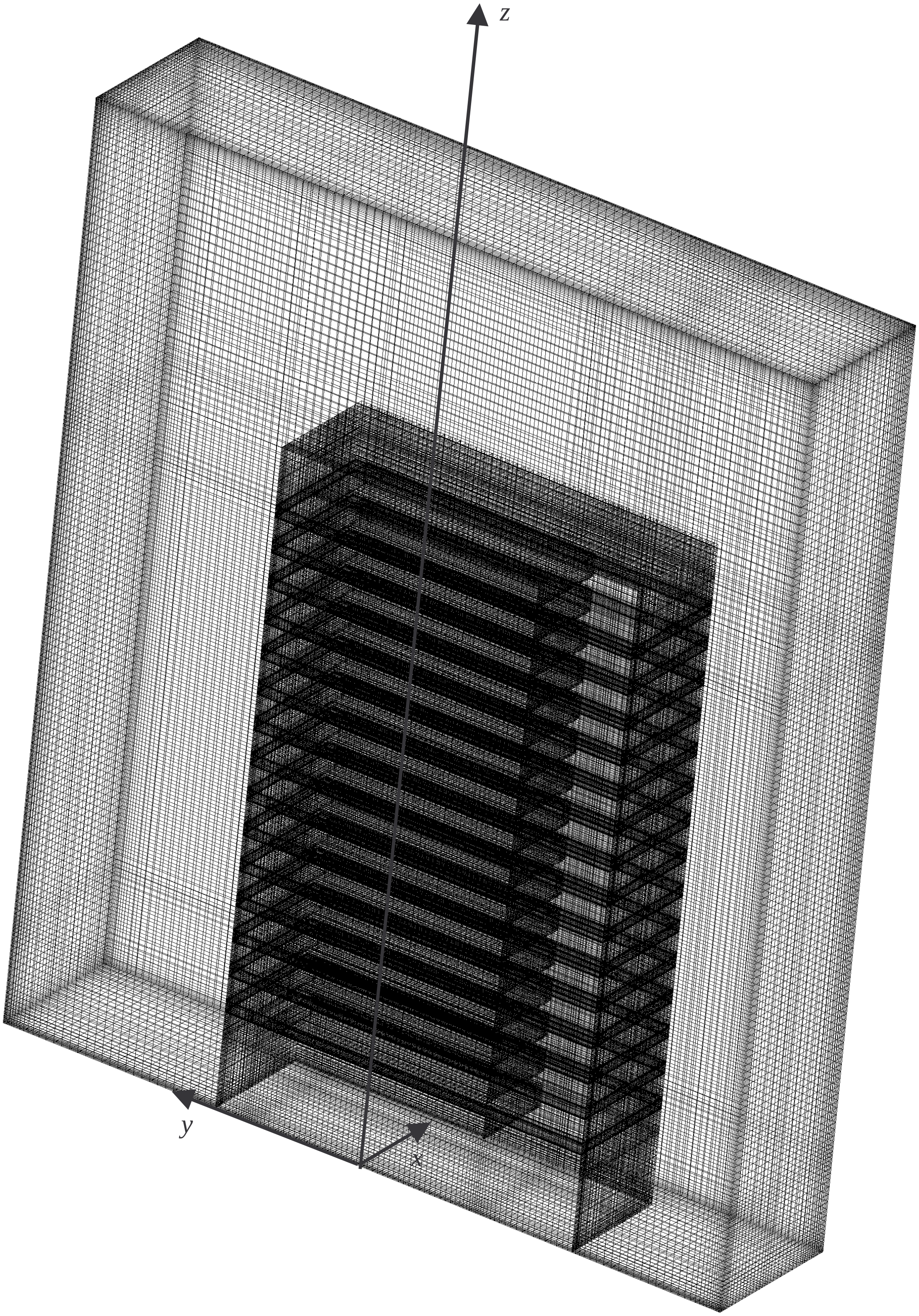

Figure C.5: Completed computational grid for Case 22

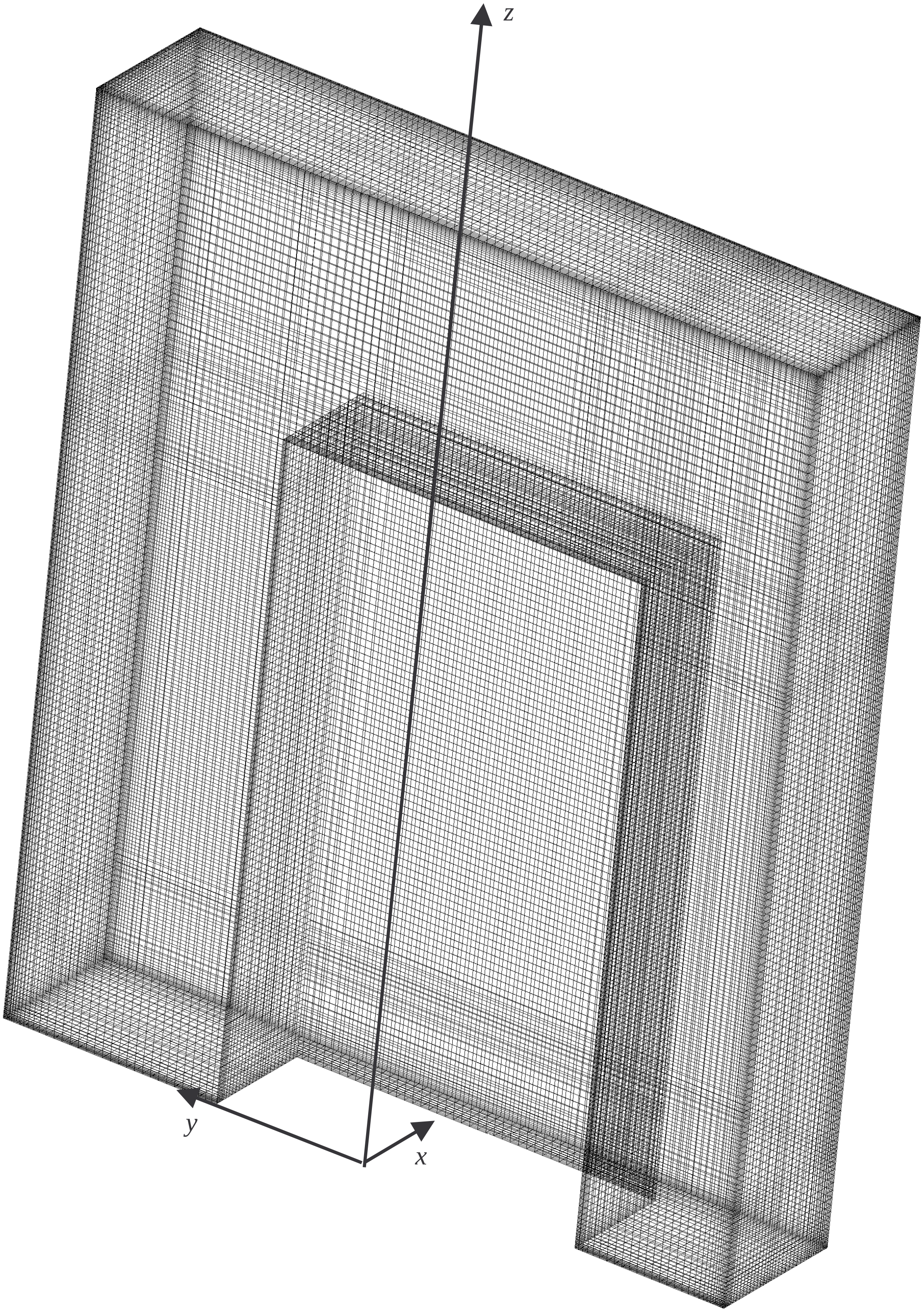

Figure C.6: Outer grid for Case 22

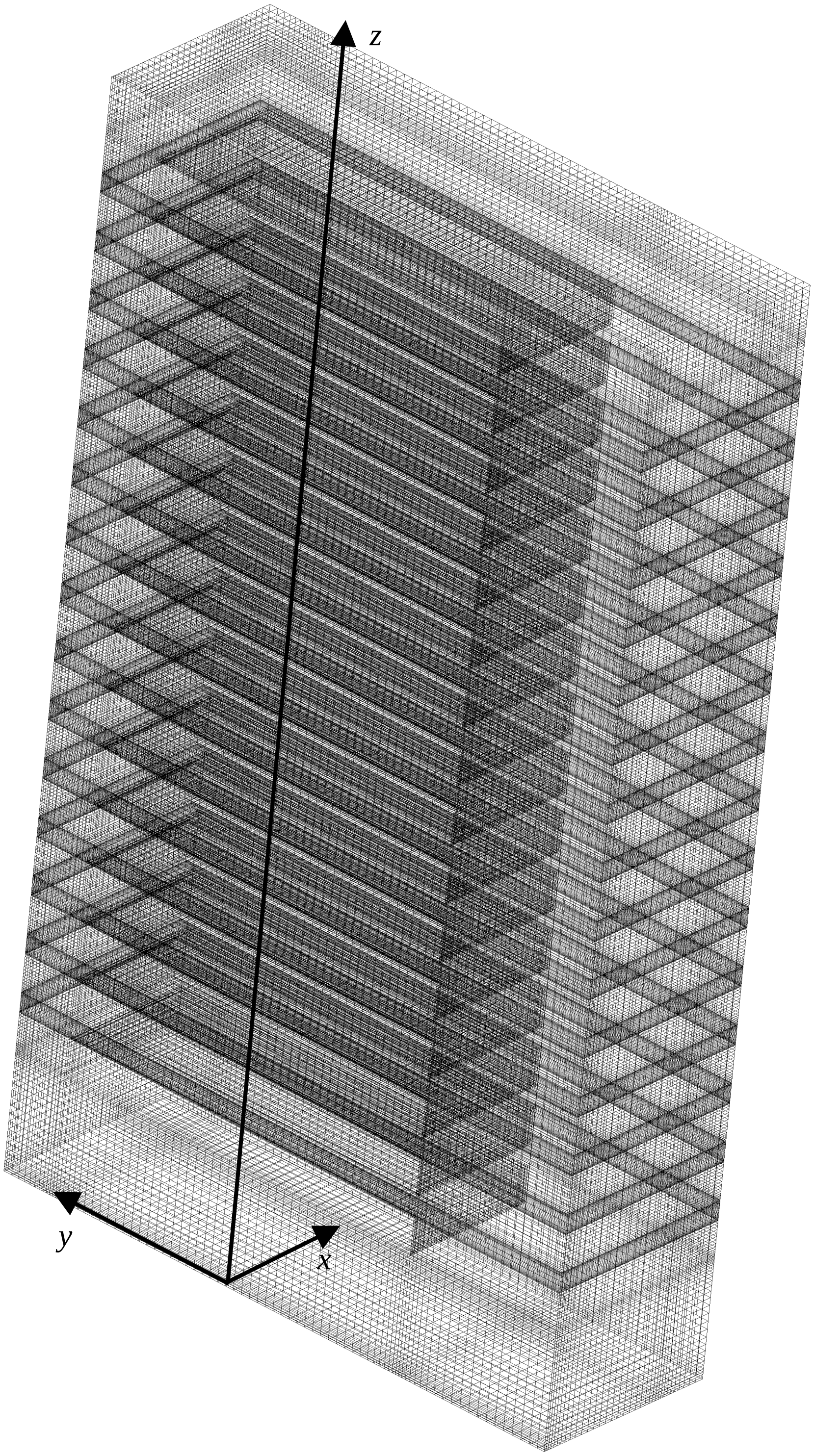

Figure C.7: Inner grid for Case 22

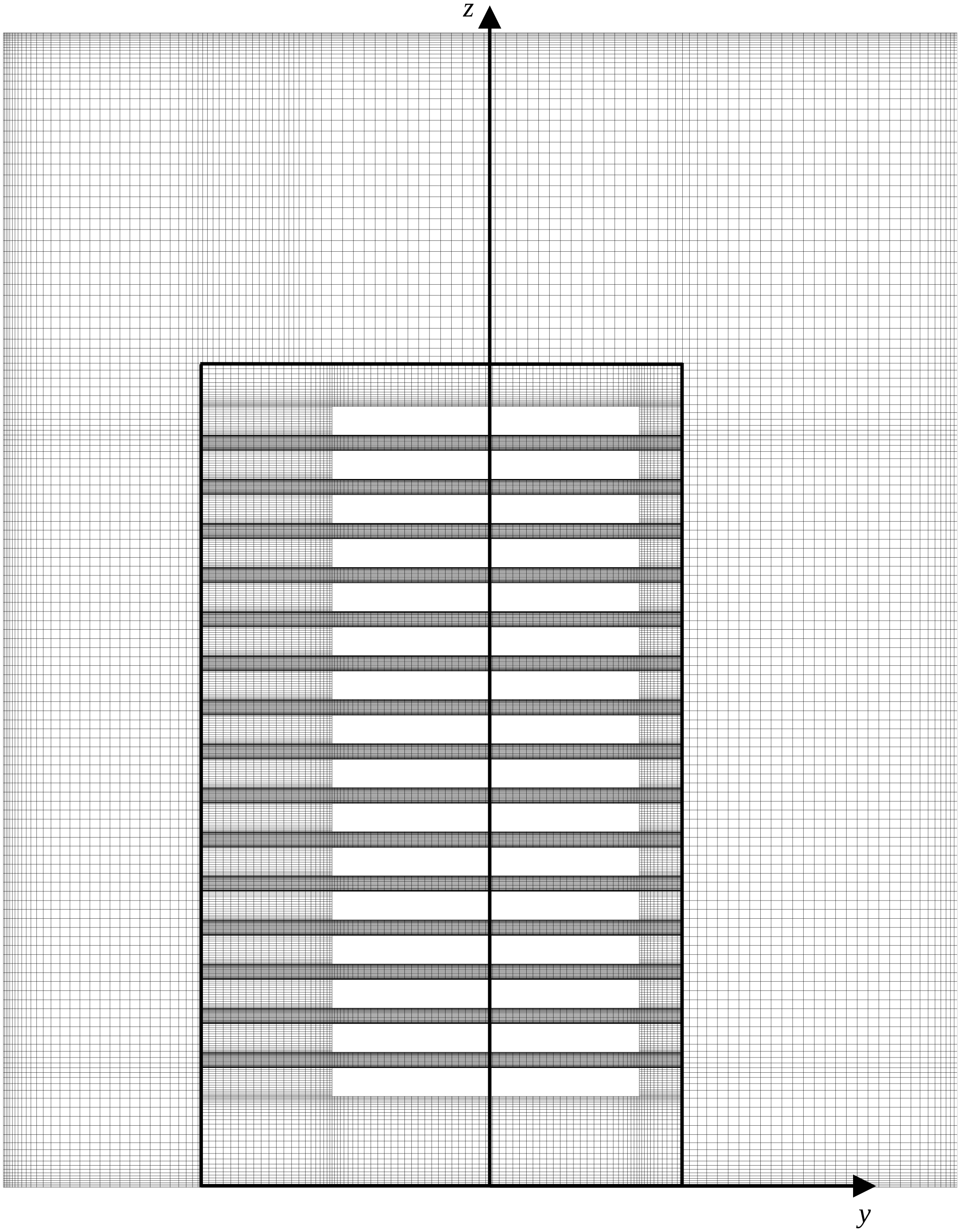

Figure C.8: Cross section of mesh on S1 for Case 22

Appendix D

CFX-5 PARAMETERS

D.1 Domain Parameters

The following domain parameters were set in CFX-5 in all of the simulations for both computational domains (default values were used for all other parameters):

Basic Settings:
Domain Type: Fluid Domain
Fluids List: Air Ideal Gas

Pressure:
Reference Pressure: 1 atm

Buoyancy:
Option: Buoyant
Gravity X Dim.: 0 m/s^2
Gravity Y Dim.: 0 m/s^2
Gravity Z Dim.: -9.8 m/s^2
Buoy. Ref. Density: 1.2001 kg/m^3

Heat Transfer Model:
Option: Thermal Energy

Turbulence Model:
Option: k-Epsilon
Buoyancy Turbulence:

Option: None

Turbulent Wall Functions:

Option: Scalable

D.2 Solver Control Parameters

The following solver control parameters were used in all of the simulations for both computational domains (default values were used for all other parameters):

Advection Scheme:

Option: High Resolution

Convergence Control:

Timescale Control: Physical Timescale

Physical Timescale: 0.5 s

Max. No. Iterations: 10000

Convergence Criteria:

Residual Type: MAX

Residual Target: 1×10^{-5}

D.3 Expert Parameters

The following expert parameters were activated for all of the simulations with both computational domains in order to aid in convergence with a hexahedral mesh as opposed to the default tetrahedral mesh:

Pressure Diffusion Scheme = 1

Scalar Diffusion Scheme = 1

Stress Diffusion Scheme =1

Appendix E

SAMPLE INFRARED THERMOGRAPHS

Figure E.1 shows a sample infrared thermograph taken of the upper tier of one of the thyristor towers. This image was used to determine the temperature of the surface of the towers in Area 1 (discussed in Chapter 5). This image also shows that the temperature of the lower surface of the tier blocks is higher than the temperature of the surrounding air. Figure E.2 shows a sample infrared thermograph used to determine the temperature of the black tape targets in Area 2. Figure E.3 shows a sample infrared thermograph used to determine the temperature of the black tape targets in Area 3.

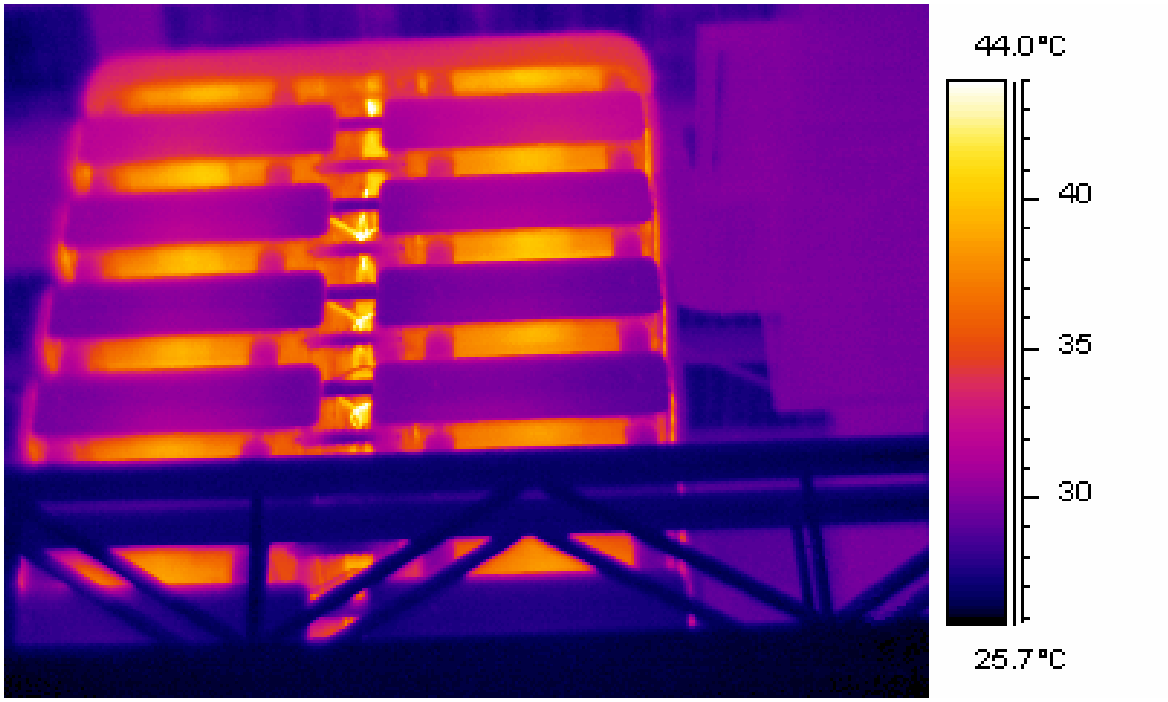

Figure E.1: Sample infrared thermograph used to determine temperatures in Area 1

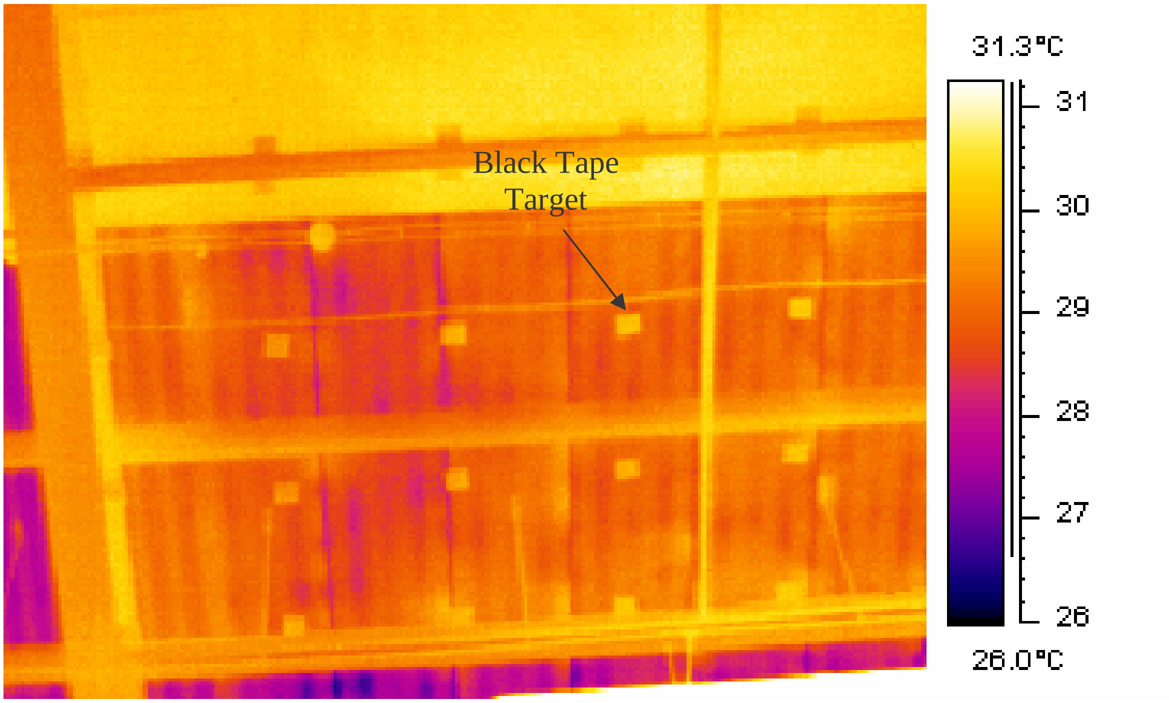

Figure E.2: Sample infrared thermograph used to determine temperatures in Area 2

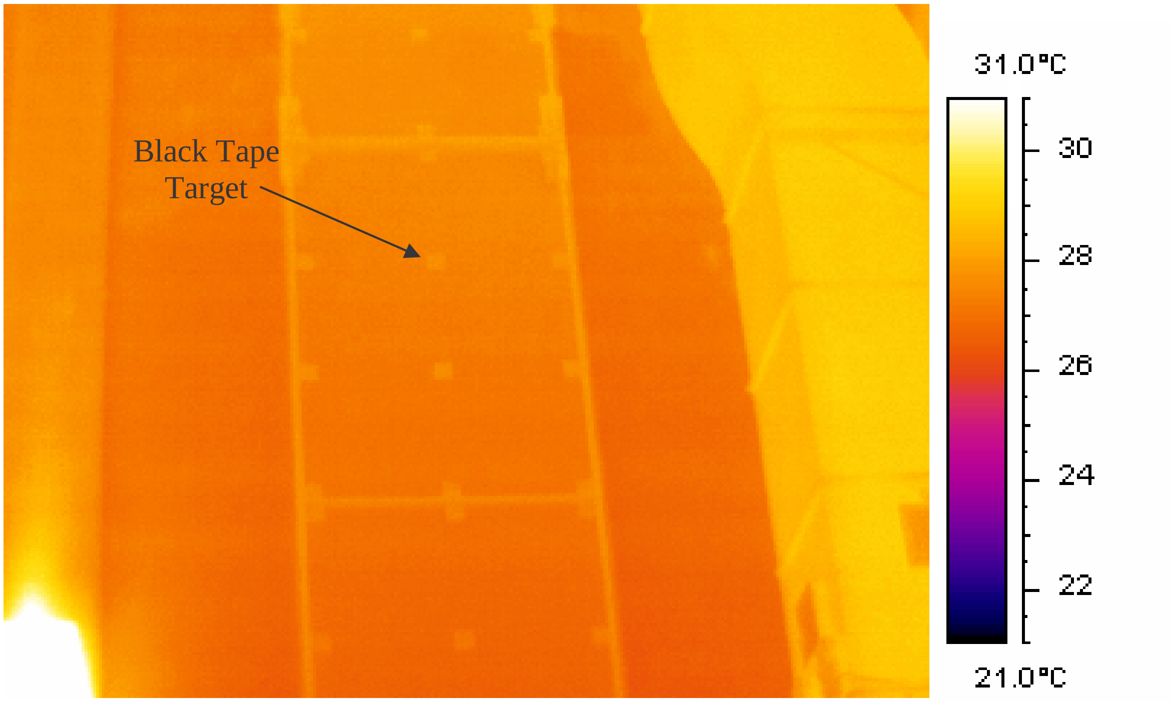

Figure E.3: Sample infrared thermograph used to determine temperatures in Area 3

Appendix F

FULL DOMAIN STREAMLINE PLOTS

Figures F.1 to F.23 show full-domain streamline plots showing the overall flow structure for all twenty-three cases studied.

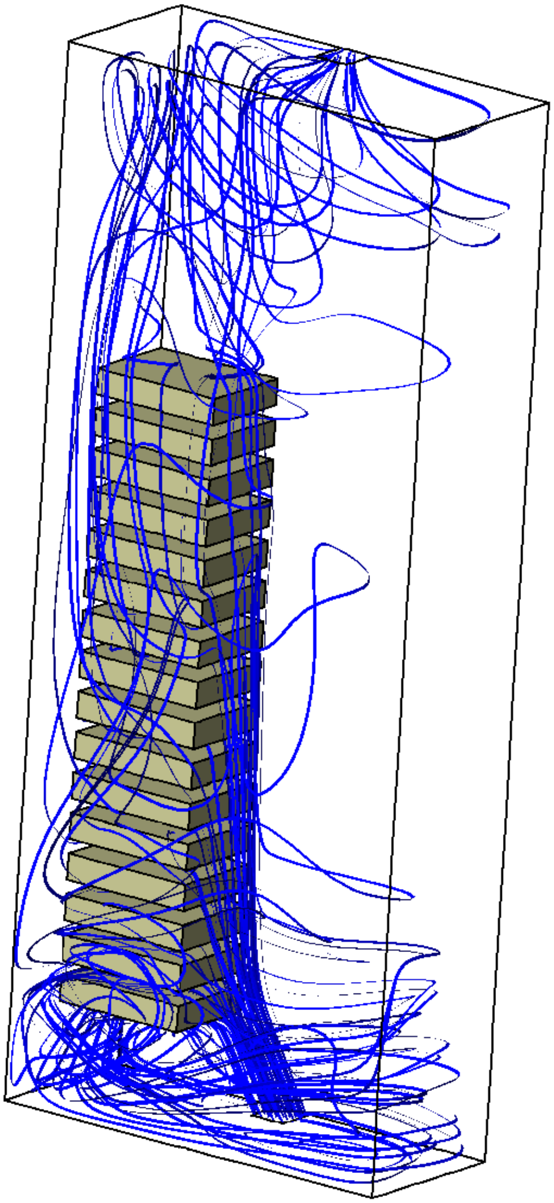

Figure F.1: Streamline plot showing overall flow structure for Case 1

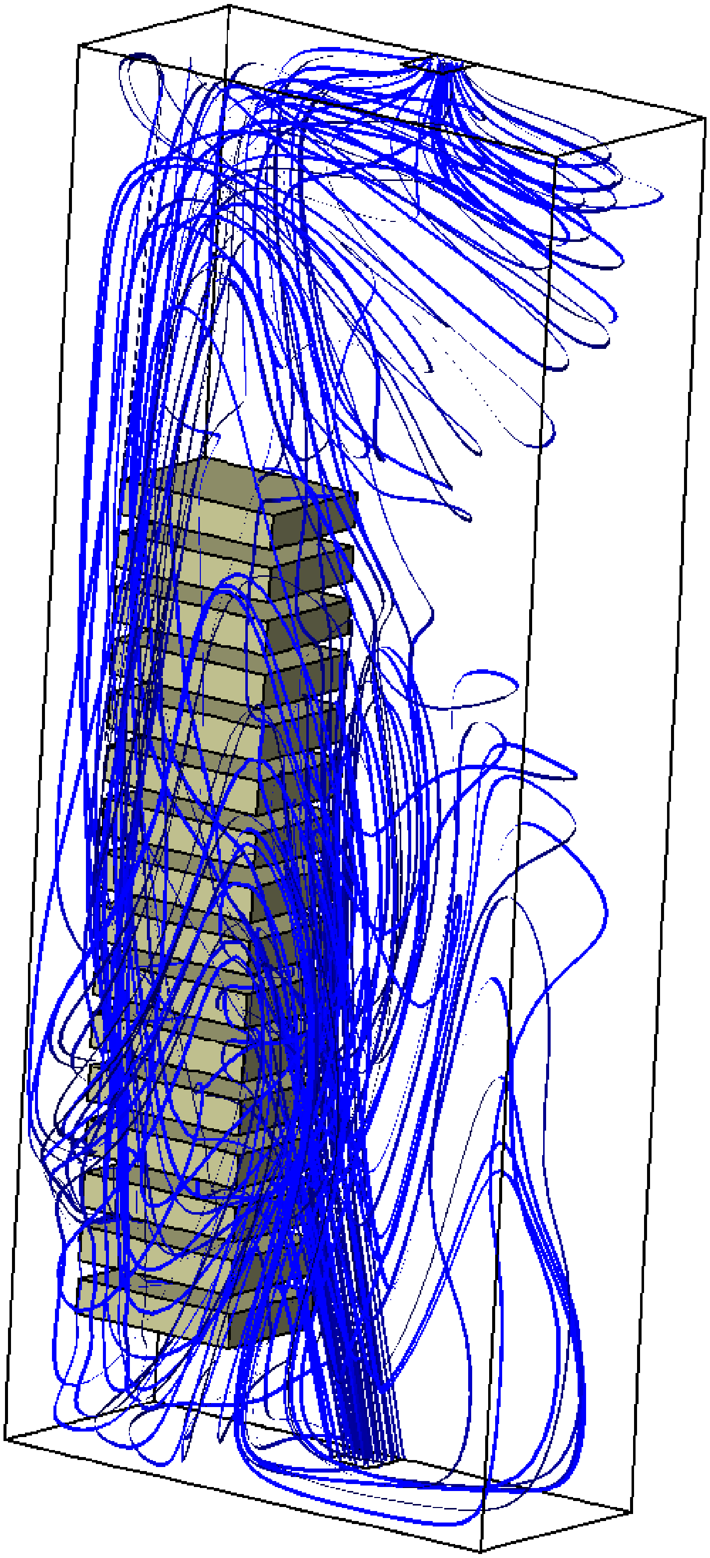

Figure F.2: Streamline plot showing overall flow structure for Case 2

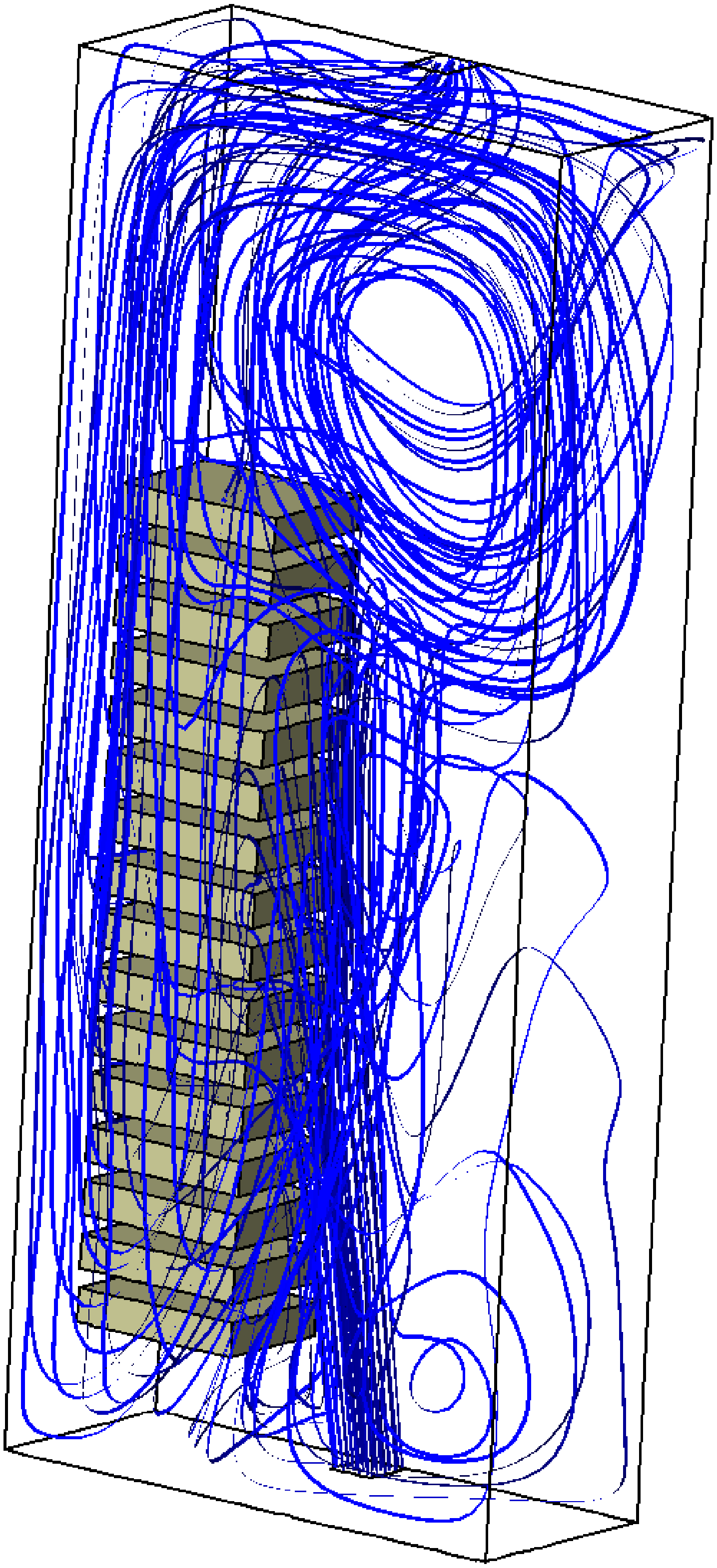

Figure F.3: Streamline plot showing overall flow structure for Case 3

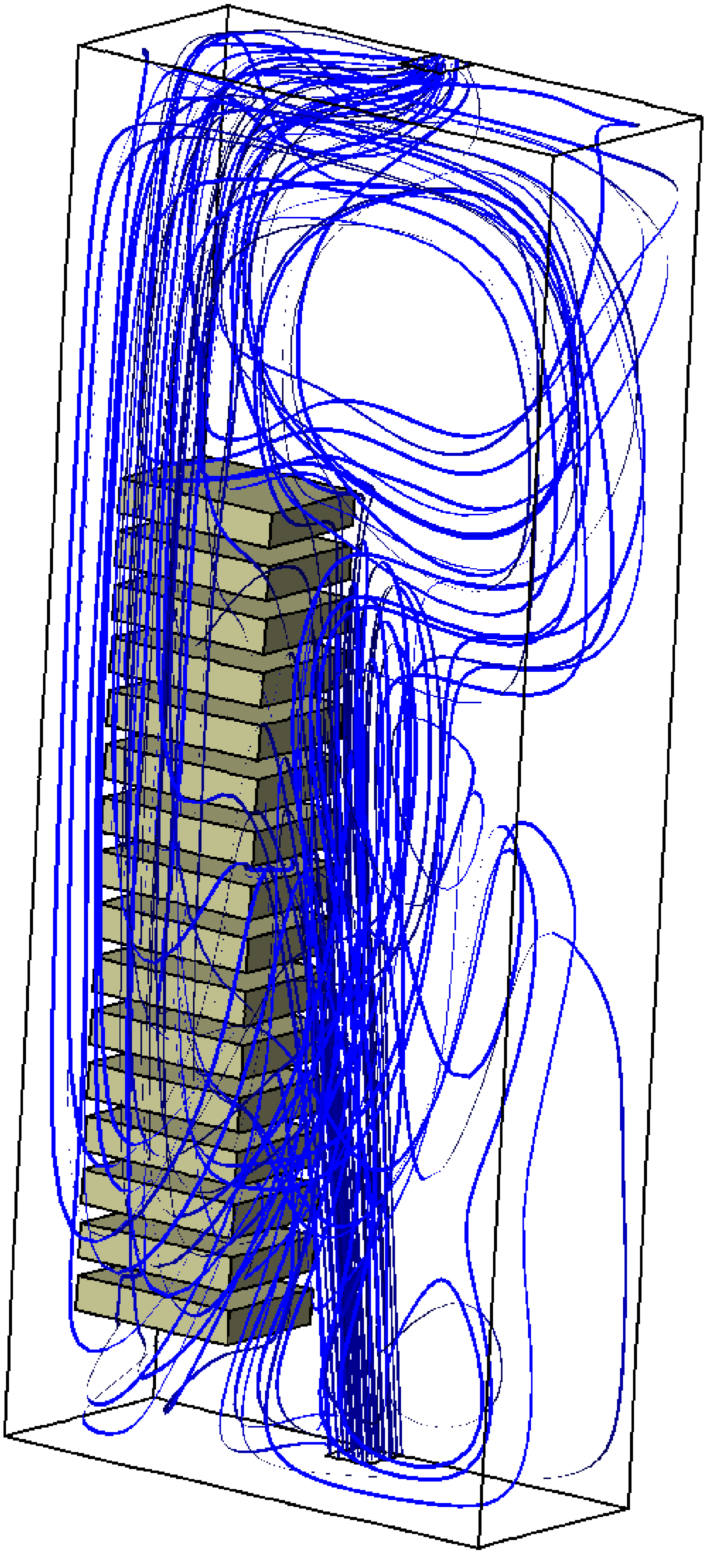

Figure F.4: Streamline plot showing overall flow structure for Case 4

Figure F.5: Streamline plot showing overall flow structure for Case 5

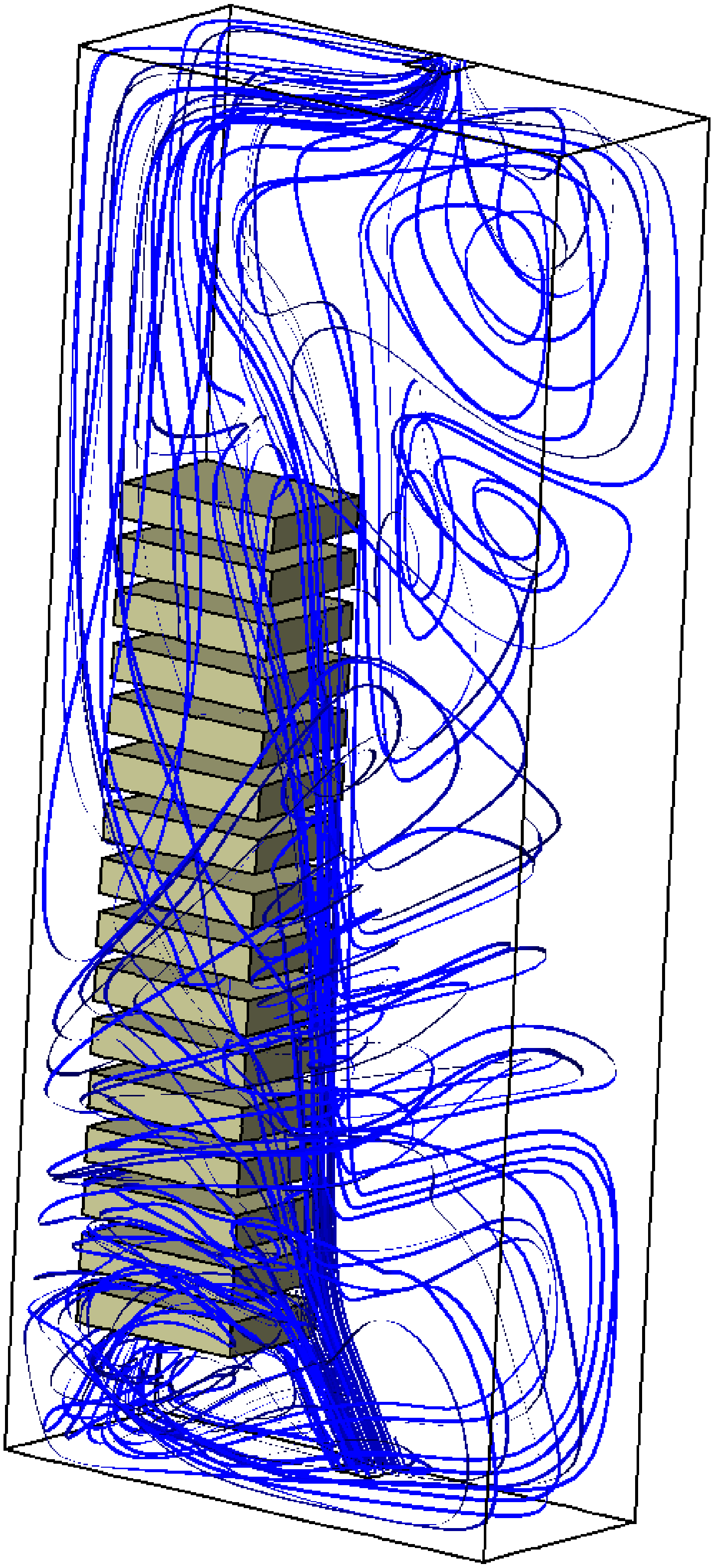

Figure F.6: Streamline plot showing overall flow structure for Case 6

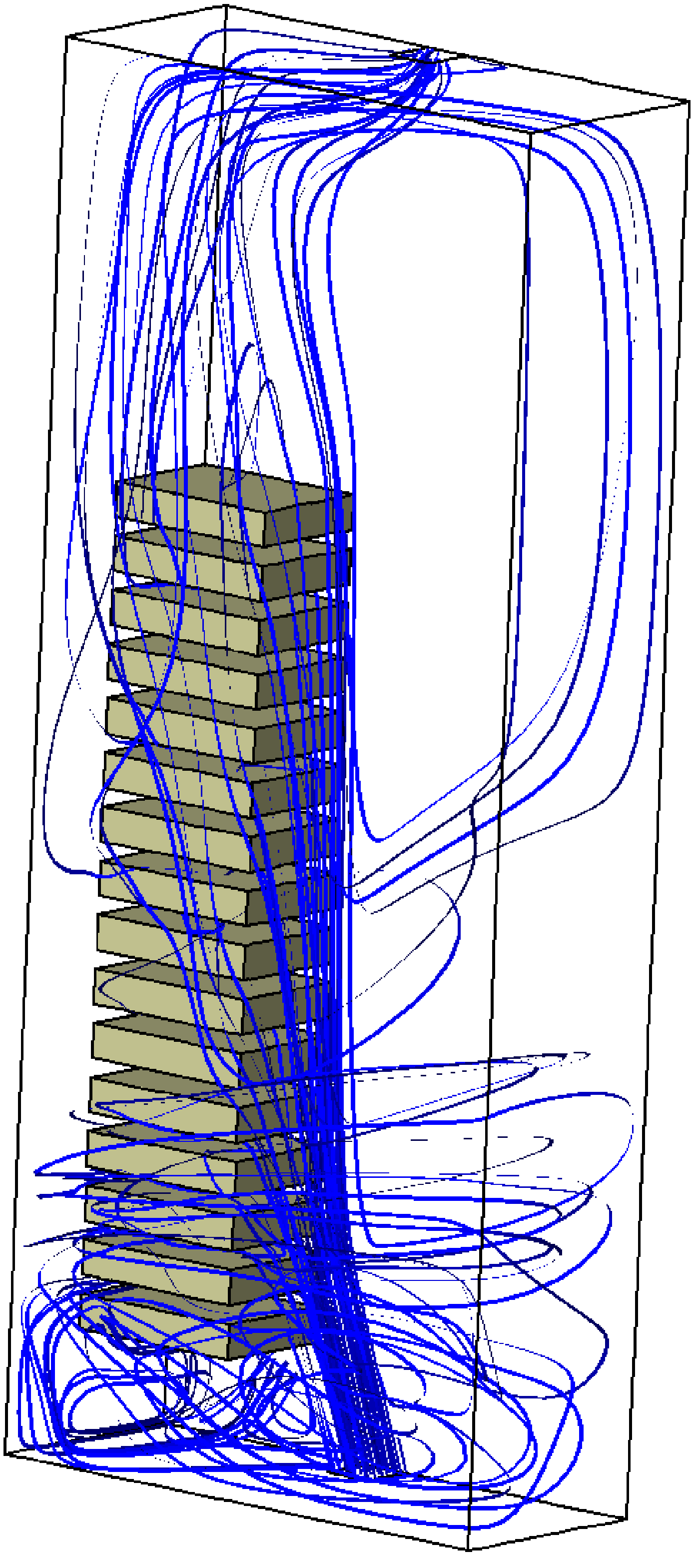

Figure F.7: Streamline plot showing overall flow structure for Case 7

Figure F.8: Streamline plot showing overall flow structure for Case 8

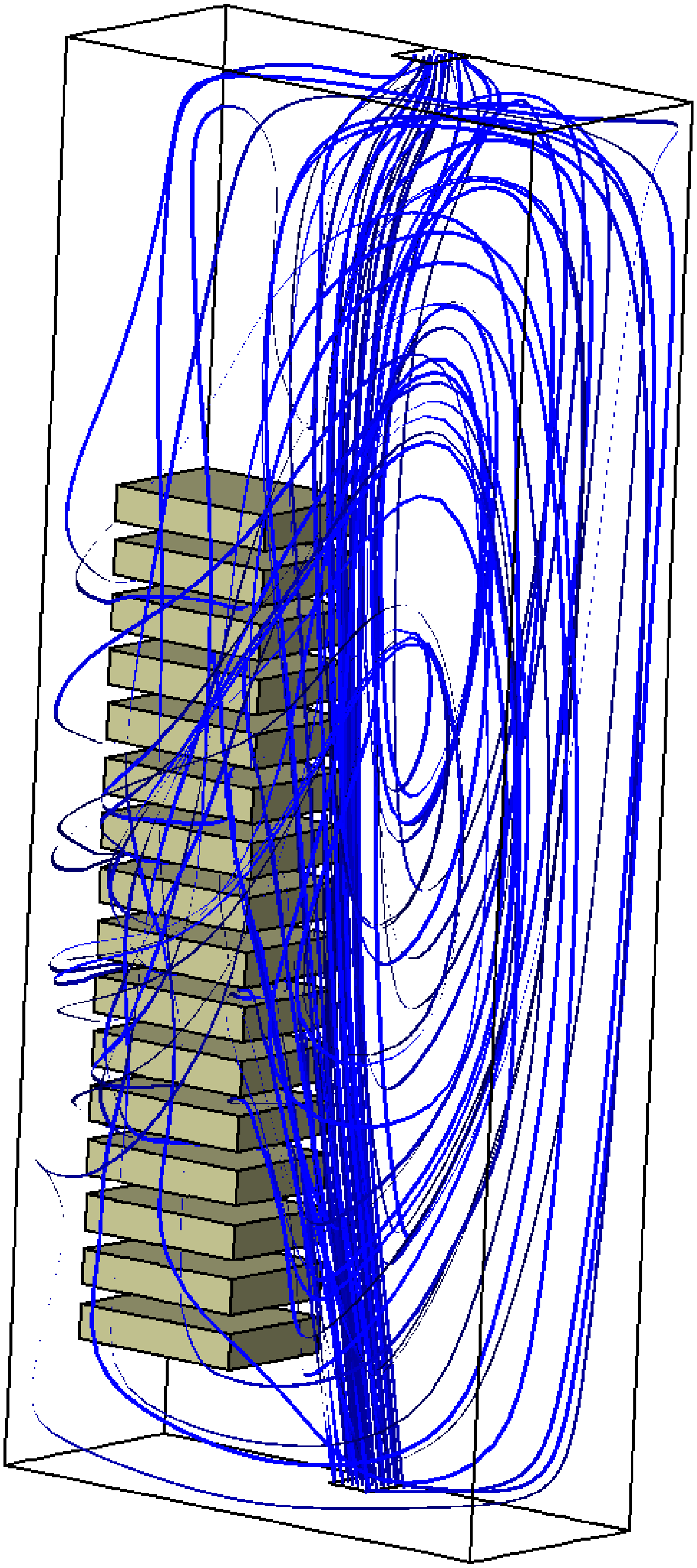

Figure F.9: Streamline plot showing overall flow structure for Case 9

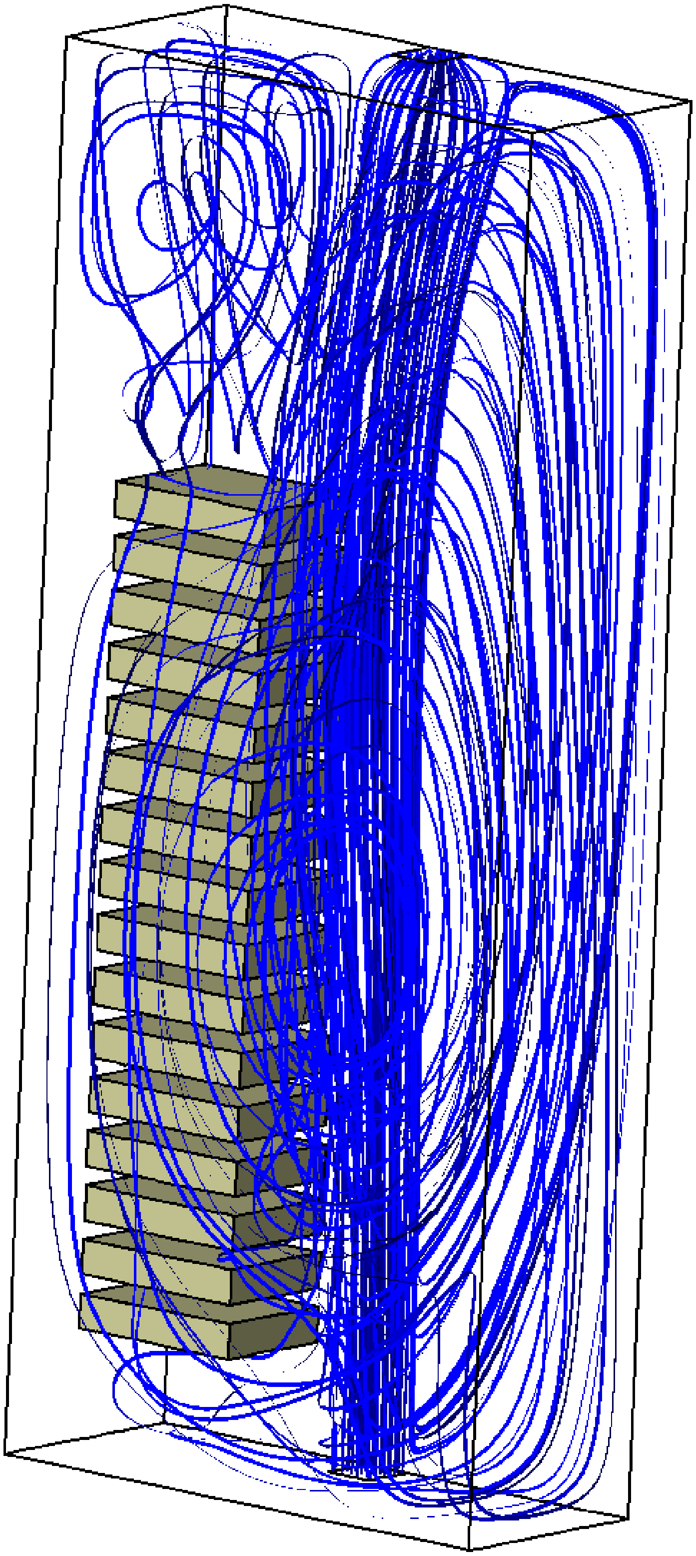

Figure F.10: Streamline plot showing overall flow structure for Case 10

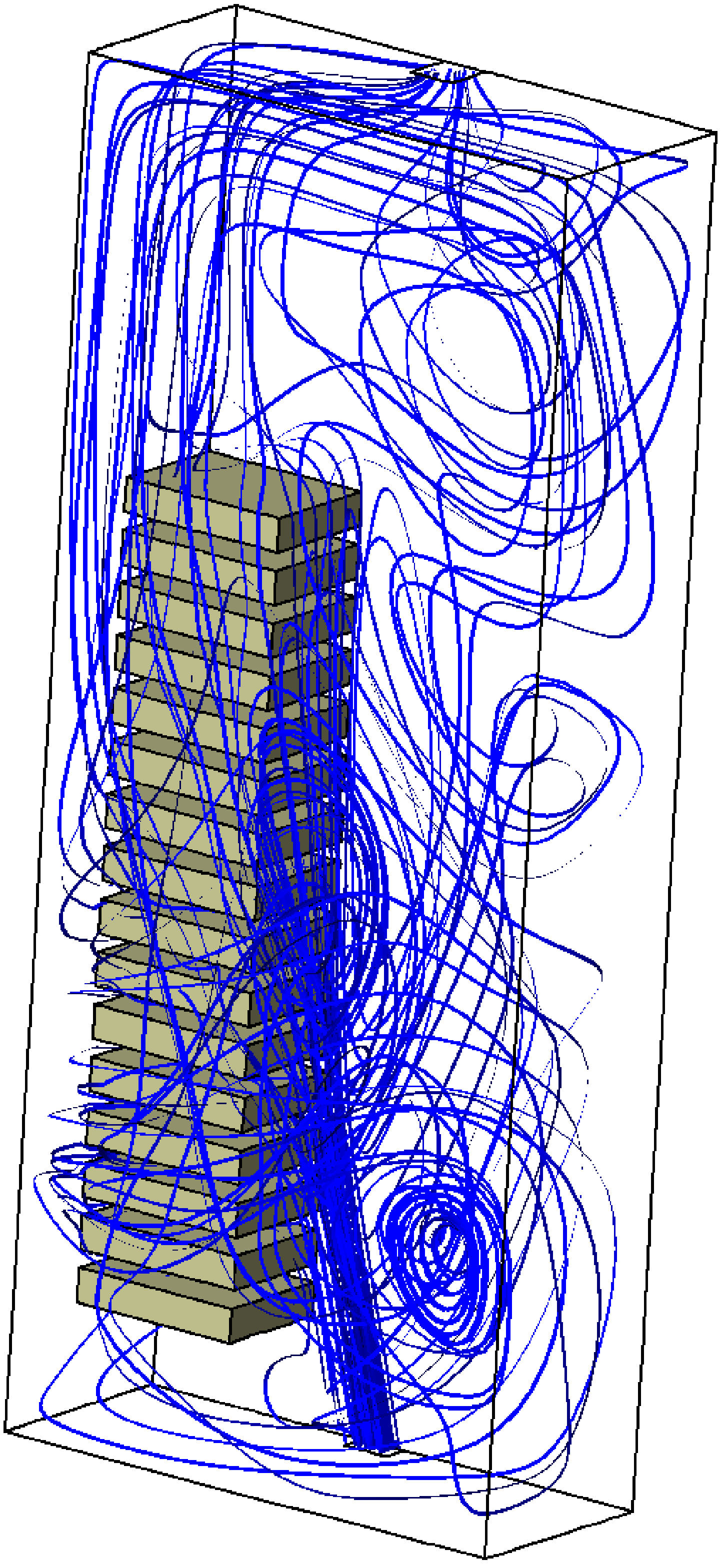

Figure F.11: Streamline plot showing overall flow structure for Case 11

Figure F.12: Streamline plot showing overall flow structure for Case 12

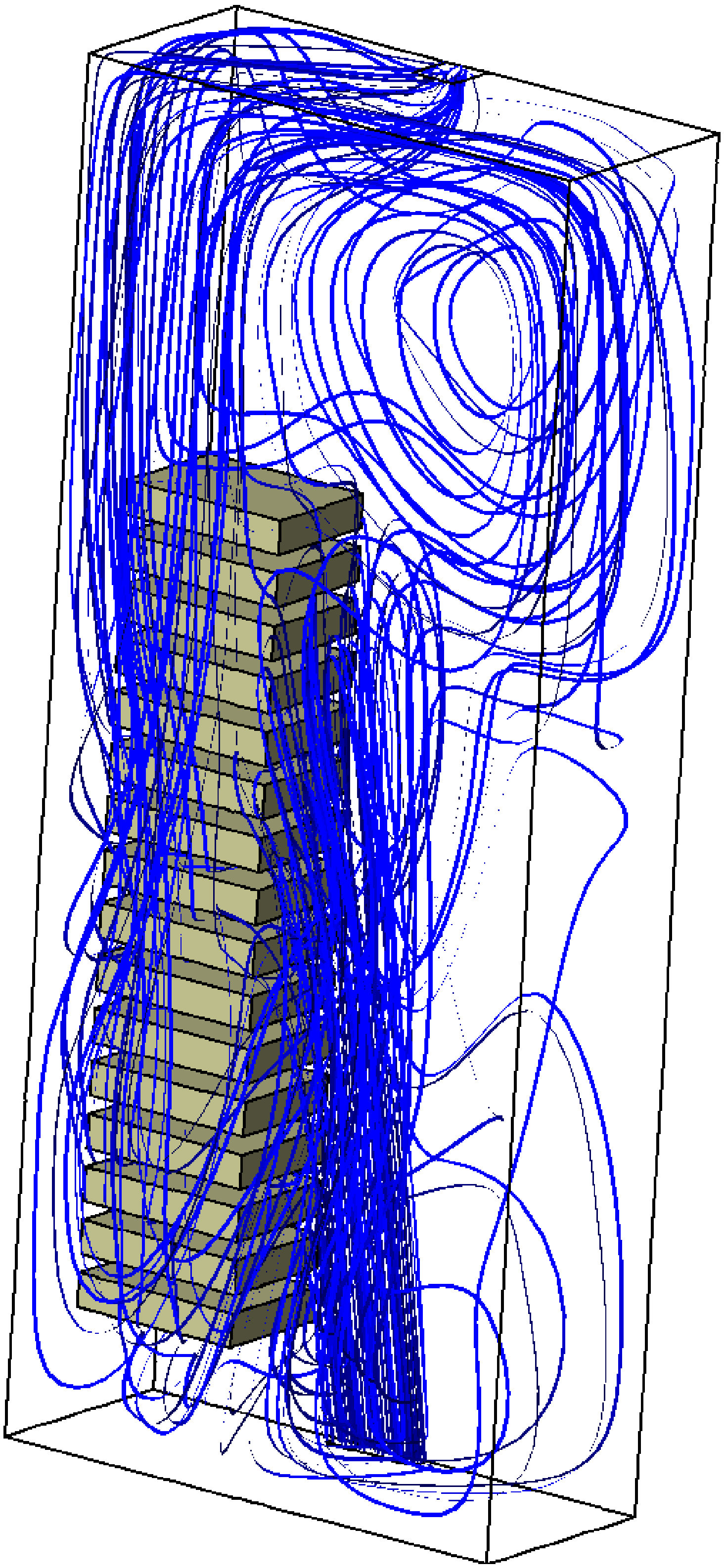

Figure F.13: Streamline plot showing overall flow structure for Case 13

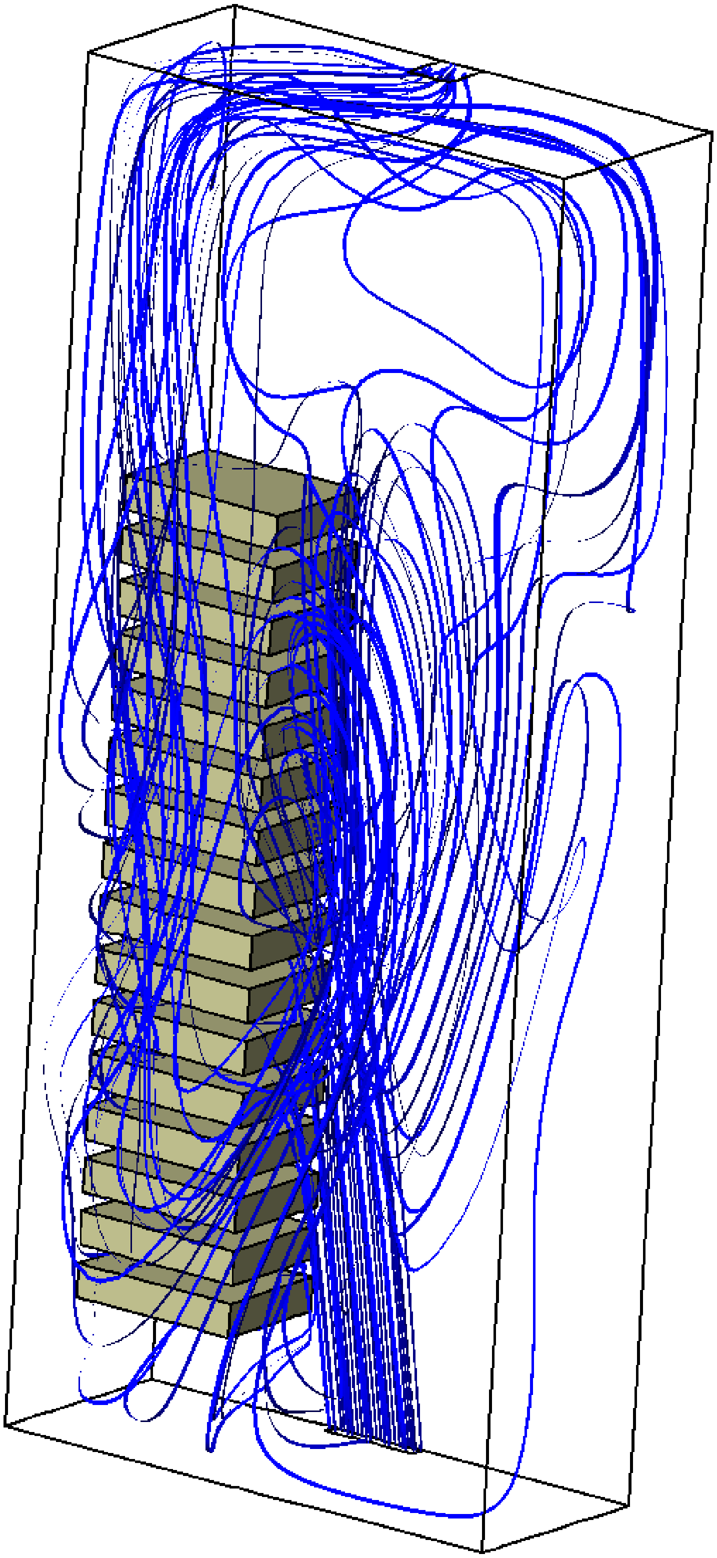

Figure F.14: Streamline plot showing overall flow structure for Case 14

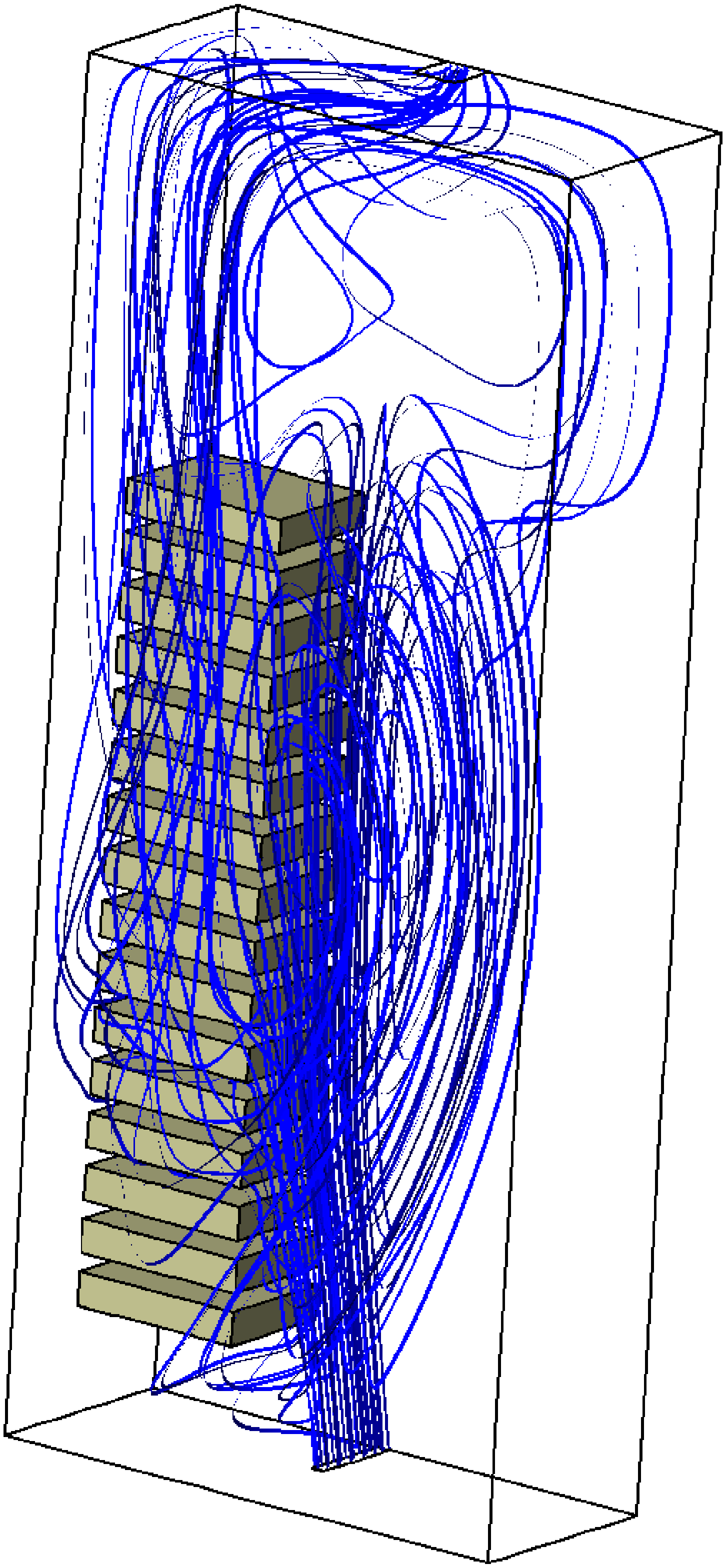

Figure F.15: Streamline plot showing overall flow structure for Case 15

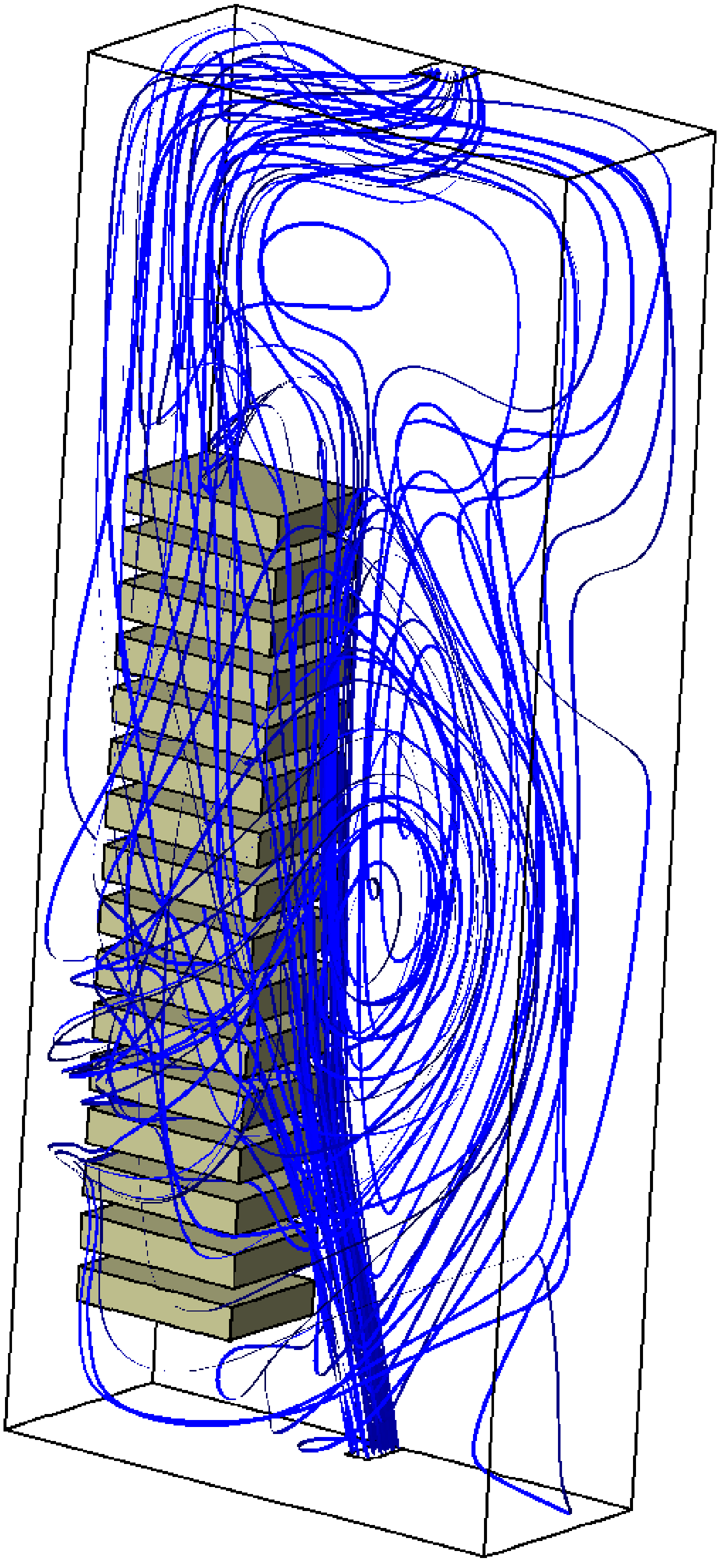

Figure F.16: Streamline plot showing overall flow structure for Case 16

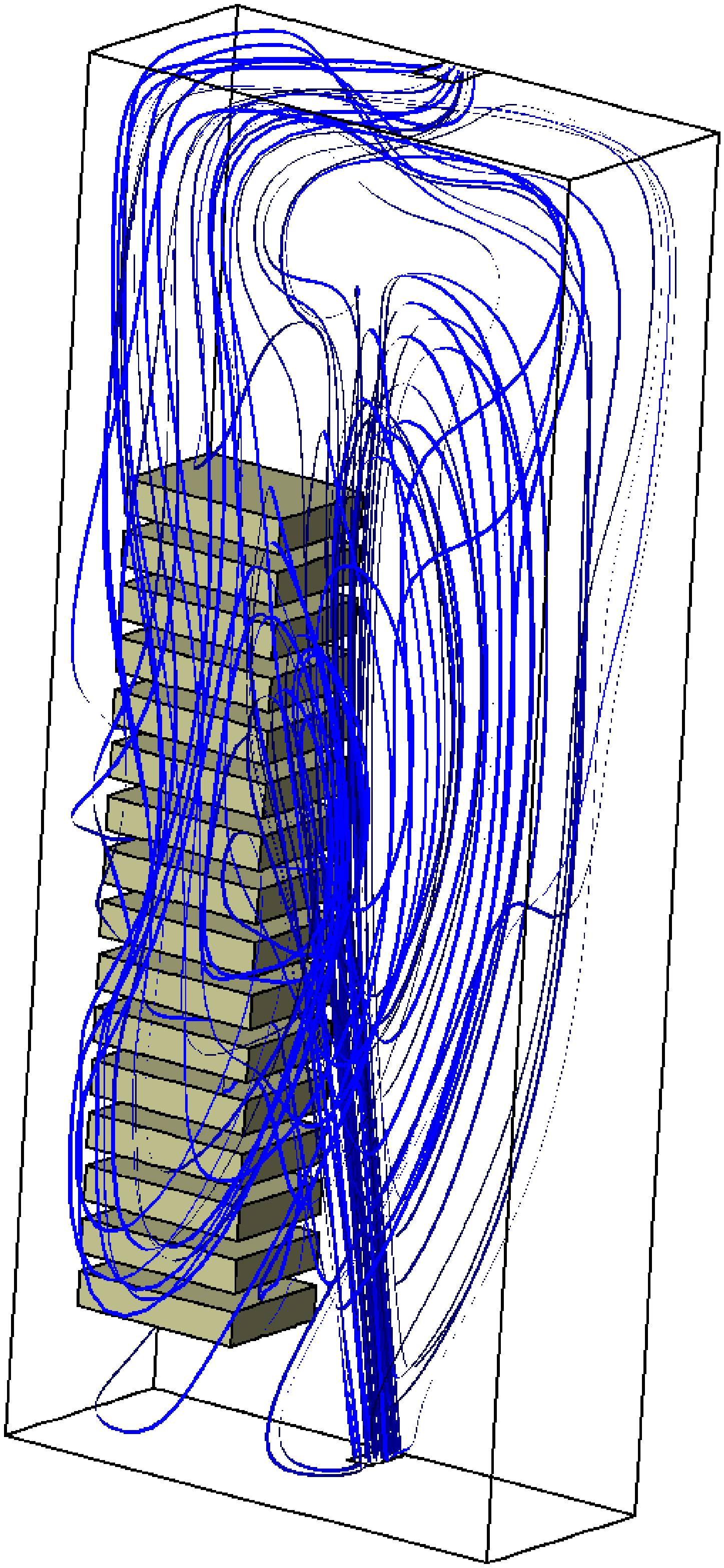

Figure F.17: Streamline plot showing overall flow structure for Case 17

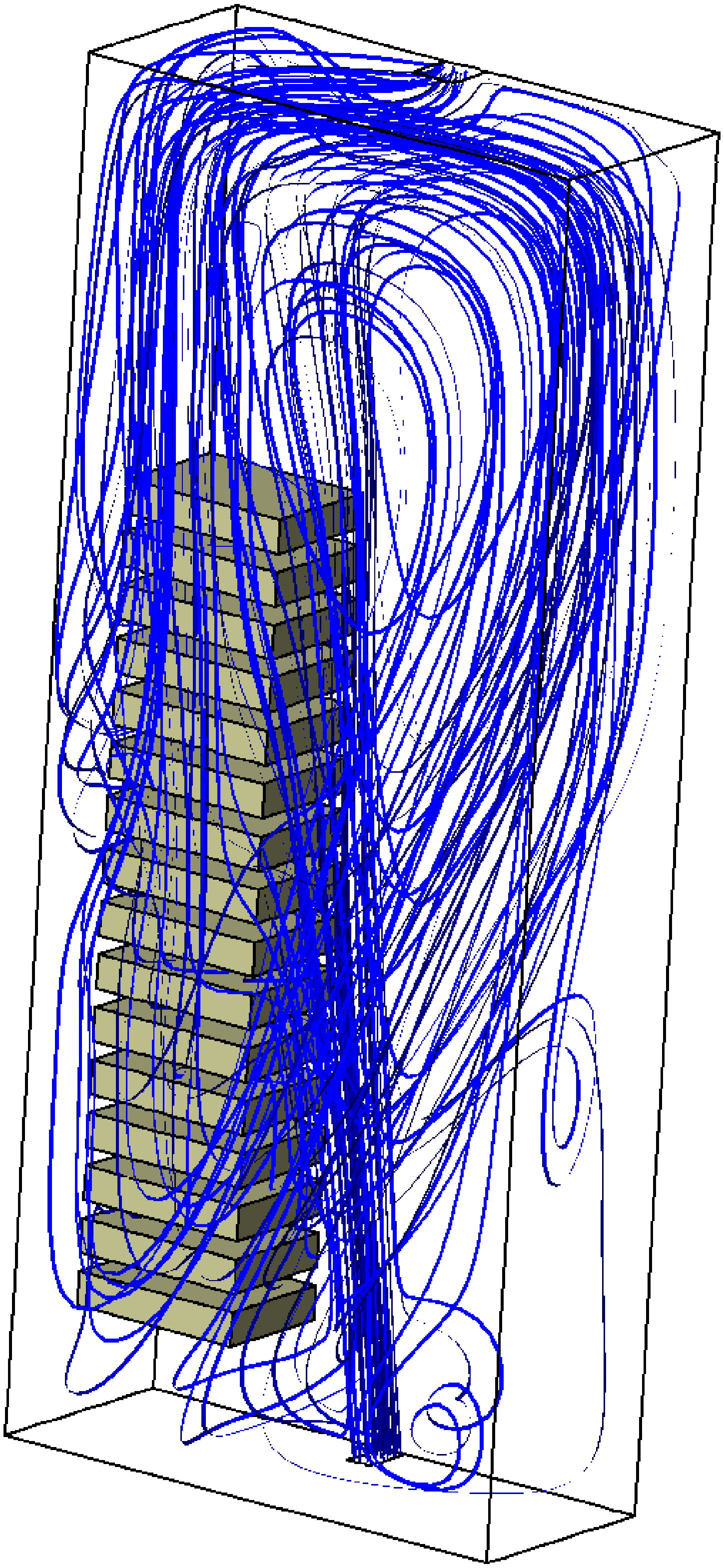

Figure F.18: Streamline plot showing overall flow structure for Case 18

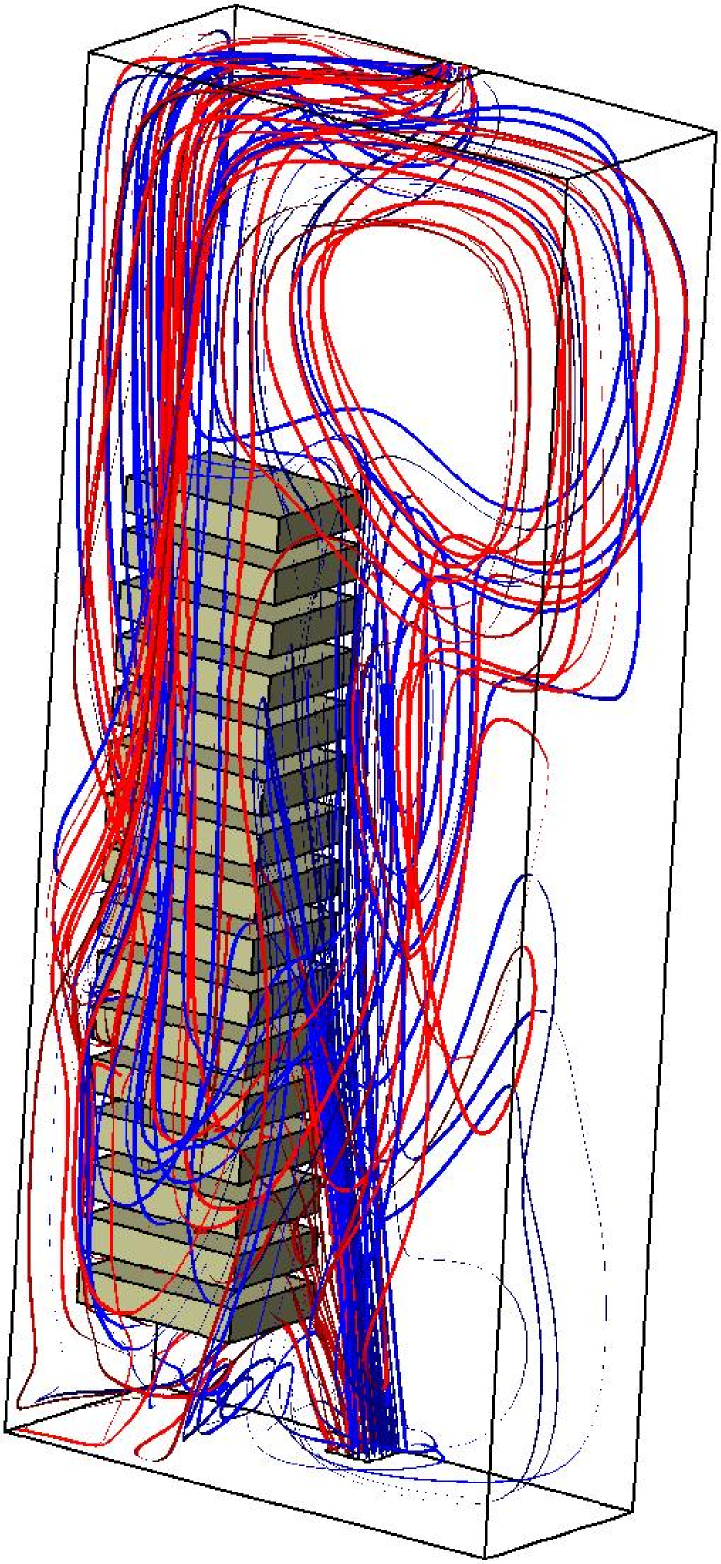

Figure F.19: Streamline plot showing overall flow structure for Case 19

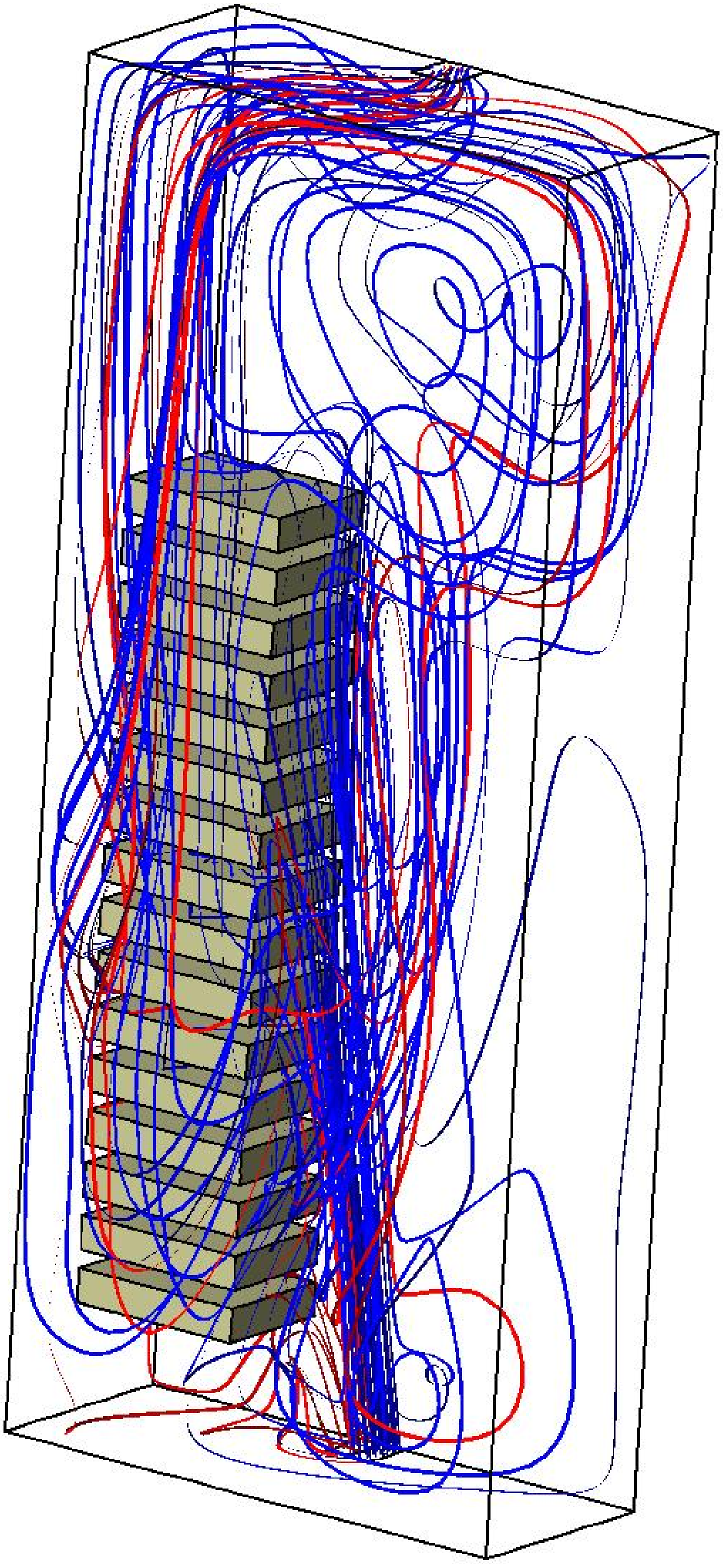

Figure F.20: Streamline plot showing overall flow structure for Case 20

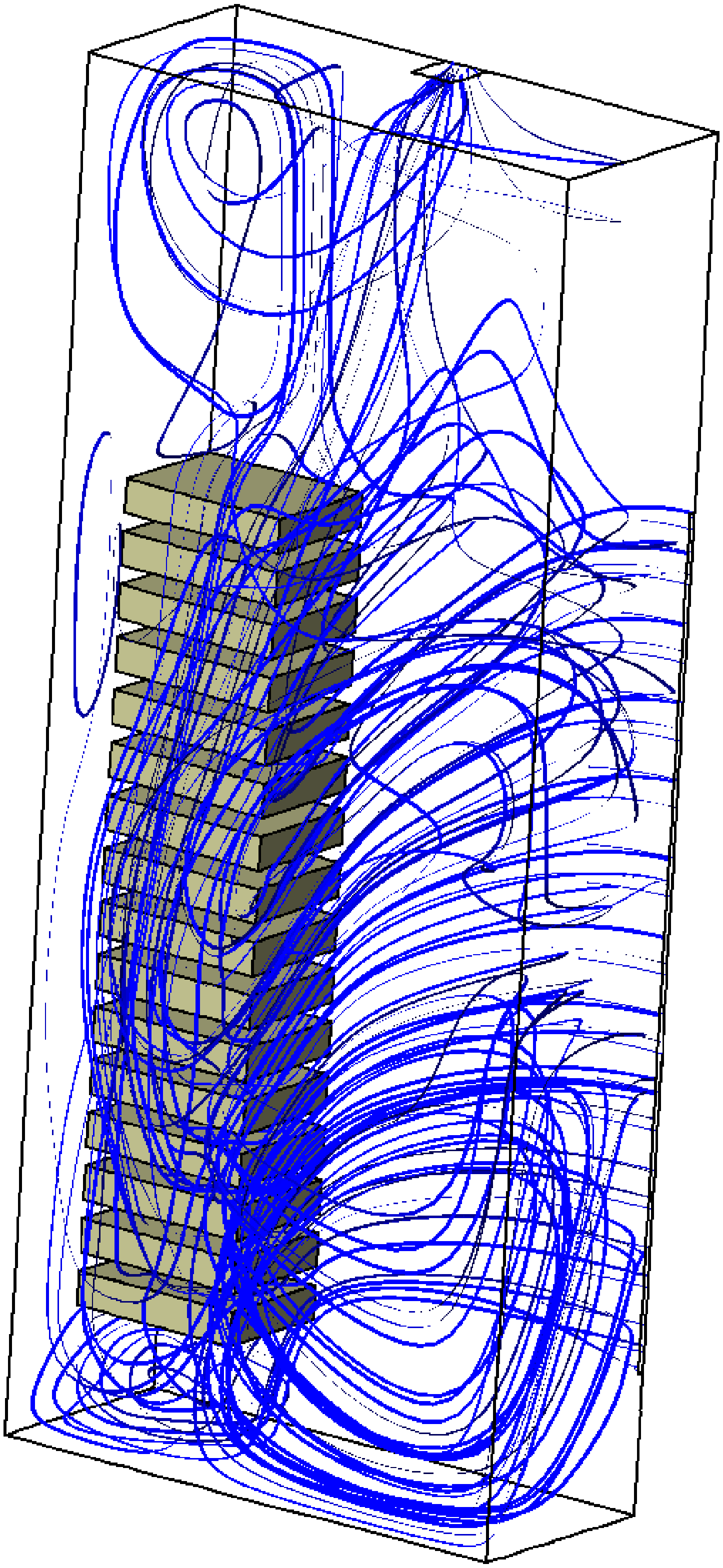

Figure F.21: Streamline plot showing overall flow structure for Case 21

Figure F.22: Streamline plot showing overall flow structure for Case 22

Figure F.23: Streamline plot showing overall flow structure for Case 23

Appendix G

TRIAL COMPUTATIONS FOR COMPUTATIONAL DOMAIN 2

G.1 Introduction

This appendix describes the flow patterns for two non-converged trial computations for Computational Domain 2. These computations with henceforth be known as Trial Case 1 and Trial Case 2. In Trial Case 1, 2812 iterations of the solver were performed, while 2530 iterations of the solver were performed for Trial Case 2. This number of iterations should have been sufficient to obtain a steady-state solution. Instead, oscillations were observed in the residuals. The frequency and magnitude of these oscillations appeared to be approximately constant indicating that they would not diminish with further computation. Because a steady state solution was not obtained for these cases, they are not presented in Chapter 6. Valuable insight, however, can be still be obtained by looking at the flow patterns of the non-converged trial computations. Because these are not converged solutions, the temperature profiles for these cases are not presented. Instead, the cooling effectiveness of these cases can be inferred by the velocity streamlines.

G.2 Dimensions for Trial Cases 1 and 2

The particular parameters for Trial Cases 1 and 2 are summarized in Table G.1. For both of these cases, the inlet opening is located on one side wall of the domain and the outlet opening is located on the other side wall of the domain.

Table G.1: Summary of dimensions used in Trial Cases 1 and 2

Trial Case	L_7 (m)	L_8 (m)	L_9 (m)	L_{13} (m)	L_{14} (m)	L_{15} (m)	$\dot{m}_i$ (kg/s)
1	4.8	0.48	1.09	4.8	0.48	1.09	1.368
2	1.38	7.32	0.545	3.21	3.66	0.545	1.368

G.3 Trial Case 1

For Trial Case 1, the inlet opening is located in the centre of the tower in the *z* direction. The length of the inlet opening in the *z* direction is the same as the length of the inlet opening in the *x* direction for Case 1. The length of the inlet opening in the *y* direction is double the length of the inlet opening in the *y* direction for Case 1. The velocity normal to the opening for Trial Case 1 is identical to that of Case 1. This results in equivalent mass flow rates for the two cases. Figure G.1 shows a three-dimensional velocity streamline plot for Trial Case 1 on the entire domain. In this plot, particles are seeded at the inlet opening and lines are created following the path of these particles through the domain to the outlet. As in Cases 22 and 23, the flow in Trial Case 1 descends in the *z* direction as it approaches the tower due to the fact that it is colder than the surrounding air. The flow also spreads very little in the *z* direction. As a result, the majority of the flow passes through Gaps 6, 7, and 8 and exits through the outlet with very little flow passing through any other tiers. Some the flow makes contact with the lower portion of the opposite wall, changes direction, rises as it approaches the tower, and swirls above the tower before finally exiting at the outlet. There is also some flow that passes under the towers and exits through the outlet without passing through any of the gaps As a result of the lack of flow in 13 of the 16 gaps, it is expected that the maximum temperature for this case would be relatively high. This case reinforces the conclusion that effective cooling is not guaranteed by placing inlet openings on the side walls.

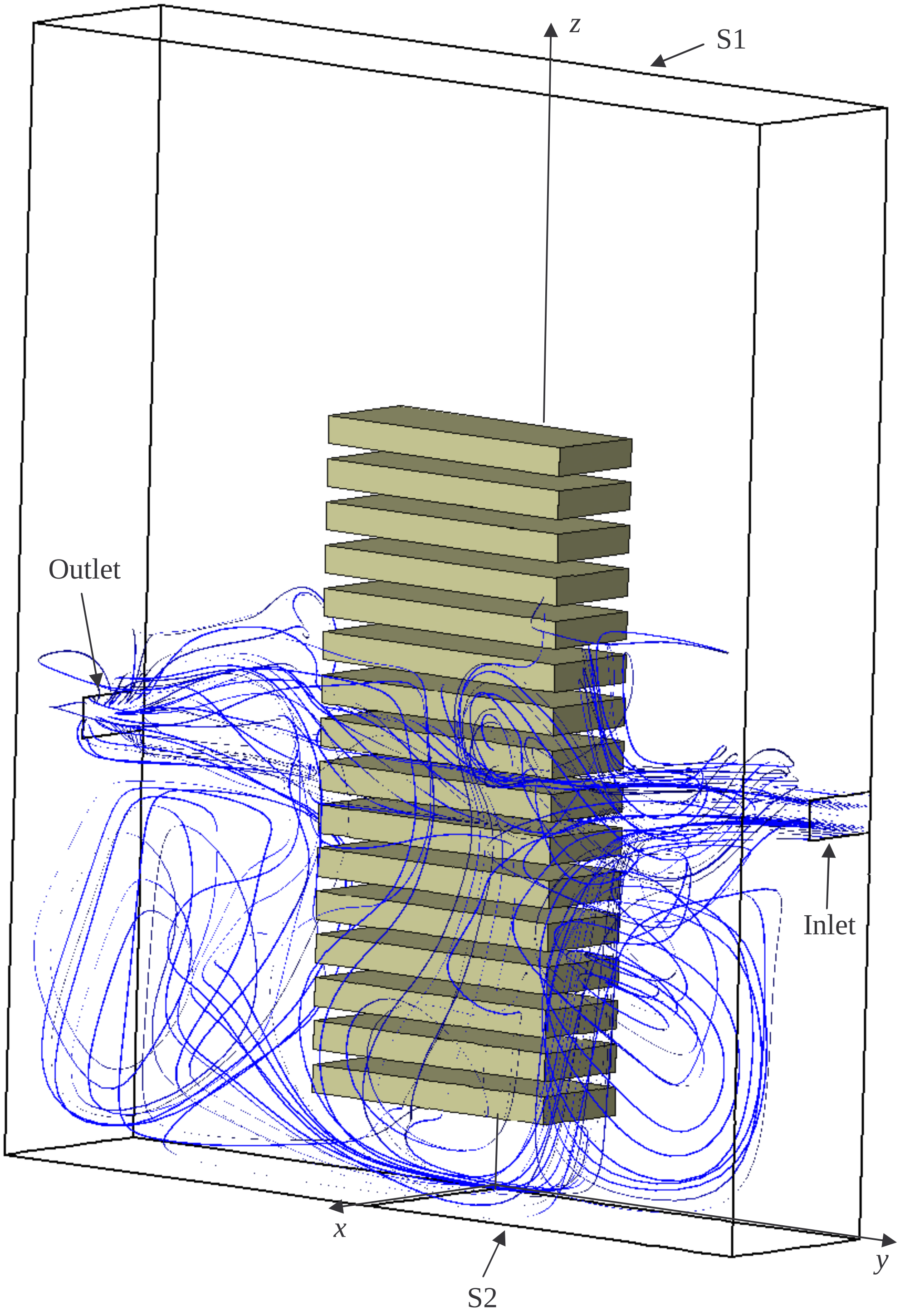

Figure G.1: Three-dimensional streamline plot showing overall flow structure for Trial Case 1

G.4 Trial Case 2

For Trial Case 2, again the inlet opening is located in the centre of the tower in the *z* direction. The length of the inlet opening in the *z* direction was increased from Trial Case 1 in an attempt to force more air through all of the tiers. With the inlet opening parameters described in Table E.1, the inlet opening velocity becomes 0.343 m/s. This results in equivalent mass flow rates between this case and Case 1. Figure G.2 shows a three-dimensional velocity streamline plot Trial Case 2 on the entire domain. In this plot, particles are seeded at the inlet opening and lines are created following the path of these particles through the domain to the outlet. As in all other cases for Computational Domain 2, the flow in Case 24 descends in the z direction as it approaches the tower due to the fact that it is colder than the surrounding air. In this case, however, it is much more dramatic, with all of the stream lines falling below the height of the first gap because the horizontal momentum in this case is much lower than in other cases for Computational Domain 2. Most of the streamlines pass under the tower and exit the outlet without passing through any of the gaps. The remainder of the streamlines rise as they approach the tower before they finally exit through the outlet. Very little flow passes through any of the gaps in the tower. As a result of the lack of flow in the gaps, it is expected that the maximum temperature between all of the gaps would be relatively high for this case. Once again, this case further reinforces the conclusion that effective cooling is not guaranteed by placing inlet openings on the side walls.

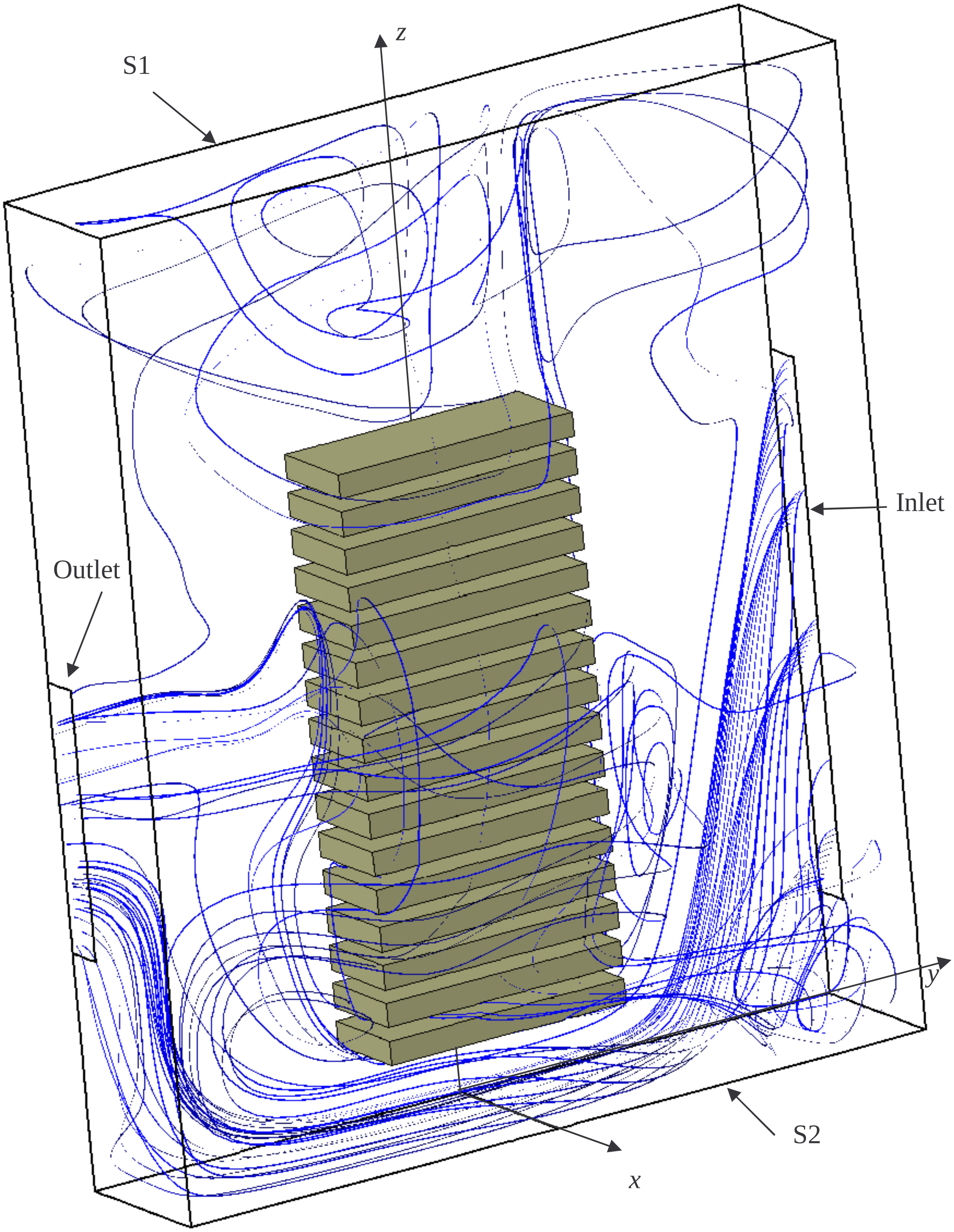

Figure G.2: Three-dimensional streamline plot showing overall flow structure for Trial Case 2